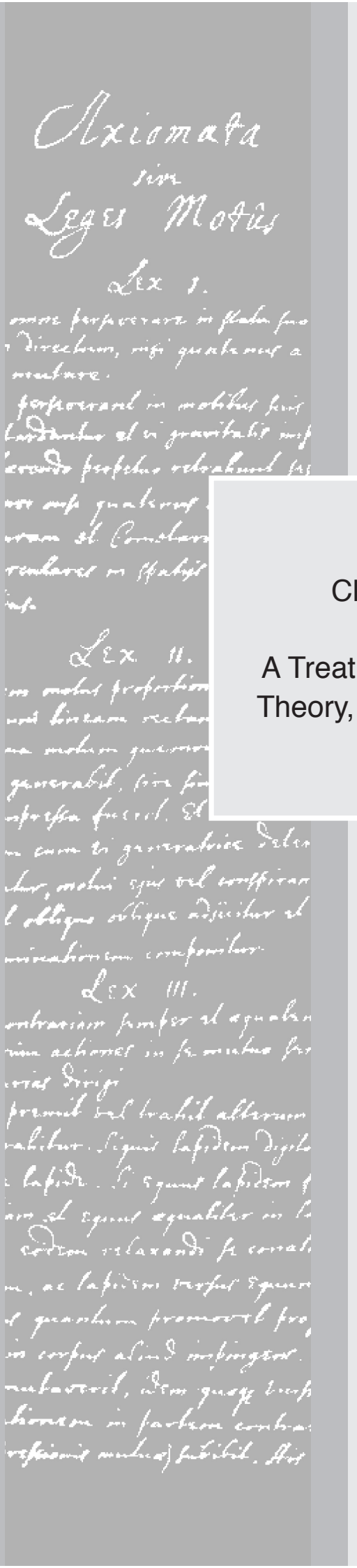

Technische Universität
Kaiserslautern

Claudia Britta Hirschberger

A Treatise on Micromorphic Continua. Theory, Homogenization, Computation

UKL/LTM T 08-03 Juni 2008
Lehrstuhl für Technische Mechanik

Bibliografische Information Der Deutschen Bibliothek
Die Deutsche Bibliothek verzeichnet diese Publikation in der Deutschen Nationalbibliografie; detaillierte bibliografische Daten sind im Internet über **http://dnb.ddb.de** abrufbar.

Bibliographic information published by Die Deutsche Bibliothek
Die Deutsche Bibliothek lists this publication in the Deutsche Nationalbibliografie; detailed bibliographic data is available in the Internet at **http://dnb.ddb.de.**

Farbig erschienen auf http://kluedo.ub.uni-kl.de

Herausgeber: Fachbereich Maschinenbau und Verfahrenstechnik
Lehrstuhl für Technische Mechanik
Postfach 3049
Technische Universität Kaiserslautern
D-67653 Kaiserslautern

Verlag: Technische Universität Kaiserslautern

Druck: Technische Universität Kaiserslautern
ZBT – Abteilung Foto-Repro-Druck

D-386

Als Manuskript gedruckt. Printed in Germany.

ISSN 1610-4641
ISBN 978-3-939432-80-7

A Treatise on Micromorphic Continua.

Theory, Homogenization, Computation

vom Fachbereich Maschinenbau und Verfahrenstechnik
der Technischen Universität Kaiserslautern
zur Verleihung des akademischen Grades
Doktor-Ingenieur (Dr.-Ing.)
genehmigte Dissertation

von
Dipl.–Ing. Claudia Britta Hirschberger
aus Diez

Hauptreferent:	Prof. Dr.–Ing. P. Steinmann
Korreferenten:	Prof. dr. ir. M. G. D. Geers
	Prof. Dr.–Ing. C. Tsakmakis
	Prof. Dr.–Ing. M. Maier
Vorsitzender:	Prof. Dr.–Ing. J. C. Aurich
Dekan:	Prof. Dr.–Ing. S. Ripperger

Tag der Einreichung:	13. Februar 2008
Tag der mündl. Prüfung:	28. April 2008

Kaiserslautern, Juni 2008

D 386

Preface

The research presented in this thesis was carried out during my time as a PhD student at the Chair of Applied Mechanics at the University of Kaiserslautern from April 2005 to February 2008. The financial support by the DFG within the International Research Training Group 1131 entitled *"Visualization of Large and Unstructured Data Sets – Applications in Geospatial Planning, Modeling, and Engineering"* is gratefully acknowledged.

First of all, I would like to express my gratitude to Professor Paul Steinmann for his supervision during the last three years, in which he created a scientifically stimulating and inspiring work atmosphere, and especially for giving me the opportunity to spend some time abroad and to participate in several international conferences and summer schools. I gratefully appreciate Professor Ellen Kuhl for both her supervision and her encouragement to exploit the internationality of the project. As a project partner abroad, Professor Natarajan Sukumar deserves my special thanks for his cheerful support and collaboration during my stays at University of California at Davis and thereafter. Moreover I would like to thank the referees of my thesis, Professor Charalampos Tsakmakis, Professor Marc Geers, and Professor Martin Maier, as well as the head of the commission Professor Jan Aurich for their effort within the proceeding. Charalampos Tsakmakis is moreover thanked for laying my fundaments in continuum mechanics, and Marc Geers for providing inspiring discussions at various occasions.

Special thanks also go to all my colleagues at LTM in Kaiserslautern, especially to Rouven Mohr, Andreas Menzel, Natalia Kondratieva, Sarah Ricker, Michael Scherer, Johannes Utzinger, for creating an enjoyable work atmosphere. Furthermore I would like to thank my teammates Elke Eichhorn, Dr. Dagmar Roth, and Heike Spies and especially Andrea Scherer for making me feel at home in the Palatinate. Andrea's and Dagmar's efforts of real-time proof-reading the manuscript of this thesis are especially acknowledged. Last but not least, I thank my family, particularly my parents for their love and support.

Kaiserslautern, June 2008 Britta Hirschberger

Contents

Zusammenfassung

Die vorliegende Arbeit behandelt die kontinuumsmechanische Beschreibung und die numerische Simulation von Materialien, die größenabhängiges Verhalten aufweisen. Besondere Beachtung findet dabei die numerische Modellierung dünner Materialschichten, die aus heterogenen oder mikrostrukturierten Materialien bestehen. Diese Ziele werden durch die Verwendung eines mikromorphen Kontinuums und mithilfe von Homogenisierungsverfahren erreicht, die es erlauben, gleichzeitig mehrere räumliche Skalen zu betrachten.

Motivation

Grössenabhängige Effekte. Materialen, obgleich sie makroskopisch homogen erscheinen mögen, besitzen normalerweise eine ausgeprägte Mikrostruktur, wenn sie auf besonders kleinen Skalen betrachtet werden. Ihre Mikrobestandteile, die auf aufsteigenden Skalen zutage treten, sind zum Beispiel Atome, Moleküle, Einkristalle, Mehrkristalle oder einzelne Körner. Während Methoden der Atomistik, der Molekulardynamik oder partikelbasierte Methoden diesen einzelnen Bestandteilen Rechnung tragen, löst der phänomenologische Zugang, der in der Kontinuumsmechanik verfolgt wird, diese Einheiten nicht einzeln auf. Ihre kontinuierliche Repräsentation behandelt die effektiven globalen Eigenschaften, die in Feldgleichungen beschrieben werden. Diese Vorgehensweise bildet das tatsächliche Verhalten sehr gut ab, solange sich die räumlichen Skalen des Kontinuums und die der zugrundeliegenden Mikrostruktur um mehrere Größenordnungen unterscheiden. In üblichen Ingenieuranwendungen genügt dieses Kontinuumsbeschreibung vollkommen, insbesondere, wenn sie mit ausgefeilten konstitutiven Modellen einhergeht, die ein komplexes Materialverhalten abbilden. Wenn jedoch die betrachtete Struktur oder Probe klein gegenüber ihrer intrinsischen Mikrostruktur ist, treten ausgeprägte Größeneffekte auf. Solche Größeneffekte, wie sie beispielsweise von Aifantis (1984), Fleck et al. (1994) berichtet wurden, wirken sich typischerweise als höhere Steifigkeit bei kleinerer Probengröße aus, wenn sich die Probengröße einer charakteristischen Abmessung der intrinsischen Mikrostruktur annähert.

Heterogene Materialien. Neben der intrinsischen Mikrostruktur, die durch die beispielsweise molekulare oder polykristalline Beschaffenheit der jeweiligen Materie ins Spiel kommt, besitzen auch viele Materialien strukturelle Inhomogenitäten.

Solche Heterogenitäten zeigen sich bespielsweise als Risse, kleine Einschlüsse oder Hohlräume. Sie treten unter anderem in faserverstärkten Ingenieurmaterialien, wie zum Beispiel Metal–Polymer-Matrix-Materialien, Beton, oder in natürlich vorkommenden Verbundmaterialien, wie z. B. geologischen Konglomeraten, auf. Weitere Beispiele liegen in Metalllegierungen, Polymermischungen, porösen oder gerissenen Medien, sowie polykristallinen Materialien. Neben den Materialeigenschaften des umgebenden Matrixmaterials bestimmen die jeweiligen Eigenschaften dieser Heterogenitäten die Gesamteigenschaften des Materials. Dabei beeinflussen sowohl die eigentlichen Materialeigenschaften des zugrundeliegenden Materials als auch die Größe, die Form und die räumliche Verteilung der Heterogenitäten die globale Materialantwort. Wenn Heterogenitäten regelmäßig im Material verteilt sind, können homogenisierte Modelle eingesetzt werden, um die Eigenschafte des Gesamtmaterials zu erfassen, ohne dabei die individuellen Bestandteile einzeln erfassen zu müssen.

Materialschichten. Adhäsive Schichten, die zwei Festkörper miteinander verbinden und dabei kohäsive Kräfte übertragen, kommen in vielen Ingenieuranwendungen vor. Schweißverbindungen, adhäsive Klebeverbindungen, laminierte Verbundstrukturen, Baumaterialien wie beispielsweise Mauerwerk, sowie geologische Materialien sind nur einige Beispiele. In vielen Fällen verhält sich das Material in der verbindenden Schicht bedeutend weicher als das des angrenzenden Festkörpers, so dass die Verformung stark in dieser Schicht konzentriert sein wird. Eine Modellierung einer solchen Schicht kann daher erreicht werden, indem es als Diskontinuität innerhalb eines kontinuierlichen Mediums angesehen wird. Solche werden üblicherweise als kohäsive Grenzfläche dargestellt, die sich durch ihre Verschiebungssprung auszeichnet und die kohäsive Kräfte überträgt. Das konstitutive Verhalten einer solchen Grenzfläche wird gewöhnlich durch ein sogenanntes kohäsives Gesetz oder Kraft–Verschiebungssprung-Gesetz beschrieben. Allerdings stößt diese phänomenologische Modellierung an die Grenze ihrer Anwendbarkeit, wenn die Materialschicht eine ausgeprägte intrinsische Mikrostruktur oder eine heterogene Mikrostruktur aufweist. Im letzten Fall wird diese Heterogenität großen Einfluss auf das globale Verhalten ausüben. Daher ist es wünschenswert, anstatt einer vorab getroffenen konstitutiven Annahme diesen Einfluss direkt zu modellieren. Für besonders dünne Materialschichten, deren zugrundeliegende intrinsische Mikrostruktur relativ groß ist, werden die oben genannten Größeneffekte auftreten. Daher soll eine Methode zur Einbeziehung von Heterogenitäten auch gleichzeitig diese Größeneffekte abbilden.

Stand der Forschung

In der Angewandten und der Numerischen Mechanik existieren Lösungsansätze, um die zuvor genannten Probleme anzugehen. Im folgenden soll ein kurzer Überblick gegeben werden.

Generalisierte Kontinua zur Behandlung von Größeneffekten. In der Kontinuumsmechanik stellen sogenannte generalisierte Kontinuumstheorien anspruchsvollere Kontinuumstheorien dar, die besonders gut geeignet sind, um die erwähnten Größeneffekte abzubilden. Die zusätzliche Komplexität liegt dabei entweder in der Einbeziehung höherer Gradienten der Verschiebung oder zusätzlicher kinematischer Freiheitsgrade. Ihre Entstehung geht auf die wegweisende Momentenspannungstheorie der Gebrüder Cosserat and Cosserat (1909) zurück, die zusätzliche Rotationsfreiheitsgrade an jedem materiellen Punkt im Kontinuum annahmen. In den Sechzigerjahren wurde diese Idee von Mindlin and Tiersten (1962), Mindlin (1963, 1964, 1965), Mindlin and Eshel (1968), Koiter (1964), Toupin (1962, 1964) sowie Eringen (1964, 1968) aufgegriffen und weiterentwikkelt. Die Theorien beziehen einen Größeneffekt durch die Einführung einer internen Länge als konstitutiven Parameter ein.

Generalisierte Kontinua und davon abgeleitete Konzepte werden vor allem auch in Verbindung mit irreversiblem Materialverhalten geschätzt. Herausragende Beispiel dafür sind zum einen die Formulierungen, die unter dem Synonym *Gradientenplastizität* (z. B. Fleck and Hutchinson (1993), Polizzotto and Borino (1998), Menzel and Steinmann (2000), Liebe and Steinmann (2001)) zusammengefasst sind und zum anderen diejenigen, die zu mikromorphen Plastizitätstheorien (z. B. Steinmann and Willam (1991), Borst (1991), Grammenoudis and Tsakmakis (2001)) gehören. Neben dem Vorteil, dass diese Formulierungen Größeneffekte in einem Bereich irreversibler Verformung abbilden, spielen sie eine entscheidende Rolle in der Regularisierung lokalisierten entfestigenden Materialverhaltens.

Mehrskalenmodellierung mittels Homogenisierung. Zur kontinuumsmechanischen und numerischen Modellierung heterogener Materialien wurden verschiedene Konzepte entwickelt, die mehrere Skalen einbeziehen. Während das theoretische Konzept der Homogenisierung weitgehend auf den wegweisenden Arbeiten von Hill (1963, 1972) aufbaut, hat die numerischen Mehrskalenmodellierung innerhalb des letzten Jahrzehnts zahlreiche Wissenschaftler beschäftigt. Was alle Mehrskalenmethoden gemeinsam haben, ist ein Procedere, um die globalen makroskopischen Charakteristiken eines heterogenen Materials zu bestimmen. Dabei müssen sie eine angemessene Methode der Mittelung über eine sorgfältig gewählten Teil des makroskopischen Körpers vorhalten, um die Gesamteigenschaften mit den Mikro-Eigenschaften in Beziehung zu setzen (Hill, 1963, 1972, Nemat-Nasser and

Hori, 1999). Unter den verschiedensten Mehrskalenmethoden in der Mechanik beschränken wir uns auf die direkten Mikro–Makro-Methoden. Hierbei werden die maßgeblichen Spannungs–Dehnungsbeziehungen am makroskopischen Punkt ermittelt, indem separate Berechnungen in einem repräsentativen Volumenelement durchgeführt werden. Um die konstitutiven Eigenschaften des (Makro-) Kontinuums aus den Eigenschaften und der Struktur des zugrundeliegenden Mikrobeschaffenheit zu erhalten, wird das repräsentativen Volumenelement Randbedingungen unterworfen, die durch gleichförmige Kontinuumsfelder auf der Makroebene diktiert werden.

Numerische Umsetzungen dieser direkten Mehrskalenmethoden innerhalb der Methode der Finiten Elemente wurden zum Beispiel in den Beiträgen von Miehe et al. (1999a,b, 2002a,b,c), Miehe and Koch (2002), Feyel and Chaboche (2000), sowie Smit et al. (1998) und Kouznetsova et al. (2001, 2002, 2004) vorgestellt. Dabei besteht das numerische Mehrskalenmodell aus zwei Ebenen, einer Makro- und einer Mikroebene und wurde daher von Feyel and Chaboche (2000) auch als FE^2 bezeichnet. Auf der Makroebene wird ein diskretisiertes Randwertproblem völlig ohne konstitutive Routinen formuliert. In den Integrationspunkten eines jeden finiten Elements dieser Ebene wird hingegen die Materialantwort mithilfe eines zugrundeliegenden repräsentativen Volumenelements ausgewertet. Dieses repräsentative Volumenelement modelliert die Mikrostruktur, die ebenfalls diskretisiert wird und einen konstitutiven Ansatz enthält. Das Mikrorandwertproblem wird auf diesem RVE unter Randbedingungen gelöst, die von der Makroebene bestimmt werden. Die Makrospannung und ein konstitutiver Tangentenoperator werden zur Makroebene zurückgegeben.

Materialschichten. Eine Materialschicht wird in der Mechanik üblicherweise als kohäsive Grenzschicht innerhalb eines Kontinuums behandelt. Die darin auftretende Deformation, nämlich die Klaffung zwischen gegenüberliegenden Seiten der Grenzschicht und die übertragende Kraft werden vektoriell und getrennt vom umgebenden Kontinuum beschrieben. Für die konstitutive Beziehung innerhalb der Grenzschicht wurden kohäsive Gesetze vorgeschlagen. Die meisten sind für Versagensprozesse entwickelt worden, siehe z. B. Needleman (1987, 1990a,b), Tvergaard and Hutchinson (1992), Xu and Needleman (1993), Ortiz and Pandolfi (1999) sowie Nguyen et al. (2001). Die meisten Ansätze nehmen eine tangential und normal entkoppelte Antwort an. Numerisch kann eine solche kohäsive Grenzschicht einfach durch ein kohäsives "Interface"- oder Übergangselement abgebildet werden (Beer, 1985, Schellekens and de Borst, 1993a,b).

Ziele und Inhalte der Arbeit

Ziele. Aus den Beobachtung von Größeneffekten, heterogenen Materialien sowie Materialschichten leiten sich einige Herausforderungen im Sinne der numerischen Kontinuumsmechanik ab. Die daraus hervorgehenden Ziele der Arbeit werden im Folgenden vorgestellt. Eine numerische Mehrskalenmethode für die Modellierung von Materialschichten mit heterogener Mikrostruktur wird benötigt. Ein angemessener numerischer Rahmen zur Einbettung in die Finite-Elemente-Methode soll besonders auch Größeneffekten Rechnung tragen. Daher soll ein generalisiertes Kontinuum auf einer zugrundeliegenden feineren Skala eingesetzt werden. Aufgrund seiner günstigen Eigenschaften im Hinblicke auf die numerischen Simulation, soll zu diesem Zweck ein mikromorphes Kontinuum verwendet werden. Um eine solche numerische Homogenisierung unter Einbindung eines mikromorphen Kontinuums durchführen zu können, muss ein passendes numerisches Schema entwickelt werden. Es wird ein konstitutiver und numerischer Rahmen angestrebt, der große Deformationen zulässt. Darauf aufbauend soll die Methode der materiellen Kräfte auf das mikromorphe Kontinuum angewandt werden.

Im Zusammenhang der generalisierten Kontinua soll das Augenmerk auch auf inelastische konstitutive Formulierungen solcher Theorien gelenkt werden. Bestehende Theorien sollen analysiert und klassifiziert werden und neue Möglichkeiten aufgezeigt werden.

Inhalt. Zunächst wird ein kurzer Überblick über generalisierte Kontinuumstheorien gegeben. Danach wird die mikromorphe Kontinuumstheorie unter der Annahme von hyperelastischem Materialverhalten genauer beleuchtet. Dabei wird ein konstitutiver Ansatz getroffen und eine numerische Formulierung eingeführt. Aufgrund der dualen Formulierung im Sinne der Deformations- und der Konfigurationsmechanik wird die Methode der Materiellen Kräfte angewandt. Numerische Beispiele demonstrieren die charakteristischen Eigenschaften des Kontinuums. Um die Homogenisierung von Materialschichten vorzubereiten, wird zunächst ein Einblick in übliche Homogenisierungsmethoden, angewandt auf Kontinua, gewährt. Darauf aufbauend wird eine Methode entwickelt, die die numerische Homogenisierung besagter Materialschichten ermöglicht. Dabei werden zunächst heterogene Mikrostrukturen betrachtet, die sich mit klassischen Formulierung modellieren lassen. Darauf aufbauend, wird das Konzept erweitert und eine der Materialschicht zugrundeliegende mikromorphe Mesostruktur betrachtet, die Größeneffekte aufweist. Numerische Beispiele demonstrieren die erfolgreiche Umsetzung dieser numerischen Homogenisierungsmethoden. In einem weiteren Kapitel wird auf Formulierungen generalisierter Plastizität eingegangen. Die Arbeit schließt mit einer Zusammenfassung und einem Ausblick auf sich ergebende weitere Herausforderungen.

Nomenclature

Tensors Tensors of zeroth order or rather scalar quantities (such as material parameters) are denoted by italic letters. Vectors (tensors of first order) as well as tensors of second and third order are denoted by boldface italic letters. Tensors of fourth or higher order are denoted by sans-serif bold-face letters. Their representation w. r. t. a kartesian basis is presented in the following:

$$
\begin{aligned}
\boldsymbol{a} &= a_i \, \boldsymbol{e}_i \,, \\
\boldsymbol{A} &= A_{ij} \, \boldsymbol{e}_i \otimes \boldsymbol{e}_j \,, \\
\boldsymbol{C} &= C_{ijk} \, \boldsymbol{e}_i \otimes \boldsymbol{e}_j \otimes \boldsymbol{e}_k \,, \\
\mathsf{E} &= \mathsf{E}_{ijkl} \, \boldsymbol{e}_i \otimes \boldsymbol{e}_j \otimes \boldsymbol{e}_k \otimes \boldsymbol{e}_l \,.
\end{aligned}
$$

Inner tensor products Between two third-order tensors the product $\boldsymbol{A} \overset{i,j}{\vdots} \boldsymbol{B}$ symbolises the contraction over the i-th and the j-th index and thus yields a second-order tensor, while the product denoted by $\boldsymbol{A} :\cdot \boldsymbol{B}$ means the contraction over all three indices and thus results in a scalar.

$$
\begin{aligned}
\boldsymbol{A} \cdot \boldsymbol{B} &= A_{ij} B_{jk} \, \boldsymbol{e}_i \otimes \boldsymbol{e}_k \,, & \qquad \boldsymbol{A} : \boldsymbol{B} &= A_{ij} B_{ij} \,, \\
\boldsymbol{C} :\cdot \boldsymbol{D} &= C_{ijk} D_{ijk} \,, & \qquad \boldsymbol{C} \overset{1,2}{\vdots} \boldsymbol{D} &= C_{ijk} D_{ijl} \, \boldsymbol{e}_k \otimes \boldsymbol{e}_l \,, \\
\boldsymbol{C} \overset{2,3}{\vdots} \boldsymbol{D} &= C_{ijk} D_{ljk} \, \boldsymbol{e}_i \otimes \boldsymbol{e}_l \,, & \qquad \boldsymbol{C} \overset{1,3}{\vdots} \boldsymbol{D} &= C_{ijk} D_{ilk} \, \boldsymbol{e}_j \otimes \boldsymbol{e}_l \,.
\end{aligned}
$$

Dyadic tensor products The regular and the modified dyadic products of two second-order tensors are defined through the relations

$$
\begin{aligned}
\boldsymbol{A} \otimes \boldsymbol{B} &= A_{ij} B_{kl} \, \boldsymbol{e}_i \otimes \boldsymbol{e}_j \otimes \boldsymbol{e}_k \otimes \boldsymbol{e}_l \,, \\
\boldsymbol{A} \overline{\otimes} \boldsymbol{B} &= A_{ik} B_{jl} \, \boldsymbol{e}_i \otimes \boldsymbol{e}_j \otimes \boldsymbol{e}_k \otimes \boldsymbol{e}_l \,, \\
\boldsymbol{A} \underline{\otimes} \boldsymbol{B} &= A_{il} B_{jk} \, \boldsymbol{e}_i \otimes \boldsymbol{e}_j \otimes \boldsymbol{e}_k \otimes \boldsymbol{e}_l \,.
\end{aligned}
$$

Identity tensors

$\boldsymbol{I}$	identity tensor of second order
$\mathsf{I} = \boldsymbol{I} \overline{\otimes} \boldsymbol{I}$	identity tensor of fourth order
$\mathsf{I}^{\mathrm{sym}} = \frac{1}{2}[\boldsymbol{I} \overline{\otimes} \boldsymbol{I} + \boldsymbol{I} \underline{\otimes} \boldsymbol{I}]$	symmetric identity tensor of fourth order

Operators

$\mathscr{O}(\bullet^n)$	terms of order $m \geq n$
$(\cdot)^{\mathrm{t}}$	transpose
$(\cdot)^{-1}$	inverse
$\partial_{\bullet}(\cdot)$	partial derivative with respect to $\bullet$
$\nabla(\cdot)$	spatial gradient
$\nabla^{\mathrm{sym}} = \frac{1}{2}[\nabla + \nabla^{\mathrm{t}}]$	symmetric gradient operator
$\nabla^N(\cdot) = \nabla(\cdot) \cdot \boldsymbol{N}$	normal gradient operator
$\nabla^T(\cdot)$	tangential gradient operator
$\mathscr{L}(\cdot)$	a differential operator
$\nabla_{\boldsymbol{X}}(\cdot)$	gradient with respect to material placement
$\nabla_{\boldsymbol{x}}(\cdot)$	gradient with respect to spatial placement
$\mathrm{Div}(\cdot) = \nabla_{\boldsymbol{X}}(\cdot) : \boldsymbol{I}$	divergence with respect to material placement
$\mathrm{div}(\cdot) = \nabla_{\boldsymbol{x}}(\cdot) : \boldsymbol{I}$	divergence with respect to spatial placement
$\Delta(\cdot) = \mathrm{div}(\nabla(\cdot))$	Laplace operator
$\mathrm{D}_{\delta}(\cdot)$	variation at fixed material placement $\boldsymbol{X}$
$\mathrm{d}_{\delta}(\cdot)$	variation at fixed spatial placement $\boldsymbol{x}$
$[\![\cdot]\!]$	jump
$\Delta(\cdot)$	finite element
$\mathrm{d}(\cdot)$	infinitesimal element
$\delta(\cdot)$	variation

Fundamental mechanical quantities

t	time
$\mathscr{P}$	material point
$\mathscr{B}$	material body
$\mathscr{S}$	material line
$\mathscr{U}$	total-energy density
$\mathscr{W}$	stored-energy density
$\mathscr{V}$	external-energy density

v	external surface potential-energy density
$\mathbb{S}$	set of state variables
$\mathfrak{C}$	consitutive functional
$\mathscr{F}$	yield function
$\mathscr{D}$	dissipation
$\mathscr{R}$	nonlocality residual

Geometric quantities

$\boldsymbol{x}$	spatial placement of a material point $\mathscr{P}$
$\boldsymbol{X}$	material placement of a material point $\mathscr{P}$
$\boldsymbol{M}$, $\boldsymbol{N}$	tangential / outward normal vector on a material surface
$\boldsymbol{m}$, $\boldsymbol{n}$	tangential / outward normal vector on a spatial surface
S, s	material / spatial line element
V, v	material / spatial volume
A, a	material / spatial area
w, h	width / height

Kinematic quantities

$\boldsymbol{u}$	displacement
$\tilde{\boldsymbol{w}}$	fluctuation
$\boldsymbol{\varphi}$	deformation map of the spatial-motion problem
$\boldsymbol{F}$	deformation gradient of the spatial-motion problem
$\boldsymbol{H}$	displacement gradient of the spatial-motion problem
$\boldsymbol{E}$	Green-Lagrange strain
$\boldsymbol{G}$	gradient of the deformation gradient of the spatial-motion problem
$\bar{\boldsymbol{F}}$	micro-deformation map of the spatial-motion problem
$\bar{\boldsymbol{G}}$	gradient of micro-deformation map of the spatial-motion problem
J	Jacobian determinant of the spatial-motion problem
K	total curvature = twice mean curvature
$\boldsymbol{\Phi}$	deformation map of the material-motion problem
$\boldsymbol{f}$	deformation gradient of the material-motion problem
$\bar{\boldsymbol{f}}$	micro-deformation map of the material-motion problem
$\bar{\boldsymbol{g}}$	gradient of micro-deformation map of the material-motion problem
j	Jacobian determinant of the material-motion problem
$\boldsymbol{\varepsilon}$	strain

$\boldsymbol{\eta}$	strain gradient
$\bar{\boldsymbol{\varepsilon}}$	(micromorphic) micro-strain
$\bar{\boldsymbol{\eta}}$	(micromorphic) micro-strain gradient

Force and stress quantities

$\boldsymbol{b}$	spatial body force
$\boldsymbol{B}$	material body force
$\boldsymbol{P}$	(macro) stress of Piola type
$\boldsymbol{Q}$	double stress of Piola type in a gradient continuum
$\bar{\boldsymbol{P}}$	micro stress of Piola type in a micromorphic continuum
$\bar{\boldsymbol{Q}}$	double stress of Piola type in a micromorphic continuum
$\boldsymbol{t}$	spatial macro traction vector
$\bar{\boldsymbol{t}}$	spatial double traction tensor in a micromorphic continuum
$\boldsymbol{\sigma}$	(macro) stress tensor of Cauchy type
$\boldsymbol{\tau}$	double stress of Cauchy type in a gradient continuum
$\bar{\boldsymbol{\sigma}}$	micro stress of Cauchy type in a micromorphic continuum
$\bar{\boldsymbol{\tau}}$	double stress of Cauchy type in a micromorphic continuum
$\boldsymbol{p}$	macro stress of Piola type of the material-motion problem
$\bar{\boldsymbol{p}}$	micro stress of Piola type of the material-motion problem in a micromorphic continuum
$\bar{\boldsymbol{q}}$	double stress of Piola type of the material-motion problem in a micromorphic continuum
$\boldsymbol{T}$	material macro traction vector
$\bar{\boldsymbol{T}}$	material double traction tensor of the material-motion problem in a micromorphic continuum
$\boldsymbol{\Sigma}$	macro stress of Eshelby type of the material-motion problem
$\bar{\boldsymbol{\Sigma}}$	micro stress of Eshelby type of the material-motion problem in a micromorphic continuum
$\bar{\boldsymbol{\tau}}$	double stress of Eshelby type of the material-motion problem in a micromorphic continuum

Material parameters

E	Young's modulus
ν	Poisson's ration
λ	Lamé constant
$\mu = G$	Lamé constant (shear modulus)

l	internal length
p	scale-transition parameter
γ	plastic Lagrange multiplier

Sub- and superscripts

$(\cdot)^{\mathrm{sym}}$	symmetric
$(\cdot)^{\mathrm{lin}}$	linear
$(\cdot)^{\mathrm{nonlin}}$	nonlinear
$(\cdot)^{\mathrm{pre}}$	prescribed
$(\cdot)_0$	quantity w. r. t. material reference
$(\cdot)_t$	quantity w. r. t. to spatial reference
$(\cdot)^P$	quantity w. r. t. Piola-type macro stress (spatial-motion problem)
$(\cdot)^{\bar{Q}}$, $(\cdot)^Q$	quantity w. r. t. Piola-type double stress (spatial-motion problem) for the micromorphic and the gradient continuum, respectively
$(\cdot)^\sigma$	quantity w. r. t. Cauchy-type macro stress (spatial-motion problem)
$(\cdot)^{\bar{\tau}}$, $(\cdot)^\tau$	quantity w. r. t. Cauchy-type double stress (spatial-motion problem) for the micromorphic and the gradient continuum, respectively
$(\cdot)_{\mathrm{e}}$	elastic
$(\cdot)_{\mathrm{p}}$	plastic
$(\cdot)^{\mathrm{ext}}$	external
$(\cdot)^{\mathrm{int}}$	internal
$(\cdot)_{\mathrm{i}}$	independent
$(\cdot)_{\mathrm{d}}$	dependent

Numerical quantities

$(\cdot)^h$	interpolated quantity
$(\cdot)^{\mathrm{e}}$	element quantity
N	element shape functions
$(\cdot)_I$, $(\cdot)_J$	nodal indices w. r. t. element test functions
$(\cdot)_L$, $(\cdot)_M$	nodal indices w. r. t. element trial functions
n^{e}_{φ}	number of elemental nodes with degree of freedom $\boldsymbol{\varphi}$
$n^{\mathrm{e}}_{\bar{F}}$	number of elemental nodes with degree of freedom $\bar{\boldsymbol{F}}$
n_{el}	total number of elements
n_{pre}	total number of nodes with prescribed deformation

$\Delta(\cdot)$	increment
$\overset{n_{\text{el}}}{\underset{e=1}{\mathsf{A}}}$	assembly operator over all elements
R	residual vector
K	stiffness matrix
C_{di}	dependency matrix
f	nodal spatial force vector
$\bar{\mathsf{f}}$	nodal spatial double force vector
F	nodal material force vector
$\bar{\mathsf{F}}$	nodal configurational double force tensor

Multiscale nomenclature

$\widehat{(\cdot)}$	quantity at the macro level
$(\cdot)$	quantity at the level of the representative volume element
$\bar{(\cdot)}$	micromorphic micro quantities

1 Introduction

This thesis deals with the continuum mechanical description and the numerical simulation of materials that exhibit size-dependent behaviour. Special emphasis is placed on the numerical modelling of thin material layers that consist of heterogeneous or microstructured material. These tasks are achieved by the use of a micromorphic continuum and homogenization procedures to account for several scales at once.

1.1 Motivation

Size dependence. Materials, although they appear macroscopically homogeneous, usually possess a distinct microstructure when viewing them at particularly fine spatial scales. Their microconstituents, which are focused at ascending spatial scales, are for instance atoms, molecules, single crystals, polycrystals, or grains. While approaches in atomistics, molecular dynamics, or particle methods, respectively, can account for these individual constituents of the matter, the phenomenological approach pursued in continuum mechanics does not individually resolve these entities. Its blurred representation rather deals with the effective global properties, which are captured in field equations. This phenomenological modus operandi works well if the spatial scales of the continuum at the upper end, and that of the underlying microstructure at a very fine scale, differ by many orders. In common engineering practise, the continuum approach fully suffices, especially when it is combined with elaborate constitutive models accounting for a complex material behaviour. However, if a structure or a specimen under consideration is comparatively small with respect to its intrinsic microstructure, size effects become pronounced. Such size effects were for instance experimentally reported by Aifantis (1984), Fleck et al. (1994) and Stölken and Evans (1998) for metals and discussed by e. g. Bazant and co-workers (Bazant et al., 1976, Bazant, 2000) for structures, for concrete and brittle geomaterials. These size effects typically appear as a stiffer response at a smaller specimen size, i. e. when the specimen size approaches a typical length of the intrinsic microstructure. They are not reproduced with the classical (or rather local) continuum theory. Instead, so-called generalized continua can be employed, which are well-suited to account for the predicted size effects.

Heterogeneous Materials. Besides the intrinsic microstructure given by e. g. the atomistic, molecular, or polycrystal nature of the respective matter, many materials contain structural inhomogeneities. Such heterogeneities can for instance appear as cracks, small inclusions, or voids (Nemat-Nasser and Hori, 1999). They can typically be found in fibre-reinforced materials such as metal–polymer matrix, concrete, or in natural materials, e. g. in geological conglomerates. Further examples are metal alloy systems, polymer blends, porous and cracked media, polycrystalline materials. Besides the material properties of the surrounding matrix material, the particular properties of these heterogeneities rule the aggregate properties of the material. Thereby, the properties of the underlying material itself, as well as the size, the shape, and the spatial distribution influence the global response (Kouznetsova et al., 2001). When the heterogeneities are distributed in a regular manner, rather than modelling each constituent individually, smeared models can account for the overall aggregate properties.

Material layers. Adhesive layers that connect two bulk materials, while they transmit cohesive tractions, are found in many engineering materials applications. Solder connections, adhesive bonding layers, laminated composite structures, building materials such as masonry, as well as geomaterials, are only some notable examples, two of which are illustrated in Figure 1.1. In most cases, the material in the connecting layer is significantly weaker than that of the surrounding bulk material and thus the deformation will be strongly localized to this layer. A modelling of such layers can be achieved by considering them as discontinuities within a continuous medium. To this end, they are represented by a cohesive interface that is governed by its opening and incorporates a cohesive traction, which is transmitted across. The constitutive behaviour is traditionally handled with a so-called cohesive or rather traction–separation law. However, this phenomenological approach to the constitutive behaviour in the material layers, reaches its limit of applicability when the material layer possesses an intrinsic microstructure or heterogeneities.

If such a material layer possesses a heterogeneous microstructure, this heterogeneity will strongly effect the global response. Rather than using a priori constitutive assumptions within the layer, it is desirable to model this influence of the heterogeneous microstructure on the macro response.

For remarkably thin material layers with an underlying material microstructure that is not of orders smaller than the layer's thickness, the above-mentioned size effects will arise. As an examples for such layers we may mention mortar layers in masonry or thin polymeric glues. Thus, a methodology that determines the global response based on the micro properties, shall furthermore reproduce these size effects.


Figure 1.1: Example for a material interfaces within a bulk material of different properties: Rock with material layer of different properties; circular polyurethane tensile-test specimen, semi-cured (courtesy of Gunnar Possart).

1.2 Approaches to the modelling of size effects, heterogeneities, material layers

For the problems motivated in the preceding section, methods within the field of applied and computational mechanics have been developed. Particular a brief overview of existing methods to handle size effects, of heterogeneous media and to treat material layers is given in the following.

Generalized continua to account for size effects. Within the framework of continuum mechanics, so-called generalized continuum theories represent more sophisticated continuum theories which are particularly suited to account for the above-mentioned size effects. Their additional sophistication lies either in the consideration of higher gradients of the displacement or of additional kinematic degrees of freedom. The development of these generalized continua bases on the pioneering couple-stress theory of the brothers Cosserat and Cosserat (1909), who considered additional rotational degrees of freedom at each continuum point. In the 1960s, this idea was taken up and further refined by Mindlin and Tiersten (1962), Mindlin (1963, 1964, 1965), Mindlin and Eshel (1968), Koiter (1964), Toupin (1962, 1964) as well as Eringen (1964, 1968). Two important resulting theories, i. e. the gradient continuum and the micromorphic continuum, are closely illuminated in Chapter 2. They incorporate a size effect by the introduction of a so-called internal length as a constitutive parameter.

Generalized continua and derived methodologies have been especially appreciated in connection with irreversible material behaviour. Notable examples are the formulations gathered under the synonym *gradient plasticity* (Fleck and Hutchinson, 1993, Polizzotto and Borino, 1998, Menzel and Steinmann, 2000, Liebe and

Steinmann, 2001) and those belonging to *micromorphic plasticity* (Steinmann and Willam, 1991, Borst, 1991, Grammenoudis and Tsakmakis, 2001). Besides the advantage that these formulations capture size effects in an irreversible range of deformation, they play a decisive role in the regularization of localized strain in softening materials. The internal length mentioned above is either taken into account within the constitutive assumption for the elastic free energy, or within the flow rule.

Multiscale modelling by means of homogenization. For the continuum-mechanical and the numerical modelling of heterogeneous materials, various concepts have been developed that regard multiple scales. While the theoretical concept of homogenization primarily builds on the pioneering contributions of Hill (1963, 1972), numerous researchers have been concerned with the numerical multiscale modelling of heterogeneous materials within the last decade.

All homogenization techniques have in common a procedure for determining the macroscopic overall characteristics of a heterogeneous material. Thereby to relate the global or rather aggregate properties to the micro-properties at a well-chosen portion of the macroscopic body, they must provide an appropriate averaging method (Hill, 1963, 1972, Nemat-Nasser and Hori, 1999). Several approaches involving a multiscale consideration have been pursued, for instance the rule of mixture, the theory of porous media, the self-consistent or effective-medium approximation, the asymptotic homogenization theory, unit cell methods (see Kouznetsova (2002) and references cited therein). While these various approaches remain untouched in the present work, we focus on direct micro–macro methods. Herein the relevant stress–strain relationships at a macroscopic point are estimated by performing separate calculations on a representative volume element (RVE). In order to obtain the constitutive properties of the continuum in terms of the properties and the structure of the microconstituents, the underlying representative volume element accounting for the heterogeneous medium is subject to prescribed boundary data which corresponds to the uniform local continuum fields (Nemat-Nasser and Hori, 1999). Numerical implementations of these direct multiscale approaches within the finite-element method were for instance performed in the contributions of Miehe et al. (1999a,b, 2002a,b,c), Miehe and Koch (2002), Feyel and Chaboche (2000), as well as of Smit et al. (1998), Kouznetsova et al. (2001, 2002, 2004). Thereby the computational multiscale framework, also referred to as FE^2 by Feyel and Chaboche (2000), consists of two levels, a macro and a micro level. On the macro scale a discretized boundary value problem is stated without any constitutive routine. At the integration points of the finite elements at this level, the constitutive macro response is evaluated within an underlying RVE. This RVE contains a microstructure, which itself is discretized and provides a constitutive framework. The micro boundary value problem is solved on the RVE subject to boundary conditions uniformly imposed from the macro level. The macro stress and a material tangent

operator are passed to the macro level.

Treatment of material layers. Mechanically a material layer can be treated as a cohesive interface within a continuum. The deformation jump, i. e. the separation between opposite edges of the interface, and the traction within such interface are described vectorially and separately from the surrounding continuum. For the constitutive relation within this interface, cohesive laws have been proposed that relate the transmitted traction and the deformation jump across the interface. Most of them concern failure, as e. g. the contributions of Needleman (1987, 1990a,b), Tvergaard and Hutchinson (1992), Xu and Needleman (1993), Ortiz and Pandolfi (1999), Nguyen et al. (2001). Most approaches assume that the tangential and normal responses of the interface are uncoupled, and therefore might not properly account for mixed-mode loading conditions. Remedies for the constitutive treatment of this more general case were e. g. proposed by van den Bosch et al. (2006). Computationally, the cohesive layer can be straightforwardly modelled as a cohesive interface element (Beer, 1985, Schellekens and de Borst, 1993a,b). Such interface elements also find their application in the context of localized plastic yielding (Larsson et al., 1993, Miehe and Schröder, 1994, Steinmann and Betsch, 2000).

Only very few approaches exist in the literature which model material layers under consideration of their distinct microstructure or their size dependence, respectively. Two contributions are know to the author which involve a homogenisation of a adhesive material layer or rather interface. The recent multiscale approach of Matous et al. (2008) treats them as interfaces and extracts the traction–separation law from a homogenisation. Thereby it is restricted to small strain and does not involve the solution of a macro boundary value problem. The contribution of Larsson and Zhang (2007) considers an interface within a a micro system exhibiting size dependence by a homogenisation with a micropolar framework at the macro level and an underlying microstructure treated as a standard continuum. This higher-order approach is also pursued within a small-strain framework and lacks the solution of global boundary value problems involving both the interface and the surrounding bulk.

1.3 Goals of the work

In Section 1.1 the phenomena of size effects, heterogeneous material and material layers were introduced. The state of the art to treat these difficulties was pointed out in Section 1.2. In this context, certain challenges evolve that shall be addressed in this thesis.

Multiscale modelling of material layers. It is evident that a numerical multiscale framework for the multiscale modelling of material layers with heterogeneous microstructure is needed. An appropriate numerical framework involving the finite-element method, shall especially reveal size effects. This motivates us to incorporate a generalized continuum at an underlying finer scale. Due to some of its convenient characteristics when it comes to the numerical implementation, a micromorphic continuum is addressed to this end.

Numerical framework for a micromorphic continuum at finite deformations. The aim to achieve such a computational homogenization involving a micromorphic continuum calls for a befitting computational framework for the latter. Based on the theoretical developments by Eringen, which are synopsised in his monograph (Eringen, 1999), and others, e. g. Kirchner and Steinmann (2005), a numerical framework is addressed. To this end a constitutive framework shall be established allowing for finite deformations.

Configurational mechanics of generalized continua. Benefiting from a comprehensive examination of both the continuum and the computational framework of the micromorphic continuum, the application of the *configurational-mechanics* perspective and in particular the *material-force method* is aspired. Heretofore, only a few approaches exist that enlighten generalized continua from a configurational-mechanics perspective, as for instance Kirchner and Steinmann (2005). However, despite this elaborate theoretical framework for gradient elasticity in this contribution, a corresponding numerical framework is still lacking. To this end, the material-force method shall be reformulated for the micromorphic continuum.

Concepts of generalized plasticity. With the insight given into generalized continuum theories in general and the micromorphic continuum in particular, it is desirable to further move focus onto plastic constitutive frameworks for generalized continua. The existing formulations of both gradient and micromorphic plasticity shall be analysed and classified. Resulting from this overview on the respective features, new formulations shall be found which anticipate further advances in the modelling of reversible size-dependent deformation processes.

1.4 Outline

This thesis is organised as follows:

Chapter 2 *(Generalized continuum theories).* A brief introduction into generalized continuum theories is given. Based upon the key characteristics with respect

to their kinematic assumptions, the classical continuum, the second-order gradient continuum, and the micromorphic continuum is illuminated more closely. Besides the essential continuum-mechanical frameworks at finite strain, the corresponding geometrically linear framework of each of these three theories is briefly recalled.

Chapter 3 *(Micromorphic hyperelasticity)*. A micromorphic continuum formulation is presented in the context of both the spatial- and the material-motion problem. For both approaches, the kinematics as well as the balance relations together with the various representations of the occurring stress fields are derived. The relations between the spatial-motion problem and the material-motion problem quantities are examined in detail. Upon a hyperelastic constitutive assumption a finite-element approximation is derived and the material-force method, which is especially suited for defect-mechanics problems, is successfully applied to the present micromorphic continuum theory.

Chapter 4 *(Computational homogenization of a continua)*. The theoretical and the computational homogenization framework is discussed for a heterogeneous continuum described by a classical continuum at the macro level. Thereby two cases of underlying microstructures are considered: In the first case, a classical continuum occupies the representative volume element. Especially in view of the following chapters, the more sophisticated case of a micromorphic mesostructure modelled at the level of this representative volume element is treated.

Chapter 5 *(Computational homogenization of heterogeneous material layers)*. A computational homogenization procedure for a material layer that possesses an underlying heterogeneous microstructure is introduced. This layer is resolved as a cohesive interface element and the underlying microstructure is treated as a continuum. A multiscale analysis involving a homogenization is performed to obtain the macroscopic material properties in the material layer based upon the microstructural properties. An admissible scale transition is guaranteed via customised boundary conditions, which account for the deformation modes in the interface and consider the height of the material layer. On the basis of this theoretical framework, a computational homogenization is achieved within a finite-element framework. The capabilities of the model are demonstrated through numerical examples.

Chapter 6 *(Computational homogenization of material layers with microstructured mesostructure)*. A multiscale approach to capture the behaviour of material layers that possess a micromorphic mesostructure is presented. To this end, we seek to obtain a macroscopic traction–separation law based on the underlying meso- and microstructure. At the macro level, a cohesive interface description is used, whereas the underlying mesostructure is resolved by a micromorphic representative volume

element. This generalized continuum theory is particularly well-suited to account for size effects in the material layer. In consideration of the height of the material layer, quantities at different scales are related by averaging theorems and the Hill condition. Boundary conditions accounting for the geometry and the deformation modes of the material layer are applied on the RVE. With this framework at hand, the macroscopic response is obtained computationally within a multiscale finite element framework along the lines of Chapter 5. Numerical examples reveal the size effects, which here occur due to the intrinsic microstructure in the material of the layer.

Chapter 7 *(Concepts of generalized plasticity)*. A classification of various formulations coined as generalized plasticity is introduced. Thereby variants of both gradient and micromorphic plasticity are presented, which prove thermodynamically consistent by fulfilling the second law of thermodynamics. In a structured manner, key characteristic features of the formulation are varied and their influence on the complexity and, in particular, on the benefit of the individual formulations are compared.

Chapter 8 *(Conclusion)*. The thesis closes with a brief summary on the aspects covered in the preceding chapters. The major achievements of this work are pointed out, before an outlook on challenges for future research which evolve from this work is given.

2 Generalized Continuum Theories

While classical continua fail to model the pointed-out size effects, generalized continuum theories prove especially beneficial in this context, because they involve a so-called internal length to account for a size effect. The notion of generalized continua unifies several classes of continuum theories that enjoy more advanced attributes than the classical continuum. They can be traced back to the monograph of the brothers Cosserat and Cosserat (1909), who in their couple-stress theory considered independent rotational degrees of freedom at each continuum point.

Within the various developments of generalized continua, which have been carried on since the centre of the 20th Century starting with the contributions of Mindlin and Tiersten (1962), Mindlin (1963, 1964, 1965), Mindlin and Eshel (1968), Koiter (1964), Toupin (1962, 1964), Eringen (1964, 1968), three major categories can be identified:

- continua of higher grade or simply gradient continua,
- continua of higher order or rather micromorphic continuum theories,
- nonlocal continua,

These theories substantially differ by the approach to the deformation of a material point and its vicinity within the continuum.

Outline. Particularly the gradient continuum and the micromorphic theories are illuminated more closely in the following. Thereby first, in Section 2.1, essential kinematic features are addressed, whereas the continuum frameworks of the classical, the gradient and the micromorphic continuum are concisely explained in the sequel, Sections 2.2–2.4. The highlighted generalized continua become more sophisticated than classical continua when it comes to their numerical implementations within a finite-element solution scheme.

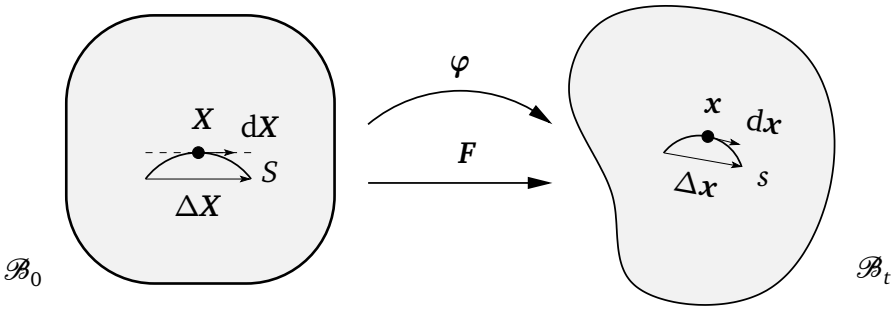

Figure 2.1: Nonlinear deformation map

2.1 Fundamental kinematic characteristics of the different continuum theories.

In the deformation of a body $\mathscr{B}$, the deformation of a material point $\mathscr{P}$ is described via the mapping $\boldsymbol{x} = \boldsymbol{\varphi}(\boldsymbol{X}, t)$ from the material configuration $\mathscr{B}_0$ to the spatial configuration $\mathscr{B}_t$. The particular characteristics of the generalized continuum theories can be explained with the aid of the deformation of a material line $\mathscr{S}$, over time $\tau \in \{0, t\}$, as depicted in Figure 2.1. A material tangent at the material finite line element S around the material point $\mathscr{P}$ with material placement $\boldsymbol{X}$ is denoted by $\Delta\boldsymbol{X}$ in $\mathscr{B}_0$. In the vicinity of $\mathscr{P}$, the mapping of this finite tangent element can be developed in a Taylor series expansion as follows:

$$\Delta\boldsymbol{x} = \nabla_X\boldsymbol{\varphi} \cdot \Delta\boldsymbol{X} + \tfrac{1}{2}\nabla_X(\nabla_X\boldsymbol{\varphi}) : [\Delta\boldsymbol{X} \otimes \Delta\boldsymbol{X}] + \mathscr{O}(\Delta\boldsymbol{X}^3) \tag{2.1}$$

Therein $\nabla_X\boldsymbol{\varphi}$ is a (linear) tangent map, its gradient $\nabla_X(\nabla_X\boldsymbol{\varphi})$ represents the quadratic term, while terms of cubic and even higher grade are abridged in $\mathscr{O}(\Delta\boldsymbol{X}^3)$.

2.1.1 Classical continuum

In the classical continuum, also coined as the Boltzmann continuum, only the linear term within the deformation map (2.1) is taken into account. Thus the remaining deformation map concerns only infinitesimal line elements or rather the tangent vector $\mathrm{d}\boldsymbol{X}$ on $\mathscr{S}$ at the placement $\boldsymbol{X}$:

$$\mathrm{d}\boldsymbol{x} = \nabla_X\boldsymbol{\varphi} \cdot \mathrm{d}\boldsymbol{X} \tag{2.2}$$

The vicinity of $\mathscr{P}$ stays unconsidered, thus this basic continuum theory is also called a *local* continuum theory. Its continuum mechanics is well treated in the canonical literature and courses on continuum mechanics, e. g. Malvern (1969), Chadwick (1976), Marsden and Hughes (1983), Ogden (1997), Holzapfel (2000).

2.1.2 Gradient continua

When beside the linear, also the quadratic term or even higher terms in the non-linear deformation mapping (2.1) are taken into account, a gradient continuum is obtained. In the case that terms of third order and higher are neglected, it amounts to a second-order gradient theory as a special case of the *second gradient of strain* model introduced by Mindlin (1965). With the second gradient $\nabla_X(\nabla_X \varphi)$, which can be related to the curvature in the material line, a size effect enters this theory. Gradient continua cover the classical continuum as a special case, being a continuum of grade one in the nomenclature of e. g. Forest and Sievert (2003, 2006).

2.1.3 Micromorphic continuum

Rather than considering higher gradients of deformation than in the classical theory, the micromorphic theory is characterized by additional degrees of freedom per continuum point. For a point $\mathscr{P}$ in the (macro-) continuum $\mathscr{B}$, a linear deformation map as in (2.2) is assumed. To each point $\mathscr{P}$ a microcontinuum is considered to be attached, the deformation map of which represents the extra degrees of freedom. This microcontinuum $\bar{\mathscr{B}}$, illustrated in Figure 2.6, undergoes an affine deformation, which is kinematically independent from that of the continuum point $\mathscr{P}$. Through the macro gradient on the microdeformation map and size of these microcontinua entering as a material parameter, the micromorphic theory captures size-effects and thus particularly well accounts for materials possessing a significant intrinsic microstructure. The micro-deformation map $\bar{\boldsymbol{F}}(\boldsymbol{X}, t)$ is introduced such that it affinely maps placements $\bar{\boldsymbol{X}}$ within the microcontinuum:

$$\bar{\boldsymbol{x}} = \bar{\boldsymbol{F}} \cdot \bar{\boldsymbol{X}}\,, \tag{2.3}$$

As illustrated in Figure 2.6. Its gradient with respect to macro placement is defined as

$$\bar{\boldsymbol{G}} := \nabla_X \bar{\boldsymbol{F}}\,, \tag{2.4}$$

Since in this most general case, the micro-deformation map comprises both stretch and rotation, $\bar{\boldsymbol{F}} = \bar{\boldsymbol{R}} \cdot \bar{\boldsymbol{U}}$, the micromorphic continuum formulation is appropriate for the modelling of the following materials that possess a distinct deformable microstructure: ”polymers with flexible molecules, liquid crystals with side chains, animal blood with deformable cells, suspensions with deformable elements, turbulent fluids with flexible vortices” (Eringen, 1999). The micro deformation at a point $\mathscr{P}$ can be illustrated with the deformable director triad shown in Figure 2.2.

The micromorphic continuum envelopes several sub-theories, which are characterized by particular constraints that apply to the deformation of the microcontinuum. The most prominent of these are the micropolar, the microstretch, and the

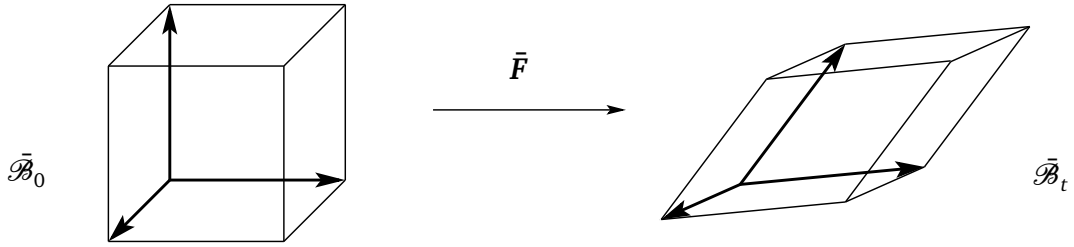

Figure 2.2: Micromorphic micro deformation: deformable director triad

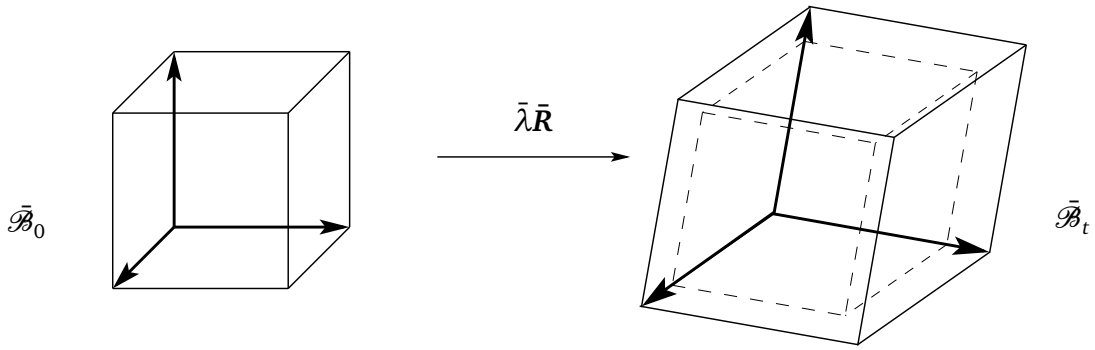

Figure 2.3: Microstretch micro deformation: extensible director triad

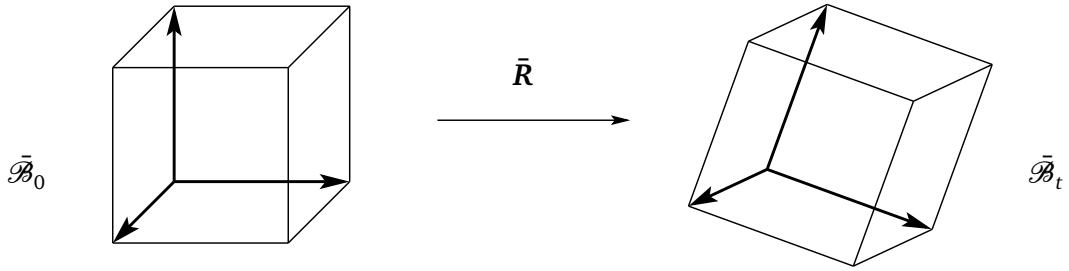

Figure 2.4: Micropolar micro deformation: rigid director triad

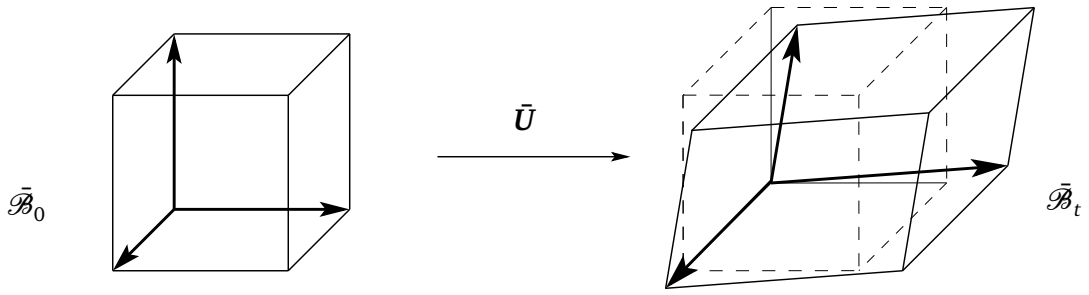

Figure 2.5: Microstrain micro deformation: stretchable director triad excluding rotation

microstrain continuum. The micromorphic theory as well as its sub-theories are grouped under the synonym "microcontinuum theories", which goes back to Eringen (1964, 1968). In his comprehensive monograph (Eringen, 1999) a classification and the corresponding continuum frameworks are well elaborated.

Micropolar continuum. For instance in the case of the micropolar continuum (often simply referred to as Cosserat continuum), this microcontinuum may only experience rotation,

$$\bar{\boldsymbol{x}} = \bar{\boldsymbol{R}} \cdot \bar{\boldsymbol{X}} \,,$$

as illustrated with the rigid director triad in Figure 2.3. Thus this theory accounts well for rigid microstructures, such as "liquid crystals with rigid molecules, rigid suspensions, chopped fibre composites, bones, magnetic fluids, clouds with dusts, concrete with sand, muddy fluids" (Eringen, 1999). To obtain a deeper insight into the micropolar continuum, the reader is referred to the contributions of Eringen (1966, 1967, 1976), Borst (1991), Steinmann (1994), Steinmann and Stein (1997), Ehlers and Volk (1998), Diebels and Steeb (2003), Steeb and Diebels (2004), Sansour and Skatulla (2007), as well as those from the group of Tsakmakis (Grammenoudis and Tsakmakis, 2001, 2005a,b, Grammenoudis, 2003, Diegele et al., 2004), just to mention a few.

Microstretch continuum. In the microstretch continuum (Eringen, 1999, Kirchner and Steinmann, 2007b), besides a rotation $\bar{\boldsymbol{R}}$, also one scalar stretch variable is considered to account for isotropic extension of the microcontinuum:

$$\bar{\boldsymbol{x}} = \bar{\lambda}\, \bar{\boldsymbol{R}} \cdot \bar{\boldsymbol{X}} \,.$$

Additionally to the micropolar director triad with fixed angles, the microstretch director triad at material point $\mathscr{P}$ is isotropically deformable or rather extensible as depicted in Figure 2.4.

Microstrain continuum. Another variant of the micromorphic theory called microstrain continuum was proposed by Forest and Sievert (2006). Therein the rotation of the microcontinuum is neglected, rather only the stretch tensor $\bar{\boldsymbol{U}}$ in the microcontinuum is considered:

$$\bar{\boldsymbol{x}} = \bar{\boldsymbol{U}} \cdot \bar{\boldsymbol{X}} \,.$$

The deformation of a microcontinuum in the microstrain theory is illustrated in Figure 2.5. The director triad allows for pure stretch, which is characterized by the fact

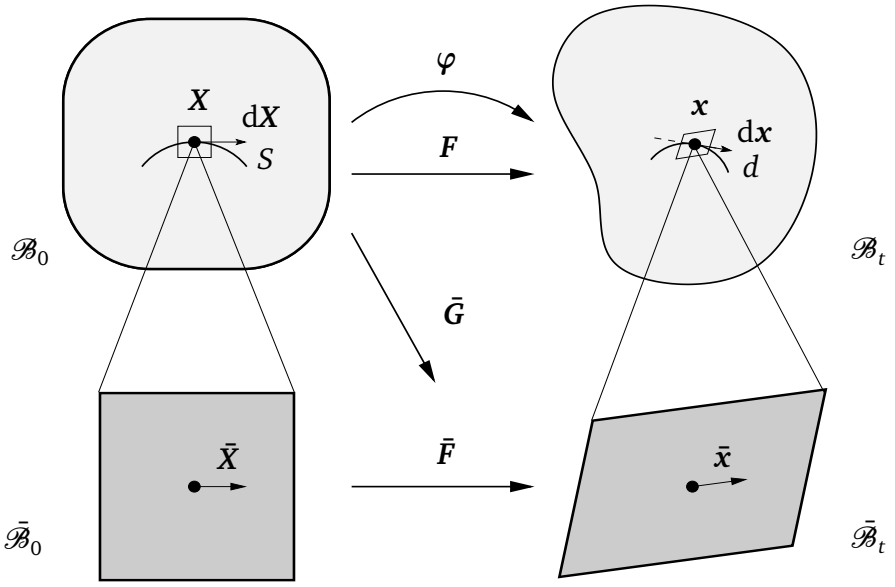

Figure 2.6: Micromorphic deformation maps

that the principle directions maintain their direction. The microstrain continuum is predicted to be useful for metallic foams (Forest and Sievert, 2006).

2.2 A review on the classical continuum

As a basis for the generalized theories and for later considerations within this work, the continuum framework of the classical continuum is reviewed here. First, the theory is discussed with respect to finite deformations, before a geometrical linearization towards infinitesimal deformations or rather small strain is performed.

2.2.1 Geometrically nonlinear classical continuum framework

As indicated in Section 2.1.1, the classical continuum bases on the linear deformation map (2.2). For conservative static problems, the principle of stationary potential energy yields the balance of momentum and the corresponding boundary conditions.

Kinematics. The deformation map φ describes the deformation of a material point over time, while its tangent is denoted as the deformation gradient $\boldsymbol{F}$:

$$\boldsymbol{x} = \varphi(\boldsymbol{X}, t) \qquad \boldsymbol{F}(\boldsymbol{X}, t) := \nabla_{\boldsymbol{X}} \varphi(\boldsymbol{X}, t) \tag{2.5}$$

Since it is obvious that the kinematic quantities represent field quantities, the dependence on the material placement $\boldsymbol{X}$ and on the time t will be presumed but not

be explicitly mentioned in the following.

Dirichlet principle and balance of momentum. The balance of momentum is derived based on the total (bulk) potential energy density $\mathscr{U}_0$, which consists of an internal and an external contribution, and the surface potential-energy density v_0 (Steinmann, 2007)

$$\mathscr{U}_0(\boldsymbol{\varphi}, \boldsymbol{F}) = \mathscr{W}_0(\boldsymbol{F}) + \mathscr{V}_0(\boldsymbol{\varphi}) \quad \text{in } \mathscr{B}_0\,, \qquad\qquad v_0(\boldsymbol{\varphi}; \boldsymbol{N}) \quad \text{on } \partial\mathscr{B}_0\,. \tag{2.6}$$

The internal contribution $\mathscr{W}_0$ is referred to as the stored-energy density, while $\mathscr{V}_0$ is the density of the external energy. $\boldsymbol{N}$ denotes the outward normal vector on the boundary $\partial\mathscr{B}_0$. For the system to be in static equilibrium, the principle of stationary potential energy, known as the Dirichlet principle, is stated as

$$\mathrm{D}_\delta \left[\int_{\mathscr{B}_0} \mathscr{U}_0(\boldsymbol{\varphi}, \boldsymbol{F})\, \mathrm{d}V - \int_{\partial\mathscr{B}_0} v_0(\boldsymbol{\varphi}, \boldsymbol{N})\, \mathrm{d}A \right] \doteq 0\,. \tag{2.7}$$

From this, the static balance of momentum, also referred to as the Euler–Lagrange equation, is derived in its local form as

$$\mathrm{Div}\, \boldsymbol{P} = -\boldsymbol{b}_0 \qquad \text{in } \mathscr{B}_0\,. \tag{2.8}$$

For the prevailing static case, this represents a localized force equilibrium. Herein $\boldsymbol{P}$ denotes the Piola stress and $\boldsymbol{b}_0$ the spatial body force acting on a material volume element $\mathrm{d}V$. The surface energy density $v_0(\boldsymbol{\varphi}) = \boldsymbol{\varphi} \cdot \boldsymbol{t}_0^{\,\mathrm{pre}}$ yields the Neumann boundary condition

$$\boldsymbol{P} \cdot \boldsymbol{N} =: \boldsymbol{t}_0^{\,\mathrm{pre}} \qquad \text{on } \partial\mathscr{B}_0^{P}\,, \tag{2.9}$$

with $\boldsymbol{t}_0^{\,\mathrm{pre}}$ defined as the spatial traction vector with respect material reference on the surface, and the Dirichlet boundary condition for the deformation:

$$\boldsymbol{\varphi} =: \boldsymbol{\varphi}^{\mathrm{pre}} \quad \text{on } \partial\mathscr{B}_0^{\varphi}\,. \tag{2.10}$$

The respective boundary regions are disjoint, i. e. $\partial\mathscr{B}_0^{P} \cap \partial\mathscr{B}_0^{\varphi} = \emptyset$.

Hyperelasticity. In a hyperelastic format, the potential-energy density constitutes a potential for the stress and the body force. In this case, the Piola stress and the body force are defined by their energetically conjugate kinematic pairings:

$$\boldsymbol{P} := \mathrm{D}_{\boldsymbol{F}} \mathscr{W}_0 \qquad\qquad \boldsymbol{b}_0 := -\partial_{\boldsymbol{\varphi}} \mathscr{V}_0\,. \tag{2.11}$$

2.2.2 Geometrically linear classical continuum framework

In many cases, the complication of finite deformation is not needed, because only states of infinitesimal deformation are considered. Then a linearization of the strain measures, based on the assumption $\boldsymbol{x} \approx \boldsymbol{X}$, yields a small strain theory. In the linearized theory, the material and the spatial configuration will not be distinguished, thus all quantities are referred to the body $\mathscr{B}$. And rather than the deformation map $\boldsymbol{\varphi}$, the displacement $\boldsymbol{u} := \boldsymbol{x} - \boldsymbol{X}$ is considered as a primary variable.

Linearization of the kinematics. This linearization can be illustrated on the basis of the material Green-Lagrange strain tensor $\boldsymbol{E}$. This symmetric strain tensor is defined as

$$\boldsymbol{E} := \tfrac{1}{2}\left[\boldsymbol{F}^{\mathrm{t}} \cdot \boldsymbol{F} - \boldsymbol{I}\right]. \tag{2.12}$$

With the displacement gradient, $\boldsymbol{H} := \nabla_{\boldsymbol{X}} \boldsymbol{u}$, which is related to the deformation gradient as $\boldsymbol{H} = \boldsymbol{F} - \boldsymbol{I}$, the Green-Lagrange strain tensor can be alternatively expressed as

$$\boldsymbol{E} = \tfrac{1}{2}\left[\boldsymbol{H} + \boldsymbol{H}^{\mathrm{t}} + \boldsymbol{H}^{\mathrm{t}} \cdot \boldsymbol{H}\right]. \tag{2.13}$$

For small deformations, the quadratic term $\frac{1}{2}\boldsymbol{H}^{\mathrm{t}} \cdot \boldsymbol{H} =: \boldsymbol{E}^{\mathrm{nonlin}}$ can be neglected. Thus we remain with the linearized strain tensor

$$\boldsymbol{E}^{\mathrm{lin}} := \tfrac{1}{2}\left[\boldsymbol{H} + \boldsymbol{H}^{\mathrm{t}}\right] = \tfrac{1}{2}\left[\nabla_{\boldsymbol{X}} \boldsymbol{u} + (\nabla_{\boldsymbol{X}} \boldsymbol{u})^{\mathrm{t}}\right]. \tag{2.14}$$

This linearized strain $\boldsymbol{E}^{\mathrm{lin}} =: \boldsymbol{\varepsilon}$ is used in a small-strain formulation,

$$\boldsymbol{\varepsilon}(\boldsymbol{u}; \boldsymbol{x}) := \nabla^{\mathrm{sym}} \boldsymbol{u}(\boldsymbol{x}). \tag{2.15}$$

It is a symmetric tensor of second order, $\varepsilon_{ij} = \varepsilon_{(ij)}$. According to the fundamental assumption of the linearized theory, i. e. $\boldsymbol{x} \approx \boldsymbol{X}$, no distinction needs to be made between the spatial and the material gradient, consequently $\nabla_{\boldsymbol{X}} \approx \nabla_{\boldsymbol{x}} =: \nabla$. With this simplification at hand, the symmetric gradient operator used in (2.15) reads $\nabla^{\mathrm{sym}} := \frac{1}{2}\left[\nabla + \nabla^{\mathrm{t}}\right]$.

Balance relations. In the small-strain case, the stored-energy density $\mathscr{W}$ is a function of the strain $\boldsymbol{\varepsilon}$, which itself is a function of the displacement $\boldsymbol{u}$:

$$\mathscr{W} = \check{\mathscr{W}}(\boldsymbol{\varepsilon}(\boldsymbol{u})) = \tilde{\mathscr{W}}(\boldsymbol{u}). \tag{2.16}$$

Table 2.1: Sample constitutive assumption for elastic continua at small strain

classical elasticity	$\mathscr{W} = \frac{1}{2}\,\boldsymbol{\varepsilon} : \mathsf{E} : \boldsymbol{\varepsilon}$
gradient elasticity	$\mathscr{W} = \frac{1}{2}\,\boldsymbol{\varepsilon} : \mathsf{E} : \boldsymbol{\varepsilon} + \frac{1}{2}\,\mu l^2 \boldsymbol{\eta} \cdot\!\cdot\, \boldsymbol{\eta}$
micromorphic elasticity	$\mathscr{W} = \frac{1}{2}\,\boldsymbol{\varepsilon} : \mathsf{E} : \boldsymbol{\varepsilon} + \frac{1}{2}\,\mu l^2 \bar{\boldsymbol{\eta}} \cdot\!\cdot\, \bar{\boldsymbol{\eta}} + \frac{1}{2}\,p\|\boldsymbol{\varepsilon} - \bar{\boldsymbol{\varepsilon}}\|^2$

The local balance of momentum reads

$$\operatorname{div} \boldsymbol{\sigma} = -\boldsymbol{b} \qquad \text{in } \mathscr{B}\,, \tag{2.17}$$

in terms of the stress $\boldsymbol{\sigma}$ and the body force $\boldsymbol{b}$. It is supplemented by the Neumann and the Dirichlet boundary condition,

$$\boldsymbol{\sigma} \cdot \boldsymbol{n} =: \boldsymbol{t}^{\text{pre}} \quad \text{on } \partial\mathscr{B}^{\sigma}\,, \qquad\qquad \boldsymbol{u} =: \boldsymbol{u}^{\text{pre}} \quad \text{on } \partial\mathscr{B}^{u}\,, \tag{2.18}$$

respectively. These boundary conditions are defined on disjoint boundary parts: $\partial\mathscr{B}^{\sigma} \cap \partial\mathscr{B}^{u} = \emptyset$.

Hyperelasticity. For an elastic material, the stress response is characterized by zero dissipation,

$$\mathscr{D} = \boldsymbol{\sigma} : \dot{\boldsymbol{\varepsilon}} - \dot{\mathscr{W}} = [\boldsymbol{\sigma} - \partial_{\boldsymbol{\varepsilon}}\mathscr{W}] : \dot{\boldsymbol{\varepsilon}} = 0\,. \tag{2.19}$$

Due to the assumption of hyperelasticity, the stored-energy density $\mathscr{W}$ serves as a potential for the stress,

$$\boldsymbol{\sigma} := \partial_{\boldsymbol{\varepsilon}}\mathscr{W}\,, \tag{2.20}$$

which is introduced as the energetically conjugate quantity to the strain. The symmetry of the stress, $\sigma_{ij} = \sigma_{(ij)}$, results from the balance of momentum and the balance of angular momentum. Note that the balance of momentum (2.17) and the boundary condition (2.18) always hold, independently of the constitutive law. A sample constitutive assumption is mentioned in Table 2.1.

2.3 Second-gradient continuum

Based upon its kinematic concept introduced in Section 2.1.2 the gradient continuum of second order is illuminated here. While its small strain framework was elaborated by Mindlin (1965), for references on finite strain, we refer the reader e. g. to the more recent contributions of Forest and Cardona (2000), Kouznetsova et al. (2002, 2004), Kouznetsova (2002), Sunyk and Steinmann (2003), Kirchner

and Steinmann (2005, 2007a). Further aspects of gradient continua were also discussed by Maugin (2007) and Forest (2007).

2.3.1 Geometrically nonlinear gradient continuum framework

The geometrically nonlinear framework of the second-gradient continuum can for instance be found in the article of Kirchner and Steinmann (2005). The higher gradient in the kinematics entails a sophisticated set of the balance of momentum and its corresponding boundary conditions.

Kinematics. As afore-mentioned, the kinematics of the second-gradient continuum incorporates both the linear and the quadratic term in the mapping (2.1). The tangent map and its gradient are in the sequel denoted as $\boldsymbol{F}$ and $\boldsymbol{G}$, respectively:

$$\boldsymbol{x} = \varphi(\boldsymbol{X}; t), \qquad \boldsymbol{F} := \nabla_{\boldsymbol{X}} \varphi\,, \qquad \boldsymbol{G} := \nabla_{\boldsymbol{X}}(\nabla_{\boldsymbol{X}} \varphi)\,. \tag{2.21}$$

The gradient $\boldsymbol{G}$ is a tensor of third order, which possesses a symmetry in the last two indices, $G_{i(JK)}$.

Dirichlet principle and balance of momentum. The potential energy density depends on the kinematic measures (2.21) as follows:

$$\mathscr{U}_0(\varphi, \boldsymbol{F}, \boldsymbol{G}) = \mathscr{W}_0(\boldsymbol{F}, \boldsymbol{G}) + \mathscr{V}_0(\varphi), \qquad v_0(\varphi, \nabla^N_{\boldsymbol{X}} \varphi; \boldsymbol{N}) \quad \text{on } \partial \mathscr{B}_0\,. \tag{2.22}$$

The Dirichlet principle, or rather principle of stationary potential energy

$$\mathrm{D}_\delta \left[\int\limits_{\mathscr{B}_0} \mathscr{U}_0(\varphi, \boldsymbol{F}, \boldsymbol{G})\,\mathrm{d}V - \int\limits_{\partial \mathscr{B}_0} v_0(\varphi, \nabla^N_{\boldsymbol{X}} \varphi; \boldsymbol{N})\,\mathrm{d}A \right] \doteq 0 \tag{2.23}$$

is used to derive the balance of momentum. In its local form this balance of momentum reads:

$$\mathrm{Div}\,(\boldsymbol{P} - \mathrm{Div}\,\boldsymbol{Q}) = -\boldsymbol{b}_0 \qquad \text{in } \mathscr{B}_0\,, \tag{2.24}$$

wherein the Piola-type stresses comprise the stress $\boldsymbol{P}$ and the double stress $\boldsymbol{Q}$, the latter quantity being a tensor of third order. The corresponding Neumann boundary conditions,

$$[\boldsymbol{P} - \mathrm{Div}\,\boldsymbol{Q}] \cdot \boldsymbol{N} + \mathscr{L}(\boldsymbol{Q} \cdot \boldsymbol{N}) =: \boldsymbol{t}_0^{P\,\mathrm{pre}} \qquad \text{on } \partial \mathscr{B}_0^P\,, \tag{2.25}$$

$$\boldsymbol{Q} : [\boldsymbol{N} \otimes \boldsymbol{N}] =: \boldsymbol{t}_0^{Q\,\mathrm{pre}} \qquad \text{on } \partial \mathscr{B}_0^Q\,, \tag{2.26}$$

define both a traction $\boldsymbol{t}_0^{P\,\mathrm{pre}}$ and a double traction $\boldsymbol{t}_0^{Q\,\mathrm{pre}}$ of the surface (the latter quantity being a tensor of second order), compare Remark 2.3.1. The Dirichlet boundary conditions

$$\boldsymbol{\varphi} =: \boldsymbol{\varphi}^{\mathrm{pre}} \qquad \text{on } \partial\mathscr{B}_0^{\varphi}\,, \tag{2.27}$$

$$\nabla_X^N \boldsymbol{\varphi} =: \left(\nabla_X^N \boldsymbol{\varphi}\right)^{\mathrm{pre}} \qquad \text{on } \partial\mathscr{B}_0^{N}\,, \tag{2.28}$$

prescribes the deformation and its normal gradient at the boundary. Note that the boundaries are pairwise disjoint, $\partial\mathscr{B}_0^P \cap \partial\mathscr{B}_0^{\varphi} = \emptyset$ and $\partial\mathscr{B}_0^Q \cap \partial\mathscr{B}_0^N = \emptyset$, while the standard and the higher-order boundary conditions can be combined.

See Appendix A for the derivation of both the balance of momentum and the corresponding Neumann boundary conditions.

Hyperelasticity. In a hyperelastic format, the Piola stresses and the body force are defined by their energetically conjugate kinematic pairings:

$$\boldsymbol{P} := \mathrm{D}_F \mathscr{W}_0\,, \qquad \boldsymbol{Q} := \mathrm{D}_G \mathscr{W}_0\,, \qquad \boldsymbol{b}_0 := -\partial_{\boldsymbol{\varphi}} \mathscr{V}_0\,. \tag{2.29}$$

Remark 2.3.1 (Differential operator) *The differential operator $\mathscr{L}(\boldsymbol{Q}\cdot\boldsymbol{N})$ is defined as $\mathscr{L}(\boldsymbol{Q}\cdot\boldsymbol{N}) = K\boldsymbol{Q} : [\boldsymbol{N}\otimes\boldsymbol{N}]\nabla_X^T(\boldsymbol{Q}\cdot\boldsymbol{N}) : \boldsymbol{I}$, wherein $K = -\nabla_X^T\boldsymbol{N} : \boldsymbol{I}$ denotes the twice the mean or rather the total curvature of the surface $\partial\mathscr{B}_0$ (Sunyk and Steinmann, 2003, Kirchner and Steinmann, 2005, 2007a). This relies on the decomposition of the total gradient into its normal and its tangential part as $\nabla_X(\bullet) = \nabla_X^N(\bullet) + \nabla_X^T(\bullet) := [\nabla_X(\bullet)\cdot N]\boldsymbol{N} + \nabla_X(\bullet)[\boldsymbol{I} - \boldsymbol{N}\otimes\boldsymbol{N}]$).*

2.3.2 Geometrically linear gradient continuum framework

For the gradient continuum, the linearization of the geometric measure is performed along the lines of the classical continuum of Section 2.2.2. Hereby, based on the strain tensor $\boldsymbol{\varepsilon}$ in (2.15), a second gradient $\boldsymbol{\eta}$ operating on this tensor is considered:

$$\boldsymbol{\varepsilon}(\boldsymbol{u}) := \nabla^{\mathrm{sym}}\boldsymbol{u}\,, \qquad \boldsymbol{\eta}(\boldsymbol{u}) := \nabla\nabla^{\mathrm{sym}}\boldsymbol{u} = \nabla\boldsymbol{\varepsilon}\,. \tag{2.30}$$

This strain gradient $\boldsymbol{\eta}$ is a third-order tensor, which obeys the symmetry with respect to the first two indices ($\varepsilon_{ij} = \varepsilon_{(ij)}$ and $\eta_{ijk} = \eta_{(ij)k}$) due to the introduction of the strain according to $(2.30)_1$.

Remark 2.3.2 (Strain gradient) *The kinematic assumption $(2.30)_2$ to treat the gradient is not unique. Alternatively, also the second gradient of the displacement $\boldsymbol{u}$ could be considered, see e. g. Kirchner and Steinmann (2005).*

Balance relations. The stored-energy density is a function of the governing kinematic quantities:

$$\mathscr{W} = \check{\mathscr{W}}(\boldsymbol{\varepsilon}(\boldsymbol{u}), \boldsymbol{\eta}(\boldsymbol{u})) = \hat{\mathscr{W}}(\boldsymbol{u}) \,. \tag{2.31}$$

Consequently, the balance of momentum (2.17) exacerbates to

$$\operatorname{div}(\boldsymbol{\sigma} - \operatorname{div}\boldsymbol{\tau}) = -\boldsymbol{b} \,, \tag{2.32}$$

wherein the $\boldsymbol{\sigma}$ is the stress and $\boldsymbol{\tau}$ the double stress. The Neumann boundary condition include both a traction and a double traction:

$$\begin{aligned} [\boldsymbol{\sigma} - \operatorname{div}\boldsymbol{\tau}] \cdot \boldsymbol{n} + \mathscr{L}(\boldsymbol{\tau} \cdot \boldsymbol{n}) &:= \boldsymbol{t}^{\sigma\,\mathrm{pre}} \qquad \text{on } \partial\mathscr{B}^{\sigma} \,, \\ \boldsymbol{\tau} : [\boldsymbol{n} \otimes \boldsymbol{n}] &:= \boldsymbol{t}^{\tau\,\mathrm{pre}} \qquad \text{on } \partial\mathscr{B}^{\tau} \,, \end{aligned} \tag{2.33}$$

whereby $\mathscr{L}(\boldsymbol{\tau} \cdot \boldsymbol{n})$ denotes the differential operator of Remark 2.3.1 operating on $\boldsymbol{\tau} \cdot \boldsymbol{n}$, $\boldsymbol{n}$ being the normal vector on the surface $\partial\mathscr{B}$. The corresponding Dirichlet boundary condition complements the displacement term of $(2.18)_2$ by another term to describe the normal gradient:

$$\boldsymbol{u} =: \boldsymbol{u}^{\mathrm{pre}} \quad \text{on } \partial\mathscr{B}^{u} \,, \qquad\qquad \nabla^N \boldsymbol{u} =: \left(\nabla^N \boldsymbol{u}\right)^{\mathrm{pre}} \quad \text{on } \partial\mathscr{B}^{N} \,. \tag{2.34}$$

The disjointness of the boundaries is equivalent to the finite-deformation case: $\partial\mathscr{B}^{\sigma} \cap \partial\mathscr{B}^{u} = \emptyset$ and $\partial\mathscr{B}^{\tau} \cap \partial\mathscr{B}^{N} = \emptyset$.

The argument of the divergence operator in (2.32) can be abbreviated as the effective stress tensor:

$$\boldsymbol{\sigma}^{\star} := \boldsymbol{\sigma} - \operatorname{div}\boldsymbol{\tau} \,. \tag{2.35}$$

Throughout this thesis, we will encounter this notation more often; hereby we refer the reader to Remark 2.3.3. Using the notion of effective stress, the balance of momentum (2.32) is rewritten as:

$$\operatorname{div}\boldsymbol{\sigma}^{\star} = -\boldsymbol{b} \,. \tag{2.36}$$

Remark 2.3.3 (Effective Quantity) *The tensorial effective quantity* $(\overset{\triangle}{\boldsymbol{a}}{}^{\square}_{\lozenge})^{\star}$ *of* n*th order is based on the definition*

$$(\overset{\triangle}{\boldsymbol{a}}{}^{\square}_{\lozenge})^{\star} := \overset{\triangle}{\boldsymbol{a}}{}^{\square}_{\lozenge} - \operatorname{div}\overset{\triangle}{\boldsymbol{b}}{}^{\square}_{\lozenge}$$

wherein $\overset{\triangle}{\boldsymbol{a}}{}^{\square}_{\lozenge}$ *is a tensor of order* n *and* $\overset{\triangle}{\boldsymbol{b}}{}^{\square}_{\lozenge}$ *of order* n+1. *Hereby the super- and subscripts represent certain properties; in particular the distinction will be made between macro or*

micro, $\triangle \in \{\emptyset, -\}$*, in view of the plasticity formulations in Chapter 7 between total or plastic,* $\Diamond \in \{\emptyset, \mathrm{p}\}$*, and between internal and external,* $\square \in \{\mathrm{int}, \mathrm{ext}\}$*, plastic quantities.*

raphHyperelasticity. The elastic case of the gradient continuum is characterized by zero dissipation. Thus the Clausius–Duhem inequality simplifies to the equality

$$\mathscr{D} = \boldsymbol{\sigma} : \dot{\boldsymbol{\varepsilon}} + \boldsymbol{\tau} \vdots \dot{\boldsymbol{\eta}} - \dot{\mathscr{W}} = [\boldsymbol{\sigma} - \partial_{\boldsymbol{\varepsilon}} \mathscr{W}] : \dot{\boldsymbol{\varepsilon}} + [\boldsymbol{\tau} - \partial_{\boldsymbol{\eta}} \mathscr{W}] : \dot{\boldsymbol{\eta}} = 0\,. \tag{2.37}$$

With this the both the stress and the double stress are for hyperelasticity given as the derivatives of the potential-energy density with respect to their energetically conjugate pairings,

$$\boldsymbol{\sigma} := \partial_{\boldsymbol{\varepsilon}} \mathscr{W}\,, \qquad\qquad \boldsymbol{\tau} := \partial_{\boldsymbol{\eta}} \mathscr{W}\,, \tag{2.38}$$

under the assumption of hyperelasticity. The symmetries of the stress measures follow those of their energetically conjugate kinematics counterparts, i. e. $\sigma_{ij} = \sigma_{(ij)}$ and $\tau_{ijk} = \tau_{(ij)k}$. A sample constitutive assumption for the small-strain gradient elasticity can be found in Table 2.1.

2.3.3 Numerical aspects

The considered higher gradients of deformation entail elevated demands with respect to the spatial continuity of the displacement. For example for the second-gradient continuum, C^1 continuity is required for the displacement, so that the second gradient represents (at least) a constant function rather than vanishes.

Especially in view of a finite-element framework, these higher demands on the continuity of the displacement (Kirchner and Steinmann, 2005) bear an arduousness, because C^n continuous approximations are difficult to realize for $n > 0$. Therefore many computational approaches seek to reduce the continuity requirement by additional degrees of freedom (Shu et al., 1999, Amanatidou and Aravas, 2002, Kouznetsova, 2002).

Mesh-free methods (Sukumar et al., 1997, 2001, Chen et al., 2000) do easily capture these continuity requirements, because they are not restricted to polynomial shape functions.

2.4 Micromorphic continuum

As aforementioned, in the micromorphic continuum theory, additional degrees of freedom are considered at each continuum point, which idealize the deformation of separate microcontinua. In the actual micromorphic continuum, these microcontinua may experience deformations that consist of both stretch of rotation as mentioned in (2.3). The micromorphic continuum will be elaborated within a

finite-deformation framework in Chapter 3. Thereby especially the configurational-mechanics aspect is envisaged and furthermore a numerical framework is introduced, as pursued by Hirschberger et al. (2007b). Therefore at this point, exclusively the corresponding small-strain framework as described by Eringen (1999), Hofer (2003) or Kirchner and Steinmann (2005) is presented.

2.4.1 Geometrically linear micromorphic continuum framework

Kinematics. The two primary kinematic variables are the macro displacement vector $\boldsymbol{u}$ and the micro strain $\bar{\boldsymbol{\varepsilon}}$. Their gradients with respect to macro placement are denoted by strain and micro-strain gradient,

$$\boldsymbol{\varepsilon}(\boldsymbol{u}) = \nabla \boldsymbol{u}\,, \qquad\qquad \bar{\boldsymbol{\eta}} := \nabla \bar{\boldsymbol{\varepsilon}}\,, \tag{2.39}$$

respectively. Since the micro strain is a second-order tensor, its gradient $\bar{\boldsymbol{\eta}}$ is a tensor of third order.

Balance relations. The stored-energy density is a function of macro and micro kinematic variables:

$$\mathscr{W} = \check{\mathscr{W}}(\boldsymbol{\varepsilon}(\boldsymbol{u}), \bar{\boldsymbol{\varepsilon}}, \nabla \bar{\boldsymbol{\varepsilon}}) = \tilde{\mathscr{W}}(\boldsymbol{u}, \bar{\boldsymbol{\varepsilon}})\,. \tag{2.40}$$

From the Dirichlet principle, the balance of momentum is derived as

$$\operatorname{div} \boldsymbol{\sigma} = -\boldsymbol{b}\,, \qquad\qquad \operatorname{div} \bar{\boldsymbol{\tau}} - \bar{\boldsymbol{\sigma}} = \boldsymbol{0} \quad \text{in } \mathscr{B} \tag{2.41}$$

and omitting body couples. It consists of a macro balance and an additional balance equations for the micro quantities and involves a stress $\boldsymbol{\sigma}$, a micro stress $\bar{\boldsymbol{\sigma}}$ and a double stress $\bar{\boldsymbol{\tau}}$. It is rewritten as:

$$\operatorname{div} \boldsymbol{\sigma} = -\boldsymbol{b}\,, \qquad\qquad \bar{\boldsymbol{\sigma}}^{\star} = \boldsymbol{0} \quad \text{in } \mathscr{B}\,, \tag{2.42}$$

in terms of the effective total micro stress $\bar{\boldsymbol{\sigma}}^{\star} := \operatorname{div} \bar{\boldsymbol{\tau}} - \bar{\boldsymbol{\sigma}}$ (compare Remark 2.3.3). While Dirichlet boundary conditions are stated for $\boldsymbol{u}$ and $\bar{\boldsymbol{\varepsilon}}$ on $\partial \mathscr{B}^{u}$ and $\partial \mathscr{B}^{\bar{\varepsilon}}$, respectively, the corresponding Neumann boundary conditions,

$$\boldsymbol{\sigma} \cdot \boldsymbol{n} =: \boldsymbol{t}^{\sigma\,\mathrm{pre}} \quad \text{on } \partial \mathscr{B}^{\sigma}\,, \qquad\qquad \bar{\boldsymbol{\tau}} \cdot \boldsymbol{n} =: \bar{\boldsymbol{t}}^{\,\bar{\tau}\,\mathrm{pre}} \quad \text{on } \partial \mathscr{B}^{\bar{\tau}}\,, \tag{2.43}$$

are constituted of a macro traction and a (micro) double traction. While the first is a vector as in the classical case (2.18), the latter quantity represents a nonsymmetric tensor of second order.

Hyperelasticity. For the elastic case of the micromorphic continuum, the dissipation inequality reads

$$\begin{aligned}\mathscr{D} &= \boldsymbol{\sigma} : \dot{\boldsymbol{\varepsilon}} + \bar{\boldsymbol{\sigma}} : \dot{\bar{\boldsymbol{\varepsilon}}} + \bar{\boldsymbol{\tau}} :\cdot \dot{\bar{\boldsymbol{\eta}}} - \dot{\mathscr{W}} \\ &= [\boldsymbol{\sigma} - \partial_{\boldsymbol{\varepsilon}} \mathscr{W}] : \dot{\boldsymbol{\varepsilon}} + [\bar{\boldsymbol{\sigma}} - \partial_{\bar{\boldsymbol{\varepsilon}}} \mathscr{W}] : \dot{\bar{\boldsymbol{\eta}}} + [\boldsymbol{\tau} - \partial_{\bar{\boldsymbol{\eta}}} \mathscr{W}] : \dot{\boldsymbol{\eta}} = 0 \,. \end{aligned} \tag{2.44}$$

Under the assumption of hyperelasticity, the energy density $\mathscr{W}$ represents a potential for the macro stress, the micro stress and the double stress, which are extracted as

$$\boldsymbol{\sigma} := \partial_{\boldsymbol{\varepsilon}} \mathscr{W} \,, \qquad \bar{\boldsymbol{\sigma}} := \partial_{\bar{\boldsymbol{\varepsilon}}} \mathscr{W} \,, \qquad \bar{\boldsymbol{\tau}} := \partial_{\bar{\boldsymbol{\eta}}} \mathscr{W} \,. \tag{2.45}$$

These are the energetically conjugate quantities to the kinematic measures (2.39) and inherit the tensorial order of their respective kinematic counterparts. A possible constitutive assumption for the stored-energy density is stated in Table 2.1 (Hirschberger et al., 2007b, Hirschberger and Steinmann, 2007).

2.4.2 Numerical aspects

Different from gradient continua, micromorphic continua require a significant number of additional degrees of freedom due to the additional kinematic quantities and the resulting additional balance relations, which makes them computationally expensive.

Nevertheless, they exhibit convenient properties with respect to their numerical implementation in a finite-element context, because they require the same continuity as the classical continuum (Kirchner and Steinmann, 2005, Hirschberger et al., 2006, 2007b).

3 Micromorphic Hyperelasticity – Deformational and Configurational Mechanics

The micromorphic continuum was already briefly discussed within the overview given on generalized continua in the preceding chapter. In this chapter, which partially bases on the articles by Hirschberger et al. (2006, 2007a,b), we particularize the micromorphic continuum framework at finite deformations. We aim at a numerical solution scheme that allows to perform finite-element simulations that display the occurring size-effects. Furthermore we strive for the predictive character of the material forces, as they are beneficial to fracture-mechanics considerations within the micromorphic continuum. Consequently, a micromorphic continuum formulation is presented from the dual perspectives of both deformational and configurational mechanics. In this sense, the full kinematics is presented at finite deformations including the macro and the micro contributions for both the direct and the inverse problem. A restriction to isotropic hyperelasticity ensures the existence of a potential energy. For conservative static problems, the Dirichlet principle results in the Euler–Lagrange equations, i. e. the balance of momentum in its local form. Based on the material-motion description, the material-force method is applied, which bears the micromorphic material forces as well as additional configurational higher-order quantities that correspond to the micro deformation.

Outline. First, the approaches of deformational vs. configurational mechanics will be illuminated using the example of the classical continuum, see Section 3.1. On this basis, in Section 3.2 a description of the micromorphic continuum is derived both from a deformational- and a configurational-mechanics perspective. A straightforward constitutive formulation is established in Section 3.3, which allows to perform a finite-element approximation for the micromorphic continuum as presented in Section 3.4. Numerical examples, incorporating parameter studies and the evaluation of the occurring material-force quantities, are computed in Section 3.5.

3.1 Deformational vs. configurational mechanics

Generally the deformation of continuum bodies can be described in two manners. While the most common perspective of the *spatial-motion problem* is treated in the so-called deformational mechanics, the other one is *material-motion problem* covered in the concept of configurational mechanics. The latter approach has gained particular attraction within the last decades (Maugin and Trimarco, 1992, Maugin, 1993, 1994, Steinmann, 2000, Maugin and Steinmann, 2005), while it is based on the pioneering contribution of Eshelby (1951) on lattice defects.

3.1.1 Spatial-motion problem

Within the spatial-motion problem the spatial motion of a physical point $\mathscr{P}$ with material position $\boldsymbol{X} \in \mathscr{B}_0$ is observed with the change of time,

$$\boldsymbol{x} = \boldsymbol{\varphi}(\boldsymbol{X}, t)\,, \tag{3.1}$$

as illustrated in Figure 3.1. This description is characterized on the one hand by a parametrization of the occurring quantities by the material placement $\boldsymbol{X}$ and on the other hand by the fact that these quantities belong to the spatial manifold $\mathscr{B}_t$ or are two-point tensors mapping towards the spatial manifold.

As seen in Section 2.2.1, the balance of momentum for the static case can be derived from the Dirichlet principle, which requires the total potential energy to be stationary for the system to be in equilibrium. Thus the variation of this potential energy $\mathscr{E} = \int_{\mathscr{B}_0} \mathscr{U}_0 \,\mathrm{d}V - \int_{\partial\mathscr{B}_0} v_0 \,\mathrm{d}A$ with respect to spatial placement at fixed material placement must be zero. If we omit the boundary potential v_0 for the sake of clarity, this requirement reads

$$\mathrm{D}_\delta \mathscr{E} = \int\limits_{\mathscr{B}_0} \mathrm{D}_\delta \mathscr{U}_0(\boldsymbol{\varphi}, \boldsymbol{F}; \boldsymbol{X}) \mathrm{d}V \doteq 0\,. \tag{3.2}$$

The balance of momentum (2.8) is obtained in the form $\mathrm{Div}\,\boldsymbol{P} = -\boldsymbol{b}_0$ accompanied by *homogeneous* Neumann boundary conditions, $\boldsymbol{P} \cdot \boldsymbol{N} =: \boldsymbol{0}$ on $\partial\mathscr{B}_0$.

In the spatial-motion problem we deal with the intuitively-known and widely-used spatial forces, which are physical forces in the sense of Newton, here denoted by $\mathbf{f}$. They are defined as being energetically conjugate to variations in the spatial placement of physical points at fixed material position. In a general case, when the external potential is not omitted, the corresponding spatial tractions can also be prescribed at the boundary $\partial\mathscr{B}_0$.

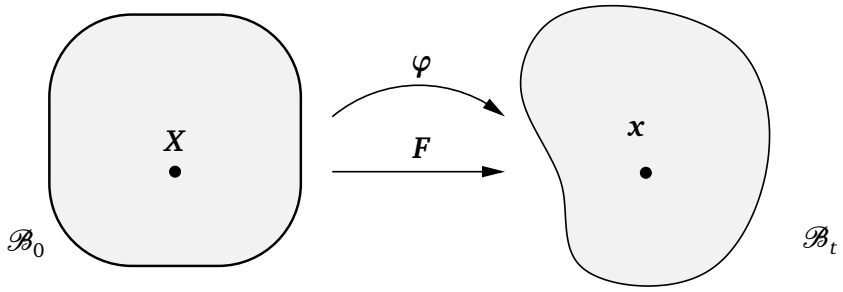

Figure 3.1: Deformation map of the spatial-motion problem

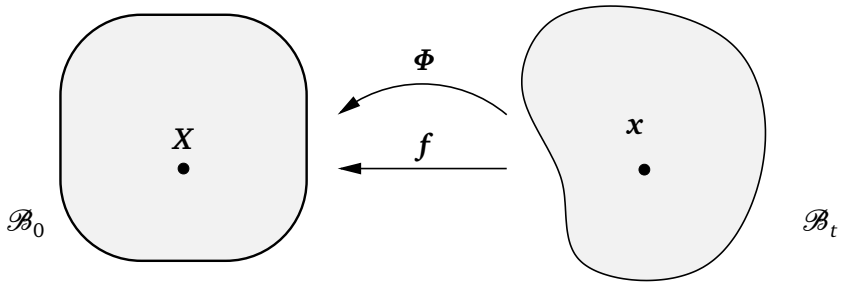

Figure 3.2: Deformation map of the material-motion problem

3.1.2 Material-motion problem

Opposed to the spatial-motion problem, in the material-motion problem at a fixed spatial placement $\boldsymbol{x}$, the material origin $\boldsymbol{X}$ of a physical point passing by is the unknown quantity of observation,

$$\boldsymbol{X} = \boldsymbol{\Phi}(\boldsymbol{x}(\boldsymbol{X}, t)), \tag{3.3}$$

compare Figure 3.2. The material-motion problem is formulated with respect to material quantities in $\mathscr{B}_0$ or two-point quantities mapping from the spatial, to the material manifold. These quantities are parametrized with respect to their spatial position $\boldsymbol{x}$. An analogous variational principle to the Dirichlet principle (3.2) in the case of the material-motion problem must account for a *release of potential energy* at a variation of the material placement at fixed spatial placement:

$$\mathrm{d}_\delta \mathscr{E} = \int_{\mathscr{B}_t} \mathrm{d}_\delta \mathscr{U}_t(\boldsymbol{\Phi}, \boldsymbol{f}; \boldsymbol{x}) \mathrm{d}v \leq 0\,. \tag{3.4}$$

At this variation of the material configuration, an external material traction vector $\boldsymbol{T}_t$ defined to capture the energy release:

$$\mathrm{d}_\delta \mathscr{E} =: \int_{\partial \mathscr{B}_t} \boldsymbol{T}_t \cdot \delta \boldsymbol{\Phi} \, \mathrm{d}a \tag{3.5}$$

In other words, in the material-motion problem, we generally obtain *nonzero* Neumann boundary conditions even if the external potential is omitted. The material traction entails the material force F, which is energetically conjugate to a variation in the material position, $\delta\boldsymbol{\Phi}$, of a particular physical point. The material balance corresponds to the *pseudo-momentum* in the nomenclature of Maugin (1993, 1994), which occurs at heterogeneities. The right-hand side of (3.4) vanishes in the absence of heterogeneities (Maugin, 1993).

The occurring material forces are also referred to as configurational or Eshelbyan forces, because they were first introduced by Eshelby (1951), as a force acting on a singularity in view of defect-mechanics problems. More recent contributions have been delivered by Epstein and Maugin (1990), Maugin and Trimarco (1992), Maugin (1993, 1994), Gurtin and Podio-Guidugli (1996, 1998), Gurtin (2000b), Steinmann (2000), Maugin and Steinmann (2005), who characterize the material force to act as driving forces for the propagation of heterogeneities.

Material-force method. This character as a driving force for heterogeneities or defects (such as cracks, dislocations, and voids) makes the material force particularly useful for instance in computational fracture mechanics. In this context, the material forces are useful in a crack-propagation criterion, because they do not only deliver an energy-based criterion, which coincides with the J-integral introduced by Rice (1968), but additionally involve a vectorial direction. This insight motivated Steinmann (2000) to develop the material force method, which allows to compute the discrete material forces in a post-processing step. This was done in view of fracture mechanics (Steinmann, 2000, Steinmann et al., 2001, Denzer et al., 2003, Nguyen et al., 2005) and refined in further contributions with respect to different applications ranging from thermoelasticity (Kuhl et al., 2004b, Denzer, 2006), damage (Liebe et al., 2003a), elastodynamics (Steinmann, 2002, Kuhl and Steinmann, 2005), over open systems (Kuhl and Steinmann, 2004, 2006, Kuhl, 2004) to inelasticity (Menzel and Steinmann, 2005, Maugin and Steinmann, 2005) and crystal plasticity (Menzel et al., 2004). The material-force method also has proven beneficial in the context of adaptive remeshing as investigated by Müller and Maugin (2002), Gross et al. (2002, 2003) as well as Denzer et al. (2007), Scherer et al. (2007, 2008). In this context the Arbitrary Eulerian–Lagrangian (ALE) formulations treated by Kuhl et al. (2004a), Askes et al. (2004), Kuhl and Steinmann (2005) and references cited therein, is noteworthy, because it utilizes the dual character of

spatial- and material-motion problem and thus provides a deeper insight.

It is desirable to extend the material-force method to generalized continua as well. To this end, the micromorphic continuum is in the sequel treated with respect to both the deformational and the configurational perspective.

3.2 The micromorphic continuum at finite deformations

Recall that the micromorphic continuum is described as a macrocontinuum, each physical point of which is endowed with a microstructure referred to as the microcontinuum. These microcontinua may experience arbitrary deformations consisting of both stretch and rotation which are required to be affine throughout the microcontinuum, nevertheless kinematically independent from the macrocontinuum. A point $\mathscr{P}$ on the macro scale is described by the placement vectors $\boldsymbol{X}$ in the material configuration $\mathscr{B}_0$ and $\boldsymbol{x}$ in the spatial configuration $\mathscr{B}_t$. On the micro scale, a point $\bar{\mathscr{P}}$ of the microcontinuum is denoted with the micro-placement vectors $\bar{\boldsymbol{X}}$ in the material configuration $\bar{\mathscr{B}}_0$ and $\bar{\boldsymbol{x}}$ in the spatial configuration $\bar{\mathscr{B}}_t$, respectively.

Since a material point is equipped with a microstructure that is kinematically independent, additional balance equations besides the ordinary or rather macro balance of momentum have to be considered for the micromorphic theory. These may be obtained by an energy consideration, which is here derived from the Dirichlet principle. The set of state variables is given by $\mathbb{S} = \{\boldsymbol{\varphi}, \bar{\boldsymbol{F}}\}$, wherein the first argument describes the macrostructural kinematics while the second one characterises the deformation of the microcontinuum. A constitutive functional is to be found, which in the most general isothermal hyperelastic case incorporates the following dependencies: $\mathfrak{C} = \mathfrak{C}(\boldsymbol{\varphi}, \nabla_X \boldsymbol{\varphi}, \bar{\boldsymbol{F}}, \nabla_X \bar{\boldsymbol{F}}; \boldsymbol{X})$.

First, the spatial-motion problem is presented in Section 3.2.1, before the material-motion problem described in Section 3.2.2. Both approaches are compared in Section 3.2.3. The following derivations of the spatial-motion problem follow the line of the finite-deformation part of Kirchner and Steinmann (2005), while for the material-motion problem, parallels to the material settings of the second-order gradient theory as presented by Kirchner and Steinmann (2007a) can be recognized.

3.2.1 Spatial-motion problem

In the framework of the spatial-motion problem of the micromorphic continuum, first the kinematic relations are introduced. By the consideration of the stationarity of the potential energy at static equilibrium, the local balance of momentum with the corresponding boundary conditions is derived in a two-point formulation. In

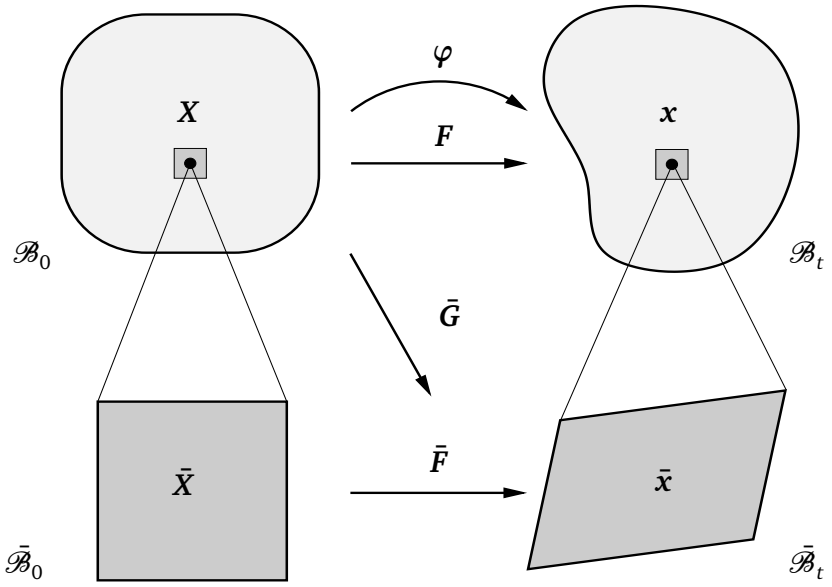

Figure 3.3: Spatial-motion problem: micromorphic deformation maps

the sequel the description is transformed to a purely spatial formulation by push-forward operations on the quantities and operators.

Kinematic relations. Within the micromorphic continuum, the macro- and the microcontinuum kinematics are considered as illustrated in Figure 3.3. On the macro scale, the spatial-motion deformation map is defined as

$$\boldsymbol{x} = \boldsymbol{\varphi}(\boldsymbol{X}) \qquad \text{with} \qquad \boldsymbol{F}(\boldsymbol{X}) := \nabla_{\boldsymbol{X}} \boldsymbol{\varphi}(\boldsymbol{X}) \tag{3.6}$$

being the macro deformation gradient. This second-order two-point tensor represents the gradient of the spatial-motion macro deformation map $\boldsymbol{\varphi}$ with respect to material coordinates. The Jacobian determinant of the spatial-motion problem is denoted by $J := \det \boldsymbol{F} = \mathrm{d}v/\mathrm{d}V > 0$, with $\mathrm{d}V$ and $\mathrm{d}v$ being infinitesimal volume elements in the material and the spatial configuration, respectively. By introducing a second-order tensor $\bar{\boldsymbol{F}}$ which we refer to as the micro deformation map, we may express the affine deformation mapping from the material to the spatial configuration on the micro scale as

$$\bar{\boldsymbol{x}} = \bar{\boldsymbol{F}}(\boldsymbol{X}) \cdot \bar{\boldsymbol{X}}\,, \qquad \text{while} \qquad \bar{\boldsymbol{G}}(\boldsymbol{X}) := \nabla_{\boldsymbol{X}} \bar{\boldsymbol{F}}(\boldsymbol{X}) \tag{3.7}$$

defines the gradient of this micro scale two-point tensor $\bar{\boldsymbol{F}}$ with respect to the material macro placement and thus is a tensor of third order linking both scales.

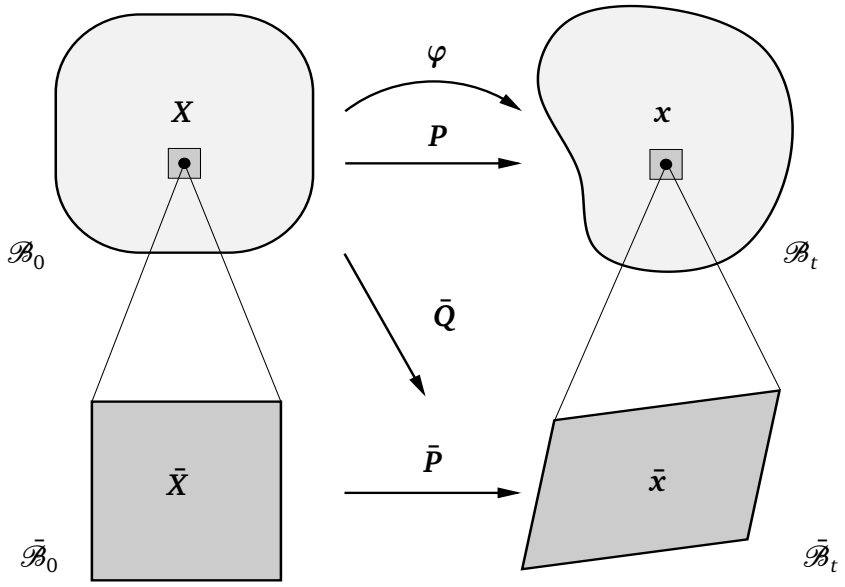

Figure 3.4: Spatial-motion problem: Piola-type stress measures derived from hyperelasticity

Energy considerations and balance relations. For the prevailing quasi-static case, the Dirichlet principle is utilized which requires the total potential energy to be stationary for the system to be in equilibrium. To achieve this, the variation of the total potential energy $\mathscr{E} = \int_{\mathscr{B}_0} \mathscr{U}_0 \mathrm{d}V$ with respect to each of the kinematic quantities defined above at fixed material placement $\boldsymbol{X}$ is required to equal zero,

$$\mathrm{D}_\delta \mathscr{E} = \mathrm{D}_\delta \int_{\mathscr{B}_0} \mathscr{U}_0(\boldsymbol{\varphi}, \boldsymbol{F}, \bar{\boldsymbol{F}}, \bar{\boldsymbol{G}}; \boldsymbol{X}) \,\mathrm{d}V \doteq 0\,. \tag{3.8}$$

Herein $\mathscr{U}_0 = \mathscr{W}_0 + \mathscr{V}_0$ is the total potential energy density per material unit volume $\mathrm{d}V$ in $\mathscr{B}_0$ with its internal and external contributions, $\mathscr{W}_0$ and $\mathscr{V}_0$, respetively.

If we assume the material to behave hyperelastically, stresses can be defined as the derivatives of $\mathscr{U}_0$ with respect to their particular energetically conjugate deformation variables at fixed material placement. Particularly, the spatial body force $\boldsymbol{b}_0$ acting on the material domain $\mathscr{B}_0$, as well the macro stress $\boldsymbol{P}$, micro stress $\bar{\boldsymbol{P}}$ and the double stress $\bar{\boldsymbol{Q}}$ of Piola type are obtained by the derivatives

$$\boldsymbol{b}_0 := -\partial_{\boldsymbol{\varphi}} \mathscr{U}_0\,, \qquad \boldsymbol{P} := \mathrm{D}_{\boldsymbol{F}} \mathscr{U}_0\,, \qquad \bar{\boldsymbol{P}} := \mathrm{D}_{\bar{\boldsymbol{F}}} \mathscr{U}_0\,, \qquad \bar{\boldsymbol{Q}} := \mathrm{D}_{\bar{\boldsymbol{G}}} \mathscr{U}_0\,. \tag{3.9}$$

The stresses $\boldsymbol{P}$ and $\bar{\boldsymbol{P}}$ are tensors of second order and $\bar{\boldsymbol{Q}}$ is of third order, respectively, and perform two-point description mappings as indicated in Figure 3.4. With these in hand, the balance (3.8) may be reformulated as the weak form of the balance of

momentum

$$\int_{\mathscr{B}_0} \boldsymbol{P} : \delta\boldsymbol{F} + \bar{\boldsymbol{P}} : \delta\bar{\boldsymbol{F}} + \bar{\boldsymbol{Q}} :\cdot \delta\bar{\boldsymbol{G}} - \boldsymbol{b}_0 \cdot \delta\boldsymbol{\varphi}\,\mathrm{d}V = 0 \qquad \forall\, \delta\boldsymbol{\varphi},\, \delta\bar{\boldsymbol{F}}\,, \tag{3.10}$$

which must hold for arbitrary variations of $\delta\boldsymbol{\varphi}$ and $\delta\bar{\boldsymbol{F}}$. By application of divergence relations and the Gaussian theorem, this equation is carried over to the local form of the balance of momentum in $\mathscr{B}_0$,

$$\mathrm{Div}\,\boldsymbol{P} + \boldsymbol{b}_0 = \boldsymbol{0}\,, \qquad\qquad \mathrm{Div}\,\bar{\boldsymbol{Q}} - \bar{\boldsymbol{P}} = \boldsymbol{0}\,, \tag{3.11}$$

which is constituted by one statement for the macro and another one for micro scale both acting in $\mathscr{B}_0$. The Dirichlet boundary conditions for the micromorphic continuum read

$$\boldsymbol{\varphi} = \boldsymbol{\varphi}^{\mathrm{pre}} \quad \text{on } \partial\mathscr{B}_0^{\varphi}\,, \qquad\qquad \bar{\boldsymbol{F}} = \bar{\boldsymbol{F}}^{\mathrm{pre}} \quad \text{on } \partial\mathscr{B}_0^{\bar{F}}\,. \tag{3.12}$$

Thereby, the boundaries follow the disjointness requirement, $\partial\mathscr{B}_0^{P} \cap \partial\mathscr{B}_0^{\varphi} = \emptyset$ and $\partial\mathscr{B}_0^{\bar{Q}} \cap \partial\mathscr{B}_0^{\bar{F}} = \emptyset$, whereas the boundary regions for the macro and the micro quantities are mutually independent. Note that at this point, without loss of generality any surface potential is neglected for the sake of simplicity, i. e. the homogeneous Neumann boundary conditions

$$\boldsymbol{P}\cdot\boldsymbol{N} = \boldsymbol{0} \quad \text{on } \partial\mathscr{B}_0^{P}\,, \qquad\qquad \bar{\boldsymbol{Q}}\cdot\boldsymbol{N} = \boldsymbol{0} \quad \text{on } \partial\mathscr{B}_0^{\bar{Q}}\,, \tag{3.13}$$

are considered for the remainder of this chapter, since otherwise the material-motion problem would become sophisticated. The local balance of momentum (3.11) may also be referred to as the Euler–Lagrange equations.

Remark 3.2.1 *Generally in the spatial-motion problem the external surface potential is not omitted. Next to the energy density $\mathscr{U}_0$ in the bulk $\mathscr{B}_0$, this surface potential-energy density v_0 acts on $\partial\mathscr{B}_0$. Consequently, the full Dirichlet principle reads*

$$\mathrm{D}_{\delta}\left[\int_{\mathscr{B}_0} \mathscr{U}_0(\boldsymbol{\varphi},\boldsymbol{F},\bar{\boldsymbol{F}},\bar{\boldsymbol{G}};\boldsymbol{X})\,\mathrm{d}V - \int_{\partial\mathscr{B}_0} v_0(\boldsymbol{\varphi},\bar{\boldsymbol{F}},\boldsymbol{N};\boldsymbol{X})\,\mathrm{d}A\right] \doteq 0\,. \tag{3.14}$$

This results in the corresponding non-homogeneous *Neumann boundary conditions*

$$\boldsymbol{P}\cdot\boldsymbol{N} = \boldsymbol{t}_0 \quad \textit{on } \partial\mathscr{B}_0^{P}\,, \qquad\qquad \bar{\boldsymbol{Q}}\cdot\boldsymbol{N} = \bar{\boldsymbol{t}}_0 \quad \textit{on } \partial\mathscr{B}_0^{\bar{Q}}\,, \tag{3.15}$$

that describe the macro traction and the double traction on the Neumann boundary $\partial\mathscr{B}_0^{P}$ and $\partial\mathscr{B}_0^{\bar{Q}}$, respectively.

Piola transform of the balance of momentum. As announced before, the present two-point formulation of the spatial-motion problem will be transferred to a purely spatial formulation as follows. A one-sided push forward, namely a Piola transformation, is applied to the balances of momentum (3.11) in order to rewrite them in terms of purely spatial stress tensors. These stress measures are of Cauchy type, namely the macro stress $\boldsymbol{\sigma}$, the micro stress $\bar{\boldsymbol{\sigma}}$ and the double stress $\bar{\boldsymbol{\tau}}$, which are illustrated in Figure 3.5. For this purpose the Piola transformation formulae

$$\{\bullet\} \to j\{\bullet\}\cdot\boldsymbol{F}^{\mathrm{t}}, \qquad\qquad \{\bullet\} \to j\{\bullet\}\cdot\bar{\boldsymbol{F}}^{\mathrm{t}}, \tag{3.16}$$

are employed for the macro- and the microcontinuum, respectively. Using the inverse Jacobian determinant $j = 1/J = \mathrm{d}V/\mathrm{d}v$, (3.16) transform the divergence operator $\mathrm{Div}(\bullet)$ with respect to material placement into the divergence operator with respect to spatial placement, $\mathrm{div}(\bullet)$. Finally, from the transformation formulae $(3.16)_1$ we obtain the classical Piola identity $\boldsymbol{\sigma} = j\boldsymbol{P}\cdot\boldsymbol{F}^{\mathrm{t}}$. Moreover, the divergence relation $j\mathrm{Div}\,\bar{\boldsymbol{Q}} = \mathrm{div}\,(j\bar{\boldsymbol{Q}}\cdot\boldsymbol{F}^{\mathrm{t}})$ as well as the relation $j\boldsymbol{b}_0 = \boldsymbol{b}_t$ are exploited towards the macro- and the micro-balance of momentum[1] in $\mathscr{B}_t$,

$$\mathrm{div}\,\boldsymbol{\sigma} + \boldsymbol{b}_t = \boldsymbol{0}, \qquad\qquad \mathrm{div}\,\bar{\boldsymbol{\tau}} - \bar{\boldsymbol{\sigma}} = \boldsymbol{0}, \tag{3.17}$$

in terms of the Cauchy-type stresses. This evaluation renders the relations

$$\boldsymbol{\sigma} := j\boldsymbol{P}\cdot\boldsymbol{F}^{\mathrm{t}}, \qquad \bar{\boldsymbol{\sigma}} := j[\bar{\boldsymbol{P}}\cdot\bar{\boldsymbol{F}}^{\mathrm{t}} + \bar{\boldsymbol{Q}} \overset{2,3}{\vdots} \bar{\boldsymbol{G}}], \qquad \bar{\boldsymbol{\tau}} := j\bar{\boldsymbol{Q}} : [\bar{\boldsymbol{F}}^{\mathrm{t}}\overline{\otimes}\boldsymbol{F}^{\mathrm{t}}] \tag{3.18}$$

between the Cauchy-type and the Piola-type stress measures of the spatial-motion problem. Furthermore $\boldsymbol{b}_t = -\partial_{\varphi} U_t$ denotes the spatial body force per spatial unit volume $\mathrm{d}v$.

Spatial isotropy. In the case of spatial isotropy, which coincides with the usual requirement of objectivity, the total energy density $\mathscr{U}_0$ must be invariant under a rigid-body rotation by any proper orthogonal tensor $\boldsymbol{R}$ superposed onto the spatial configuration:

$$\mathscr{U}_0 = \mathscr{U}_0(\boldsymbol{F}, \bar{\boldsymbol{F}}, \bar{\boldsymbol{G}}, \bullet) \doteq \mathscr{U}_0(\boldsymbol{R}\cdot\boldsymbol{F}, \boldsymbol{R}\cdot\bar{\boldsymbol{F}}, \boldsymbol{R}\cdot\bar{\boldsymbol{G}}, \bullet) \qquad \forall\, \boldsymbol{R} \in \mathrm{SO}(3). \tag{3.19}$$

[1] The Piola transformation formulae (3.16) applied to (3.11) yield (3.17) in the following manner:

$$\begin{aligned} j[\mathrm{Div}\,\boldsymbol{P} + \boldsymbol{b}_0] = j\mathrm{Div}\,(J\boldsymbol{\sigma}\cdot\boldsymbol{F}^{-\mathrm{t}}) + \boldsymbol{b}_t &= \mathrm{div}\,\boldsymbol{\sigma} + \boldsymbol{b}_t \\ j[\mathrm{Div}\,\bar{\boldsymbol{Q}} - \bar{\boldsymbol{P}}]\cdot\bar{\boldsymbol{F}}^{\mathrm{t}} = j\mathrm{Div}\,(J\bar{\boldsymbol{\tau}} : [\bar{\boldsymbol{F}}^{-\mathrm{t}}\overline{\otimes}\boldsymbol{F}^{-\mathrm{t}}])\cdot\bar{\boldsymbol{F}}^{\mathrm{t}} - j\bar{\boldsymbol{P}}\cdot\bar{\boldsymbol{F}}^{\mathrm{t}} &= \mathrm{div}\,\bar{\boldsymbol{\tau}} - \bar{\boldsymbol{\sigma}}\,. \end{aligned}$$

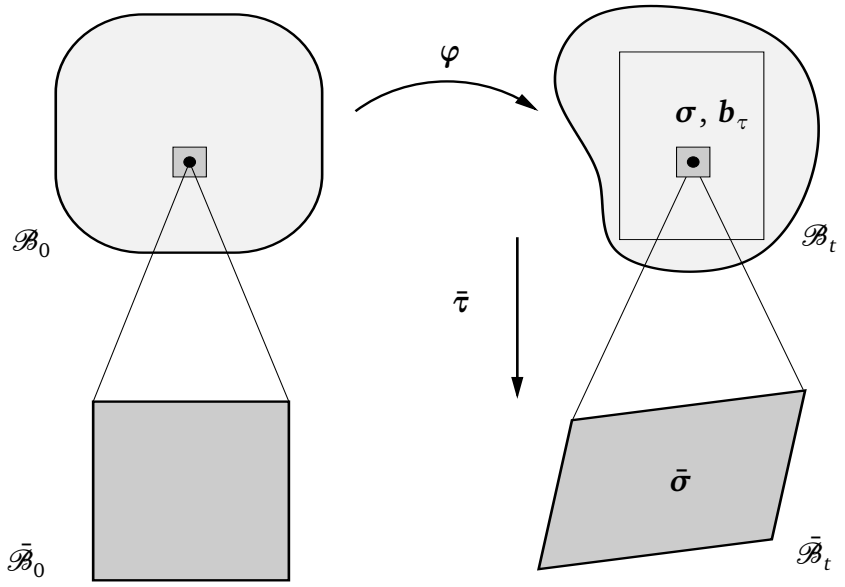

Figure 3.5: Spatial-motion problem: Cauchy-type stress measures derived from Piola transform $\tau \in \{0, t\}$.

Upon a tedious analysis, it follows that the sum $\boldsymbol{\sigma} + \bar{\boldsymbol{\sigma}}$ is symmetric. For a particular choice of constitutive equation, thus the relation

$$j[\boldsymbol{P} \cdot \boldsymbol{F}^{\mathrm{t}} + \bar{\boldsymbol{P}} \cdot \bar{\boldsymbol{F}}^{\mathrm{t}} + \bar{\boldsymbol{Q}} \overset{2,3}{\vdots} \bar{\boldsymbol{G}}] = j[\boldsymbol{F} \cdot \boldsymbol{P}^{\mathrm{t}} + \bar{\boldsymbol{F}} \cdot \bar{\boldsymbol{P}}^{\mathrm{t}} + \bar{\boldsymbol{G}} \overset{2,3}{\vdots} \bar{\boldsymbol{Q}}] \tag{3.20}$$

needs to be fulfilled in order to satisfy spatial isotropy. For further reference on this symmetry property, we suggest the contribution of Kirchner and Steinmann (2007a) and references cited therein.

3.2.2 Material-motion problem

The same micromorphic continuum formulation is now discussed from the perspective of the material-motion problem.

Kinematic relations. On the macro scale, the material placement $\boldsymbol{X}$ of a physical point is treated as a function $\boldsymbol{\Phi}$ of its spatial placement $\boldsymbol{x}$. The deformation gradient of the macrocontinuum, $\boldsymbol{f}$, is defined as the gradient of the macro deformation map $\boldsymbol{\Phi}$ with respect to the spatial placement $\boldsymbol{x}$,

$$\boldsymbol{X} = \boldsymbol{\Phi}(\boldsymbol{x}), \qquad \boldsymbol{f}(\boldsymbol{x}) := \nabla_{\boldsymbol{x}} \boldsymbol{\Phi}(\boldsymbol{x}), \tag{3.21}$$

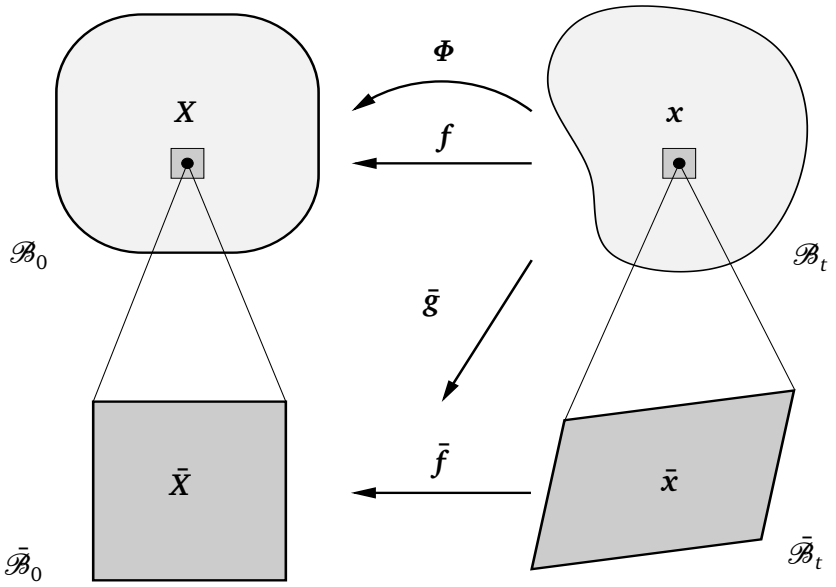

Figure 3.6: Material-motion problem: micromorphic deformation maps

see Fig. 3.6. For the microcontinuum the deformation map $\bar{\boldsymbol{f}}$ and its gradient with respect to spatial coordinates $\boldsymbol{x}$, are introduced as

$$\bar{\boldsymbol{X}} = \bar{\boldsymbol{f}}(\boldsymbol{x}) \cdot \bar{\boldsymbol{x}}\,, \qquad\qquad \bar{\boldsymbol{g}}(\boldsymbol{x}) := \nabla_{\boldsymbol{x}} \bar{\boldsymbol{f}}(\boldsymbol{x})\,. \tag{3.22}$$

The micro deformation map of the material-motion problem, $\bar{\boldsymbol{f}}$, is a two-point tensor of second order, which performs a mapping of the micro placement $\boldsymbol{x}$ from $\bar{\mathscr{B}}_t$ to $\bar{\mathscr{B}}_0$.

Energy considerations and balance relations. Within the material-motion problem, considerations along the lines of the Dirichlet principle must account for a *release of potential energy*, which will occur at any change in the material-motion problem kinematics, as implied by the second law of thermodynamics. Thus the variation of the total potential energy $\mathscr{E} = \int_{\mathscr{B}_t} \mathscr{U}_t \mathrm{d}v$ with respect to the material-motion kinematic quantities at fixed spatial position $\boldsymbol{x}$ must be non-positive:

$$\mathrm{d}_\delta \mathscr{E} = \mathrm{d}_\delta \int_{\mathscr{B}_t} \mathscr{U}_t(\boldsymbol{\Phi}, \boldsymbol{f}, \bar{\boldsymbol{f}}, \bar{\boldsymbol{g}}; \boldsymbol{x}) \mathrm{d}v \leq 0\,. \tag{3.23}$$

Herein $\mathscr{U}_t$ denotes the total-energy density with respect to the spatial unit volume $\mathrm{d}v$ in $\mathscr{B}_t$. Particularly, in case of configurational equilibrium, $\mathrm{d}_\delta \mathscr{E} = 0$, while in more

general cases material traction quantities have to be considered.

$$\mathrm{d}_\delta \mathscr{E} =: \int_{\partial \mathscr{B}_t} \mathrm{d}_\delta \boldsymbol{\Phi} \cdot \boldsymbol{T}_t + \mathrm{d}_\delta \bar{\boldsymbol{f}} : \bar{\boldsymbol{T}}_t \, \mathrm{d}a \,. \tag{3.24}$$

Hereby a material macro-traction vector $\boldsymbol{T}_t$ and a material second-order double-traction tensor $\bar{\boldsymbol{T}}_t$ on the boundaries $\partial \mathscr{B}_t^p$, $\partial \mathscr{B}_t^{\bar{q}}$ enter as *definitions* and are energetically conjugate to both a variation of the macro-deformation map $\boldsymbol{\Phi}$ and the micro deformation map $\bar{\boldsymbol{f}}$, respectively.

In analogy to the spatial-motion problem, a material body force $\boldsymbol{B}_t$ acting on the spatial volume $\mathrm{d}v$ as well as a macro stress $\boldsymbol{p}$, a micro stress $\bar{\boldsymbol{p}}$ and a double stress $\bar{\boldsymbol{q}}$ of Piola type are introduced as the derivatives of $\mathscr{U}_t$ with respect to their energetically conjugate kinematic variables (compare Fig. 3.7),

$$\boldsymbol{B}_t := -\partial_{\boldsymbol{\Phi}} \mathscr{U}_t \,, \qquad \boldsymbol{p} := \mathrm{d}_f \mathscr{U}_t \,, \qquad \bar{\boldsymbol{p}} := \mathrm{d}_{\bar{f}} \mathscr{U}_t \,, \qquad \bar{\boldsymbol{q}} := \mathrm{d}_{\bar{g}} \mathscr{U}_t \,, \tag{3.25}$$

due to the underlying assumption of a hyperelastic material. The evaluation of the energy-release condition (3.24) directly results in the weak form of the material-motion balance of momentum:

$$\int_{\mathscr{B}_t} \boldsymbol{p} : \delta \boldsymbol{f} + \bar{\boldsymbol{p}} : \delta \bar{\boldsymbol{f}} + \bar{\boldsymbol{q}} :\cdot \delta \bar{\boldsymbol{g}} - \boldsymbol{B}_t \cdot \delta \boldsymbol{\Phi} \, \mathrm{d}v =: \int_{\partial \mathscr{B}_t} \boldsymbol{T}_t \cdot \delta \boldsymbol{\Phi} + \bar{\boldsymbol{T}}_t : \delta \bar{\boldsymbol{f}} \, \mathrm{d}a \,. \tag{3.26}$$

This may again be locally expressed as the Euler–Lagrange equations

$$\operatorname{div} \boldsymbol{p} + \boldsymbol{B}_t = \boldsymbol{0} \,, \qquad \operatorname{div} \bar{\boldsymbol{q}} - \bar{\boldsymbol{p}} = \boldsymbol{0} \,, \tag{3.27}$$

i. e. the balance of macro- and micro-momentum in $\mathscr{B}_t$, which must be accompanied by the *non-homogeneous* Neumann boundary conditions

$$\boldsymbol{p} \cdot \boldsymbol{n} =: \boldsymbol{T}_t \quad \text{on } \partial \mathscr{B}_t^p \qquad\qquad \bar{\boldsymbol{q}} \cdot \boldsymbol{n} =: \bar{\boldsymbol{T}}_t \quad \text{on } \partial \mathscr{B}_t^{\bar{q}} \,, \tag{3.28}$$

since any change in the material geometry at fixed spatial configuration directly yields non-zero material boundary tractions.

Piola transform of the balance of momentum. In an analogous manner to Section 3.2.1, for the material-motion problem the transition from the two-point description of the balance relations (3.27) to a purely material description can be achieved by applying the Piola transformation formulae

$$\{\bullet\} \to J\{\bullet\} \cdot \boldsymbol{f}^{\mathrm{t}} \,, \qquad\qquad \{\bullet\} \to J\{\bullet\} \cdot \bar{\boldsymbol{f}}^{\mathrm{t}} \,, \tag{3.29}$$

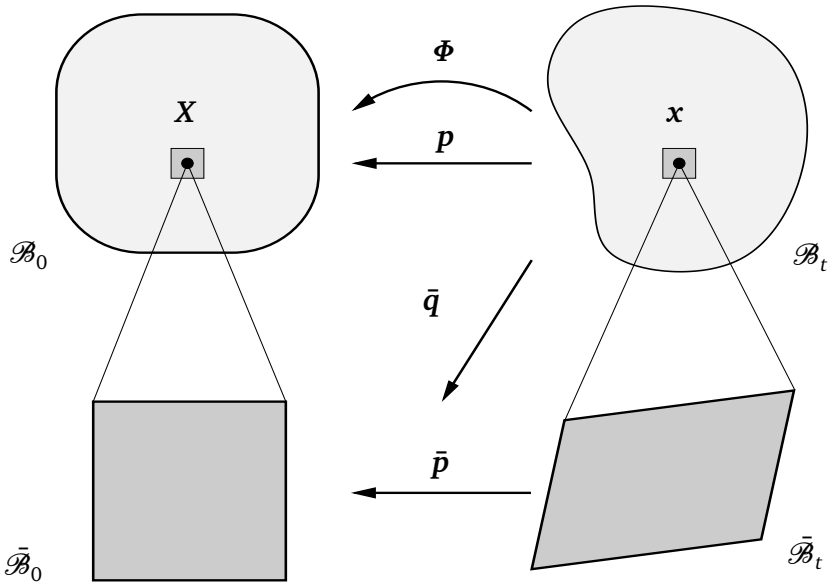

Figure 3.7: Material-motion problem: Piola-type stress measures, $\tau = 0, t$

which are here stated inversely to (3.16). With these at hand, we first obtain the divergence relations and the body force,

$$J \operatorname{div} \boldsymbol{p} = \operatorname{Div}(J\boldsymbol{p} \cdot \boldsymbol{f}^{\mathrm{t}}), \qquad J \operatorname{div} \bar{\boldsymbol{q}} = \operatorname{Div}(J\bar{\boldsymbol{q}} \cdot \boldsymbol{f}^{\mathrm{t}}), \qquad J\boldsymbol{B}_t = \boldsymbol{B}_0, \tag{3.30}$$

which finally yield the balance-of-momentum equations in $\mathscr{B}_t$ in the form

$$\operatorname{Div} \boldsymbol{\Sigma} + \boldsymbol{B}_0 = \boldsymbol{0}, \qquad \operatorname{Div} \bar{\boldsymbol{\tau}} - \bar{\boldsymbol{\Sigma}} = \boldsymbol{0} \tag{3.31}$$

in terms of the Eshelby-type stress measures, i. e. the macro stress $\boldsymbol{\Sigma}$, the micro stress $\bar{\boldsymbol{\Sigma}}$, and the double stress $\bar{\boldsymbol{\tau}}$ as shown in Fig. 3.8. The denomination of these tensors as Eshelby-type stress tensors goes back to purely material Eshelby tensor introduced by Eshelby (1975) for a classical continuum. Along the derivation of (3.31), the relations

$$\boldsymbol{\Sigma} := J\boldsymbol{p} \cdot \boldsymbol{f}^{\mathrm{t}}, \qquad \bar{\boldsymbol{\Sigma}} := J[\bar{\boldsymbol{p}} \cdot \bar{\boldsymbol{f}}^{\mathrm{t}} + \bar{\boldsymbol{q}} \overset{2,3}{\cdot\cdot} \bar{\boldsymbol{g}}], \qquad \bar{\boldsymbol{\tau}} := J\bar{\boldsymbol{q}} : [\bar{\boldsymbol{f}}^{\mathrm{t}} \overline{\otimes} \boldsymbol{f}^{\mathrm{t}}] \tag{3.32}$$

between the Eshelby-type material stress measures on the one hand, and the two-point stress measures of Piola type on the other hand, become obvious.

Material isotropy. In the special case of material isotropy, i. e. the isotropy of the material response, the energy density $\mathscr{U}_t$ for the material-motion problem is invariant under a rigid-body rotation with any proper orthogonal tensor $\boldsymbol{r}$ superposed to

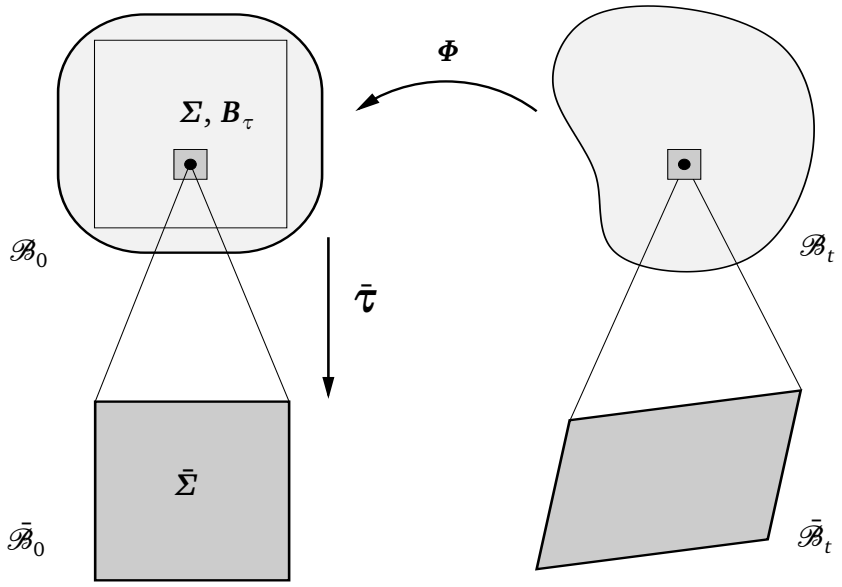

Figure 3.8: Material-motion problem: Eshelby-type stress measures, $\tau = 0, t$

the material configuration,

$$\mathscr{U}_t = \mathscr{U}_t(\boldsymbol{f}, \bar{\boldsymbol{f}}, \bar{\boldsymbol{g}}, \bullet) \doteq \mathscr{U}_t(\boldsymbol{r} \cdot \boldsymbol{f}, \boldsymbol{r} \cdot \bar{\boldsymbol{f}}, \boldsymbol{r} \cdot \bar{\boldsymbol{g}}, \bullet) \qquad \forall \qquad \boldsymbol{r} \in \mathrm{SO}(3)\,. \tag{3.33}$$

Exploiting this condition, we conclude that the sum $\boldsymbol{\Sigma} + \bar{\boldsymbol{\Sigma}}$ is symmetric, i. e. $[\boldsymbol{\Sigma} + \bar{\boldsymbol{\Sigma}}] = [\boldsymbol{\Sigma} + \bar{\boldsymbol{\Sigma}}]^{\mathrm{t}}$.

3.2.3 Relations between spatial and material motion

In order to highlight the duality of the spatial- and the material-motion problem, conversions between the spatial- and the material-motion-problem quantities are derived in the sequel.

Deformation maps and deformation gradients. As illustrated in Figure 3.9, the macro deformation map of the spatial-motion problem, $\boldsymbol{\varphi}$, introduced in (3.6) and that of the material-motion problem, $\boldsymbol{\Phi}$, of (3.21) are inverse to each other, thus their compositions $\boldsymbol{\varphi} \circ \boldsymbol{\Phi} = \boldsymbol{id}$ and $\boldsymbol{\Phi} \circ \boldsymbol{\varphi} = \boldsymbol{id}$ yield the identity. Likewise, the macro-deformation gradient of the spatial- and that of the material-motion problem are related through $\boldsymbol{F} \cdot \boldsymbol{f} = \boldsymbol{I}_t$ and $\boldsymbol{f} \cdot \boldsymbol{F} = \boldsymbol{I}_0$ vice versa, while analogously the micro deformation maps compose as $\bar{\boldsymbol{F}} \cdot \bar{\boldsymbol{f}} = \bar{\boldsymbol{I}}_t$ and $\bar{\boldsymbol{f}} \cdot \bar{\boldsymbol{F}} = \bar{\boldsymbol{I}}_0$, respectively. Furthermore the Jacobians of the spatial- and the material-motion problem are related as $j J = 1$. With these relations at hand the following expressions for the kinematic variables of the spatial-motion problem in terms of those from the material-motion problem are

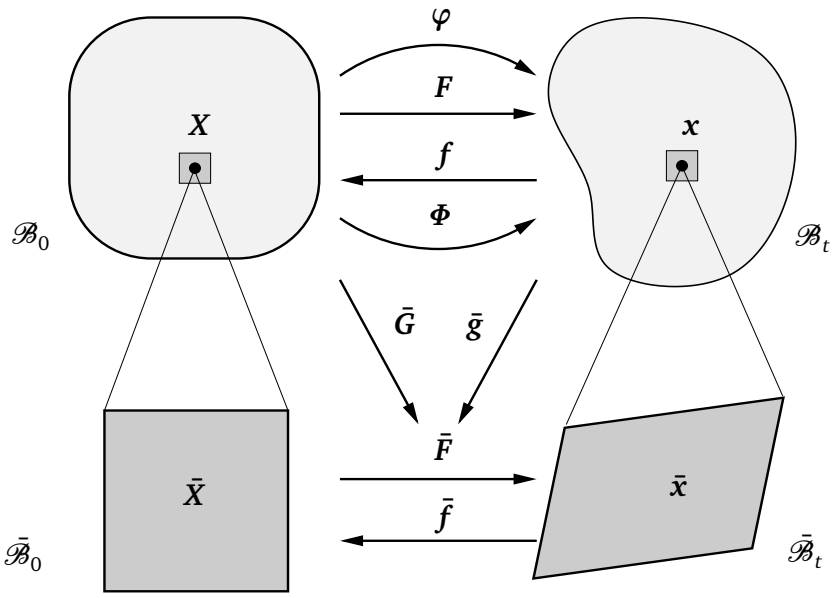

Figure 3.9: Spatial- vs. material-motion problem: deformation measures

obtained for the macro- and the microcontinuum quantities, respectively:

$$\boldsymbol{\varphi} = \boldsymbol{\Phi}^{-1}, \qquad \boldsymbol{F} = \boldsymbol{f}^{-1}, \qquad \bar{\boldsymbol{F}} = \bar{\boldsymbol{f}}^{-1}, \qquad \bar{\boldsymbol{G}} = -\bar{\boldsymbol{F}} \cdot \bar{\boldsymbol{g}} : [\bar{\boldsymbol{F}} \,\overline{\otimes}\, \boldsymbol{F}]\,. \tag{3.34}$$

Vice versa, the conversions from the spatial- to the material-motion problem obey

$$\boldsymbol{\Phi} = \boldsymbol{\varphi}^{-1}, \qquad \boldsymbol{f} = \boldsymbol{F}^{-1}, \qquad \bar{\boldsymbol{f}} = \bar{\boldsymbol{F}}^{-1}, \qquad \bar{\boldsymbol{g}} = -\bar{\boldsymbol{f}} \cdot \bar{\boldsymbol{G}} : [\bar{\boldsymbol{f}} \,\overline{\otimes}\, \boldsymbol{f}] \tag{3.35}$$

for the macro- and the microcontinuum quantities, respectively.

Energy density. In the previous derivations, the stored-energy densities $\mathscr{U}_0$ and $\mathscr{U}_t$ were assigned to a particular perspective on the deformation. With the relations (3.34) and (3.35), we may however express these in terms of kinematic quantities either from the spatial- or from the material-motion problem. Particularly, for the stored-energy density, which is related to a material unit volume, the relation

$$\mathscr{U}_0(\boldsymbol{F}, \bar{\boldsymbol{F}}, \bar{\boldsymbol{G}}) = \mathscr{U}_0(\boldsymbol{f}, \bar{\boldsymbol{f}}, \bar{\boldsymbol{g}}(\bar{\boldsymbol{G}}, \bar{\boldsymbol{f}}, \boldsymbol{f})) \tag{3.36}$$

holds. Analogously, we can transform the total stored-energy density in the spatial configuration which is usually expressed in terms of material-motion quantities as follows:

$$\mathscr{U}_t(\boldsymbol{f}, \bar{\boldsymbol{f}}, \bar{\boldsymbol{g}}) = \mathscr{U}_t(\boldsymbol{F}, \bar{\boldsymbol{F}}, \bar{\boldsymbol{G}}(\bar{\boldsymbol{g}}, \bar{\boldsymbol{F}}, \boldsymbol{F}))\,. \tag{3.37}$$

Furthermore the transformations between the stored-energy density of the spatial and the material configuration, respectively, read

$$\mathscr{U}_0 = J\,\mathscr{U}_t \qquad \text{and} \qquad \mathscr{U}_t = j\,\mathscr{U}_0\,. \tag{3.38}$$

The relations of the partial derivative of the energy density with respect to a deformation measure at fixed material position to derivatives at fixed spatial position are computed as follows:

$$\begin{aligned}
\mathrm{D}_f\mathscr{U}_0 &= \mathrm{d}_f\mathscr{U}_0 : \partial_f\boldsymbol{f} + \mathrm{d}_{\bar f}\mathscr{U}_0 : \partial_f\bar{\boldsymbol{f}} + \mathrm{d}_{\bar g}\mathscr{U}_0 \mathbin{:\cdot} \partial_f\bar{\boldsymbol{g}} &&= \mathrm{d}_f\mathscr{U}_0 + \mathrm{d}_{\bar g}\mathscr{U}_0 \mathbin{:\cdot} \partial_f\bar{\boldsymbol{g}}\,,\\
\mathrm{D}_{\bar f}\mathscr{U}_0 &= \mathrm{d}_f\mathscr{U}_0 : \partial_{\bar f}\boldsymbol{f} + \mathrm{d}_{\bar f}\mathscr{U}_0 : \partial_{\bar f}\bar{\boldsymbol{f}} + \mathrm{d}_{\bar g}\mathscr{U}_0 \mathbin{:\cdot} \partial_{\bar f}\bar{\boldsymbol{g}} &&= \mathrm{d}_{\bar f}\mathscr{U}_0 + \mathrm{d}_{\bar g}\mathscr{U}_0 \mathbin{:\cdot} \partial_{\bar f}\bar{\boldsymbol{g}}\,,\\
\mathrm{D}_{\bar g}\mathscr{U}_0 &= \mathrm{d}_f\mathscr{U}_0 : \partial_{\bar g}\boldsymbol{f} + \mathrm{d}_{\bar f}\mathscr{U}_0 : \partial_{\bar g}\bar{\boldsymbol{f}} + \mathrm{d}_{\bar g}\mathscr{U}_0 \mathbin{:\cdot} \partial_{\bar g}\bar{\boldsymbol{g}} &&= \mathrm{d}_{\bar g}\mathscr{U}_0\,,
\end{aligned} \tag{3.39}$$

while the reverse relations are obtained analogously as

$$\begin{aligned}
\mathrm{d}_F\mathscr{U}_t &= \mathrm{D}_F\mathscr{U}_t + \mathrm{D}_{\bar G}\mathscr{U}_t \mathbin{:\cdot} \partial_F\bar{\boldsymbol{G}}\,,\\
\mathrm{d}_{\bar F}\mathscr{U}_t &= \mathrm{D}_{\bar F}\mathscr{U}_t + \mathrm{D}_{\bar G}\mathscr{U}_t \mathbin{:\cdot} \partial_{\bar F}\bar{\boldsymbol{G}}\,.\\
\mathrm{d}_{\bar G}\mathscr{U}_t &= \mathrm{D}_{\bar G}\mathscr{U}_t\,.
\end{aligned} \tag{3.40}$$

These are in the following utilized to relate the spatial- and material-motion-problem stresses to each other.

Push forward of the stress measures from the spatial-motion problem. The Piola-type stresses $\boldsymbol{P} = \mathrm{D}_F\mathscr{U}_0$, $\bar{\boldsymbol{P}} = \mathrm{D}_{\bar F}\mathscr{U}_0$, and $\bar{\boldsymbol{Q}} = \mathrm{D}_{\bar G}\mathscr{U}_0$ in Eq. (3.9) of the spatial-motion problem enjoy the following relations

$$\begin{aligned}
\mathrm{D}_F\mathscr{U}_0 &= && = \mathrm{D}_f\mathscr{U}_0 : [-\boldsymbol{f}\,\overline{\otimes}\,\boldsymbol{f}^{\mathrm{t}}] && = -\boldsymbol{f}^{\mathrm{t}}\cdot\mathrm{D}_f\mathscr{U}_0\cdot\boldsymbol{f}^{\mathrm{t}},\\
\mathrm{D}_{\bar F}\mathscr{U}_0 &= \mathrm{D}_{\bar f}\mathscr{U}_0 : \partial_{\bar F}\bar{\boldsymbol{f}} && = \mathrm{D}_{\bar f}\mathscr{U}_0 : [-\bar{\boldsymbol{f}}\,\overline{\otimes}\,\bar{\boldsymbol{f}}^{\mathrm{t}}] && = -\bar{\boldsymbol{f}}^{\mathrm{t}}\cdot\mathrm{D}_{\bar f}\mathscr{U}_0\cdot\bar{\boldsymbol{f}}^{\mathrm{t}},\\
\mathrm{D}_{\bar G}\mathscr{U}_0 &= \mathrm{D}_{\bar g}\mathscr{U}_0 \mathbin{:\cdot} \partial_{\bar G}\bar{\boldsymbol{g}} && = \mathrm{D}_{\bar g}\mathscr{U}_0 \mathbin{:\cdot} [-\bar{\boldsymbol{f}}\,\underline{\otimes}\,[\bar{\boldsymbol{f}}^{\mathrm{t}}\,\overline{\otimes}\,\boldsymbol{f}^{\mathrm{t}}]] && = -\bar{\boldsymbol{f}}^{\mathrm{t}}\cdot\mathrm{D}_{\bar g}\mathscr{U}_0 : [\bar{\boldsymbol{f}}^{\mathrm{t}}\,\overline{\otimes}\,\boldsymbol{f}^{\mathrm{t}}],
\end{aligned} \tag{3.41}$$

based on the relations (3.34). This fact may be exploited under consideration of the energy-density relations (3.36) and (3.39) as well as the Piola transform (3.16). Thus we obtain the relations

$$\begin{aligned}
j\mathrm{D}_F\mathscr{U}_0\cdot\boldsymbol{F}^{\mathrm{t}} &= -j\boldsymbol{f}^{\mathrm{t}}\cdot\mathrm{D}_f\mathscr{U}_0 = -j\boldsymbol{f}^{\mathrm{t}}\cdot[\mathrm{d}_f\mathscr{U}_0 + \mathrm{d}_{\bar g}\mathscr{U}_0 \mathbin{:\cdot} \partial_f\bar{\boldsymbol{g}}]\,,\\
j\mathrm{D}_{\bar F}\mathscr{U}_0\cdot\bar{\boldsymbol{F}}^{\mathrm{t}} &= -j\bar{\boldsymbol{f}}^{\mathrm{t}}\cdot\mathrm{D}_{\bar f}\mathscr{U}_0 = -j\bar{\boldsymbol{f}}^{\mathrm{t}}\cdot[\mathrm{d}_{\bar f}\mathscr{U}_0 + \mathrm{d}_{\bar g}\mathscr{U}_0 \mathbin{:\cdot} \partial_{\bar f}\bar{\boldsymbol{g}}]\,,\\
j\mathrm{D}_{\bar G}\mathscr{U}_0 : [\bar{\boldsymbol{F}}^{\mathrm{t}}\,\overline{\otimes}\,\boldsymbol{F}^{\mathrm{t}}] &= -j\bar{\boldsymbol{f}}^{\mathrm{t}}\cdot\mathrm{D}_{\bar g}\mathscr{U}_0 = -\bar{\boldsymbol{f}}^{\mathrm{t}}\cdot\mathrm{d}_{\bar g}\mathscr{U}_t\,.
\end{aligned} \tag{3.42}$$

With these, the Cauchy-type spatial stress measures from the spatial-motion problem (3.18) expressed in terms of the Piola-type stress measures of the material-

motion problem (3.25) read

$$\begin{aligned}\boldsymbol{\sigma} &= \mathscr{U}_t \boldsymbol{I} - \boldsymbol{f}^{\mathrm{t}} \cdot \boldsymbol{p} - \bar{\boldsymbol{g}} \overset{1,2}{\vdots} \bar{\boldsymbol{q}}\,,\\ \bar{\boldsymbol{\sigma}} &= -\bar{\boldsymbol{f}}^{\mathrm{t}} \cdot \bar{\boldsymbol{p}} - \bar{\boldsymbol{g}} \overset{1,3}{\vdots} \bar{\boldsymbol{q}}\,,\\ \bar{\boldsymbol{\tau}} &= -\bar{\boldsymbol{f}}^{\mathrm{t}} \cdot \bar{\boldsymbol{q}}\,.\end{aligned} \tag{3.43}$$

Pull back of the stress measures from the material-motion problem. In analogy to the previous paragraph, a pull back of the stress formats obtained in the material-motion problem can be executed. Using the relations (3.34), we may write

$$\begin{aligned}\mathrm{d}_f \mathscr{U}_t &= \mathrm{d}_F \mathscr{U}_t : \partial_f \boldsymbol{F} &&= -\boldsymbol{F}^{\mathrm{t}} \cdot \mathrm{d}_F \mathscr{U}_t \cdot \boldsymbol{F}^{\mathrm{t}},\\ \mathrm{d}_{\bar{f}} \mathscr{U}_t &= \mathrm{d}_{\bar{F}} \mathscr{U}_t : \partial_{\bar{f}} \bar{\boldsymbol{F}} &&= -\bar{\boldsymbol{F}}^{\mathrm{t}} \cdot \mathrm{d}_{\bar{F}} \mathscr{U}_t \cdot \bar{\boldsymbol{F}}^{\mathrm{t}},\\ \mathrm{d}_{\bar{g}} \mathscr{U}_t &= \mathrm{d}_{\bar{G}} \mathscr{U}_t \mathbin{:\cdot} \partial_{\bar{g}} \bar{\boldsymbol{G}} &&= -\bar{\boldsymbol{F}}^{\mathrm{t}} \cdot \mathrm{d}_{\bar{G}} \mathscr{U}_t : [\bar{\boldsymbol{F}}^{\mathrm{t}} \overline{\otimes} \boldsymbol{F}^{\mathrm{t}}]\end{aligned} \tag{3.44}$$

for the Piola-type stress quantities $\boldsymbol{p}$, $\bar{\boldsymbol{p}}$, and $\bar{\boldsymbol{q}}$ of (3.25). Furthermore, we obtain the relations

$$\begin{aligned}J \mathrm{d}_f \mathscr{U}_t \cdot \boldsymbol{f}^{\mathrm{t}} &= -J \boldsymbol{F}^{\mathrm{t}} \cdot \mathrm{d}_F \mathscr{U}_t &&= -J \boldsymbol{F}^{\mathrm{t}} \cdot [\mathrm{D}_F \mathscr{U}_t + \mathrm{D}_{\bar{G}} \mathscr{U}_t \mathbin{:\cdot} \partial_F \bar{\boldsymbol{G}}]\,,\\ J \mathrm{d}_{\bar{f}} \mathscr{U}_t \cdot \bar{\boldsymbol{f}}^{\mathrm{t}} &= -J \bar{\boldsymbol{F}}^{\mathrm{t}} \cdot \mathrm{d}_{\bar{F}} \mathscr{U}_t &&= -J \bar{\boldsymbol{F}}^{\mathrm{t}} \cdot [\mathrm{D}_{\bar{F}} \mathscr{U}_t + \mathrm{D}_{\bar{G}} \mathscr{U}_t \mathbin{:\cdot} \partial_{\bar{F}} \bar{\boldsymbol{G}}]\,,\\ J \mathrm{d}_{\bar{g}} \mathscr{U}_t : [\bar{\boldsymbol{f}}^{\mathrm{t}} \overline{\otimes} \boldsymbol{f}^{\mathrm{t}}] &= -J \bar{\boldsymbol{F}}^{\mathrm{t}} \cdot \mathrm{D}_{\bar{G}} \mathscr{U}_t\,,\end{aligned} \tag{3.45}$$

now departing from Eqs. (3.29), (3.38) and (3.40). Finally we end up with the material stress measures of Eshelby type from the material-motion problem, which particularly read

$$\begin{aligned}\boldsymbol{\Sigma} &= \mathscr{U}_0 \boldsymbol{I} - \boldsymbol{F}^{\mathrm{t}} \cdot \boldsymbol{P} - \bar{\boldsymbol{G}} \overset{1,2}{\vdots} \bar{\boldsymbol{Q}}\,,\\ \bar{\boldsymbol{\Sigma}} &= -\bar{\boldsymbol{F}}^{\mathrm{t}} \cdot \bar{\boldsymbol{P}} - \bar{\boldsymbol{G}} \overset{1,3}{\vdots} \bar{\boldsymbol{Q}}\,,\\ \bar{\boldsymbol{\tau}} &= -\bar{\boldsymbol{F}}^{\mathrm{t}} \cdot \bar{\boldsymbol{Q}}\end{aligned} \tag{3.46}$$

in terms of the Piola-type stress measures of the spatial-motion problem (3.9).

Push forward and pull back of the balance relations. The relations for the balance of momentum were originally derived in terms of stresses in two-point descriptions for both the spatial- and the material-motion problem, confer Sections 3.2.1 and 3.2.2. In both cases, Piola-transformation procedures were applied in order to obtain the respective purely spatial or purely material stress format and balance relations expressed in terms of these. Alternatively to this approach, one may also proceed directly from the two-point formulation of the spatial-motion problem, Section 3.2.1, to a fully material description in terms of Eshelby-type stresses by a

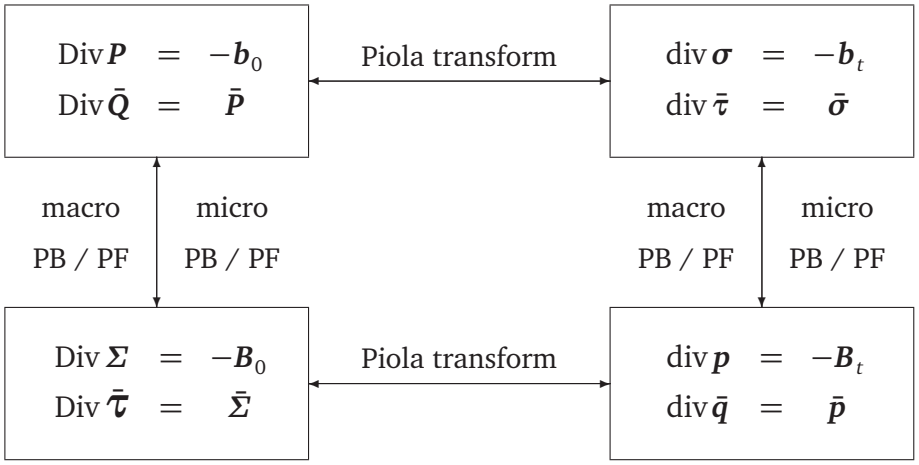

Figure 3.10: Micromorphic balance-of-momentum tetragon

pull-back operation, or analogously from the two-point formulation of the material-motion problem, Section 3.2.2, to a purely spatial description in terms of Cauchy-type stresses by a push-forward procedure.

Particularly, in order to move from the two-point description of the spatial-motion problem (3.11) to the purely material Eshelby-type description, the pull-back operations

$$\begin{aligned} -\boldsymbol{F}^{\mathrm{t}}\cdot[\operatorname{Div}\boldsymbol{P}+\boldsymbol{b}_0] \;-\; \bar{\boldsymbol{G}} \overset{1,2}{:} [\operatorname{Div}\bar{\boldsymbol{Q}}-\bar{\boldsymbol{P}}] &= \operatorname{Div}\boldsymbol{\Sigma}+\boldsymbol{B}_0 = \boldsymbol{0}, \\ -\bar{\boldsymbol{F}}^{\mathrm{t}}\cdot[\operatorname{Div}\bar{\boldsymbol{Q}}-\bar{\boldsymbol{P}}] &= \operatorname{Div}\bar{\boldsymbol{\tau}}-\bar{\boldsymbol{\Sigma}} = \boldsymbol{0}, \end{aligned} \tag{3.47}$$

are applied to the macro- and the micro-term of the balance relations and we directly obtain the expressions (3.31).
Analogously, the following push forward operates on the material-motion-problem balances (3.27) and yields the purely spatial description of the balance of momentum

$$\begin{aligned} -\boldsymbol{f}^{\mathrm{t}}\cdot[\operatorname{div}\boldsymbol{p}+\boldsymbol{B}_t] \;-\; \bar{\boldsymbol{g}} \overset{1,2}{:} [\operatorname{div}\bar{\boldsymbol{q}}-\bar{\boldsymbol{p}}] &= \operatorname{div}\boldsymbol{\sigma}+\boldsymbol{b}_t = \boldsymbol{0}, \\ -\bar{\boldsymbol{f}}^{\mathrm{t}}\cdot[\operatorname{div}\bar{\boldsymbol{q}}-\bar{\boldsymbol{p}}] &= \operatorname{div}\bar{\boldsymbol{\tau}}-\bar{\boldsymbol{\sigma}} = \boldsymbol{0}, \end{aligned} \tag{3.48}$$

in terms of stresses of Cauchy type as we also find it in equation (3.17).

Overall picture: Balance-of-momentum tetragon. For the micromorphic continuum, the balance relations as derived for the spatial- and the material-motion problem in purely material respectively spatial quantities as well as in the respective two-point descriptions, may be summarized in a transformation scheme as shown in Figure 3.10 where the elements of the balance relations are transformed either with direct pull back (PB) or push-forward (PF) operations or via Piola transforma-

tions. This extends the similar representation for a classical continuum proposed by Maugin (1993).

3.3 Constitutive relations

In order to close the set of equations, a straightforward hyperelastic constitutive theory is chosen. Since the macro- and the micro-continuum behave kinematically independently, a constitutive formulation must be chosen to provide a relation between the scales. Thus in a straightforward manner, we introduce a scale-transition term into the constitutive formulation. This formulation is first proposed for the spatial-motion problem and later transferred to the material-motion problem. The according stress measures are derived from this assumption for both perspectives and the symmetries imposed by spatial and material isotropy are shown.

3.3.1 Spatial-motion problem

Constitutive assumption for the stored-energy density. For the internally stored-energy density $\mathscr{W}_0$ we suggest a hyperelastic constitutive ansatz,

$$\mathscr{W}_0(\boldsymbol{\varphi}, \bar{\boldsymbol{F}}) = \mathscr{W}_0^{\mathrm{mac}} + \mathscr{W}_0^{\mathrm{mic}} + \mathscr{W}_0^{\mathrm{scale}}, \tag{3.49}$$

which consists of a Neo-Hooke-type term $\mathscr{W}_0^{\mathrm{mac}}$ on the macro scale, a straightforward quadratic formulation on the micro scale, $\mathscr{W}_0^{\mathrm{mic}}$, and an additional scale-transition term $\mathscr{W}_0^{\mathrm{scale}}$ to couple both scales:

$$\begin{aligned} \mathscr{W}_0^{\mathrm{mac}}(\boldsymbol{\varphi}) &= \tfrac{1}{2}\,\lambda \ln^2 J + \tfrac{1}{2}\,\mu\,[\boldsymbol{F} : \boldsymbol{F} - n^{\mathrm{dim}} - 2\ln J]\,, \\ \mathscr{W}_0^{\mathrm{mic}}(\bar{\boldsymbol{F}}) &= \tfrac{1}{2}\,\mu\, l^2\, \bar{\boldsymbol{G}} \cdot\cdot \bar{\boldsymbol{G}}\,, \\ \mathscr{W}_0^{\mathrm{scale}}(\boldsymbol{\varphi}, \bar{\boldsymbol{F}}) &= \tfrac{1}{2}\,p\,[\bar{\boldsymbol{F}} - \boldsymbol{F}] : [\bar{\boldsymbol{F}} - \boldsymbol{F}]\,. \end{aligned} \tag{3.50}$$

Herein the material parameters λ and μ are the Lamé constants known from the classical or rather Boltzmann continuum. Additionally the so-called internal length l accounts for the size dependence and may be interpreted as a characteristic size of the microcontinuum. The parameter p plays the part of a penalty parameter that controls the interaction between the macro- and the micro-deformation. Furthermore n^{dim} denotes the number of dimensions in space. With the internal-stored-energy density formulation, Eqs. (3.49), the different stress fields may be evaluated, utilising the definitions (3.9) and the relations (3.18).

Remark 3.3.1 (Choice of the constitutive formulation) *Note that the present choice for the stored-energy density function $\mathscr{W}_0$ is a rather straightforward assumption. Of course, different formulations with more complex relations could*

be used and can be considered as a challenge for future research. An alternative formulation is examined in Appendix B.

Spatial-motion stresses. With the constitutive formulation (3.49) the Piola-type stresses (3.9) particularly result in

$$\begin{aligned} \boldsymbol{P} &= \mathrm{D}_{\boldsymbol{F}}\mathscr{W}_0 = [\lambda \ln J - \mu]\boldsymbol{F}^{-\mathrm{t}} + \mu\boldsymbol{F} - p[\bar{\boldsymbol{F}} - \boldsymbol{F}]\,, \\ \bar{\boldsymbol{P}} &= \mathrm{D}_{\bar{\boldsymbol{F}}}\mathscr{W}_0 = p[\bar{\boldsymbol{F}} - \boldsymbol{F}]\,, \\ \bar{\boldsymbol{Q}} &= \mathrm{D}_{\bar{\boldsymbol{G}}}\mathscr{W}_0 = \mu l^2 \bar{\boldsymbol{G}}\,. \end{aligned} \tag{3.51}$$

Furthermore, we evaluate the Cauchy-type stresses as

$$\begin{aligned} \boldsymbol{\sigma} &= j[[\lambda \ln J - \mu]\boldsymbol{F}^{-\mathrm{t}} + \mu\boldsymbol{F} - p[\bar{\boldsymbol{F}} - \boldsymbol{F}]] \cdot \boldsymbol{F}^{\mathrm{t}}\,, \\ \bar{\boldsymbol{\sigma}} &= jp[\bar{\boldsymbol{F}} - \boldsymbol{F}] \cdot \bar{\boldsymbol{F}}^{\mathrm{t}} + j\mu l^2 \bar{\boldsymbol{G}} \overset{2,3}{\vdots} \bar{\boldsymbol{G}}\,, \\ \bar{\boldsymbol{\tau}} &= j\mu l^2 \bar{\boldsymbol{G}} : [\bar{\boldsymbol{F}}^{\mathrm{t}} \overline{\otimes} \boldsymbol{F}^{\mathrm{t}}] \end{aligned} \tag{3.52}$$

based on (3.18). Due to the scale-transition term $(3.50)_3$, both the Cauchy-type macro and the micro stress will generally be nonsymmetric, with the degree of symmetry depending on the choice of the penalty parameter. As indicated before, in the case of spatial isotropy, however, the sum $\boldsymbol{\sigma} + \bar{\boldsymbol{\sigma}}$ is always symmetric.

Remark 3.3.2 (Relation to the gradient continuum) *For a very small scale-transition parameter, i. e. $p \to 0$, the macro and the micro stress, $\boldsymbol{P}$ and $\bar{\boldsymbol{P}}$ respectively, will be decoupled.*

Contrary, the limit case of $p \to \infty$ constrains the micromorphic deformation such that the micro deformation map equals the macro-deformation gradient, $\bar{\boldsymbol{F}} \equiv \boldsymbol{F}$, and consequently the gradient becomes $\bar{\boldsymbol{G}} \equiv \nabla_X \boldsymbol{F}$. Thus the behaviour of a second-order gradient continuum is approached. This coincides with the observation of Kirchner and Steinmann (2005) who showed that this limit consideration transfers the micromorphic continuum to a second-order gradient continuum.

Similar constitutive constraints on the kinematics as the one we have chosen were also used by Shu et al. (1999) as well as by Kouznetsova et al. (2002, 2004) for higher-order gradient theories. In their case they yield the major advantage of enabling C^0 approximation functions in the numerical implementation, since they reversely approach a micromorphic continuum.

3.3.2 Material-motion problem

Stored-energy density. Upon the assumption of zero external bulk potential, i. e. $\mathscr{V}_0 = 0$, which comes along with zero spatial body force, we may directly transfer the relation (3.38) of the total stored-energy density to the internal part, i. e. $\mathscr{W}_t = j\mathscr{W}_0$.

Material-motion stresses. For the application of the material-force method, the stresses of the material-motion problem need to be evaluated. From (3.25) with $\mathscr{U}_t \equiv \mathscr{W}_t$ and (3.49) we obtain the Piola-type stresses of the material-motion problem

$$\begin{aligned}
\boldsymbol{p} &= j[[\mathscr{W}_0 - \lambda \ln J + \mu]\boldsymbol{I} - \mu \boldsymbol{F}^{\mathrm{t}} \cdot \boldsymbol{F} + p\boldsymbol{F}^{\mathrm{t}} \cdot [\bar{\boldsymbol{F}} - \boldsymbol{F}] - \mu l^2 \bar{\boldsymbol{G}} \overset{1,2}{\vdots} \bar{\boldsymbol{G}}] \cdot \boldsymbol{F}^{\mathrm{t}} \\
\bar{\boldsymbol{p}} &= -jp\bar{\boldsymbol{F}}^{\mathrm{t}} \cdot [\bar{\boldsymbol{F}} - \boldsymbol{F}] \cdot \bar{\boldsymbol{F}}^{\mathrm{t}} \\
\bar{\boldsymbol{q}} &= -j\mu l^2 \bar{\boldsymbol{F}}^{\mathrm{t}} \cdot \bar{\boldsymbol{G}} : \bar{\boldsymbol{F}}^{\mathrm{t}} \overline{\otimes} \boldsymbol{F}^{\mathrm{t}},
\end{aligned} \tag{3.53}$$

from which the Eshelby-type stresses are evaluated as

$$\begin{aligned}
\boldsymbol{\Sigma} &= [\mathscr{W}_0 - \lambda \ln J + \mu]\boldsymbol{I} - \mu \boldsymbol{F}^{\mathrm{t}} \cdot \boldsymbol{F} + p\boldsymbol{F}^{\mathrm{t}} \cdot [\bar{\boldsymbol{F}} - \boldsymbol{F}] - \mu l^2 \bar{\boldsymbol{G}} \overset{1,2}{\vdots} \bar{\boldsymbol{G}}, \\
\bar{\boldsymbol{\Sigma}} &= -p\bar{\boldsymbol{F}}^{\mathrm{t}} \cdot [\bar{\boldsymbol{F}} - \boldsymbol{F}] - \mu l^2 \bar{\boldsymbol{G}} \overset{1,3}{\vdots} \bar{\boldsymbol{G}}, \\
\bar{\boldsymbol{\tau}} &= -\mu l^2 \bar{\boldsymbol{F}}^{\mathrm{t}} \cdot \bar{\boldsymbol{G}}
\end{aligned} \tag{3.54}$$

utilising (3.32).

For this particular choice of stresses, the symmetry of the sum of the Eshelby-type macro and the micro stress, $\boldsymbol{\Sigma} + \bar{\boldsymbol{\Sigma}}$, resulting from material isotropy as stated in Eq. (3.33) can be shown. Observing

$$\begin{aligned}
\boldsymbol{\Sigma} + \bar{\boldsymbol{\Sigma}} = {} & [\mathscr{W}_0 - \lambda \ln J + \mu]\boldsymbol{I} - \mu \boldsymbol{F}^{\mathrm{t}} \cdot \boldsymbol{F} + p\boldsymbol{F}^{\mathrm{t}} \cdot \bar{\boldsymbol{F}} - p\boldsymbol{F}^{\mathrm{t}} \cdot \boldsymbol{F} \\
& - p\bar{\boldsymbol{F}}^{\mathrm{t}} \cdot \bar{\boldsymbol{F}} + p\bar{\boldsymbol{F}}^{\mathrm{t}} \cdot \boldsymbol{F} - \mu l^2 [\bar{\boldsymbol{G}} \overset{1,2}{\vdots} \bar{\boldsymbol{G}}] - \mu l^2 [\bar{\boldsymbol{G}} \overset{1,3}{\vdots} \bar{\boldsymbol{G}}],
\end{aligned} \tag{3.55}$$

we notice that $\boldsymbol{\Sigma} + \bar{\boldsymbol{\Sigma}} = [\boldsymbol{\Sigma} + \bar{\boldsymbol{\Sigma}}]^{\mathrm{t}}$ and thus this symmetry is fulfilled.

3.4 Finite-element approximation

For the continuum theory presented in Section 3.2, a finite-element approximation scheme is derived in a general format, for which the constitutive formulation of Section 3.3 is incorporated. For the finite-element approximation we choose the macro and the micro deformation map, which constitute the set of state variables $\mathscr{S}$, as the unknown quantities to be solved for.

3.4.1 Spatial-motion problem

Approximations. The unknown fields of the deformation quantities are approximated using a standard Bubnov-Galerkin approach, which allows to use the same interpolation functions for the unknowns as well as for the test functions. Particularly, a finite-element mesh consists of n_φ nodes at which the macro deformation map $\boldsymbol{\varphi}$ is evaluated and $n_{\bar{F}}$ nodes for the unknown micro deformation map $\bar{\boldsymbol{F}}$. Within

the finite element their approximations are formulated with the element shape functions N_L^{φ} for the deformation and $N_M^{\bar{F}}$ for the micro deformation map, respectively as

$$\boldsymbol{\varphi}^h = \sum_{L=1}^{n_{\varphi}^{\mathrm{e}}} N_L^{\varphi} \boldsymbol{\varphi}_L \,, \qquad \delta\boldsymbol{\varphi}^h = \sum_{I=1}^{n_{\varphi}^{\mathrm{e}}} N_I^{\varphi} \delta\boldsymbol{\varphi}_I \,, \tag{3.56}$$

$$\bar{\boldsymbol{F}}^h = \sum_{M=1}^{n_{\bar{F}}^{\mathrm{e}}} N_M^{\bar{F}} \bar{\boldsymbol{F}}_M \,, \qquad \delta\bar{\boldsymbol{F}}^h = \sum_{J=1}^{n_{\bar{F}}^{\mathrm{e}}} N_J^{\bar{F}} \delta\bar{\boldsymbol{F}}_J \,. \tag{3.57}$$

Herein the nodal indices I and L account for the discrete values of the unknown $\boldsymbol{\varphi}$ and its variation, while J and M number the nodes for unknown $\bar{\boldsymbol{F}}$ and their variation, respectively. Accordingly, the discrete approximations for the gradient variables $\boldsymbol{F} = \nabla_{\boldsymbol{X}}\boldsymbol{\varphi}$ and $\bar{\boldsymbol{G}} = \nabla_{\boldsymbol{X}}\bar{\boldsymbol{F}}$ and their respective variations $\delta\boldsymbol{F} = \nabla_{\boldsymbol{X}}\delta\boldsymbol{\varphi}$ and $\delta\bar{\boldsymbol{G}} = \nabla_{\boldsymbol{X}}\delta\bar{\boldsymbol{F}}$ read

$$\boldsymbol{F}^h = \sum_{L=1}^{n_{\varphi}^{\mathrm{e}}} \boldsymbol{\varphi}_L \otimes \nabla_{\boldsymbol{X}} N_L^{\varphi} \,, \qquad \delta\boldsymbol{F}^h = \sum_{I=1}^{n_{\varphi}^{\mathrm{e}}} \delta\boldsymbol{\varphi}_I \otimes \nabla_{\boldsymbol{X}} N_I^{\varphi} \,, \tag{3.58}$$

$$\bar{\boldsymbol{G}}^h = \sum_{M=1}^{n_{\bar{F}}^{\mathrm{e}}} \bar{\boldsymbol{F}}_M \otimes \nabla_{\boldsymbol{X}} N_M^{\bar{F}} \,, \qquad \delta\bar{\boldsymbol{G}}^h = \sum_{J=1}^{n_{\bar{F}}^{\mathrm{e}}} \delta\bar{\boldsymbol{F}}_J \otimes \nabla_{\boldsymbol{X}} N_J^{\bar{F}} \,. \tag{3.59}$$

The constitutive assumption of Section 3.3, which incorporates the difference between the micro deformation map $\bar{\boldsymbol{F}}$ and the macro tangent map $\boldsymbol{F}$, necessitates the use of shape functions of different order in the finite-element approximation. Due to the comparison of macro tangent map and micro deformation map, the approximation for the macro deformation map must be of one order higher than their micro counterparts. A detailed reference for the suitability of different kinds of elements for such formulations can be found in Kouznetsova et al. (2002, 2004), see also Shu et al. (1999) and Amanatidou and Aravas (2002).

Residual and stiffness matrix. The discrete residual vector of the spatial-motion problem is composed of a contribution of the macro and another one of the micro degrees of freedom, $\mathsf{R} = [\mathsf{R}_I^{\varphi}, \mathsf{R}_J^{\bar{F}}]^{\mathrm{t}}$. These in particular read

$$\mathsf{R}_I^{\varphi} = \mathop{\mathsf{A}}_{e=1}^{n_{\mathrm{el}}} \int_{\mathscr{B}_0^{\mathrm{e}}} \boldsymbol{P} \cdot \nabla_{\boldsymbol{X}} N_I^{\varphi} \,\mathrm{d}V \qquad - \mathsf{f}_I^{\mathrm{ext}} \doteq \mathbf{0} \,, \tag{3.60}$$

$$\mathsf{R}_J^{\bar{F}} = \mathop{\mathsf{A}}_{e=1}^{n_{\mathrm{el}}} \int_{\mathscr{B}_0^{\mathrm{e}}} \bar{\boldsymbol{Q}} \cdot \nabla_{\boldsymbol{X}} N_J^{\bar{F}} + \bar{\boldsymbol{P}} N_J^{\bar{F}} \,\mathrm{d}V - \bar{\mathsf{f}}_J^{\mathrm{ext}} \doteq \mathbf{0} \,. \tag{3.61}$$

including external contributions. Therein the Piola-type stresses $\boldsymbol{P}$, $\bar{\boldsymbol{P}}$, and $\bar{\boldsymbol{Q}}$ are e. g. specified by (3.51). The discrete external force and double force vector (containing the components of the double force tensor) in (3.60) are given as

$$\mathsf{f}_I^{\text{ext}} = \operatorname*{\mathsf{A}}_{e=1}^{n_{\text{el}}} \int_{\partial \mathscr{B}_0^e} N_I^{\varphi} \boldsymbol{t}_0 \, \mathrm{d}A + \int_{\mathscr{B}_0^e} N_I^{\varphi} \boldsymbol{b}_0 \, \mathrm{d}V \,, \tag{3.62}$$

$$\bar{\mathsf{f}}_J^{\text{ext}} = \operatorname*{\mathsf{A}}_{e=1}^{n_{\text{el}}} \int_{\partial \mathscr{B}_0^e} N_J^{\bar{F}} \bar{\boldsymbol{t}}_0 \, \mathrm{d}A \,. \tag{3.63}$$

as long as both external surface and external bulk potential are considered. However these both become zero for the present choice of zero external bulk and surface potential. The linearized coupled problem

$$\begin{bmatrix} \mathsf{K}_{IL}^{\varphi\varphi} & \mathsf{K}_{IM}^{\varphi\bar{F}} \\ \mathsf{K}_{JL}^{\bar{F}\varphi} & \mathsf{K}_{JM}^{\bar{F}\bar{F}} \end{bmatrix} \begin{bmatrix} \Delta\boldsymbol{\varphi}_L^h \\ \Delta\bar{\boldsymbol{F}}_M^h \end{bmatrix} = \begin{bmatrix} \mathsf{f}_I^{\text{ext}} - \mathsf{f}_I^{\text{int}} \\ \bar{\mathsf{f}}_J^{\text{ext}} - \bar{\mathsf{f}}_J^{\text{int}} \end{bmatrix} \tag{3.64}$$

is to be solved for increments of $\boldsymbol{\varphi}_L^h$ and $\bar{\boldsymbol{F}}_M^h$. The component matrices of the global tangent stiffness matrix are given as

$$\mathsf{K}_{IL}^{\varphi\varphi} = \partial_{\boldsymbol{\varphi}_L} \mathsf{R}_I^{\varphi} = \operatorname*{\mathsf{A}}_{e=1}^{n_{\text{el}}} \int_{\mathscr{B}_0^e} \mathrm{D}_{\boldsymbol{F}} \left(\boldsymbol{P} \cdot \nabla_{\boldsymbol{X}} N_I^{\varphi} \right) \cdot \nabla_{\boldsymbol{X}} N_L^{\varphi} \, \mathrm{d}V \,, \tag{3.65}$$

$$\mathsf{K}_{IM}^{\varphi\bar{F}} = \partial_{\bar{\boldsymbol{F}}_M} \mathsf{R}_I^{\varphi} = \operatorname*{\mathsf{A}}_{e=1}^{n_{\text{el}}} \int_{\mathscr{B}_0^e} \mathrm{D}_{\bar{\boldsymbol{F}}} \left(\boldsymbol{P} \cdot \nabla_{\boldsymbol{X}} N_I^{\varphi} \right) N_M^{\bar{F}} \, \mathrm{d}V \,, \tag{3.66}$$

$$\mathsf{K}_{JL}^{\bar{F}\varphi} = \partial_{\boldsymbol{\varphi}_L} \mathsf{R}_J^{\bar{F}} = \operatorname*{\mathsf{A}}_{e=1}^{n_{\text{el}}} \int_{\mathscr{B}_0^e} \mathrm{D}_{\boldsymbol{F}} \left(\bar{\boldsymbol{Q}} \cdot \nabla_{\boldsymbol{X}} N_J^{\bar{F}} \right) \cdot \nabla_{\boldsymbol{X}} N_L^{\varphi} + \mathrm{D}_{\boldsymbol{F}} \left(\bar{\boldsymbol{P}} N_J^{\bar{F}} \right) \cdot \nabla_{\boldsymbol{X}} N_L^{\varphi} \mathrm{d}V \,, \tag{3.67}$$

$$\mathsf{K}_{JM}^{\bar{F}\bar{F}} = \partial_{\bar{\boldsymbol{F}}_M} \mathsf{R}_J^{\bar{F}} = \operatorname*{\mathsf{A}}_{e=1}^{n_{\text{el}}} \int_{\mathscr{B}_0^e} \mathrm{D}_{\bar{\boldsymbol{G}}} \left(\bar{\boldsymbol{Q}} \cdot \nabla_{\boldsymbol{X}} N_J^{\bar{F}} \right) \cdot \nabla_{\boldsymbol{X}} N_M^{\bar{F}} + \mathrm{D}_{\bar{\boldsymbol{F}}} \left(\bar{\boldsymbol{P}} N_J^{\bar{F}} \right) N_M^{\bar{F}} \, \mathrm{d}V \,. \tag{3.68}$$

The actual implementation is done element-wise with assembly to a global system of equations as in standard finite- element procedures. Also the standard procedure of Gauss quadrature is used for the numerical evaluation of the integrals above. The tangent operators and stresses are computed at each element integration point.

Tangent operators. The specific tangent operators in the stiffness matrix (3.65) are given by the derivatives of the stress measures of Piola type with respect to the deformation gradient, the micro deformation map, and the gradient of the latter.

For the constitutive ansatz of Section 3.3, the fourth-order tangent operators arising from the macro stress read:

$$\mathrm{D}_{\boldsymbol{F}}\boldsymbol{P} = \lambda\, \boldsymbol{F}^{-\mathrm{t}} \otimes \boldsymbol{F}^{-\mathrm{t}} - \left[\lambda \ln J - \mu\right] \boldsymbol{F}^{-\mathrm{t}} \underline{\otimes} \boldsymbol{F}^{-1} + [\mu + p]\, \boldsymbol{I} \overline{\otimes} \boldsymbol{I}\,, \tag{3.69}$$

$$\mathrm{D}_{\bar{\boldsymbol{F}}}\boldsymbol{P} = -p\, \boldsymbol{I} \overline{\otimes} \boldsymbol{I}\,. \tag{3.70}$$

Those tangent operatores stemming from the micro stress are given by

$$\mathrm{D}_{\boldsymbol{F}}\bar{\boldsymbol{P}} = -p\, \boldsymbol{I} \overline{\otimes} \boldsymbol{I} \qquad\qquad \mathrm{D}_{\bar{\boldsymbol{F}}}\bar{\boldsymbol{P}} = p\, \boldsymbol{I} \overline{\otimes} \boldsymbol{I} \tag{3.71}$$

and are tensors of fourth order as well. The derivatives of the double stress obey:

$$\mathrm{D}_{\boldsymbol{F}}\bar{\boldsymbol{Q}} = \boldsymbol{0}\,, \qquad\qquad \mathrm{D}_{\bar{\boldsymbol{G}}}\bar{\boldsymbol{Q}} = \mu l^2\, \boldsymbol{I} \underline{\otimes} \left[\boldsymbol{I} \overline{\otimes} \boldsymbol{I}\right]\,. \tag{3.72}$$

Thereby $\mathrm{D}_{\bar{\boldsymbol{G}}}\bar{\boldsymbol{Q}}$ represents a tensor of sixth order, while the fifth-order tensor $\mathrm{D}_{\boldsymbol{F}}\bar{\boldsymbol{Q}}$ vanishes for the present formulation.

3.4.2 Material-motion problem

Approximations. Accordingly, the approximations of the unknown quantities of the material-motion problem, the macro deformation map $\boldsymbol{\Phi}$ and the micro deformation map $\bar{\boldsymbol{f}}$, are formulated in terms of the material-motion shape functions N^{Φ}_{L} and $N^{\bar{f}}_{M}$, respectively, as

$$\boldsymbol{\Phi}^h = \sum_{L=1}^{n^{\mathrm{e}}_{\Phi}} N^{\Phi}_{L} \boldsymbol{\Phi}_L\,, \qquad\qquad \delta\boldsymbol{\Phi}^h = \sum_{I=1}^{n^{\mathrm{e}}_{\Phi}} N^{\Phi}_{I} \delta\boldsymbol{\Phi}_I\,, \tag{3.73}$$

$$\bar{\boldsymbol{f}}^h = \sum_{M=1}^{n^{\mathrm{e}}_{\bar{f}}} N^{\bar{f}}_{M} \bar{\boldsymbol{f}}_M\,, \qquad\qquad \delta\bar{\boldsymbol{f}}^h = \sum_{J=1}^{n^{\mathrm{e}}_{\bar{f}}} N^{\bar{f}}_{J} \delta\bar{\boldsymbol{f}}_J\,. \tag{3.74}$$

Herein, $n^{\mathrm{e}}_{\Phi} = n^{\mathrm{e}}_{\varphi}$, $n^{\mathrm{e}}_{\bar{F}} = n^{\mathrm{e}}_{\bar{F}}$, as well as $N^{\Phi}_{L} \equiv N^{\varphi}_{L}$ and $N^{\bar{f}}_{M} \equiv N^{\bar{F}}_{M}$, but here the gradients are derived with respect to the spatial coordinates. Particularly, $\boldsymbol{f} = \nabla_{\boldsymbol{x}}\boldsymbol{\Phi}$ and $\bar{\boldsymbol{g}} = \nabla_{\boldsymbol{x}}\bar{\boldsymbol{f}}$ and their respective variations read

$$\boldsymbol{f}^h = \sum_{L=1}^{n^{\mathrm{e}}_{\Phi}} \boldsymbol{\Phi}_L \otimes \nabla_{\boldsymbol{x}} N^{\Phi}_{L}\,, \qquad\qquad \delta\boldsymbol{f}^h = \sum_{I=1}^{n^{\mathrm{e}}_{\Phi}} \delta\boldsymbol{\Phi}_I \otimes \nabla_{\boldsymbol{x}} N^{\Phi}_{I}\,, \tag{3.75}$$

$$\bar{\boldsymbol{g}}^h = \sum_{M=1}^{n^{\mathrm{e}}_{\bar{f}}} \bar{\boldsymbol{f}}_M \otimes \nabla_{\boldsymbol{x}} N^{\bar{f}}_{M}\,, \qquad\qquad \delta\bar{\boldsymbol{g}}^h = \sum_{J=1}^{n^{\mathrm{e}}_{\bar{f}}} \delta\bar{\boldsymbol{f}}_J \otimes \nabla_{\boldsymbol{x}} N^{\bar{f}}_{J}\,. \tag{3.76}$$

With these test and trial functions in hand, we may now apply the material-force method to our micromorphic continuum in the spirit of, for instance, Steinmann

et al. (2001), Liebe et al. (2003a), Denzer et al. (2003).

Material-force method for the material balance of macro momentum. From the integral version of the balance of momentum for the macrocontinuum $(3.27)_1$, we obtain

$$\int_{\mathscr{B}_t} \delta\boldsymbol{\Phi} \cdot [\operatorname{div} \boldsymbol{p} + \boldsymbol{B}_t] \, \mathrm{d}v = 0 \qquad \forall\ \delta\boldsymbol{\Phi}\,, \tag{3.77}$$

wherein the body force is kept here for the sake of completeness. For arbitrary variations $\delta\boldsymbol{\Phi}$ and with the finite-element approximations (3.73) and (3.75) we obtain a quantity that we define as the nodal material force of the macro scale:

$$\mathsf{F}_I := \mathop{\mathsf{A}}_{e=1}^{n_{\mathrm{el}}} \int_{\mathscr{B}_t^e} \boldsymbol{p} \cdot \nabla_{\boldsymbol{x}} N_I^{\Phi} - \boldsymbol{B}_t N_I^{\Phi} \, \mathrm{d}v\,. \tag{3.78}$$

This force vector acts on the material manifold and is energetically conjugate to the material virtual node-point displacements at node L, $\delta\boldsymbol{\Phi}_I$. The material force F_I exclusively concerns the macro momentum and thus appears in the same format as for a classical or rather Boltzmann continuum.

Remark 3.4.1 *The material force may be equally derived in terms of the purely material stresses of Eshelby type*

$$\int_{\mathscr{B}_0} \delta\boldsymbol{\Phi} \cdot J[\operatorname{div} \boldsymbol{p} + \boldsymbol{B}_t] \, \mathrm{d}V = \int_{\mathscr{B}_0} \delta\boldsymbol{\Phi} \cdot [\operatorname{Div} \boldsymbol{\Sigma} + \boldsymbol{B}_0] \, \mathrm{d}V = 0$$

from the pull back and by execution of the Piola transformation (3.29).

Material-force method for the material balance of micro momentum. For the sake of completeness, we attempt to obtain a comparable nodal configurational double-traction based on the material balance of the micro momentum. Thus the material-motion balance of $(3.27)_2$ is brought into a weak form,

$$\int_{\mathscr{B}_t} \delta\bar{\boldsymbol{f}} : \left[\operatorname{div} \bar{\boldsymbol{q}} - \bar{\boldsymbol{p}}\right] \, \mathrm{d}v = 0 \qquad \forall\ \delta\bar{\boldsymbol{f}}\,, \tag{3.79}$$

by multiplication with the virtual micro deformation map $\delta\bar{\boldsymbol{f}}$ of the material-motion problem. From this we obtain what we call a *nodal configurational double force*,

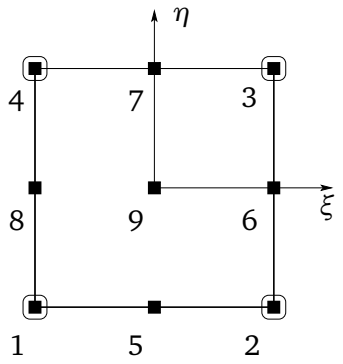

Figure 3.11: Isoparametric quadrilateral master element with 9 nodes for the macro deformation map $\boldsymbol{\varphi}$ and $\boldsymbol{\Phi}$ and 4 nodes for the micro deformation map $\bar{\boldsymbol{F}}$ and $\bar{\boldsymbol{f}}$.

which in the discretized version with the approximations (3.74) and (3.76) reads

$$\bar{\mathsf{F}}_J := \mathop{\mathsf{A}}_{e=1}^{n_{\mathrm{el}}} \int_{\mathscr{B}_t^e} \bar{\boldsymbol{q}} \cdot \nabla_{\boldsymbol{x}} N_J^{\bar{f}} + \bar{\boldsymbol{p}} N_J^{\bar{f}} \, \mathrm{d}v \,. \tag{3.80}$$

This discrete configurational micro double force is energetically conjugate to the micro deformation map $\bar{\boldsymbol{f}}$ of the material-motion problem and discretely evaluated at the nodes of the finite-element mesh. Contrary to the material force F_L the configurational micro double force $\bar{\mathsf{F}}_J$ represents a nonsymmetric two-point tensor.

Remark 3.4.2 (Double-force in terms of Eshelby-type stress) *Alternatively the configurational micro double force can be expressed in terms of Eshelby-type stresses by performing a pull-back and a Piola-transformation on the micro balance of momentum* (3.79)*:*

$$\int_{\mathscr{B}_0} [J \left[\operatorname{div} \bar{\boldsymbol{q}} - \bar{\boldsymbol{p}} \right] \cdot \bar{\boldsymbol{f}}^{\mathrm{t}}] : [\delta \bar{\boldsymbol{f}} \cdot \bar{\boldsymbol{F}}] \mathrm{d}V = \int_{\mathscr{B}_0} [\operatorname{Div} \bar{\boldsymbol{\tau}} - \bar{\boldsymbol{\Sigma}}] : [\delta \bar{\boldsymbol{f}} \cdot \bar{\boldsymbol{F}}] \mathrm{d}V = 0 \,.$$

3.5 Numerical examples

The proposed algorithm for the micromorphic continuum is now applied to selected numerical examples.

First, a finite-element solution for the spatial-motion problem is obtained according to Section 3.4.1 in a two-point formulation. From the directly obtained nodal values for $\boldsymbol{\varphi}$ and $\bar{\boldsymbol{F}}$, all other kinematic quantities can be derived (compare Section 3.2.3). With these at hand, for instance all presented stress fields can be evaluated using the relations of Sections 3.3.1 and 3.3.2. The material-force method, which was presented for the present micromorphic continuum in Section 3.4.2, is

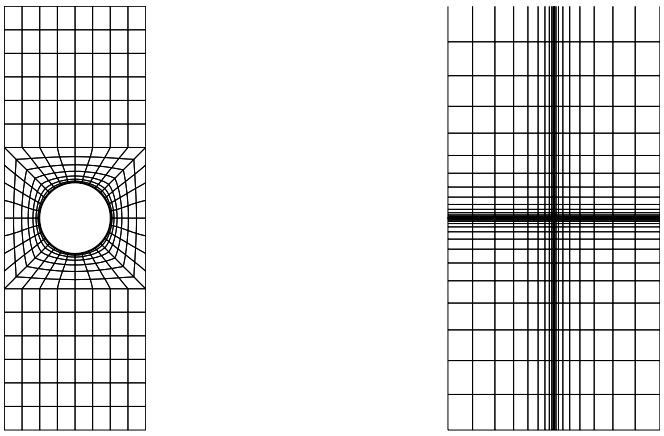

Figure 3.12: Material discretization of specimens for the numerical examples.

employed to obtain the material forces and configurational double forces of the micromorphic continuum. According to the requirement on the order of approximation mentioned in Section 3.4.1, quadrilateral plane elements with a biquadratic approximation for the macro deformation map $\boldsymbol{\varphi}$ and a bilinear approximation for the micro deformation map $\bar{\boldsymbol{F}}$ as shown in Figure 3.11 are used.

The response is studied at two different boundary value problems, which are depicted in Figure 3.12: The first geometry under consideration is a specimen with a circular hole under uniaxial loading, while the second one is a rectangularly shaped specimen with a static crack under mode-I loading. Both geometries are discretized with the finite elements depicted in Figure 3.11. The boundary conditions applied consist of non-homogeneous Dirichlet and homogeneous Neumann boundary conditions for the macro deformation map as well as homogeneous Neumann boundary conditions for the micro deformation map.

3.5.1 Uniaxial loading of specimen with hole

Into the rectangular specimen of length L_0 and width $L_0/3$, an inhomogeneity is introduced by means of a centred circular hole of radius $r = L_0/12$, as shown in Figure 3.13. While the nodes at the bottom edge of the discretized geometry are fixed in longitudinal direction, a constant displacement boundary condition in the same direction is applied on the top nodes step-wise until the final length of $1.5L_0$ is reached.

Results from the spatial-motion problem

The internal length l is varied for fixed scale-transition parameter $p = 20E$ in order to firstly investigate the resulting field of the normal Cauchy-type macro stress σ_{22} in loading direction, and secondly the scale-transition term $\|\bar{\boldsymbol{F}} - \boldsymbol{F}\|^2$ of the internally stored-energy density (3.49).

Cauchy-type stress. Figure 3.13 shows the distribution of the Cauchy-type macro stress component σ_{22} for different internal length ratios and a fixed scale-transition parameter $p = 20E$ plotted in the spatial mesh. The first aspect to observe is that the overall behaviour of the specimen becomes stiffer with increasing internal length, i. e. the deformation of the hole is less distinct compared to the overall deformation. Moreover, the stress field is influenced more distinctively in a wider region by the inhomogeneity represented by the hole. Especially the first effect can be attributed to an increased stiffness in the micro term of Eq. (3.49) at increasing the internal-length parameter l.

In Figure 3.14 we compare the stress components of the Cauchy-type macro stress for two different internal lengths. For zero internal length, the fields appear symmetric while for the larger internal length of $l = L_0/6$ the non-symmetry of the tensor $\boldsymbol{\sigma}$ is revealed. This coincides with a nonsymmetric macro stress tensor generally predicted by the literature for non-local formulations.

Scale-transition term. Now the influence of the internal length on the scale-transition term is investigated. Its contour is displayed in Figure 3.15 for varied internal length l at fixed scale-transition parameter $p = 20E$. Herein mainly the shape of the region with a significantly large term $\|\bar{\boldsymbol{F}} - \boldsymbol{F}\|^2$ differs with increasing internal length: For larger l, the term appears more restricted to the direct circumference of the hole but less effectively controlled by the parameter p. For explanation of these effects, one may point to the fact that for zero internal length, no microstructural effects are incorporated. As the micro deformation map $\bar{\boldsymbol{F}}$ vanishes, the scale-transition term is of the order of the macro deformation gradient $\boldsymbol{F}$ and therefore has no decisive significance. Otherwise, if $l > 0$, the influence of the scale-transition term becomes larger and also more closely aligned along the edge of the hole due to stronger micro deformation.

Results from the material-motion problem

In the following, the material-force method is applied to the current boundary value problem. In particular, the nodal material forces at the finite-element nodes as well as the nodal configurational double forces are evaluated.

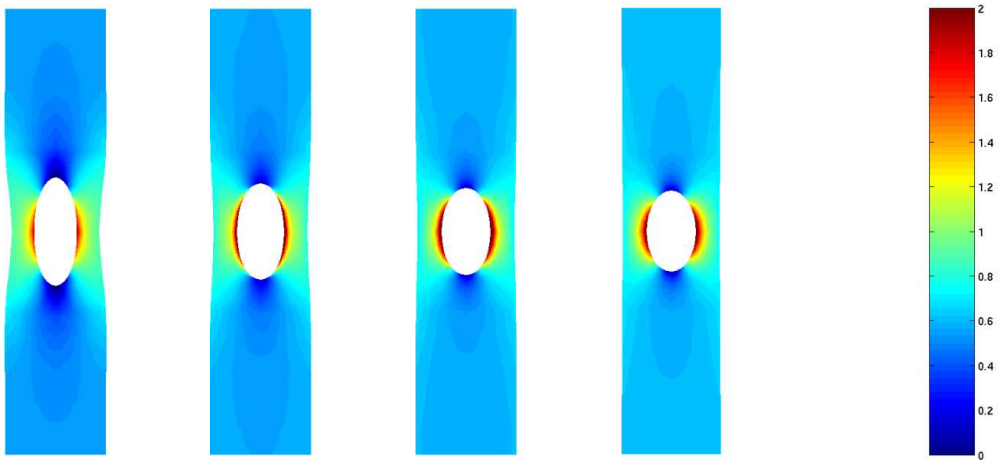

$l = 0$ $l = L_0/12$ $l = L_0/6$ $l = L_0/3$

Figure 3.13: Cauchy-type macro stress σ_{22} for different internal lengths.

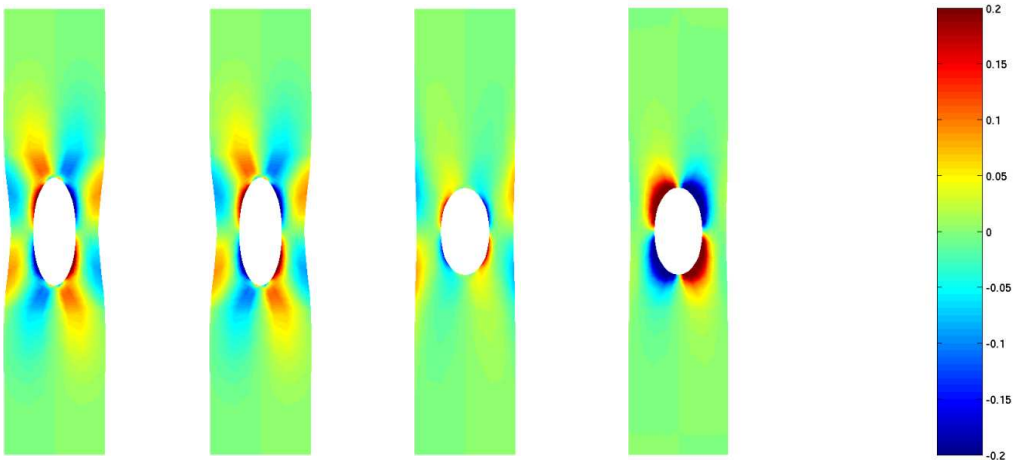

σ_{12} σ_{21} σ_{12} σ_{21}

$l = 0$ $l = L_0/6$

Figure 3.14: Cauchy-type macro stress σ_{12} and σ_{21}, for different internal lengths.

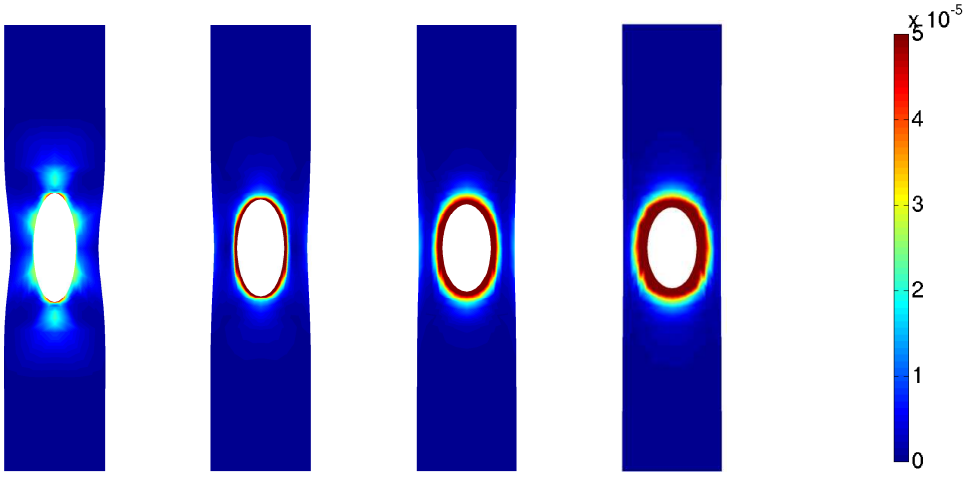

$l = 0$ $l = L_0/12$ $l = L_0/6$ $l = L_0/0.6$

Figure 3.15: Scale-transition measure $\|\bar{\boldsymbol{F}} - \boldsymbol{F}\|^2$ for different internal lengths.

Nodal material forces. In Figure 3.16, the nodal material forces at the spatial mesh are plotted for a variation of the internal lengths l at the same (fixed) scale-transition parameter p as before. We observe that for zero internal length, the material force at the hole exhibits a distinct maximum at the lateral edges, while for increasing internal length, the material forces are more evenly distributed along the edge. The size of the material force vectors reflects the deformation along the free edges, particularly around the hole. Consequently, we may conclude that the additional stiffness imposed by the microstructure for larger internal length reduces the possible energy release at the defect.

Configurational double forces. Now we consider the nodal configurational double force $\bar{\mathbf{F}}_J$, which is a nonsymmetric tensor of second-order.

First we investigate its modulus, $\|\bar{\mathbf{F}}_J\|$, plotted continuously over the entire domain in Figure 3.19. Generally it can be observed that the configurational double force occurs in the interior of the domain, especially at the defect. For zero internal length, the double force vanishes. This observation correlates with the fact that for this particular set of parameters the micromorphic continuum is very similar to the classical continuum due to the vanishing size of the microstructure being represented by the internal length l. Once a non-zero internal length is present, the nodal configurational double force arises. But due to the more homogeneous deformation at large l, the distribution becomes more homogeneous and overall smaller.

To illustrate this quantity more characteristically, in Figures 3.17–3.18 we display the results of the eigenvalue problem (confer Remark 3.5.1).

Particularly, in Figure 3.17 the first left and right eigenvectors, and in Figure 3.18 the corresponding second eigenvectors of the nodal configurational double force at the finite element nodes are plotted, each one scaled by its corresponding eigenvalue. Here we notice a very distinct pattern: The first impression is that with increasing internal length the quantity decreases as already seen before in Figure 3.19. Furthermore, we observe that the first left and the second right eigenvectors are oriented normal to each other, also the second left and the first right, which coincides with the eigenproblem theory. Especially for the first right eigenvectors, we notice that with increasing internal length, the arrows of significant size become less aligned at the hole. The first eigenvectors represent the "stronger" direction. Thus we conclude that the nodal configurational double force, which is the micro quantity being energetically conjugate to the micro deformation map of the material-motion problem, reflects a deflection of the loading from the edge of the hole to the remaining bulk aside.

Remark 3.5.1 (Eigenvalue problem) *For the nonsymmetric tensor of second order,* $\bar{\mathfrak{m}}_J$*, both the left*

$$\bar{\boldsymbol{a}}_J \cdot \bar{\mathbf{F}}_J = \lambda_{aJ}\, \bar{\boldsymbol{a}}_J$$

and the right

$$\bar{\mathbf{F}}_J \cdot \bar{\boldsymbol{b}}_J = \lambda_{bJ}\, \bar{\boldsymbol{b}}_J$$

eigenvalue problem need to be considered. Herein $\bar{\mathbf{a}}_J$ *denotes the left and* $\bar{\mathbf{b}}_J$ *the right eigenvector of* $\bar{\mathbf{F}}_J$*, while the right and left eigenvalues are given by* $\lambda_{aJ} = \lambda_{bJ}$*.*

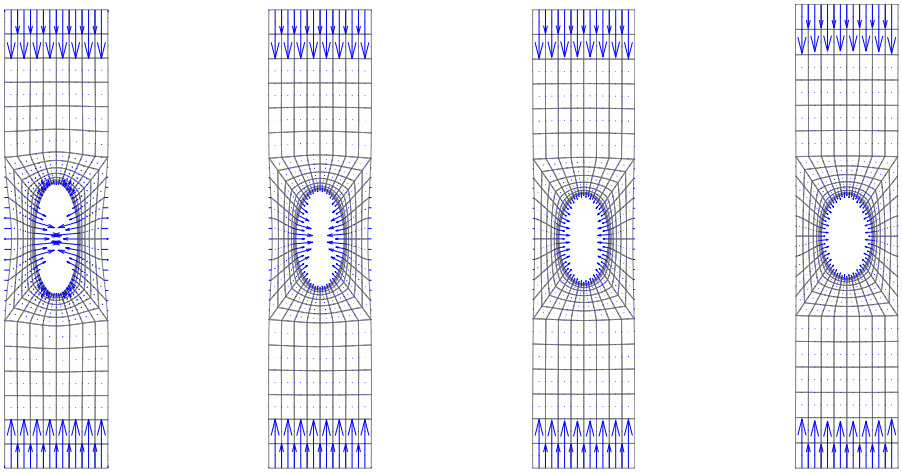

$l = 0$ $l = L_0/12$ $l = L_0/6$ $l = L_0/3$

Figure 3.16: Material forces $\mathbf{F}_I$ on spatial mesh for different internal lengths.

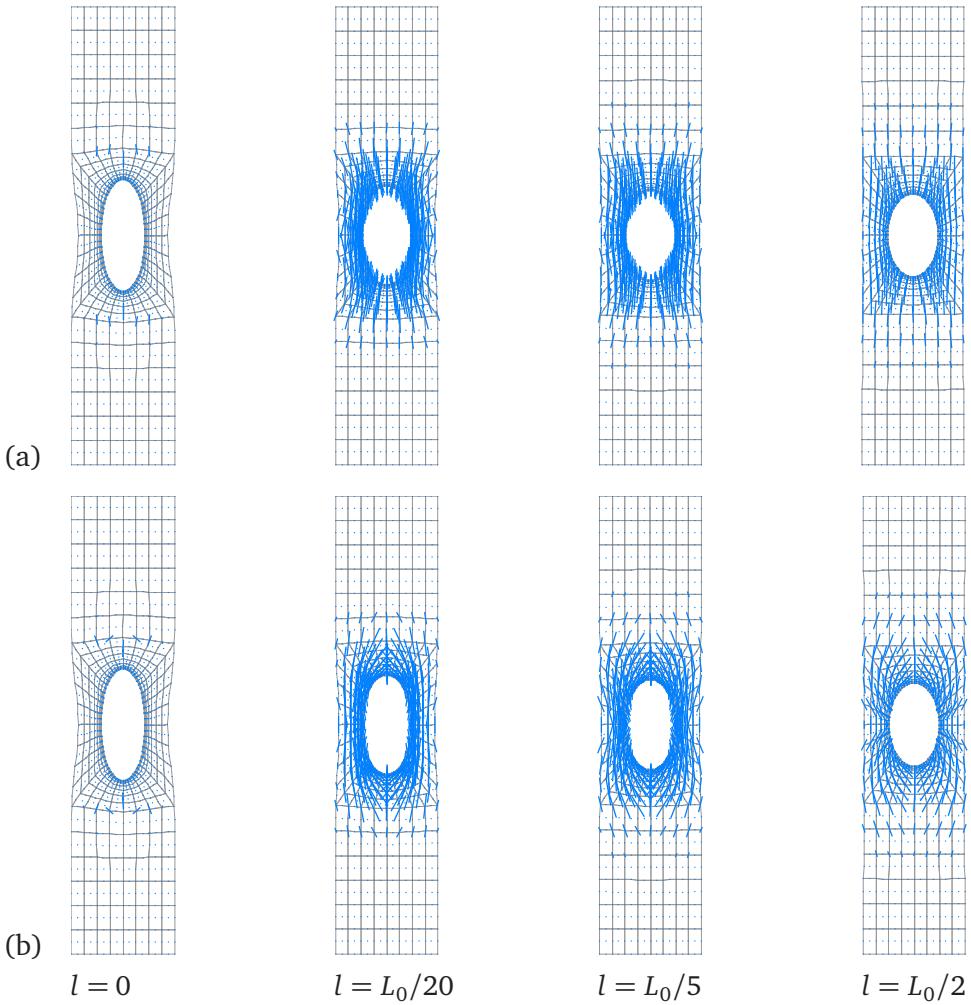

(a)

(b)

$l = 0$ $l = L_0/20$ $l = L_0/5$ $l = L_0/2$

Figure 3.17: First left (a) and right (b) eigenvectors of nodal configurational double forces $\bar{\mathbf{F}}_J$: eigenvector, scaled by corresponding eigenvalues, for different internal lengths.

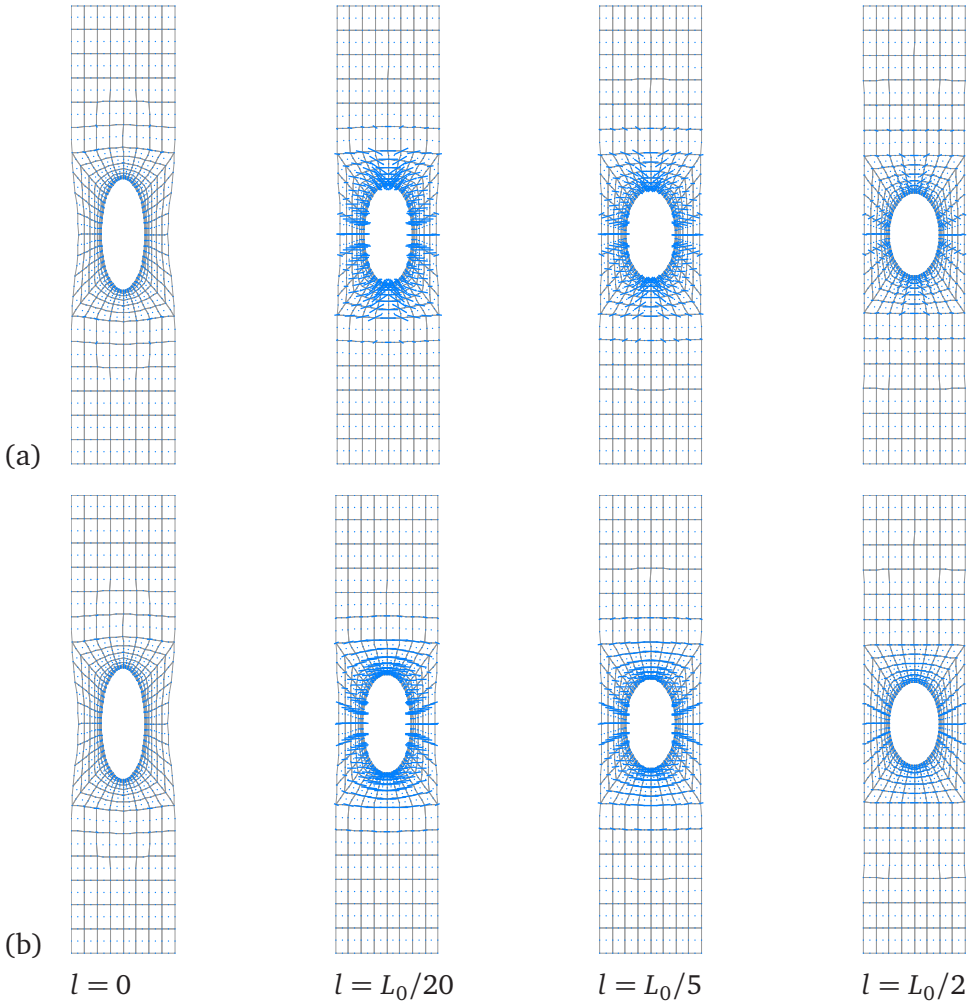

Figure 3.18: Second (a) left and (b) right eigenvectors of nodal configurational double forces $\bar{\mathbf{F}}_J$, scaled by corresponding eigenvalues, for different internal lengths.

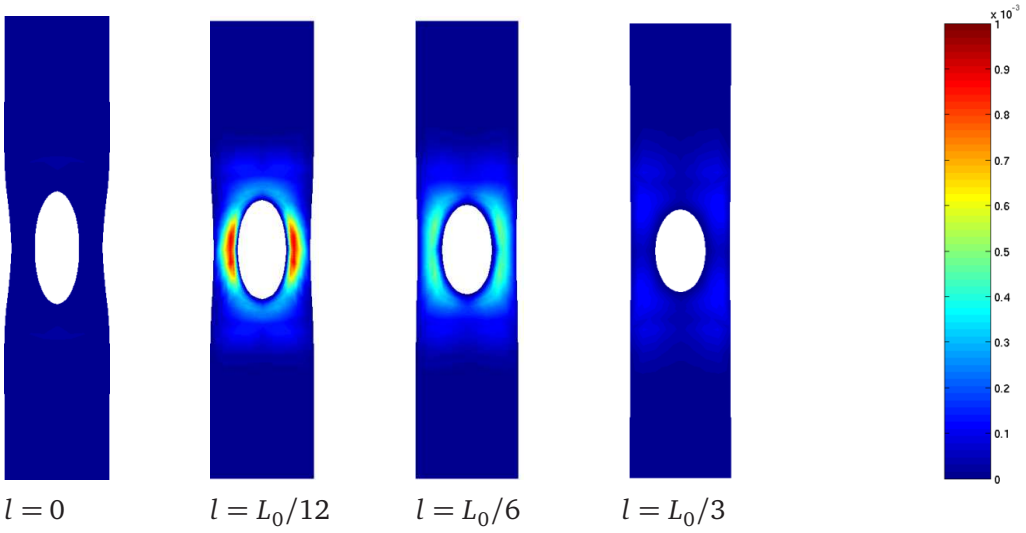

Figure 3.19: Modulus of nodal configurational double forces, $\|\bar{\mathbf{F}}_J\|$, plotted continuously, for different internal lengths.

3.5.2 Uniaxial loading of cracked specimen

As a second geometry, the rectangular specimen with a one-sided, non-propagating crack at half length of Figure 3.12(b) is examined under uniaxial quasi-static loading. The crack, which experiences mode-I loading, is explicitly modelled by an additional edge in the finite-element mesh. For this boundary value problem, first the internal length l and thereafter the penalty p is varied. Like in the previous example, the specimen is fixed at the bottom, and a constant displacement boundary condition is applied at the top nodes in longitudinal direction step-wise until a final elongation of $L_0/3$ is reached.

Results from the spatial-motion problem

First the different components of the Cauchy type stresses are shown for the considered boundary value problem. Then the influence of a variation of the internal length is studied at fixed scale-transition parameter, before the latter parameter is varied for fixed internal length.

Components of the Cauchy type stress. To illustrate the additionally arising stress fields, besides the Cauchy-type macro stress of Figure 3.20, the components of Cauchy-type micro and double stress are plotted in Figures 3.21 and 3.22, respectively.

For the present boundary value problem, the normal macro stress component in longitudinal or rather loading direction is dominant. The macro stress of Figure 3.20 is nonsymmetric, so is the micro stress of Figure 3.21. Their sum must be symmetric, and in fact it is observed that for instance the sign of e. g. σ_{21} and $\bar{\sigma}_{21}$ is reverse around the crack tip. Of the double stress being a tensor of third order eight components are considered for the two-dimensional boundary value problem. These themselves are difficult to interpret, however they are significant for the micromorphic model in that sense their contribution in the residual is directly related to the influence of the higher gradient on the response.

Influence of the internal length. For variation of the internal length l, the normal component of the Cauchy-type macro stress in loading direction at penalty parameter $p = 20E$ is plotted on the spatial configuration in Figure 3.23. We observe that for increasing internal length, the crack opening becomes much smaller, which we can interpret as overall behaviour of the specimen becoming ascendingly stiff. For smaller l the regions within the specimen carrying none or minor load, are much larger. Contrarily, for a large internal length the stress is distributed over almost the entire specimen, and this distribution deflected strongly next to the crack.

Figure 3.24 shows the modulus of the difference between macro- and micro-deformation from the scale-transition term $\|\bar{\boldsymbol{F}} - \boldsymbol{F}\|^2$ for varying internal length

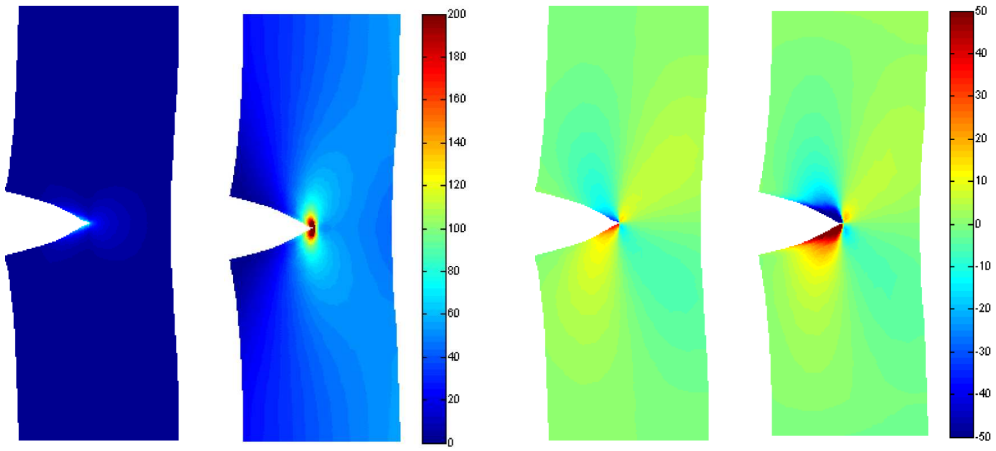

Figure 3.20: Cauchy-type macro stress $\boldsymbol{\sigma}$

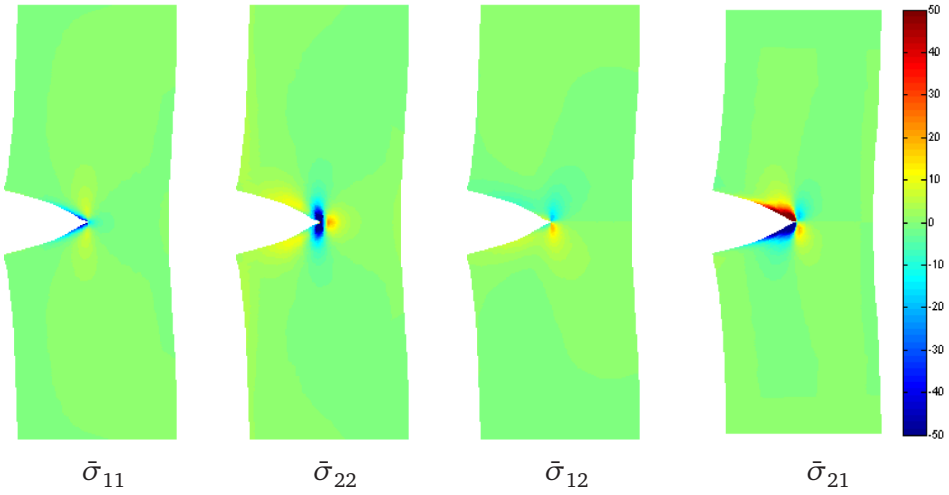

Figure 3.21: Cauchy-type micro stress $\bar{\boldsymbol{\sigma}}$

plotted on the spatial configuration at a penalty of $p = 20E$. For larger internal length, the region, in which this term is significant, increases, but remains narrowly aligned around the crack tip.

Influence of the scale-transition parameter. Further studies are made on the influence of the scale-transition parameter p. In Figure 3.25, the normal Cauchy-type macro stress component in longitudinal direction, σ_{22}, is plotted on the spatial mesh and compared for different scale-transition parameters p. The spatial mesh changes in such manner that, for increasing p, the shape of the crack tip changes from rounded to sharp. The influence of p on the stress σ_{22} is not as strong as that of the internal length. Mainly the field at the crack tip changes its shape from a '0' towards that of an '8'.

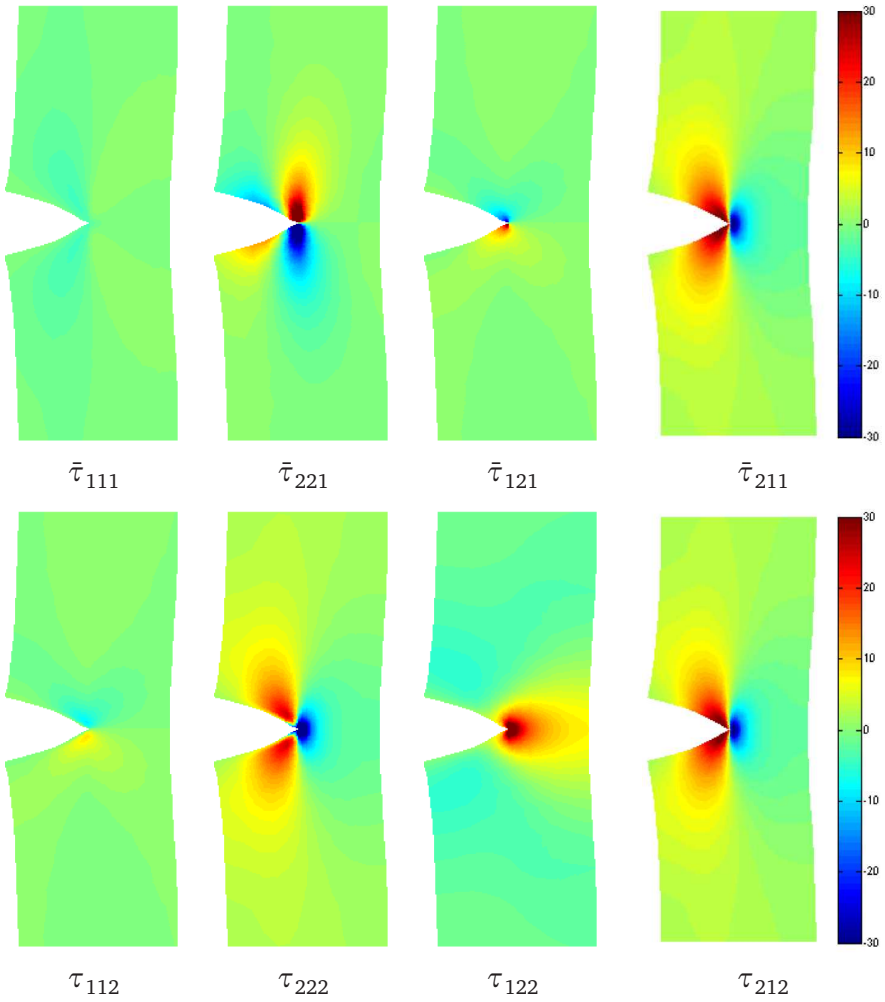

Figure 3.22: Cauchy-type double stress $\bar{\tau}_{ijk}$

Now the influence of the parameter p on the kinematic measurement from the scale-transition term, $\|\bar{\boldsymbol{F}} - \boldsymbol{F}\|^2$, is investigated. From the plot of this field in Figure 3.26, we may perceive that only a rather high scale-transition parameter leads to a successful penalisation of the quantity, since then the macro-tangent and the micro-deformation map, $\boldsymbol{F}$ and $\bar{\boldsymbol{F}}$ approach each other. Only around the crack tip, an occurrence can still be recognized for a penalisation being sufficient elsewhere over the domain. This behaviour is characteristic for the formulation as explained in the sequel: For small values of p the microcontinuum deforms more independently as characteristic for microcontinuum theory. Opposed to that, the formulation approaches a gradient continuum for larger values of p. This goes along with locally compatible deformations, which are here imposed by the penalising scale-transition term.

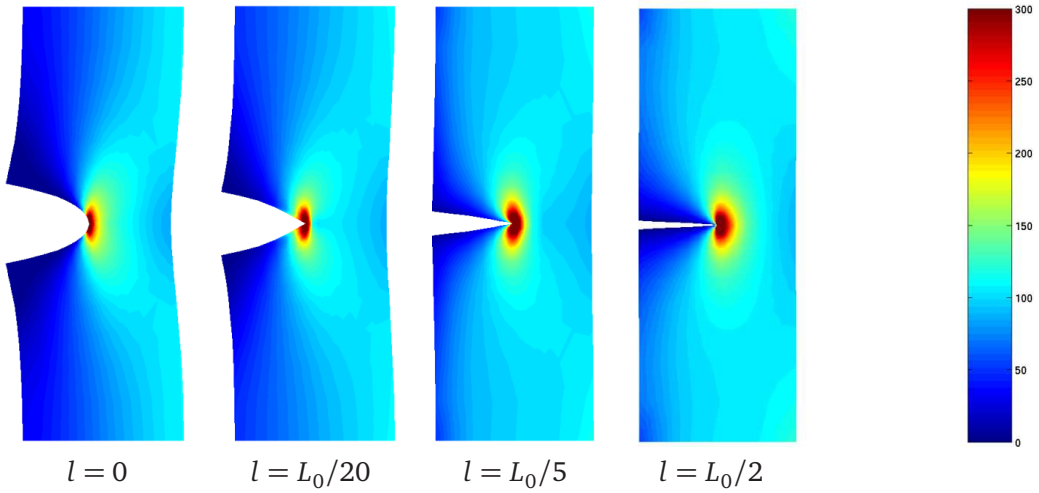

Figure 3.23: Cauchy stress σ_{22} for different internal lengths.

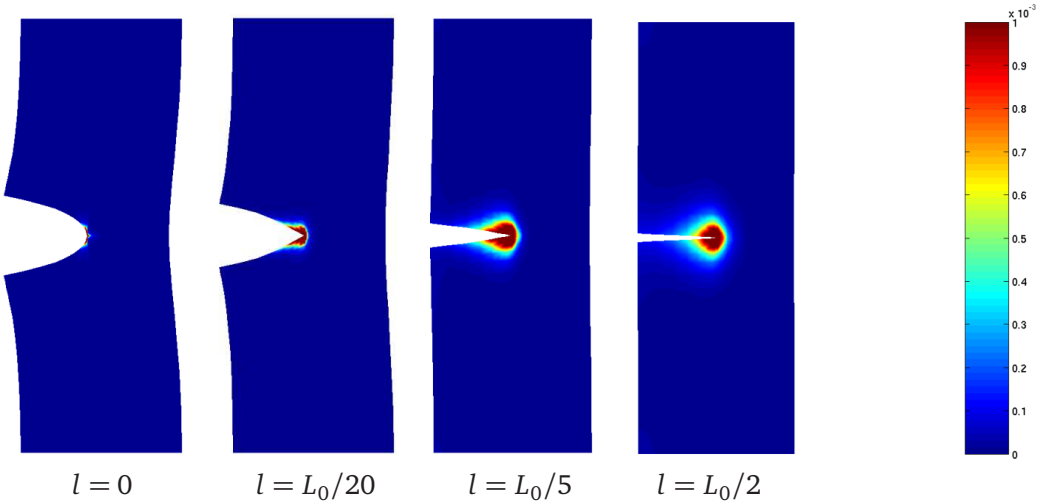

Figure 3.24: Scale-transition measure $\|\bar{\boldsymbol{F}} - \boldsymbol{F}\|^2$ for different internal lengths.

Results from the material-motion problem

For the cracked specimen, the material-force method is applied. First the nodal material forces resulting from the balance of macro-momentum are plotted for a variation of the internal length and of the scale-transition parameter, before the nodal configurational double forces are presented for the same sets of parameters.

Influence of the internal length. In Figure 3.27 the discrete nodal material forces F_{L} are plotted for different values of the internal length. The material forces occur along all edges, especially on the fixed boundaries at the upper and lower at end of the specimen and at the crack tip. Particularly, there is one large lateral

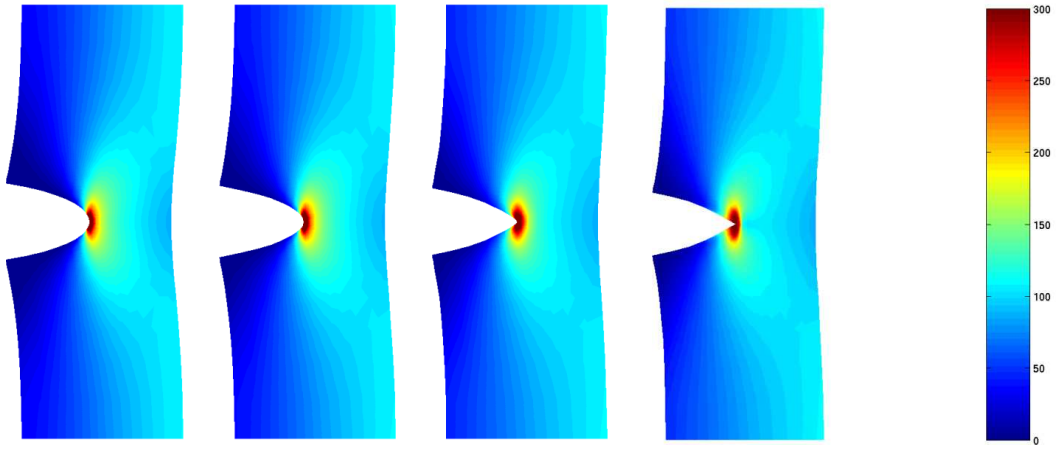

Figure 3.25: Cauchy stress σ_{22} for different scale-transition parameters.

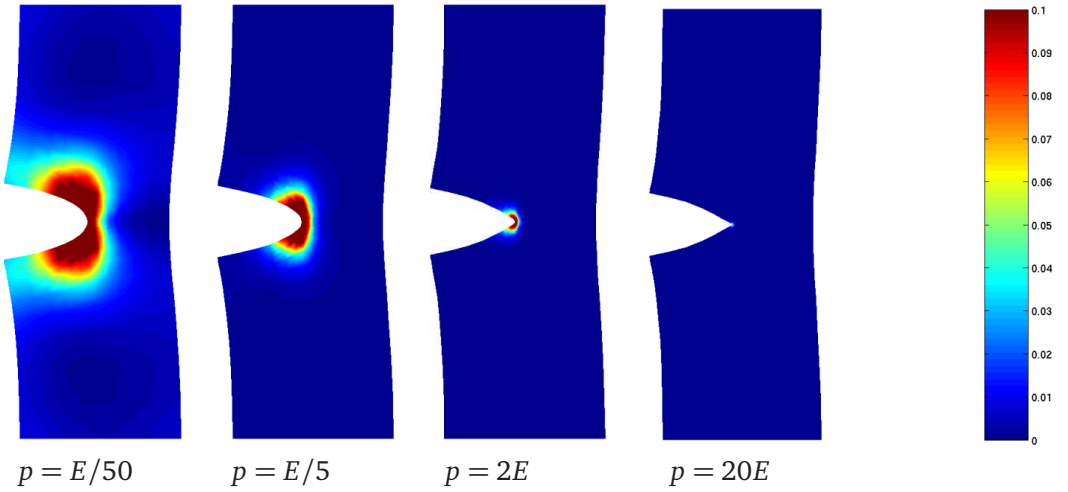

Figure 3.26: Scale-transition measure $\|\bar{\boldsymbol{F}} - \boldsymbol{F}\|^2$ for different scale-transition parameters.

material force located at the crack tip and directed opposite to the direction into which the crack would propagate. We observe that with increasing internal length, the overall deformation is more homogeneous and the major material force vector at the crack tip decreases. At the same time, those material force vectors representing the boundary reaction forces become larger. This can be attributed to the fact that the parameter increases the stiffness: for the same displacement, the stiffer specimen will exhibit higher stresses and thus bear a larger load.

In the sequel, we regard the results for the nodal configurational double force of the micro scale, $\bar{\mathsf{F}}_J$. In this context, Figure 3.30 shows its modulus, $\|\bar{\mathsf{F}}_J\|$, again plotted continuously over the mesh. Here we observe the same phenomenon as for the previous specimen: For zero internal length the modulus is zero everywhere, while the quantity has the biggest values for the smallest non-zero internal length and the

occurrence decreases with growing internal length. This behaviour is also reflected in the illustration of the eigenvalue problem in Figure 3.28–3.29. Besides this, we moreover observe that, with increasing internal length, the orientation of the eigenvectors changes. This could be attributed to a switch in the order of the corresponding eigenvalues, which consequently determine the direction of the eigenvectors.

Influence of the scale-transition parameter. We now look at the influence of the scale-transition parameter p on the material forces, see Figure 3.31. Despite the aforementioned change in the crack shape, for larger p the material force distribution experiences no significant sensibility to the scale-transition parameter. Only the material forces at the supported edge become slightly larger, which indicates a slightly stiffer behaviour of the specimen for increasing p.
Contrary to this, the norm of the nodal configurational double force of the micro scale, $\|\bar{\mathbf{F}}_J\|$, plotted in Figure 3.34, occurs increasingly stronger for increasing scale-transition parameter p. This strong influence of p on the quantity of the nodal configurational double force also becomes obvious in Figures 3.28 and 3.29. This time, there is no significant change in direction of the eigenvectors. We may conclude that, as the formulation approaches a second-order gradient continuum, the micro nodal configurational double forces grow.

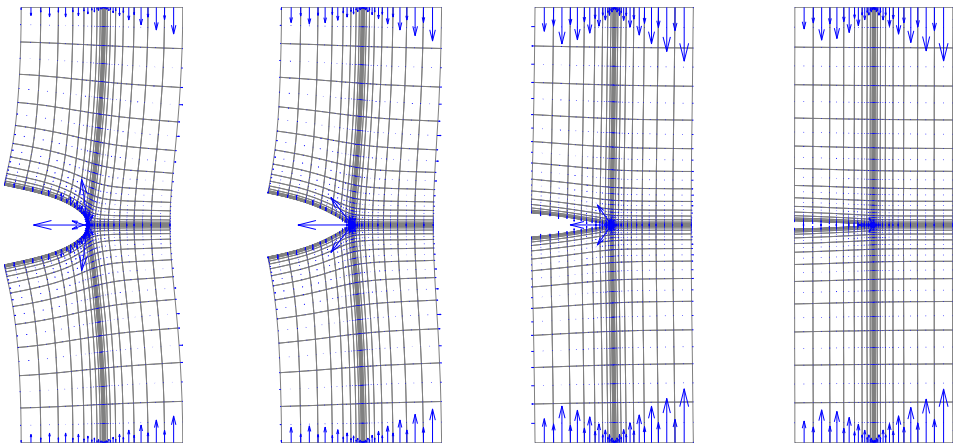

$l = 0$ $l = L_0/20$ $l = L_0/5$ $l = L_0/2$

Figure 3.27: Nodal material forces $\mathbf{F}_I$ for different internal lengths.

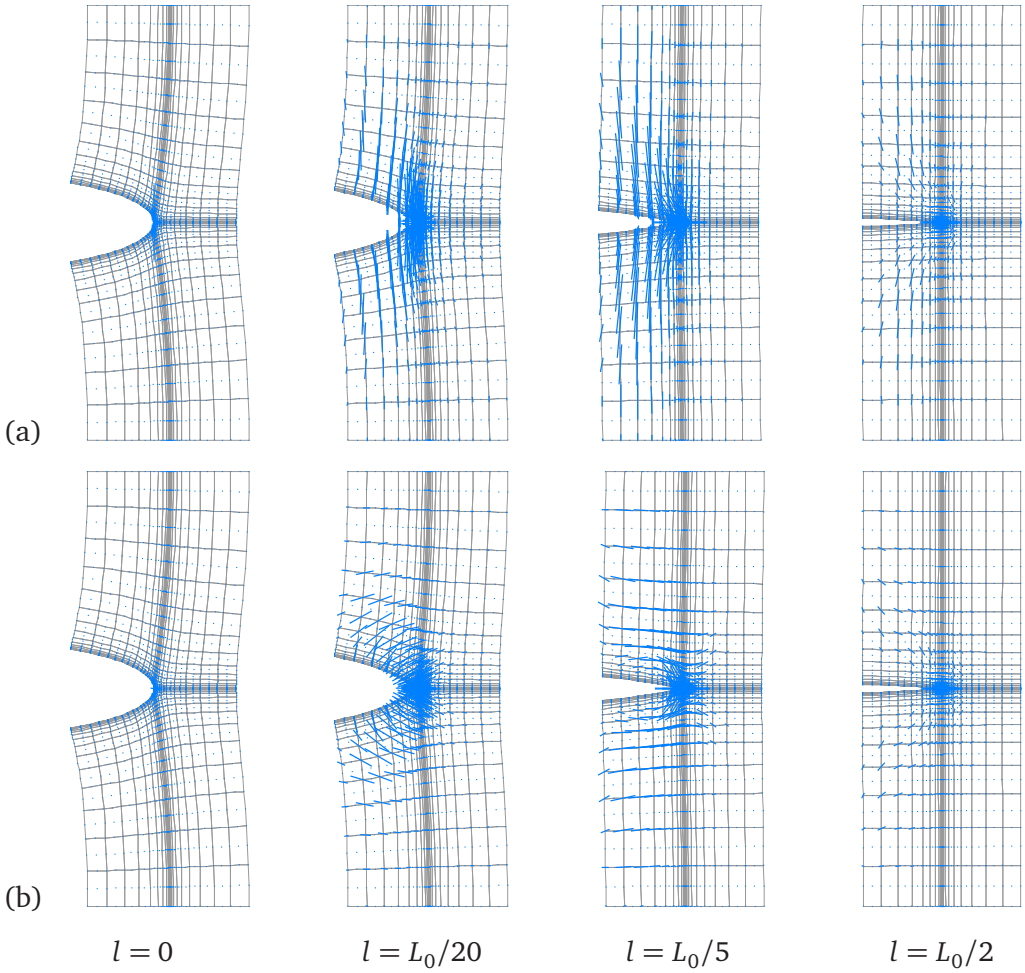

(a)

(b)

$l = 0$ $l = L_0/20$ $l = L_0/5$ $l = L_0/2$

Figure 3.28: First left eigenvectors of nodal configurational double force $\bar{\mathbf{F}}_J$, scaled by corresponding eigenvalues, for different internal lengths.

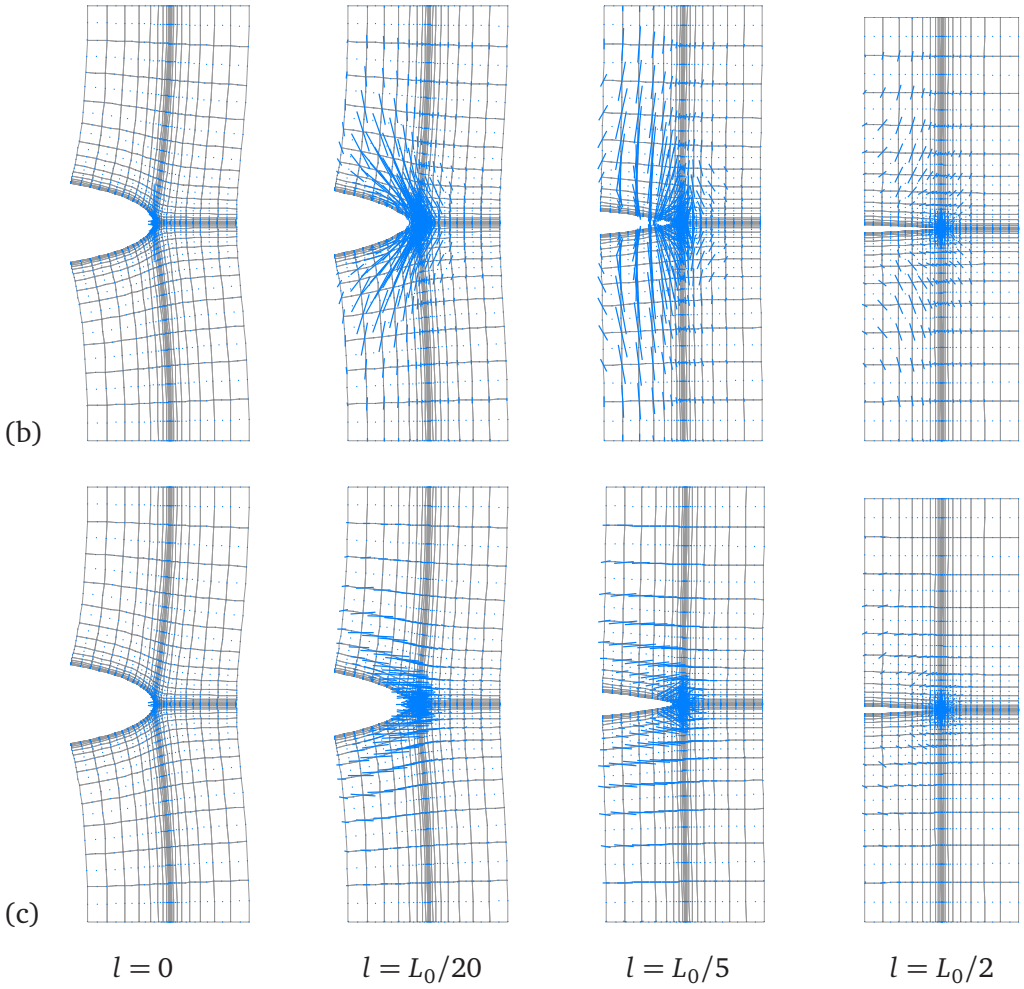

Figure 3.29: First right (a), second left (b) and right (c) eigenvectors of nodal configurational double force $\bar{\mathbf{F}}_J$, scaled by corresponding eigenvalues, plotted at spatial mesh for different internal lengths.

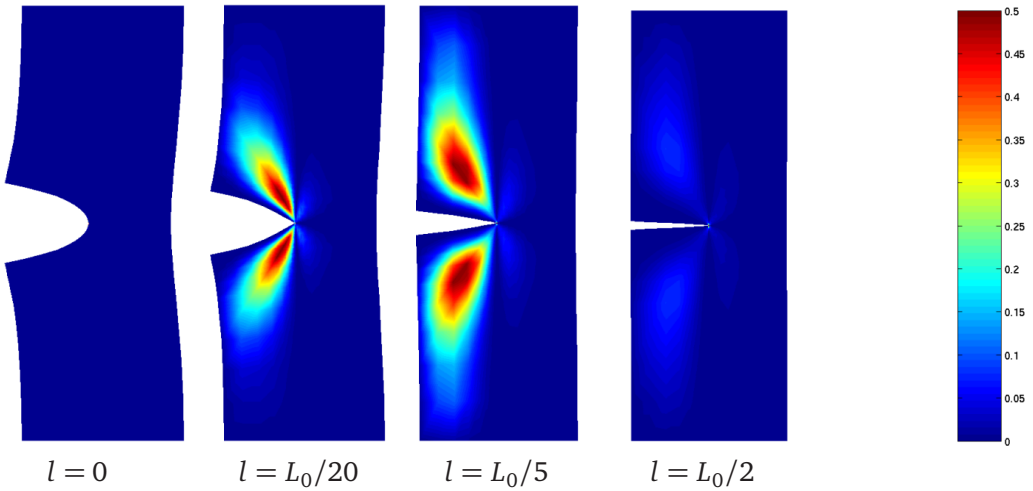

Figure 3.30: Modulus of nodal configurational double force, $\|\bar{\mathbf{F}}_J\|$, plotted continuously for different internal lengths.

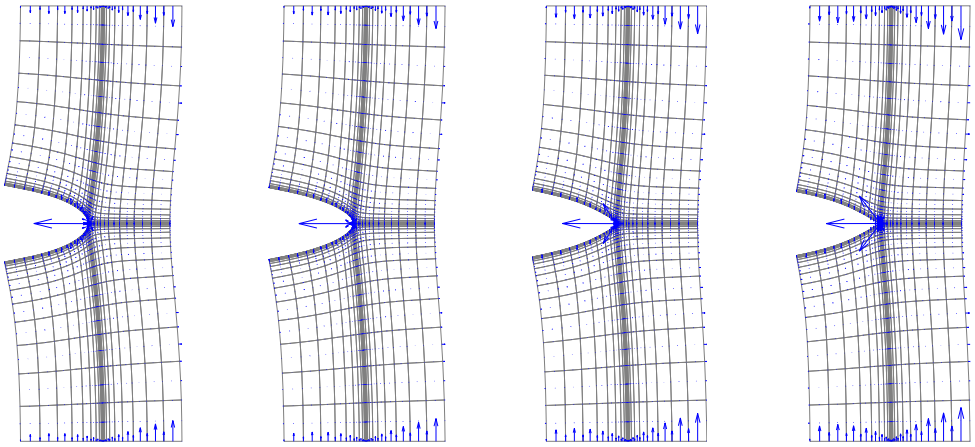

$p = E/50$ $p = E/5$ $p = 2E$ $p = 20E$

Figure 3.31: Nodal material forces $\mathbf{F}_{\mathrm{I}}$ for different scale-transition parameters.

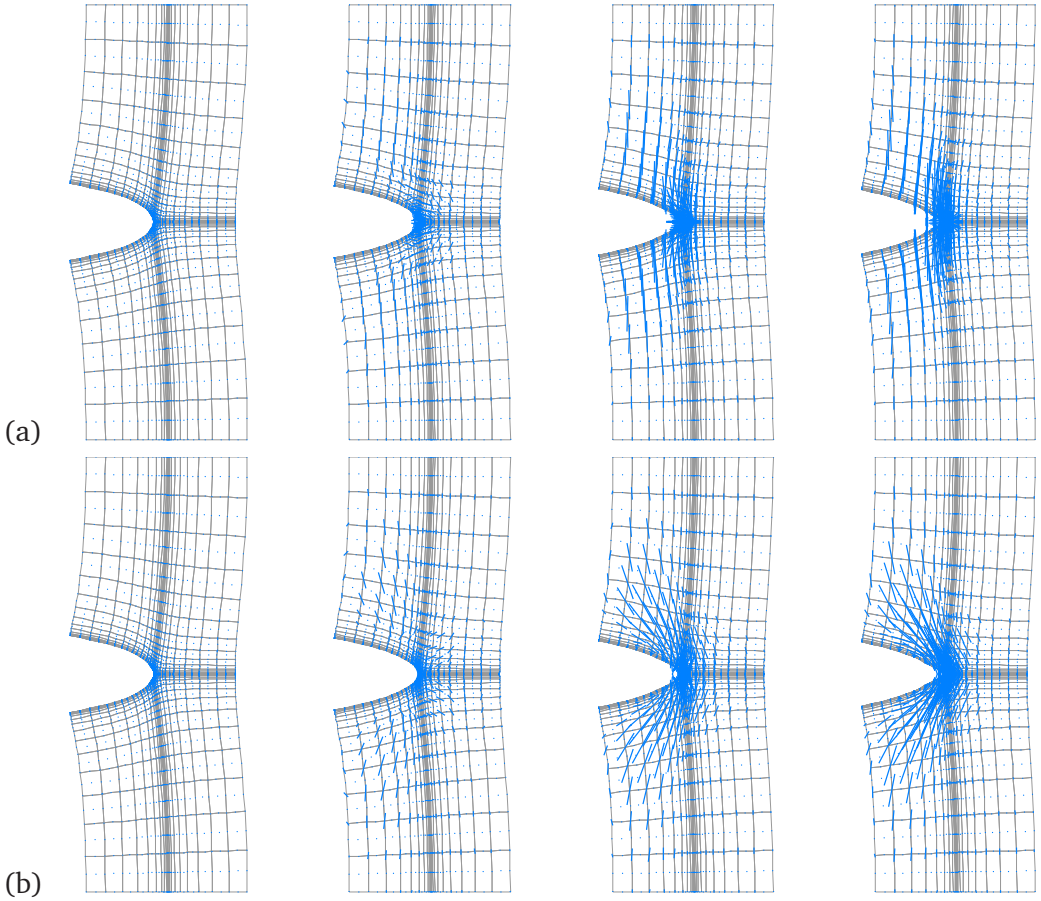

(a)

(b)

$p = E/50$ $p = E/5$ $p = 2E$ $p = 20E$

Figure 3.32: First and second left eigenvectors of nodal configurational double forces $\bar{\mathbf{F}}_J$, scaled by corresponding eigenvalues, for different scale-transition parameters.

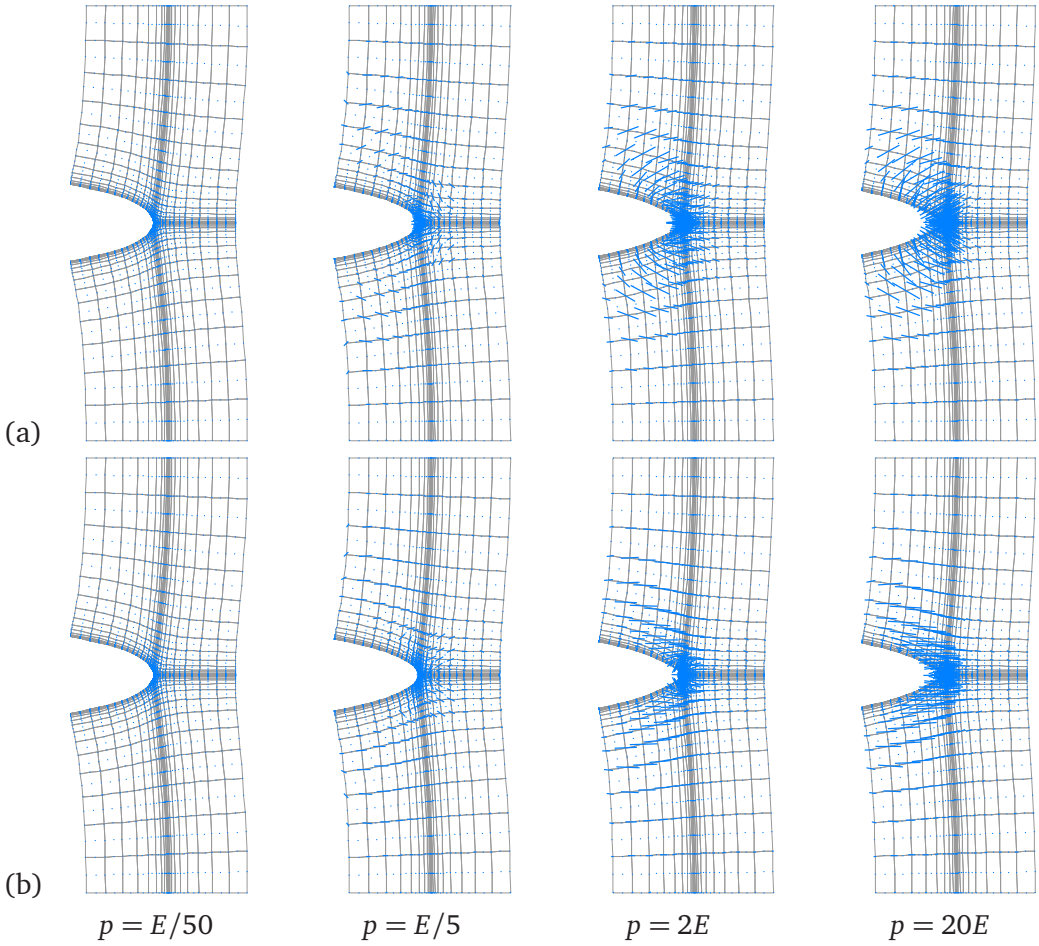

Figure 3.33: First (a) and second (b) right eigenvectors of nodal configurational double force $\bar{\mathbf{F}}_J$: eigenvectors scaled by corresponding eigenvalues, plotted on spatial mesh for different scale-transition parameters.

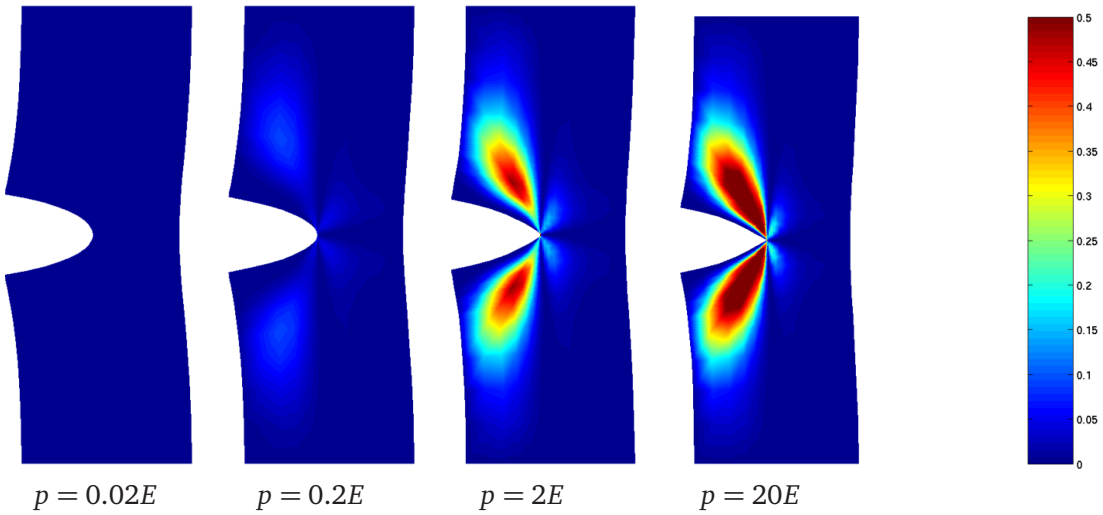

Figure 3.34: Modulus of nodal configurational double force, $\|\bar{\mathbf{F}}_J\|$, plotted continuously, for different of scale-transition parameters.

4 On the Computational Homogenization of a Heterogeneous Continuum

For a material that possesses a heterogeneous microstructure, rather than explicitly resolving each of these heterogeneities in the modelling, we are interested in a methodology to obtain the overall response more efficiently. This can be achieved by a direct multi-scale method or rather a homogenization, which is based on the self-consistent estimates proposed by Hill (1963) and Kröner (1967). The global properties at a material point are obtained based on the averaging of properties over a representative portion of the microstructure. In the computational homogenization this theoretical framework is adopted in order to solve multiscale boundary value problems numerically.

As a step towards the homogenization of material layers, which will be treated in Chapters 5 and 6, in the current chapter, a homogenization framework for a microscopically heterogeneous continuum is considered. First we illuminate the general procedure of computational homogenization including its key theoretical assumptions, see Section 4.1. Thereafter two particular cases of continuum homogenization are considered. First, in Section 4.2, the homogenization framework is presented with a classical continuum at both the macro and the micro level, as illustrated in Figure 4.1. Subsequently in Section 4.3, within the same macro framework a micromorphic mesostructure in the underlying RVE is considered instead. This approach is converse to that of the contributions of Kouznetsova et al. (2002, 2004), who employed the generalized continuum at the macro level. However, the current approach with the generalized continuum at the RVE level shall first of all serve as a foundation for the subsequent development of a homogenization with an interface at the macro level, as will be presented in Chapter 6. By the choice of a micromorphic RVE, the model accounts for size effects occurring due to a relatively large intrinsic microstructure in the material.

The homogenization is accomplished within a continuum-mechanics framework at finite deformations based on the concept of Hill (1972). The notation $\widehat{(\cdot)}$ denotes the quantities at the macro level. When a classical continuum is considered at the RVE level, i. e. in Section 4.2, this RVE embodies the micro level. Differently for the micromorphic RVE, the level of the RVE acts as the meso level, since with the

microcontinua attached to each of its points, a third level namely the micro level comes in.

4.1 General procedure of computational homogenization

A material point $\widehat{\mathscr{P}}$ within the material body $\widehat{\mathscr{B}}$ is considered. While the framework of kinematics and balance relations are given by continuum mechanics, to solve a boundary value problem in $\widehat{\mathscr{B}}$ the constitutive behaviour is needed. In cases when the material body consists of a heterogeneous microstructure that determines its behaviour, a constitutive assumption posed a priori can only give a coarse estimate of the effective constitutive behaviour. Thus instead the local vicinity of a point in $\widehat{\mathscr{B}}$ at the macro scale, i. e. an infinitesimally small material element, is focused at on a finer scale, the micro scale. The further homogenization relies on the assumption that the two considered scales are well separated, i. e. a typical size on the macro scale is much greater than a typical size of the underlying microstructure, $\widehat{L} \gg L$. For the micro scale, a so-called representative volume element $\mathscr{B}$ models the microstructure underlying to the macroscopic material point. Under boundary conditions which are determined by the macroscopic state of deformation, stress, etc., a boundary value problem is defined on this representative volume element. At this level, both the governing balance relations and the constitutive behaviour are known. The goal of this consideration is to return this constitutive information obtained from a finer scale to the macro level.

The key ingredients of the homogenization procedure are the definition of the boundary value problem at the macro level excluding a constitutive framework, the choice of a representative volume element to model the microstructure, the definition of the boundary value problem at the micro level including a constitutive framework, and the actual homogenization with the corresponding boundary conditions to link the two scales.

Continuum on the macro scale. In the described multiscale framework, different kinds of continua can be chosen at the macro level. While the standard choice covers a classical continuum, for instance in the contributions of Kouznetsova et al. (2002, 2004) a second-gradient continuum is employed at the macro level, whereas e. g. Forest et al. (2000), Ebinger et al. (2005) use a Cosserat continuum. By this choice, rather than an entirely local or infinitesimal, a finite vicinity of the material point is considered and thus with the corresponding spatial macro gradients a curvature measure can be delivered to the RVE, which involves a size effect across the scales.

Representative volume element on the micro scale. This representative volume element (RVE) acts as a statistically representative portion of the heterogeneous microstructure (Nemat-Nasser and Hori, 1999). Its size must be chosen such that it is large enough to be representative or rather such that it sufficiently accounts for the character and distribution of the heterogeneities.. Nevertheless it should be much smaller than the specimen considered at the macro level to ensure a scale separation on the one hand, and to achieve an increased efficiency on the other hand. If the material or geometric properties of the underlying microstructures spatially vary within a macro specimen, as e. g. in functionally graded materials, the representative volume element can be chosen differently in different macro regions if only a local periodicity is required.

Besides a continuum representation, any appropriate mechanical framework could be employed at the RVE level, for instance discrete particles to account for granular media, molecular dynamics, or quasi-static atomistics, just to mention a few. Particle assemblies were e. g. considered by Ehlers et al. (2003), Ehlers and Wenz (2004), D'Addetta et al. (2004), Miehe and Dettmar (2004), Dettmar (2006).

Micro–macro transition. The micro–macro transition links the two considered scales, namely the macro continuum point with its underlying RVE. It is based on the averaging of the deformation gradient or strain and the corresponding stress measures and the virtual energy (or power) over the RVE. This volume averages of a quantity $(\bullet)$ over the representative volume element $\mathscr{B}_0$ of material volume V_0 is given as

$$\langle \bullet \rangle := \frac{1}{V_0} \int_{\mathscr{B}_0} (\bullet) \, \mathrm{d}V \,. \tag{4.1}$$

These averages must be equivalent to their corresponding aggregate quantities at the corresponding macro point, i. e. $\langle \bullet \rangle \equiv \widehat{\bullet}$. These corresponding aggregate quantities of stress, deformation measure, and power or virtual work deliver the boundary conditions on the RVE. Especially the virtual work performed within the RVE must balance the virtual work at a macroscopic point, a requirement that is referred to as the Hill condition (Hill, 1972).

As outlined by Miehe et al. (1999a,b) and Bayreuther (2005), the deformation field within the RVE is defined as the superposition of the homogeneous field given by the linear mapping by the macroscopic deformation gradient $\widehat{\boldsymbol{F}}$ and a non-homogeneous fluctuation field $\widetilde{\boldsymbol{w}}$ as:

$$\boldsymbol{\varphi} := \widehat{\boldsymbol{F}} \cdot \boldsymbol{X} + \widetilde{\boldsymbol{w}} \,. \tag{4.2}$$

This mapping is based on (2.1) in case of a classical continuum framework on the

macro scale. This assumption is based on a sufficient separation of scales. It corresponds to he superposition of the microscopic deformation gradient as $\boldsymbol{F} = \widehat{\boldsymbol{F}} + \widetilde{\boldsymbol{F}}$ with $\widetilde{\boldsymbol{F}} := \nabla_X \widetilde{\boldsymbol{w}}$. Thus a condition for this fluctuation field follows:

$$\frac{1}{V_0} \int_{\mathscr{B}_0} \widetilde{\boldsymbol{F}} \, \mathrm{d}V = \frac{1}{V_0} \int_{\partial \mathscr{B}_0} \widetilde{\boldsymbol{w}} \otimes \boldsymbol{N} \, \mathrm{d}A = \boldsymbol{0} \,. \tag{4.3}$$

This conditions restricts the choice of boundary conditions on the RVE, because it is fulfilled for (i) $\widetilde{\boldsymbol{w}} = \boldsymbol{0}$ everywhere in $\mathscr{B}_0$, for (ii) $\widetilde{\boldsymbol{w}} = \boldsymbol{0}$ on the entire RVE boundary $\partial \mathscr{B}_0$, or for (iii) $\widetilde{\boldsymbol{w}}^+ = \widetilde{\boldsymbol{w}}^-$ on opposite boundaries $\partial \mathscr{B}_0^+$ and $\partial \mathscr{B}_0^-$. Case (i), which assumes a homogeneous deformation of the entire RVE, yields the Voigt–Taylor bound (Voigt, 1889, Taylor, 1938), which strongly overestimates the stiffness. The contrary assumption of constant stress over the entire RVE, referred to as Reuss–Sachs bound (Reuss, 1929, Sachs, 1928), yields a strongly underestimated response.

Boundary conditions. Boundary conditions consistent with the Hill condition are imposed on the boundary of the RVE determined by the macroscopic quantities. It is well-known that different types of boundary conditions yield a differently stiff response (Wriggers et al., 2005, Geers et al., 2005). Within the upper and lower bound given by the simplified assumptions of Voigt–Taylor and Reuss–Sachs, the prescription of a linear or rather homogeneous displacements field on the boundary as well as the application of constant traction on the boundary yield a more reasonable intermediate response. Linear displacements on the boundary, $\widetilde{\boldsymbol{w}} = \boldsymbol{0}$ on $\partial \mathscr{B}_0$, yield a stiffer global response, whereas constant boundary tractions lead to a softer global response. Another option is based on the assumption of the periodicity of the superimposed fluctuation field, $\widetilde{\boldsymbol{w}}^+ = \widetilde{\boldsymbol{w}}^-$, on opposite boundaries $\partial \mathscr{B}_0^+$ and $\partial \mathscr{B}_0^-$ (Miehe et al., 1999a,b, 2002a, Kouznetsova, 2002, Geers et al., 2005). The latter alternative of periodic boundary conditions comes along with an intermediately stiff response and is appreciated to give a better estimation for the macro response, compare Kouznetsova (2002) and references cited therein.

Computational homogenization. To make the homogenization available for numerical simulations involving the advantages of the illuminated multiscale approach, within the field of computational mechanics it was translated into so-called computational homogenization approaches. The finite-element based computational homogenization or, in the nomenclature of e. g. Miehe and Koch (2002), *direct micro-to-macro transitions* of e. g. Miehe et al. (1999a, 2002c), Miehe (2003), Michel et al. (1999), Smit et al. (1998), Feyel and Chaboche (2000), Kouznetsova et al. (2001, 2002, 2004) relies on a nested solution involving a discretized boundary value problem at the macro level and many discretized boundary value problem in the underlying RVEs. The macro constitutive behaviour is evaluated at the in-

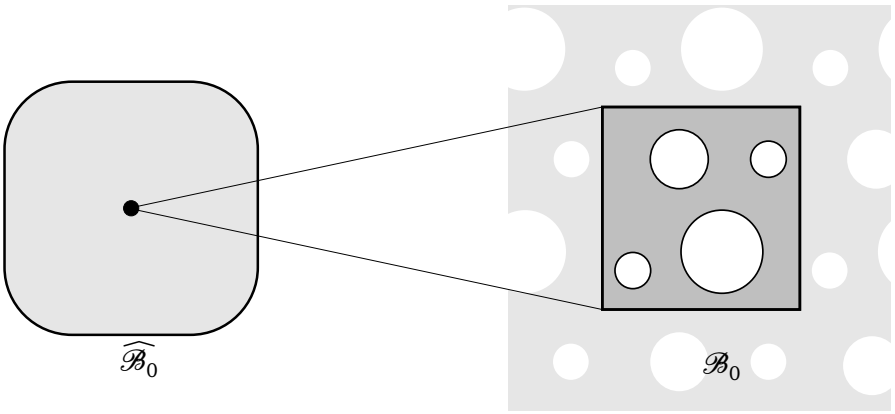

Figure 4.1: Multiscale approach for continuum $\widehat{\mathscr{B}_0}$ with RVE $\mathscr{B}_0$ occupied by classical continuum.

tegration points of each finite element based on a homogenization employing the underlying micro boundary value problem. The aggregate stress and tangent operators of a typical microstructure may exclusively be defined in terms of the discrete reaction forces and the stiffness associated with the kinematic degrees of freedom on the RVE boundary (Miehe and Koch, 2002).

4.2 Homogenization of a continuum with a heterogeneous continuous microstructure

The homogenization between a continuum at the macro level and a continuum at the micro level is introduced here. At both levels the classical continuum formulation of Section 2.2 in the framework of finite deformations is used. The presented first-order homogenization (in the nomenclature of Kouznetsova (2002)) was similarly also described in Hirschberger et al. (2007c). As indicated above and illustrated in Figure 4.1, at the macro level a material body $\widehat{\mathscr{B}_0}$ is considered. The corresponding volume element at a material point $\widehat{\mathscr{P}}$ is resolved by a representative volume element denoted by $\mathscr{B}_0$. The *local* constitutive behaviour at $\widehat{\mathscr{P}}$ is evaluated within this RVE.

4.2.1 Classical continuum formulation at the macro level

The framework of classical continuum mechanics of Section 2.2, used at the macro level, is reviewed for the sake of convenience in Table 4.1. No constitutive assumption is posed at this level. Rather we seek to obtain the constitutive behaviour in a multiscale consideration from the underlying microstructure. Note that at this level body forces can be incorporated.

Table 4.1: Governing equations at the macro and the micro level.

macro boundary value problem		
kinematics	$\widehat{\boldsymbol{x}} = \widehat{\boldsymbol{\varphi}}(\widehat{\boldsymbol{X}}, t)$	$\widehat{\boldsymbol{F}} = \nabla_{\widehat{\boldsymbol{X}}} \widehat{\boldsymbol{\varphi}}$
balance of momentum	$\mathrm{Div}\, \widehat{\boldsymbol{P}} + \widehat{\boldsymbol{b}}_0 = \boldsymbol{0}$	in $\widehat{\mathscr{B}_0}$
Neumann boundary condition	$\widehat{\boldsymbol{t}}_0^{\mathrm{pre}} := \widehat{\boldsymbol{P}} \cdot \widehat{\boldsymbol{N}}$	on $\partial \widehat{\mathscr{B}_0}^{\widehat{P}}$
Dirichlet boundary condition	$\widehat{\boldsymbol{\varphi}}^{\mathrm{pre}} := \widehat{\boldsymbol{\varphi}}$	on $\partial \widehat{\mathscr{B}_0}^{\widehat{\varphi}}$
weak formulation	$\int_{\widehat{\mathscr{B}_0}} \widehat{\boldsymbol{P}} : \delta \widehat{\boldsymbol{F}} \, \mathrm{d}V = \int_{\partial \widehat{\mathscr{B}_0}} \widehat{\boldsymbol{t}}_0 \cdot \delta \widehat{\boldsymbol{\varphi}} \, \mathrm{d}A + \int_{\widehat{\mathscr{B}_0}} \widehat{\boldsymbol{b}}_0 \cdot \delta \widehat{\boldsymbol{\varphi}} \, \mathrm{d}V$	
constitutive formulation	*not stated, but obtained from the micro level*	
micro boundary value problem		
kinematics	$\boldsymbol{x} = \boldsymbol{\varphi}(\boldsymbol{X}, t)$	$\boldsymbol{F} = \nabla_{\boldsymbol{X}} \boldsymbol{\varphi}$
balance of momentum	$\mathrm{Div}\, \boldsymbol{P} = \boldsymbol{0}$	in $\mathscr{B}_0$
Neumann boundary condition	$\boldsymbol{t}_0^{\mathrm{pre}} := \boldsymbol{P} \cdot \boldsymbol{N}$	on $\partial \mathscr{B}_0^{P}$
Dirichlet boundary condition	$\boldsymbol{\varphi}^{\mathrm{pre}} := \boldsymbol{\varphi}$	on $\partial \mathscr{B}_0^{\varphi}$
weak formulation	$\int_{\mathscr{B}_0} \boldsymbol{P} : \delta \boldsymbol{F} \, \mathrm{d}V = \int_{\partial \mathscr{B}_0} \boldsymbol{t}_0 \cdot \delta \boldsymbol{\varphi} \, \mathrm{d}A$	
constitutive formulation	*a priori stated*	

4.2.2 Representative volume element at the micro level occupied by classical continuum

The set of governing equations at the RVE level comprises both the classical continuum framework and a constitutive formulation. Both are adopted from Section (2.2) and are reviewed as well in Table 4.1. In view of the homogenization of the subsequent section, in particular the conversion between surface and volume integrals, body forces are omitted at this level.

Any suitable constitutive behaviour can be attributed to the RVE at the micro level. For instance for a hyperelastic formulation for the stored-energy density, the Piola stress can be derived from the potential-energy density as $\boldsymbol{P} = \mathrm{D}_{\boldsymbol{F}} \mathscr{W}_0$ as already stated in (2.11).

4.2.3 Micro–macro transition: Homogenization

The relation between a macro continuum point and its underlying microstructure is based on the averaging of the decisive quantities over the corresponding representative volume element. These averages are introduced first, before the relation

between them and the corresponding quantities at the macro level, the actual homogenisation, is performed.

Averaging of quantities over the RVE. The volume averages over the RVE of the deformation gradient, the Piola stress, and the virtual work are recalled here:

$$\langle \boldsymbol{F} \rangle = \frac{1}{V_0} \int_{\mathscr{B}_0} \boldsymbol{F} \, \mathrm{d}V \,, \qquad \langle \boldsymbol{P} \rangle = \frac{1}{V_0} \int_{\mathscr{B}_0} \boldsymbol{P} \, \mathrm{d}V \,, \qquad \langle \boldsymbol{P} : \delta \boldsymbol{F} \rangle = \frac{1}{V_0} \int_{\mathscr{B}_0} \boldsymbol{P} : \delta \boldsymbol{F} \, \mathrm{d}V \,. \tag{4.4}$$

The following canonical auxiliary relations (e. g. Miehe (2003), Costanzo et al. (2005) and references cited therein),

$$\boldsymbol{F} = \mathrm{Div}(\boldsymbol{\varphi} \otimes \boldsymbol{I}) \,, \qquad \boldsymbol{P}^{\mathrm{t}} = \mathrm{Div}(\boldsymbol{X} \otimes \boldsymbol{P}) \,, \qquad \boldsymbol{P} : \boldsymbol{F} = \mathrm{Div}(\boldsymbol{\varphi} \cdot \boldsymbol{P}) \,, \tag{4.5}$$

convert the volume integrals in (4.4) to boundary integrals:

$$\langle \boldsymbol{F} \rangle = \frac{1}{V_0} \int_{\partial \mathscr{B}_0} \boldsymbol{\varphi} \otimes \boldsymbol{N} \, \mathrm{d}A, \quad \langle \boldsymbol{P} \rangle = \frac{1}{V_0} \int_{\partial \mathscr{B}_0} \boldsymbol{t}_0 \otimes \boldsymbol{X} \, \mathrm{d}A, \quad \langle \boldsymbol{P} : \delta \boldsymbol{F} \rangle = \frac{1}{V_0} \int_{\partial \mathscr{B}_0} \boldsymbol{t}_0 \cdot \delta \boldsymbol{\varphi} \, \mathrm{d}A. \tag{4.6}$$

These conversions rely on the balance of momentum at the micro level in omission of body forces. The averages over the RVE will be related to the macroscopic quantities next.

Equivalence of RVE averages and macro quantities. The Hill condition (Hill, 1972) requires the virtual work at the macro and the micro level to equal:

$$\widehat{\boldsymbol{P}} : \delta \widehat{\boldsymbol{F}} \equiv \langle \boldsymbol{P} : \delta \boldsymbol{F} \rangle \,. \tag{4.7}$$

It was hence also denoted as the macro-homogeneity condition by Costanzo et al. (2005). Likewise, it is postulated that both the macroscopic deformation gradient $\widehat{\boldsymbol{F}}$ and Piola stress $\widehat{\boldsymbol{P}}$ are equivalent to the respective averages of the deformation gradient and the Piola stress over the RVE:

$$\widehat{\boldsymbol{F}} \equiv \langle \boldsymbol{F} \rangle \,, \qquad \widehat{\boldsymbol{P}} \equiv \langle \boldsymbol{P} \rangle \,. \tag{4.8}$$

From this, we obtain the requirement that the work performed by the respective averages of stress and deformation over the RVE equals the average of the work over the RVE:

$$\langle \boldsymbol{P} \rangle : \langle \delta \boldsymbol{F} \rangle \equiv \langle \boldsymbol{P} : \delta \boldsymbol{F} \rangle \,. \tag{4.9}$$

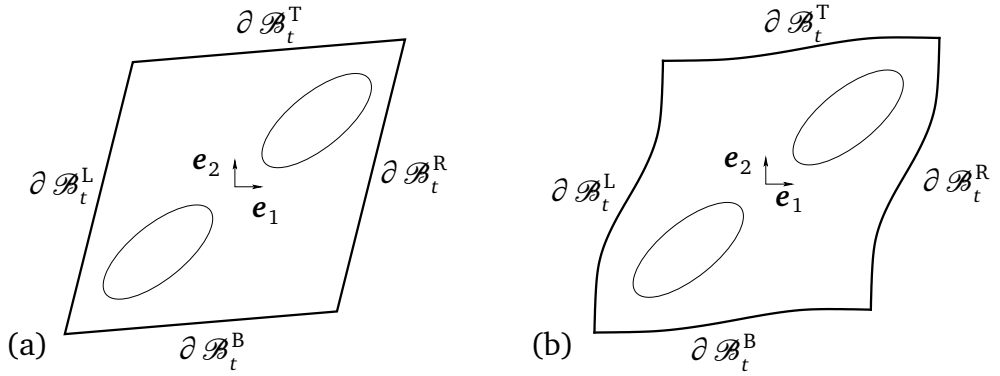

Figure 4.2: Deformed RVE due to (a) linear displacement boundary conditions and (b) periodic displacement boundary conditions.

4.2.4 Micro–macro transition: Boundary conditions on the classical representative volume element

With this equivalence framework at hand, consistent boundary conditions stemming from the macroscopic quantities, are imposed on the RVE using (4.6) and this way complete the micro–macro transition. The most common standard approaches to apply boundary conditions on the RVE based on the macroscopic quantities are linear displacement boundary conditions, periodic displacements and antiperiodic tractions, and constant tractions on the boundary. Any choice of boundary conditions imposed on the RVE must fulfil the Hill condition (4.7) to be appropriate and admissible.

The implementations of the boundary conditions are based on the assumption that the origin of the coordinate system is placed in the volumetric centre of the RVE. Although the options discussed in the sequel are well-established and their admissibility was extensively discussed in the literature, see e. g. Miehe et al. (1999a,b), Kouznetsova (2002), Geers et al. (2005) and references cited therein, we address this issue for each of the presented cases. To this end, the following relations

$$\langle \boldsymbol{P} \rangle : \langle \delta \boldsymbol{F} \rangle = \langle \boldsymbol{P} : \langle \delta \boldsymbol{F} \rangle \rangle = \langle \langle \boldsymbol{P} \rangle : \delta \boldsymbol{F} \rangle \tag{4.10}$$

are used. With these, the Hill condition (4.9) is rewritten as

$$\langle \boldsymbol{P} : \delta \boldsymbol{F} \rangle - \langle \boldsymbol{P} : \langle \delta \boldsymbol{F} \rangle \rangle \doteq 0 \tag{4.11}$$

$$\langle \boldsymbol{P} : \delta \boldsymbol{F} \rangle - \langle \langle \boldsymbol{P} \rangle : \delta \boldsymbol{F} \rangle \doteq 0 \tag{4.12}$$

which must be fulfilled for the displacement and the traction boundary conditions, respectively, to be admissible.

Displacement boundary conditions. The first option is to prescribe the displacement at the entire RVE boundary $\partial \mathscr{B}_0^{\varphi} \equiv \partial \mathscr{B}_0$ as a Dirichlet boundary condition.

This reflects the choice of zero boundary fluctuation in (4.3). Precisely, at large strain, the deformation map is prescribed as a linear mapping of the reference placement $\boldsymbol{X}$ by means of the macro deformation gradient:

$$\boldsymbol{\varphi} \equiv \widehat{\boldsymbol{F}} \cdot \boldsymbol{X} \quad \text{on } \partial \mathscr{B}_0 \,, \tag{4.13}$$

This case is depicted in Figure 4.2(a). Its fulfilment of the Hill condition (4.9) is verified utilizing (4.11):

$$\begin{aligned} \langle \boldsymbol{P} : \delta \boldsymbol{F} \rangle - \langle \boldsymbol{P} : \langle \delta \boldsymbol{F} \rangle \rangle &= \frac{1}{V_0} \int_{\partial \mathscr{B}_0} \delta \boldsymbol{\varphi} \cdot \boldsymbol{P} \cdot \boldsymbol{N} - \langle \delta \boldsymbol{F} \rangle : [\boldsymbol{P} \cdot \boldsymbol{N} \otimes \boldsymbol{X}] \, \mathrm{d}A \\ &= \frac{1}{V_0} \int_{\partial \mathscr{B}_0} [\delta \boldsymbol{\varphi} - \langle \delta \boldsymbol{F} \rangle \cdot \boldsymbol{X}] \cdot \boldsymbol{t}_0 \, \mathrm{d}A = 0 \end{aligned} \tag{4.14}$$

This term identically equals zero if the deformation is prescribed at the entire RVE boundary $\partial \mathscr{B}_0$ according to (4.13).

Traction boundary conditions. Constant traction boundary conditions fulfilling the Hill condition (4.7) can be imposed on the representative volume element as follows:

$$\boldsymbol{t}_0 \equiv \widehat{\boldsymbol{P}} \cdot \boldsymbol{N} \quad \text{on } \partial \mathscr{B}_0 \,. \tag{4.15}$$

These tractions are prescribed at the entire boundary and fulfil the Hill condition (4.9) as shown here:

$$\begin{aligned} \langle \boldsymbol{P} : \delta \boldsymbol{F} \rangle - \langle \langle \boldsymbol{P} \rangle : \delta \boldsymbol{F} \rangle &= \frac{1}{V_0} \int_{\partial \mathscr{B}_0} \delta \boldsymbol{\varphi} \cdot [\boldsymbol{P} - \langle \boldsymbol{P} \rangle] \cdot \boldsymbol{N} \, \mathrm{d}A \\ &= \frac{1}{V_0} \int_{\partial \mathscr{B}_0} \delta \boldsymbol{\varphi} \cdot [\boldsymbol{t}_0 - \langle \boldsymbol{P} \rangle \cdot \boldsymbol{N}] \, \mathrm{d}A \doteq 0 \ . \end{aligned} \tag{4.16}$$

It can easily be observed that for the choice of traction boundary conditions (4.15), with the equivalence $(4.8)_2$ this requirement is fulfilled identically.

Periodic boundary conditions. In case of periodic boundary conditions, the deformation at three independent points of the RVE, i. e. three corner nodes, is prescribed according to (4.13). The deformations of opposite boundaries are forced to

be periodic, i. e.

$$\boldsymbol{\varphi}^{+} - \boldsymbol{\varphi}^{-} \equiv \widehat{\boldsymbol{F}} \cdot [\boldsymbol{X}^{+} - \boldsymbol{X}^{-}] \quad \text{on } \partial \mathscr{B}_0^{\pm}. \tag{4.17}$$

This way they fulfil (4.3) by means of a periodic fluctuation field $\widetilde{\boldsymbol{w}}$ (Miehe et al., 1999a,b, Kouznetsova, 2002). From equilibrium, the tractions on opposite edges follow to be antiperiodic:

$$\boldsymbol{t}_0^{+} + \boldsymbol{t}_0^{-} \equiv \boldsymbol{0} \quad \text{on } \partial \mathscr{B}_0^{\pm}. \tag{4.18}$$

Thereby the positive and negative boundaries, $\partial \mathscr{B}_0^{+}$ and $\partial \mathscr{B}_0^{-}$, respectively, are located on opposite edges of the RVE. Figure 4.2(b) shows the positive boundary, which comprises $\partial \mathscr{B}_\tau^{+} = \partial \mathscr{B}_\tau^{\mathrm{T}} \cup \partial \mathscr{B}_\tau^{\mathrm{T}}$, and the negative boundary is composed of $\partial \mathscr{B}_\tau^{-} = \partial \mathscr{B}_\tau^{\mathrm{L}} \cup \partial \mathscr{B}_\tau^{\mathrm{B}}$ $\tau \in \{0, t\}$.

The admissibility of the periodic boundary conditions with respect to the Hill condition (4.9) can be shown based on that for fully prescribed displacement on the boundary. Particularly, $\langle \delta \boldsymbol{F} \rangle \cdot \boldsymbol{X}$ is a priori periodic for the macro deformation gradient affinely imposed on the RVE. With this, the fluctuation term $\widetilde{\boldsymbol{w}} = [\delta \boldsymbol{\varphi} - \langle \delta \boldsymbol{F} \rangle \cdot \boldsymbol{X}]$ is periodic over opposite boundaries,

$$\frac{1}{V_0} \int_{\partial \mathscr{B}_0} [\delta \boldsymbol{\varphi} - \langle \delta \boldsymbol{F} \rangle \cdot \boldsymbol{X}] \otimes \boldsymbol{N} \, \mathrm{d}A = \boldsymbol{0}. \tag{4.19}$$

Together with antiperiodic tractions (4.18), the integral over opposite boundaries vanishes,

$$\frac{1}{V_0} \int_{\partial \mathscr{B}_0^{-}} [\delta \boldsymbol{\varphi} - \langle \delta \boldsymbol{F} \rangle \cdot \boldsymbol{X}] \cdot \boldsymbol{t}_0 + \frac{1}{V_0} \int_{\partial \mathscr{B}_0^{+}} [\delta \boldsymbol{\varphi} - \langle \delta \boldsymbol{F} \rangle \cdot \boldsymbol{X}] \cdot \boldsymbol{t}_0 = 0. \tag{4.20}$$

Thus the choice of periodic boundary conditions (4.17) proves admissible.

4.2.5 Computational homogenization for a classical representative volume element

The introduced homogenization concept is embedded into a nonlinear finite-element framework. A deformation-driven nested solution scheme of a first-order homogenization in the nomenclature of Kouznetsova (2002) is to be solved. To this end, both the macro specimen and the underlying microstructure are discretized by a finite element mesh. During the simulation of the macro boundary value problem, at each integration point of each finite element at this macro level, the macro constitutive properties are evaluated on the underlying RVE along the lines of the

contributions of Miehe et al. (1999a), Feyel and Chaboche (2000), Kouznetsova et al. (2001, 2002), Geers et al. (2005). To achieve this, a boundary value problem on the discretized RVE is solved subject to boundary conditions imposed by the deformation at the superordinate macro integration point. Due to the geometrically and physically nonlinear framework, this multi-scale computation requires an iterative solution at both the macro and the micro level. A Newton–Raphson scheme will usually be applied.

Nonlinear system at the macro level. Along the lines of the numerical solution scheme presented in Section 3.4.1, at the macro level, the global residual must vanish. For the macro system of equations the assembly is obtained as in (3.60). Therefore the nonlinear system of equations

$$\widehat{\mathsf{K}}_{IL} \cdot \Delta \widehat{\boldsymbol{\varphi}}_L^h = \widehat{\mathsf{f}}_I^{\,\mathrm{ext}} - \widehat{\mathsf{f}}_I^{\,\mathrm{int}}, \tag{4.21}$$

is solved iteratively. Therein the stiffness or rather algorithmic tangent matrix is the derivative of the residual $\widehat{\mathsf{R}}$ with respect to the deformation map $\widehat{\boldsymbol{\varphi}}$. It is analogous to the pure macro contribution $\widehat{\mathsf{K}}_{IL}^{\widehat{\varphi}\widehat{\varphi}}$ in (3.65). Both the residual vector and the stiffness matrix are evaluated element-wise using a Gauss quadrature and assembled to a global system of equations. Therein both the macro stress $\widehat{\boldsymbol{P}}$ and the macro tangent operator $\mathrm{D}_{\widehat{\boldsymbol{F}}}\widehat{\boldsymbol{P}}$ at the particular integration points are obtained from a homogenization at the RVE level.

Evaluation of the RVE boundary value problem. At each integration point of each macro element a computational homogenization must provide both the stress $\widehat{\boldsymbol{P}}$ and the tangent operator $\mathrm{D}_{\widehat{\boldsymbol{F}}}\widehat{\boldsymbol{P}}$. This homogenization in the first place bases on the application of the boundary conditions on the RVE governed by the macroscopic increments of deformation and stress in the current macro iteration step.

According to Section 4.2.4, different types of boundary conditions can be applied onto the RVE. In case of linear displacements on the boundary, the displacements of all boundary nodes are prescribed as shown in Figure 4.2(a). For the periodic case depicted in Figure 4.2(b), only the displacements of three independent corner nodes are prescribed. To enforce the periodicity constraint (4.17), the procedure described in Remark 4.2.1 proves useful. The case of constant tractions at the boundary is somewhat more complicated. A further consideration is omitted here for the sake of brevity since its implementation will not be needed for the later chapters.

With the respective boundary conditions, the micro system of equations is solved. Hereby an a priori constitutive formulation is used in each element of the micro structure. The global residual vector at the micro level must become zero to find equilibrium, compare compare Section 3.4, equation (3.60). This leads to the lin-

earized system of equations with the algorithmic tangent matrix K_{IL},

$$\mathsf{K}_{IL} \cdot \Delta\boldsymbol{\varphi}_L = \mathbf{f}_I^{\text{ext}} - \mathbf{f}_I^{\text{int}}. \tag{4.22}$$

The stiffness matrix of the micro problem is given by the pure macro contribution in (3.65), $\mathsf{K}_{IL} = \mathsf{K}_{IL}^{\varphi\varphi}$. With the displacement boundary condition stemming from the current increment of the macro deformation gradient, an iterative solution algorithm (e. g. Newton–Raphson) is used to find the solution at (micro) equilibrium. This solution procedure is straightforward in the case of fully prescribed boundary displacements. For the periodic boundary conditions the periodicity must be involved in the system during the solution. With this information at hand the system is first reduced, then the current iteration step is solved. After this, the deformations of all nodes are gathered for a new iteration. see Remark 4.2.1.

Remark 4.2.1 (Periodicity constraint) *For periodic displacement and anti-periodic traction on the RVE boundary the periodicity constraints must be imposed before the solution of the system is performed. We transform the system* (4.22) *towards a new system only formulated in terms of independent degrees of freedom*

$$\mathsf{K}^\star \cdot \Delta\boldsymbol{\varphi}_{\text{i}}^h = \Delta\mathbf{f}^\star$$

as proposed by Kouznetsova (2002). These independent degrees of freedom comprise those of all corner nodes, those on the negative boundaries (left and bottom nodes), as well as those in the interior of the RVE mesh, while all the other nodes, i. e. the positive boundary excluding corner nodes, contribute the dependent degrees of freedom. Thereby the transformed stiffness matrix and the transformed incremental load vector read:

$$\begin{aligned}\mathsf{K}^\star &= \mathsf{K}_{\text{ii}} + \mathsf{C}_{\text{di}}^{\text{t}} \cdot \mathsf{K}_{\text{id}} + \mathsf{K}_{\text{id}} \cdot \mathsf{C}_{\text{di}} + \mathsf{C}_{\text{di}}^{\text{t}} \cdot \mathsf{K}_{\text{dd}} \cdot \mathsf{C}_{\text{di}} \\ \Delta\mathbf{f}^\star &= \Delta\mathbf{f}_{\text{i}} + \mathsf{C}_{\text{di}}^{\text{t}} \cdot \Delta\mathbf{f}_{\text{d}},\end{aligned}$$

which is based on the relation $\Delta\boldsymbol{\varphi}_{\text{d}} = \mathsf{C}_{\text{di}} \cdot \Delta\boldsymbol{\varphi}_{\text{i}}$ between the dependent and the independent degrees of freedom with the so-called dependency matrix C_{di}. In this case, the deformation is prescribed in the reduced system at the corner nodes only.

In the special case of an infinitesimal deformation framework, when a linear systems of equations is to be solved once, the degrees of freedom of the internal nodes are also attributed to the dependent degrees of freedom.

Other techniques to enforce the periodicity have been proposed in the literature. For instance Miehe (2003) proposes the use of a Lagrange multiplier, which appears rather expensive, but has the advantage that arbitrarily shaped representative volume elements can be considered as opposed to only rectangular ones. This procedures and the alternative of using a penalty term were also discussed by Bayreuther (2005), Dettmar (2006). The periodicity can also be achieved by the the modification of the basis func-

tions of the respective degrees of freedom on the positive and corresponding negative boundary of the RVE.

Homogenized macro stress and tangent operator. Once the micro solution has been obtained iteratively, the macroscopic stress and tangent operator are computed from a homogenization. To this end, the reaction at all boundary nodes the deformation is prescribed at, is extracted. They deliver the macro response based on the relation 4.8 between the macro stress and the average micro stress. In the case of linear displacement boundary conditions, all boundary nodes are taken into account, whereas for periodic boundary conditions, only the three independent boundary nodes are considered. In each of these cases a condensation is applied to the stiffness matrix at the solved state to extract the contributions of these nodes only.

With the equivalence $(4.8)_2$ and the average $(4.6)_2$, the macro Piola stress $\widehat{\boldsymbol{P}}$ is discretely evaluated as a summation over all prescribed boundary nodes:

$$\widehat{\boldsymbol{P}} = \frac{1}{V_0} \sum_{I}^{n_{\text{pre}}} \mathsf{f}_I \otimes \boldsymbol{X}_I \,. \tag{4.23}$$

With (4.22), the tangent operator in the relation $\Delta\widehat{\boldsymbol{P}} = \partial_{\bar{\boldsymbol{F}}}\widehat{\boldsymbol{P}} : \Delta\widehat{\boldsymbol{F}}$ is extracted. Particularly, the following steps are undertaken:

$$\begin{aligned}\Delta\widehat{\boldsymbol{P}} &= \frac{1}{V_0} \sum_{I}^{n_{\text{pre}}} \Delta\mathsf{f}_I^{\text{ext}} \otimes \boldsymbol{X}_I = \frac{1}{V_0} \sum_{I}^{n_{\text{pre}}} \sum_{L}^{n_{\text{pre}}} [\mathsf{K}_{IL} \cdot \Delta\boldsymbol{\varphi}_L] \otimes \boldsymbol{X}_I \\ &= \frac{1}{V_0} \sum_{I}^{n_{\text{pre}}} \sum_{L}^{n_{\text{pre}}} \left[\mathsf{K}_{IL}^{\varphi\varphi} \cdot \Delta\widehat{\boldsymbol{F}} \cdot \boldsymbol{X}_L\right] \otimes \boldsymbol{X}_I = \left[\frac{1}{V_0} \sum_{I}^{n_{\text{pre}}} \sum_{L,M}^{n_{\text{pre}}} \mathsf{K}_{IL}^{\varphi\varphi} \,\overline{\otimes}\, [\boldsymbol{X}_L \otimes \boldsymbol{X}_I]\right] : \Delta\widehat{\boldsymbol{F}} \,.\end{aligned}$$

The term in brackets represents the homogenized macro tangent operator, i. e.

$$\widehat{\mathsf{A}} \equiv \partial_{\bar{\boldsymbol{F}}}\widehat{\boldsymbol{P}} = \frac{1}{V_0} \sum_{I}^{n_{\text{pre}}} \sum_{L}^{n_{\text{pre}}} \mathsf{K}_{IL} \,\overline{\otimes}\, [\boldsymbol{X}_L \otimes \boldsymbol{X}_I] \,. \tag{4.24}$$

With both the homogenized stress and the tangent operator, the macro boundary value problem is complete and it can be solved.

4.3 Computational homogenization of a continuum with micromorphic mesostructure

Based on the framework reviewed in the previous section, a procedure for the modelling of a continuous material with an underlying (heterogeneous) mesostructure that consist of a microstructured material is introduced. While at the macro level,

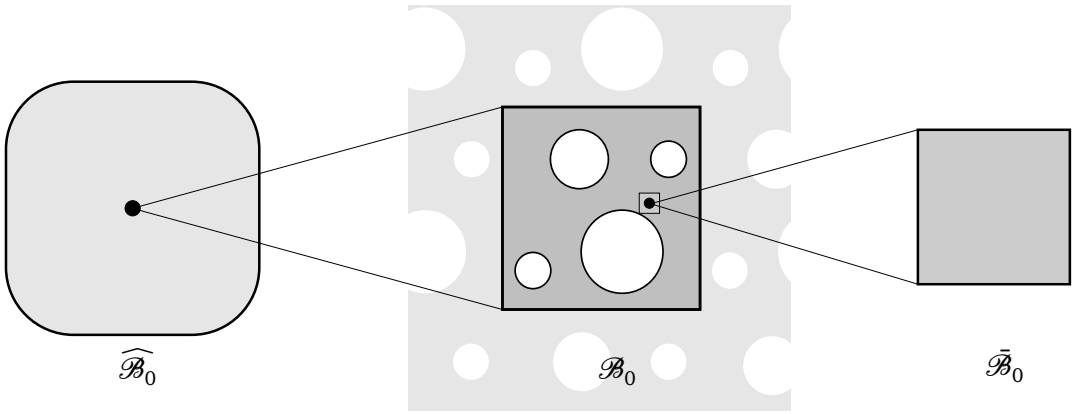

Figure 4.3: Multiscale approach for continuum $\widehat{\mathscr{B}}_0$ with RVE occupied by micromorphic continuum $\mathscr{B}_0$ with microcontinua $\bar{\mathscr{B}}_0$.

the classical continuum formulation is preserved, we alternatively employ the micromorphic formulation discussed in Chapter 3 for the representative volume element, see Figure 4.3. With this choice, the model shall account for size effects due to an intrinsic microstructure in the underlying material. Above all, this framework prepares the homogenization applied to material interfaces at the macro level which will be proposed in Chapter 6.

For this enhanced homogenization framework, the continuum formulation at the macro level is directly adopted from Section 4.2.1 and recalled in Table 4.2. Based on a micromorphic framework at the RVE level, which is briefly reviewed Section 4.3.1, the homogenization scheme of Section 4.2.3 is refashioned, such that it allows to determine equivalent macroscopic quantities based on the averages of the respective quantities over the micromorphic RVE. The slightly more sophisticated computational framework is treated in Section 4.3.4.

4.3.1 Micromorphic representative volume element at the meso level

For the micromorphic RVE, the continuum and constitutive framework as presented in Chapter 3 are adopted. Nevertheless, unlike in the simplified spatial-motion problem of Section 3.2.1, prescribed spatial tractions and double tractions at the boundary are necessary to consider here, see Remark 3.2.1. The governing equations are gathered in Table (4.2). The boundary value problem on the RVE level needs to be solved under boundary conditions imposed by the continuum point at the macro level. Thereby the constitutive behaviour should be chosen appropriately for a specific material. If a hyperelastic framework is suitable, for instance the micromorphic formulation for the stored-energy density (3.49)–(3.50) following the contribution of Hirschberger et al. (2007b) can be adopted.

Table 4.2: Governing equations at the macro and the meso/micro level

macro boundary value problem		
	kinematics	
macro deformation	$\widehat{\boldsymbol{x}} = \widehat{\boldsymbol{\varphi}}(\widehat{\boldsymbol{X}}, t)$	$\widehat{\boldsymbol{F}} = \nabla_{\widehat{\boldsymbol{X}}} \widehat{\boldsymbol{\varphi}}$
	balance of momentum	
weak formulation	$\int_{\widehat{\mathscr{B}_0}} \widehat{\boldsymbol{P}} : \delta \widehat{\boldsymbol{F}} \, \mathrm{d}V = \int_{\partial \widehat{\mathscr{B}_0}} \widehat{\boldsymbol{t}}_0 \cdot \delta \widehat{\boldsymbol{\varphi}} \, \mathrm{d}A + \int_{\widehat{\mathscr{B}_0}} \widehat{\boldsymbol{b}}_0 \cdot \delta \widehat{\boldsymbol{\varphi}} \, \mathrm{d}V$	
macro balance	$\mathrm{Div}\, \widehat{\boldsymbol{P}} + \widehat{\boldsymbol{b}}_0 = \boldsymbol{0}$	in $\widehat{\mathscr{B}_0}$
	boundary conditions	
traction	$\widehat{\boldsymbol{t}}_0^{\mathrm{pre}} := \widehat{\boldsymbol{P}} \cdot \widehat{\boldsymbol{N}}$	on $\partial \widehat{\mathscr{B}_0^P}$
macro deformation	$\widehat{\boldsymbol{\varphi}}^{\mathrm{pre}} := \widehat{\boldsymbol{\varphi}}$	on $\partial \widehat{\mathscr{B}_0^{\varphi}}$
	constitutive formulation	
	obtained from the meso level	
meso boundary value problem		
	kinematics	
meso map, gradient	$\boldsymbol{x} = \boldsymbol{\varphi}(\boldsymbol{X})$	$\boldsymbol{F} = \nabla_{\boldsymbol{X}} \boldsymbol{\varphi}$
micro map, gradient	$\bar{\boldsymbol{x}} = \bar{\boldsymbol{F}} \cdot \bar{\boldsymbol{X}}$	$\bar{\boldsymbol{G}} = \nabla_{\boldsymbol{X}} \bar{\boldsymbol{F}}$
	balance of momentum	
weak formulation	$\int_{\mathscr{B}_0} \boldsymbol{P} : \delta \boldsymbol{F} + \bar{\boldsymbol{P}} : \bar{\boldsymbol{F}} + \bar{\boldsymbol{Q}} \vdots \bar{\boldsymbol{G}} \, \mathrm{d}V = \int_{\partial \mathscr{B}_0} \boldsymbol{t}_0 \cdot \delta \boldsymbol{\varphi} + \bar{\boldsymbol{t}}_0 : \delta \bar{\boldsymbol{F}} \, \mathrm{d}A$	
meso balance	$\mathrm{Div}\, \boldsymbol{P} = \boldsymbol{0}$	in $\mathscr{B}_0$
micro balance	$\mathrm{Div}\, \bar{\boldsymbol{Q}} - \bar{\boldsymbol{P}} = \boldsymbol{0}$	in $\mathscr{B}_0$
	boundary conditions	
traction, double traction	$\boldsymbol{t}_0^{\mathrm{pre}} := \boldsymbol{P} \cdot \boldsymbol{N}$ on $\partial \mathscr{B}_0^P$,	$\bar{\boldsymbol{t}}_0^{\mathrm{pre}} := \bar{\boldsymbol{Q}} \cdot \boldsymbol{N}$ on $\partial \mathscr{B}_0^{\bar{Q}}$
meso, micro deformation	$\boldsymbol{\varphi}^{\mathrm{pre}} := \boldsymbol{\varphi}$ on $\partial \mathscr{B}_0^{\varphi}$,	$\bar{\boldsymbol{F}}^{\mathrm{pre}} := \bar{\boldsymbol{F}}$ on $\partial \mathscr{B}_0^{\bar{F}}$
	constitutive formulation	
	a priori stated	

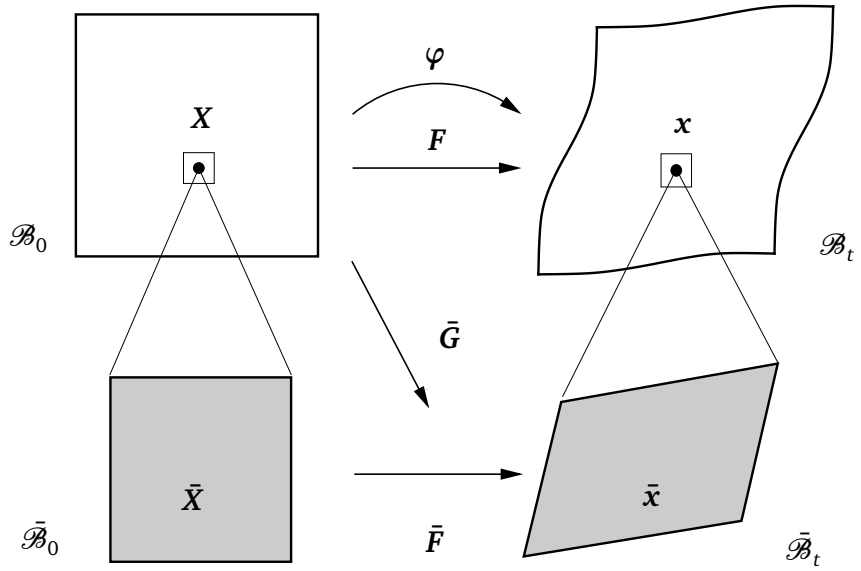

Figure 4.4: Micromorphic representative volume element: deformation mapping.

4.3.2 Meso–macro transition: Homogenization

The relation between a macro-continuum point $\widehat{\mathscr{P}}$ and its underlying meso- and microstructure is based on the averaging of the decisive quantities over the corresponding representative volume element. Although the continuum at the meso/micro level is of higher order, this micro–macro transition falls into the first-order homogenization (Kouznetsova, 2002) due to the classical continuum at the macro level.

The averages of the meso deformation gradient and the Piola-type meso stress $(4.6)_{1,2}$ within the RVE are related to the deformation gradient and the stress at the macro level analogously to (4.8),

$$\widehat{\boldsymbol{F}} \equiv \langle \boldsymbol{F} \rangle \,, \qquad\qquad \widehat{\boldsymbol{P}} \equiv \langle \boldsymbol{P} \rangle \,. \tag{4.25}$$

The Hill condition must be fulfilled, which requires the total virtual work at the macro continuum point to equal the average of the virtual work over the RVE. While the first is identical to the macro virtual work in (4.7), the latter quantity also involves contributions of the micro deformation map and its gradient:

$$\widehat{\boldsymbol{P}} : \delta\widehat{\boldsymbol{F}} \equiv \langle \boldsymbol{P} : \delta\boldsymbol{F} + \bar{\boldsymbol{P}} : \delta\bar{\boldsymbol{F}} + \bar{\boldsymbol{Q}} :\cdot \delta\bar{\boldsymbol{G}} \rangle \,. \tag{4.26}$$

For these choices of the scale transition for deformation gradient and the Piola stress, (4.25), it follows that the product of the averages of the deformation gradient and the stress, respectively, has to equal the average of the virtual work over the micro-

morphic RVE:

$$\langle \boldsymbol{P} \rangle : \langle \delta \boldsymbol{F} \rangle = \langle \boldsymbol{P} : \delta \boldsymbol{F} + \bar{\boldsymbol{P}} : \delta \bar{\boldsymbol{F}} + \bar{\boldsymbol{Q}} \vdots \delta \bar{\boldsymbol{G}} \rangle \,. \tag{4.27}$$

4.3.3 Meso–macro transition: Boundary conditions on the micromorphic representative volume element

In order to achieve the scale transition, boundary conditions stemming from the macro level are to be imposed on the micromorphic RVE. Three different types of boundary conditions are presented and their admissibility with respect to the Hill condition is shown in each case.

In view of the cases of prescribed deformation and constant traction on the the micromorphic RVE boundary the Hill condition (4.27) is rewritten as

$$\langle \boldsymbol{P} : \delta \boldsymbol{F} + \bar{\boldsymbol{P}} : \delta \bar{\boldsymbol{F}} + \bar{\boldsymbol{Q}} \vdots \delta \bar{\boldsymbol{G}} \rangle - \langle \boldsymbol{P} : \langle \delta \boldsymbol{F} \rangle \rangle \doteq 0 \,, \tag{4.28}$$

$$\langle \boldsymbol{P} : \delta \boldsymbol{F} + \bar{\boldsymbol{P}} : \delta \bar{\boldsymbol{F}} + \bar{\boldsymbol{Q}} \vdots \delta \bar{\boldsymbol{G}} \rangle - \langle \langle \boldsymbol{P} \rangle : \delta \boldsymbol{F} \rangle \doteq 0 \,, \tag{4.29}$$

using the relation (4.10).

Deformation boundary conditions. We propose the following linear deformation boundary conditions following (3.12) as

$$\boldsymbol{\varphi} \equiv \widehat{\boldsymbol{F}} \cdot \boldsymbol{X} \quad \text{on } \partial \mathscr{B}_0 \,, \qquad\qquad \bar{\boldsymbol{F}} \equiv \boldsymbol{I} \quad \text{on } \partial \mathscr{B}_0 \,, \tag{4.30}$$

to be prescribed at the entire boundary. We can show that this choice fulfils the Hill condition using (4.28):

$$\begin{aligned} &\langle \boldsymbol{P} : \delta \boldsymbol{F} + \bar{\boldsymbol{P}} : \delta \bar{\boldsymbol{F}} + \bar{\boldsymbol{Q}} \vdots \delta \bar{\boldsymbol{G}} \rangle - \langle \boldsymbol{P} : \langle \delta \boldsymbol{F} \rangle \rangle \\ =& \frac{1}{V_0} \int_{\partial \mathscr{B}_0} \delta \boldsymbol{\varphi} \cdot \boldsymbol{P} \cdot \boldsymbol{N} - \langle \delta \boldsymbol{F} \rangle : [\boldsymbol{P} \cdot \boldsymbol{N} \otimes \boldsymbol{X}] + \delta \bar{\boldsymbol{F}} : \bar{\boldsymbol{Q}} \cdot \boldsymbol{N} \, \mathrm{d}A \\ =& \frac{1}{V_0} \int_{\partial \mathscr{B}_0} [\delta \boldsymbol{\varphi} - \langle \delta \boldsymbol{F} \rangle \cdot \boldsymbol{X}] \cdot \boldsymbol{t}_0 + \delta \bar{\boldsymbol{F}} : \bar{\boldsymbol{t}}_0 \, \mathrm{d}A = 0 \,. \end{aligned} \tag{4.31}$$

This term identically equals zero if both the meso and the micro deformation is prescribed as (4.30) at the entire RVE boundary $\partial \mathscr{B}_0$ assuming the equivalence of the deformation gradient, $(4.25)_1$.

Traction boundary conditions. Boundary conditions prescribing uniform tractions and double tractions on the entire boundary of the micromorphic representa-

tive volume element can be imposed as

$$\boldsymbol{t}_0 \equiv \widehat{\boldsymbol{P}} \cdot \boldsymbol{N} \quad \text{on } \partial\mathscr{B}_0\,, \qquad\qquad \bar{\boldsymbol{t}}_0 \equiv \boldsymbol{0} \quad \text{on } \partial\mathscr{B}_0 \tag{4.32}$$

based on the Neumann boundary condition (3.15).

Their admissibility is shown straightforwardly with identity (4.29) in the following steps:

$$\begin{aligned} &\langle \boldsymbol{P} : \delta\boldsymbol{F} + \bar{\boldsymbol{P}} : \delta\bar{\boldsymbol{F}} + \bar{\boldsymbol{Q}} :\cdot \delta\bar{\boldsymbol{G}} \rangle - \langle \langle \boldsymbol{P} \rangle : \delta\boldsymbol{F} \rangle \\ =&\frac{1}{V_0} \int\limits_{\partial\mathscr{B}_0} \delta\boldsymbol{\varphi} \cdot [\boldsymbol{P} - \langle \boldsymbol{P} \rangle] \cdot \boldsymbol{N} + \delta\bar{\boldsymbol{F}} : \bar{\boldsymbol{Q}} \cdot \boldsymbol{N} \, \mathrm{d}A \\ =&\frac{1}{V_0} \int\limits_{\partial\mathscr{B}_0} \delta\boldsymbol{\varphi} \cdot [\boldsymbol{t}_0 - \langle \boldsymbol{P} \rangle \cdot \boldsymbol{N}] + \delta\bar{\boldsymbol{F}} : \bar{\boldsymbol{t}}_0 \, \mathrm{d}A \doteq 0 \ . \end{aligned} \tag{4.33}$$

From this result, it can easily be seen that for the choice of traction boundary conditions (4.32), because with the Piola-type stress equivalence $(4.25)_2$, this requirement is fulfilled identically.

Periodic boundary conditions. We propose the periodic deformation and antiperiodic traction boundary conditions for a micromorphic RVE as

$$\boldsymbol{\varphi}^+ - \boldsymbol{\varphi}^- \equiv \widehat{\boldsymbol{F}} \cdot [\boldsymbol{X}^+ - \boldsymbol{X}^-] \quad \text{on } \partial\mathscr{B}_0^{\pm}\,, \qquad \boldsymbol{t}_0^+ + \boldsymbol{t}_0^- \equiv \boldsymbol{0} \quad \text{on } \partial\mathscr{B}_0^{\pm}\,, \tag{4.34}$$

$$\bar{\boldsymbol{F}}^+ - \bar{\boldsymbol{F}}^- \equiv \boldsymbol{0} \quad \text{on } \partial\mathscr{B}_0^{\pm}\,, \qquad \bar{\boldsymbol{t}}_0^+ + \bar{\boldsymbol{t}}_0^- \equiv \boldsymbol{0} \quad \text{on } \partial\mathscr{B}_0^{\pm}\,. \tag{4.35}$$

Herein the positive boundary $\partial\mathscr{B}_0^+$ for instance consists of the top and the right edge, whereas the left and the bottom edge constitute the negative boundary $\partial\mathscr{B}_0^-$, analogously to the sketch in Figure 4.2(b) and the literature (Kouznetsova, 2002, Miehe, 2003). Within the case of periodic boundary conditions, the deformation at the corners of the RVE is prescribed according to (4.30).

The admissibility of the periodic boundary conditions can be verified based on the Hill condition (4.27). From the derivation (4.31) for prescribed deformations, it is straightforward to recognize that periodicity in deformations and anti-periodicity in tractions (4.34)–(4.35) fulfil the condition (4.28). Particularly, $\langle \delta\boldsymbol{F} \rangle \cdot \boldsymbol{X}$ is a priori periodic for the macro-deformation affinely imposed on the RVE. With this, the fluctuation term $\widetilde{\boldsymbol{w}} = [\delta\boldsymbol{\varphi} - \langle \delta\boldsymbol{F} \rangle \cdot \boldsymbol{X}]$ is periodic over opposite boundaries,

$$\frac{1}{V_0} \int\limits_{\partial\mathscr{B}_0} [\delta\boldsymbol{\varphi} - \langle \delta\boldsymbol{F} \rangle \cdot \boldsymbol{X}] \otimes \boldsymbol{N} \, \mathrm{d}A = \boldsymbol{0}\,. \tag{4.36}$$

Together with the antiperiodic tractions (4.34), the integral over opposite bound-

aries vanishes:

$$\frac{1}{V_0}\int\limits_{\partial\mathscr{B}_0^-}[\delta\boldsymbol{\varphi}-\langle\delta\boldsymbol{F}\rangle\cdot\boldsymbol{X}]\cdot\boldsymbol{t}_0+\frac{1}{V_0}\int\limits_{\partial\mathscr{B}_0^+}[\delta\boldsymbol{\varphi}-\langle\delta\boldsymbol{F}\rangle\cdot\boldsymbol{X}]\cdot\boldsymbol{t}_0=0\,. \tag{4.37}$$

The same holds for the micro deformation map. With the trivial assumption $(4.30)_2$ it is a priori periodic,

$$\frac{1}{V_0}\int\limits_{\partial\mathscr{B}_0^-}\delta\bar{\boldsymbol{F}}:\bar{\boldsymbol{t}}_0\,\mathrm{d}A+\frac{1}{V_0}\int\limits_{\partial\mathscr{B}_0^+}\delta\bar{\boldsymbol{F}}:\bar{\boldsymbol{t}}_0\,\mathrm{d}A=0\,. \tag{4.38}$$

For the antiperiodic double tractions (4.35) the sum of these two integrals vanishes. Thus the present choice of periodic boundary conditions (4.34)–(4.35) proves admissible.

4.3.4 Computational homogenization for a micromorphic representative volume element

The computational homogenization between a classical continuum at the macro level and a micromorphic representative volume element follows the procedure of Section 4.2.5. Compared to the classical case, the system of equations at the level of the representative volume element exacerbates as described in Section 3.4.

Micromorphic system of equations. The problem on the RVE level consists of the coupled problem described in Equation (3.64). In the solved state when equilibrium is reached, this system of equation reduces to

$$\begin{bmatrix}\mathsf{K}_{IL}^{\varphi\varphi} & \mathsf{K}_{IM}^{\varphi\bar{F}}\\ \mathsf{K}_{JL}^{\bar{F}\varphi} & \mathsf{K}_{JM}^{\bar{F}\bar{F}}\end{bmatrix}\begin{bmatrix}\Delta\boldsymbol{\varphi}_L^h\\ \Delta\bar{\boldsymbol{F}}_M^h\end{bmatrix}=\begin{bmatrix}\mathsf{f}_I^{\mathrm{pre}}\\ \bar{\mathsf{f}}_J^{\mathrm{pre}}\end{bmatrix} \tag{4.39}$$

and yields the spatial reaction force $\mathsf{f}_I^{\mathrm{pre}}$ and double force $\bar{\mathsf{f}}_J^{\mathrm{pre}}$ at the boundary nodes with prescribed deformation.

Homogenized macro stress and tangent operator. The sought-for macroscopic quantities, i. e. the Piola stress $\widehat{\boldsymbol{P}}$ and the tangent operator $\widehat{\mathbf{A}}=\partial_{\widehat{F}}\widehat{\boldsymbol{P}}$, at the superordinate integration point of the macro element are extracted from the micro system analogously to Section 4.2.5. The macro Piola stress is obtained based on

the average $(4.6)_2$ in terms of the RVE boundary contributions as

$$\widehat{\boldsymbol{P}} = \frac{1}{V_0} \sum_{I}^{n_{\text{pre}}} \mathsf{f}_I^{\text{pre}} \otimes \boldsymbol{X}_I \,. \tag{4.40}$$

The summation runs over all prescribed boundary nodes I. The tangent operator is derived from the increment of the macro Piola stress (4.40). Thereby the spatial force given in the first row of the coupled meso/micro system is extracted (4.39):

$$\begin{aligned}
\Delta\widehat{\boldsymbol{P}} &= \frac{1}{V_0} \sum_{I}^{n_{\text{pre}}} \Delta\mathsf{f}_I^{\text{pre}} \otimes \boldsymbol{X}_I \\
&= \frac{1}{V_0} \sum_{I}^{n_{\text{pre}}} \sum_{L,M}^{n_{\text{pre}}} [\mathsf{K}_{IL}^{\varphi\varphi} \cdot \Delta\boldsymbol{\varphi}_L + \mathsf{K}_{IM}^{\varphi\bar{F}} \cdot \Delta\bar{\boldsymbol{F}}_M] \otimes \boldsymbol{X}_I \\
&= \frac{1}{V_0} \sum_{I}^{n_{\text{pre}}} \sum_{L,M}^{n_{\text{pre}}} \left[\mathsf{K}_{IL}^{\varphi\varphi} \cdot \Delta\widehat{\boldsymbol{F}} \cdot \boldsymbol{X}_L + \mathsf{K}_{IM}^{\varphi\bar{F}} \cdot \Delta\bar{\boldsymbol{F}}_M \right] \otimes \boldsymbol{X}_I \\
&= \left[\frac{1}{V_0} \sum_{I}^{n_{\text{pre}}} \sum_{L}^{n_{\text{pre}}} \mathsf{K}_{IL}^{\varphi\varphi} \,\overline{\otimes}\, [\boldsymbol{X}_L \otimes \boldsymbol{X}_I] \right] : \Delta\widehat{\boldsymbol{F}} \,.
\end{aligned} \tag{4.41}$$

In the derivation the identity $\Delta\widehat{\boldsymbol{F}}_M = \boldsymbol{0}$ follows from the prescribed micro deformation map (4.30) at the boundary. The term in brackets is identified as the tangent operator

$$\widehat{\mathsf{A}} = \frac{1}{V} \sum_{I}^{n_{\text{pre}}} \sum_{L}^{n_{\text{pre}}} \mathsf{K}_{IL}^{\varphi\varphi} \,\overline{\otimes}\, [\boldsymbol{X}_L \otimes \boldsymbol{X}_I] \,. \tag{4.42}$$

Note that different assumptions of the boundary conditions will yield a different macro stress and tangent.

With these two quantities at hand, the macro boundary value problem is entirely defined and can be solved iteratively.

5 Computational Homogenization of Heterogeneous Material Layers

Besides bulk materials, in many engineering applications thin layers of a certain material are used. These for instance occur as adhesive bonding layers e. g. in composites, masonry, etc. In most cases, the material in the connecting layer is significantly weaker than the surrounding bulk material and thus the deformation will be strongly localized to this layer. Consequently, in a mechanical description they can be considered separately from the bulk, for instance as a cohesive interface. Cases in which the material of such a layer possesses a heterogeneous microstructure, which governs its global behaviour, call for a determination of its constitutive properties based on this microstructure. This motivates to customise the afore-discussed bulk homogenization to these layers.

The key issue of the current chapter is to account for the underlying microstructure of the material layer in an appropriate and efficient way. To this end, we in fact choose the representation of the layer as a cohesive interface and avail ourselves of the homogenization approach, which provides an appropriate framework to relate the mechanical behaviour within the different spatial scales of observation, as described in Chapter 4. Following Hirschberger et al. (2008a), the material layer at the macro scale is treated as a cohesive interface situated within a continuum. The governing quantities in the cohesive interface, i. e. the opening separation and the cohesive traction, are determined based on the underlying microstructure rather than employing an a priori constitutive assumption coined as a cohesive traction–separation law. At the micro level, a representative volume element (RVE) of the material layer advocates its heterogeneous microstructure as illustrated in Figure 5.1. The micro–macro transition is achieved based upon the averaging of the governing kinematic, stress and energetic quantities over this RVE and their equivalence to the traction, the separation, and the virtual work performed in the interface. Thereby the initial height of the material layer itself represents the height of the RVE. Boundary conditions stemming from the cohesive interface are imposed on the microstructure. In a deformation-driven procedure they are governed by the vectorial representation of the opening. These must be chosen consistently such that they fulfil the Hill-condition, which ensures the equivalence of the macro and the

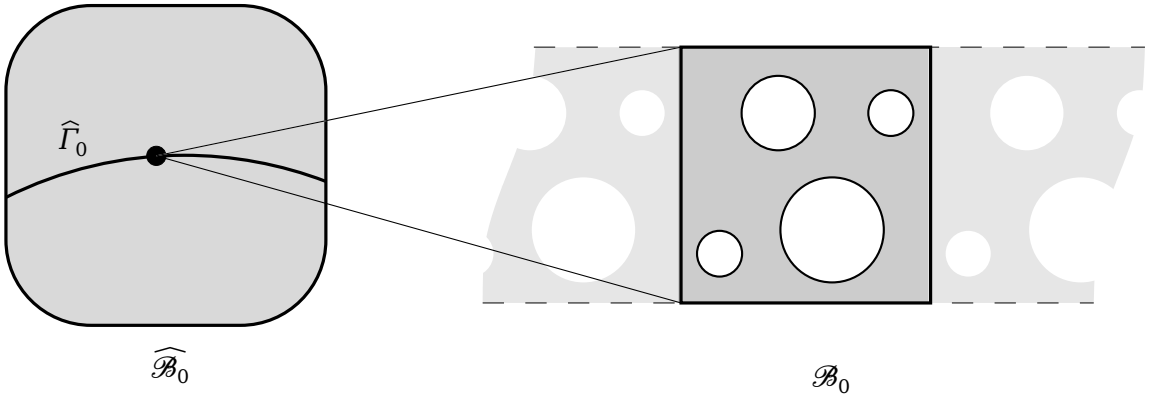

Figure 5.1: Multiscale framework for material layer with heterogeneous microstructure.

micro response. Moreover these boundary conditions shall account for the interface geometry and capture the occurring deformation modes, i. e. a shearing and tensile mode that emerge from the vectorial representation. The homogenization approach is implemented into a computational homogenization along the lines of the approaches of Miehe et al. (1999a, 2002b), Miehe and Koch (2002), Miehe (2003), Kouznetsova et al. (2001, 2002, 2004) for a classical continuum, which were reviewed in Section 4.2.

Here within a geometrically nonlinear multiscale finite-element framework, the material layer is at the macro level represented by a cohesive interface element (see e. g. the contributions of Xu and Needleman (1993), Schellekens and de Borst (1993a), Mergheim et al. (2004), van den Bosch et al. (2008), Utzinger et al. (2008, 2007) and references cited therein) located within the bulk finite elements. In a two-dimensional continuum framework, which is the focus in this chapter, the interface elements are one-dimensional. The multiscale numerical solution is performed by involving a microstructure at the integration points of this interface element. This microstructure advocated by an RVE, is subject to the customised boundary conditions stemming from the interface. Based upon a computational homogenization along the lines of Section 4.2.5, the required macroscopic constitutive quantities are extracted at the boundaries of the RVEs.

At the macro level, the contribution of these interface elements to the global stiffness and the residual is obtained by numerical integration that involves vectorial traction and separation quantities rather than the complete stress and strain tensor. The constitutive relation between the traction and the interface separation is numerically evaluated at each integration point of the interface element via the finite element solution of the mesostructural boundary value problem.

Outline. The remainder of this chapter is structured as follows: In Section 5.1, we present the continuum-mechanics framework at the macro level with the material layer treated as a cohesive interface. In the following Section 5.2, the governing

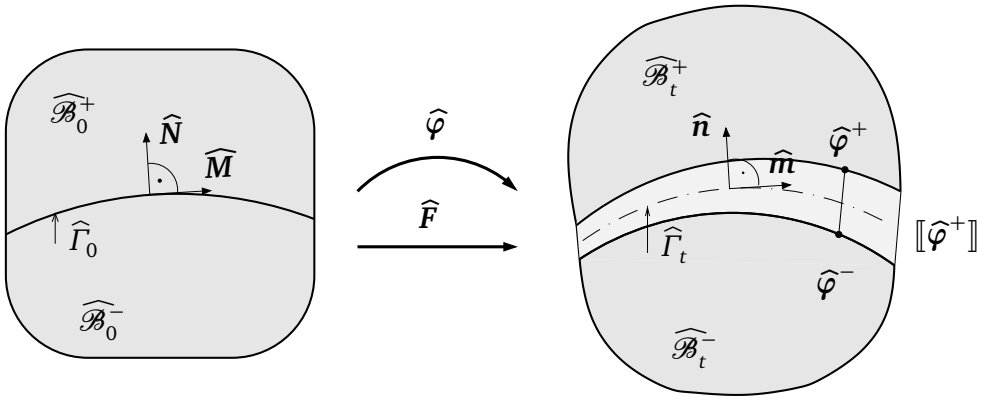

Figure 5.2: Interface geometry and deformation mapping.

equations for the representative volume element, which advocates the underlying microstructure, are presented. Once both the macro and the micro level descriptions are present, the micro–macro transition based on the homogenization of the decisive micro-quantities is examined in Section 5.3. Section 5.4 provides the numerical framework of the above-mentioned computational homogenization. The numerical examples shown in Section 5.5 exhibit the successful implementation of the proposed approach.

5.1 Material layer represented by an interface at the macro level

At the macro level we consider a body $\widehat{\mathcal{B}_0}$ that consists of a bulk, which is separated by a thin material layer of significantly deviating properties, see Figure 5.2. The material macro placement of a material point $\widehat{\mathcal{P}}$ at this level is denoted by $\widehat{\boldsymbol{X}}$. The layer is treated as an interface $\widehat{\Gamma}_0$ with the unit normal vector $\widehat{\boldsymbol{N}}$ onto its plane defined as:

$$\widehat{\boldsymbol{N}}(\widehat{\boldsymbol{X}}) = -\widehat{\boldsymbol{N}}^+(\widehat{\boldsymbol{X}}) = +\widehat{\boldsymbol{N}}^-(\widehat{\boldsymbol{X}}), \qquad \forall\, \widehat{\boldsymbol{X}} \in \widehat{\Gamma}_0\,. \tag{5.1}$$

Thereby $\widehat{\boldsymbol{N}}^+(\widehat{\boldsymbol{X}})$ is the outward normal on the positive part $\widehat{\mathcal{B}_0^+}$ and $\widehat{\boldsymbol{N}}^-(\widehat{\boldsymbol{X}})$ on the negative part $\widehat{\mathcal{B}_0^-}$, respectively. We address the governing boundary value problem of the macro level involving this interface. The governing equations concerning the interface are introduced in the following. For the sake of convenience, the entire framework of both the bulk problem at the macro level , already described in Section 2.2, are assembled in Table 5.1.

Table 5.1: Governing equations at the macro and the micro level

macro boundary value problem			
	kinematics		
bulk deformation	$\widehat{\boldsymbol{x}} = \widehat{\boldsymbol{\varphi}}(\widehat{\boldsymbol{X}}, t)$	$\widehat{\boldsymbol{F}} = \nabla_{\widehat{\boldsymbol{X}}} \widehat{\boldsymbol{\varphi}}$	$\forall\, \widehat{\boldsymbol{X}}$ in $\widehat{\mathscr{B}_0} \backslash \widehat{\Gamma}_0$
interface separation	$[\![\widehat{\boldsymbol{\varphi}}]\!] = \widehat{\boldsymbol{\varphi}}^{+} - \widehat{\boldsymbol{\varphi}}^{-}$		$\forall\, \widehat{\boldsymbol{X}}$ in $\widehat{\Gamma}_0$
	equilibrium		
weak formulation	$\int_{\widehat{\mathscr{B}_0} \backslash \widehat{\Gamma}_0} \widehat{\boldsymbol{P}} : \delta \widehat{\boldsymbol{F}} \, \mathrm{d}V + \int_{\widehat{\Gamma}_0} \widehat{\boldsymbol{t}}_0 \cdot [\![\delta \widehat{\boldsymbol{\varphi}}]\!] \, \mathrm{d}A = \int_{\partial \widehat{\mathscr{B}_0}} \widehat{\boldsymbol{t}}_0 \cdot \delta \widehat{\boldsymbol{\varphi}} \, \mathrm{d}A + \int_{\widehat{\mathscr{B}_0}} \widehat{\boldsymbol{b}}_0 \cdot \delta \widehat{\boldsymbol{\varphi}} \, \mathrm{d}V$		
bulk equilibrium	$\mathrm{Div}\, \widehat{\boldsymbol{P}} + \widehat{\boldsymbol{b}}_0 = \boldsymbol{0}$		in $\widehat{\mathscr{B}_0} \backslash \widehat{\Gamma}_0$
boundary conditions	$\widehat{\boldsymbol{P}} \cdot \widehat{\boldsymbol{N}} =: \widehat{\boldsymbol{t}}_0^{\,\mathrm{pre}}$ on $\partial \widehat{\mathscr{B}}_0^{\widehat{P}}$,	$\widehat{\boldsymbol{\varphi}} =: \widehat{\boldsymbol{\varphi}}^{\mathrm{pre}}$	on $\partial \widehat{\mathscr{B}}_0^{\widehat{\varphi}}$
interface equilibrium	$[\![\widehat{\boldsymbol{P}}]\!] \cdot \widehat{\boldsymbol{N}} = \boldsymbol{0}$,	$\{\widehat{\boldsymbol{P}}\} \cdot \widehat{\boldsymbol{N}} = \widehat{\boldsymbol{t}}_0$	on $\widehat{\Gamma}_0$
	constitutive formulation		
bulk	e. g. a priori stated		
interface	not stated, but obtained from micro level		
micro boundary value problem			
	kinematics		
deformation	$\boldsymbol{x} = \boldsymbol{\varphi}(\boldsymbol{X}, t)$	$\boldsymbol{F} = \nabla_{\boldsymbol{X}} \boldsymbol{\varphi}$	$\forall\, \widehat{\boldsymbol{X}}$ in $\widehat{\mathscr{B}_0}$
	micro equilibrium		
weak formulation	$\int_{\mathscr{B}_0} \boldsymbol{P} : \delta \boldsymbol{F} \, \mathrm{d}V = \int_{\partial \mathscr{B}_0} \boldsymbol{t}_0 \cdot \delta \boldsymbol{\varphi} \, \mathrm{d}A$		
local equilibrium	$\mathrm{Div}\, \boldsymbol{P} = \boldsymbol{0}$		in $\mathscr{B}_0$
boundary conditions	$\boldsymbol{P} \cdot \boldsymbol{N} =: \boldsymbol{t}_0^{\,\mathrm{pre}}$ on $\partial \mathscr{B}_0^{P}$,	$\boldsymbol{\varphi}^{\mathrm{pre}} := \boldsymbol{\varphi}$	on $\partial \mathscr{B}_0^{\varphi}$
	constitutive formulation		
	a priori stated		

Deformation. The primary deformation quantity of the interface is the deformation separation between the opposite spatial edges of the interface, defined as:

$$[\![\widehat{\boldsymbol{\varphi}}]\!](\widehat{\boldsymbol{X}}) := \widehat{\boldsymbol{\varphi}}^{+}(\widehat{\boldsymbol{X}}) - \widehat{\boldsymbol{\varphi}}^{-}(\widehat{\boldsymbol{X}}) \qquad \forall\, \widehat{\boldsymbol{X}} \in \widehat{\Gamma}_0\,. \tag{5.2}$$

Due to this vectorial deformation representation, two possible deformation modes may occur in the interface: a tensile mode and a shearing mode. A height h_0, which in most concepts of cohesive interfaces (Larsson et al., 1993, Steinmann, 1998) represents an artificial parameter regularising the problem, here is instead identified as the initial thickness of the material layer.

Equilibrium in the interface. Across the interface, cohesive tractions are transmitted. The additional equilibrium condition concerning the interface,

$$[\![\widehat{\boldsymbol{P}}]\!] \cdot \widehat{\boldsymbol{N}} = \boldsymbol{0}\,, \qquad\qquad \{\widehat{\boldsymbol{P}}\} \cdot \widehat{\boldsymbol{N}} = \widehat{\boldsymbol{t}}_0 \qquad \text{on } \partial\widehat{\Gamma}_0\,, \tag{5.3}$$

consists of a relation for the jump of the Piola stress, $[\![\widehat{\boldsymbol{P}}]\!]$, and for its average $\{\widehat{\boldsymbol{P}}\} := \frac{1}{2}[\widehat{\boldsymbol{P}}^{+} + \widehat{\boldsymbol{P}}^{-}]$ across the discontinuity. The transmitted traction $\widehat{\boldsymbol{t}}_0$ is energetically conjugate to the separation jump $[\![\widehat{\boldsymbol{\varphi}}]\!]$.

Constitutive framework. The relation between the stress and the deformation measures is supplied by a constitutive relation. For the surrounding bulk, we avail ourselves of a hyperelastic constitutive formulation which is stated a priori, e. g. a neo-Hookean ansatz for $\widehat{\mathscr{W}_0}$. Thus the stress is evaluated as $\widehat{\boldsymbol{P}} = \mathrm{D}_{\widehat{\boldsymbol{F}}}\widehat{\mathscr{W}_0}$.

In the interface, within a reversible constitutive framework, the transmitted cohesive traction is a function of the interface separation, $\widehat{\boldsymbol{t}}_0([\![\widehat{\boldsymbol{\varphi}}]\!])$. Our objective is to find such a relation based on the underlying microstructure in a multiscale approach. Particularly, in the context of a numerical simulation utilising a Newton–Raphson procedure, we are interested in the tangent operator $\widehat{\boldsymbol{A}}$ in an incremental traction–separation law,

$$\delta\widehat{\boldsymbol{t}}_0 = \widehat{\boldsymbol{A}} \cdot [\![\delta\widehat{\boldsymbol{\varphi}}]\!]\,, \qquad\qquad \widehat{\boldsymbol{A}} := \mathrm{D}_{[\![\widehat{\boldsymbol{\varphi}}]\!]}\widehat{\boldsymbol{t}}_0\,. \tag{5.4}$$

Towards a multiscale framework we will next present a formulation for the underlying microstructure and thereafter bridge the two scales by means of a homogenization.

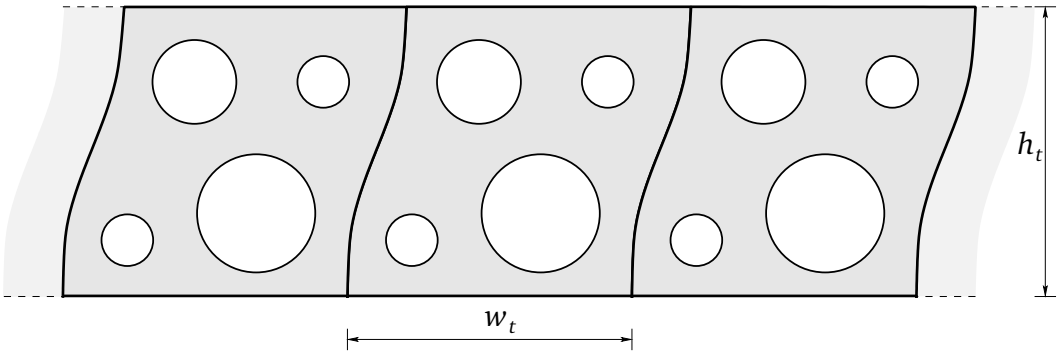

Figure 5.3: Material interface with periodic microstructure: choice of the RVE height h_t and width w_t.

5.2 Representative volume element at the micro level

Within the envisaged multiscale approach for the material layer, now the modelling of its underlying heterogeneous microstructure is considered. A representative volume element (RVE) is used to model a statistically representative portion of the material layer. To match it with the interface geometry, we align the RVE with the interfacial plane and limit its dimension out of plane by the actual height of the material interface. Thereby the dimension of the RVE in plane must be chosen sufficiently large to make the element representative, yet small enough compared to the in-plane dimension of the interface to exclude macro boundary effects. For a perfectly periodic sample microstructure a possible choice for an RVE is illustrated in Figure 5.3 at the deformed microstructure. In the two-dimensional setting pursued here, this element has an material width w_0 and height h_0 and thus a material volume (or rather area) of $V_0 = w_0 h_0$, while the spatial volume is denoted by $V_t = w_t h_t$ in terms of the spatial height h_t and width w_t.

As indicated in Section 4.1, any appropriate mechanical framework could be employed on the RVE level. However, in this chapter we restrict ourselves to a classical continuum as described in Section 2.2. To clarify the notation at the micro level, we will briefly review the governing equations in a geometrically nonlinear framework in Table 5.1. The influence of the body force is neglected at the micro level, in view of the averaging (4.6). Although any appropriate constitutive formulation could be incorporated within the RVE. Here we avail ourselves of a straightforward hyperelastic format for the stored-energy density.

The representative volume element is subject to boundary conditions that stem from the interfacial traction and separation at the macro level. The necessary relations connecting the two scales consistently with respect to the geometry of the material layer will be addressed in the following section.

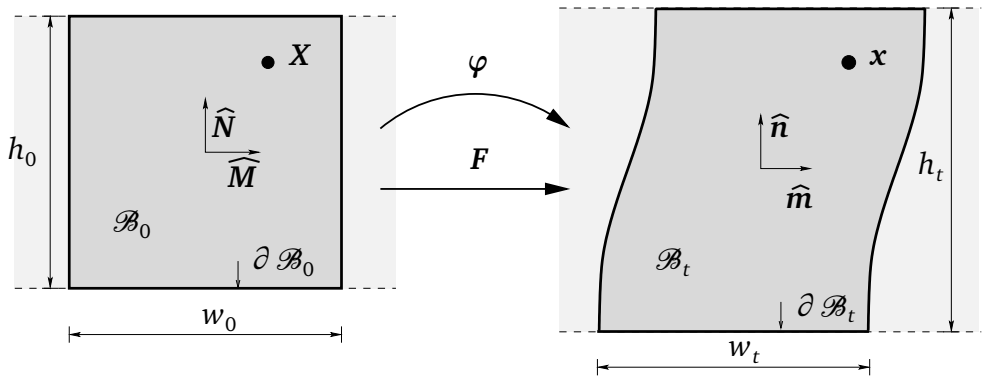

Figure 5.4: RVE geometry and deformation mappings.

5.3 Micro–macro transition

The proposed homogenization approach is based on the averaging of the governing quantities over the volume of the RVE. Thereby the volume averages of the deformation gradient, the stress, and the virtual work over the RVE of Section 4.2.3 are recalled. These averages are related to the governing quantities in the interface. In (4.4), the average deformation gradient needs to be related to the macroscopic deformation jump $[\![\widehat{\varphi}]\!]$, while the average stress correlates to the macroscopic traction vector $\widehat{t}_0$ in $(5.3)_2$. Moreover the averaged RVE virtual work needs to be related to the virtual work at a point on the interface. Boundary conditions on the RVE finalise a consistent scale transition.

5.3.1 Homogenization

To accomplish a consistent scale transition between the micro and the macro level, the averaged RVE quantities (4.4) are related to the governing interface quantities.

Deformation jump. Upon consideration of the initial height h_0 of the material layer, the averaged deformation gradient $(4.4)_1$ is linked to the interface kinematics at the macro level as

$$\boldsymbol{I} + \frac{1}{h_0}[\![\widehat{\boldsymbol{\varphi}}]\!] \otimes \widehat{\boldsymbol{N}} \equiv \langle \boldsymbol{F} \rangle \,. \tag{5.5}$$

This macroscopic kinematic quantity, which is comparable to a deformation gradient, is adopted from the approaches to localized large strain plasticity of e. g. Larsson et al. (1991, 1993).

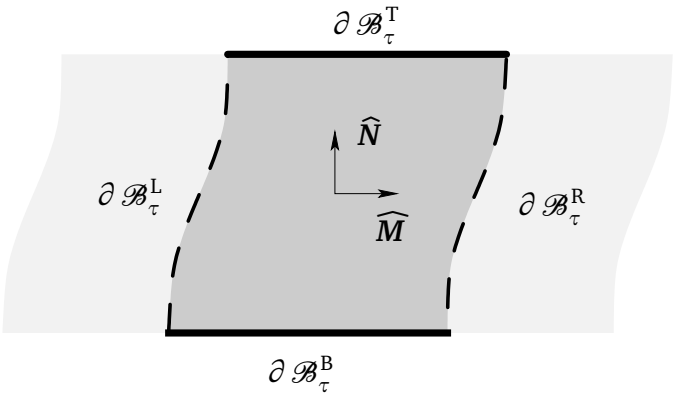

Figure 5.5: Hybrid boundary conditions on the RVE: prescribed deformation on $\partial \mathscr{B}_\tau^{\mathrm{T}}$ and $\partial \mathscr{B}_\tau^{\mathrm{B}}$; periodic deformation $\partial \mathscr{B}_\tau^{\mathrm{R}}$ and $\partial \mathscr{B}_\tau^{\mathrm{L}}$

Traction. The traction $\widehat{\boldsymbol{t}}_0$ in the interface is related to the averaged Piola stress $(4.4)_2$ in the underlying RVE based on the Cauchy theorem $(5.3)_2$,

$$\widehat{\boldsymbol{t}}_0 \equiv \langle \boldsymbol{P} \rangle \cdot \widehat{\boldsymbol{N}} \,, \tag{5.6}$$

assuming the average RVE stress to equal the average stress across the cohesive interface, $\langle \boldsymbol{P} \rangle \equiv \{\widehat{\boldsymbol{P}}\}$.

Virtual work. The Hill condition must be fulfilled. It here requires the virtual work performed in the interface to equal the averaged RVE virtual work given by $(4.4)_3$ scaled by the height h_0 of the material layer:

$$\widehat{\boldsymbol{t}}_0 \cdot [\![\delta \widehat{\boldsymbol{\varphi}}]\!] \equiv h_0 \langle \boldsymbol{P} : \delta \boldsymbol{F} \rangle \,. \tag{5.7}$$

Upon the relations (5.5)–(5.6), this is translated into

$$\langle \boldsymbol{P} \rangle : \langle \delta \boldsymbol{F} \rangle \equiv \langle \boldsymbol{P} : \delta \boldsymbol{F} \rangle \,. \tag{5.8}$$

Consequently the average of the virtual work performed in the RVE must equal the virtual work performed by the respective averages of the deformation gradient and the stress in (4.4).

5.3.2 Boundary conditions on the RVE

The micro–macro transition is achieved by the choice of appropriate boundary conditions on the RVE. These are governed by the corresponding quantities in the interface and must fulfil the Hill condition (5.7) to be admissible.

Generally the boundary conditions to impose on the RVE will depend on the deformation and the traction in the interface. The two above-mentioned deformation

modes can occur in the interface, i. e. relative shear and normal tension. To account for these modes, we pursue a concept that is hybrid between linear displacement and periodic displacement and antiperiodic traction boundary conditions, as depicted in Figure 5.5. Particularly, on the top and the bottom boundaries of the RVE, which are conceptually aligned with the positive and negative edges of the interface, $\widehat{\Gamma}_0^+$ and $\widehat{\Gamma}_0^-$, respectively, we fully prescribe the boundary conditions by means of the interface separation $[\![\widehat{\boldsymbol{\varphi}}]\!]$ as

$$\boldsymbol{\varphi}(\boldsymbol{X}) = \left[\boldsymbol{I} + \frac{1}{h_0}\left[[\![\widehat{\boldsymbol{\varphi}}]\!] \otimes \widehat{\boldsymbol{N}}\right]\right] \cdot \boldsymbol{X} = \begin{cases} \frac{1}{2}[\![\widehat{\boldsymbol{\varphi}}]\!] & \forall \boldsymbol{X} \in \partial\mathscr{B}_0^{\mathrm{T}} \\ -\frac{1}{2}[\![\widehat{\boldsymbol{\varphi}}]\!] & \forall \boldsymbol{X} \in \partial\mathscr{B}_0^{\mathrm{B}} \end{cases}, \tag{5.9}$$

whereby the identity $\widehat{\boldsymbol{N}} \cdot \boldsymbol{X} = h_0/2 \; \forall \boldsymbol{X} \in \partial\mathscr{B}_0^{\mathrm{T}}$, $\widehat{\boldsymbol{N}} \cdot \boldsymbol{X} = -h_0/2 \; \forall \boldsymbol{X} \in \partial\mathscr{B}_0^{\mathrm{B}}$ is used.

In tangential direction of the interface (or rather in plane), we assume periodic deformation and antiperiodic traction boundary conditions, i. e.

$$\boldsymbol{\varphi}^{\mathrm{R}} - \boldsymbol{\varphi}^{\mathrm{L}} = \boldsymbol{0}, \qquad \boldsymbol{t}_0^{\mathrm{R}} + \boldsymbol{t}_0^{\mathrm{L}} = \boldsymbol{0}, \tag{5.10}$$

on the RVE, whereby the notations

$$\boldsymbol{\varphi}^{\mathrm{R}} := \boldsymbol{\varphi}(\boldsymbol{X}), \qquad \boldsymbol{t}^{\mathrm{R}} := \boldsymbol{t}(\boldsymbol{X}) \qquad \forall \boldsymbol{X} \in \partial\mathscr{B}_0^{\mathrm{R}}, \tag{5.11}$$

$$\boldsymbol{\varphi}^{\mathrm{L}} := \boldsymbol{\varphi}(\boldsymbol{X}), \qquad \boldsymbol{t}^{\mathrm{L}} := \boldsymbol{t}(\boldsymbol{X}) \qquad \forall \boldsymbol{X} \in \partial\mathscr{B}_0^{\mathrm{L}} \tag{5.12}$$

are used.

The vectorial representation of both separation and traction in the interface restricts the deformation to two deformation modes: shearing tangential to the interface plane and tension out of the interface plane. Therefore, with this model, it is not possible to account for in-plane tension within the RVE.

Admissibility of hybrid boundary conditions. To prove that this choice of boundary conditions fulfils the Hill condition (5.8), the relations (4.10) are used. The Hill condition for the micro–macro transition between the classical representative volume element and the interface holds for prescribed displacement boundary conditions if the following identity is fulfilled:

$$h_0\langle \boldsymbol{P} : \delta\boldsymbol{F}\rangle - h_0\langle \boldsymbol{P} : \langle\delta\boldsymbol{F}\rangle\rangle \doteq 0\,. \tag{5.13}$$

This relation, which takes the height of the layer into consideration, is transformed to

$$h_0\langle \boldsymbol{P} : \delta\boldsymbol{F}\rangle - h_0\langle \boldsymbol{P} : \langle\delta\boldsymbol{F}\rangle\rangle = \frac{1}{w_0}\int_{\partial\mathscr{B}_0} \boldsymbol{t}_0 \cdot [\delta\boldsymbol{\varphi} - \langle\delta\boldsymbol{F}\rangle \cdot \boldsymbol{X}]\,\mathrm{d}A\,. \tag{5.14}$$

As was to be shown, this term in fact equals zero for the choice (5.9) for the prescribed boundary conditions, because the term in brackets vanishes.

The periodic boundary conditions (5.10) can be shown to be admissible by regarding (5.14). Since for a macro deformation (5.9) affinely imposed on the RVE, $\langle \delta \boldsymbol{F} \rangle \cdot \boldsymbol{X}$ is periodic to begin with, thus the fluctuation term $\delta \boldsymbol{\varphi} - \langle \delta \boldsymbol{F} \rangle \cdot \boldsymbol{X}$ proves periodic as well. Consequently the integral

$$\frac{1}{w_0} \int\limits_{\partial \mathscr{B}_0^{\mathrm{L}}} \boldsymbol{t}_0 \cdot [\delta \boldsymbol{\varphi} - \langle \delta \boldsymbol{F} \rangle \cdot \boldsymbol{X}] \mathrm{d}A + \frac{1}{w_0} \int\limits_{\partial \mathscr{B}_0^{\mathrm{R}}} \boldsymbol{t}_0 \cdot [\delta \boldsymbol{\varphi} - \langle \delta \boldsymbol{F} \rangle \cdot \boldsymbol{X}] \mathrm{d}A = 0 \tag{5.15}$$

will vanish over opposite periodic boundaries if the traction $\boldsymbol{t}_0$ is antiperiodic, which itself follows from equilibrium. For the proposed hybrid boundary conditions, the integral over the top and the bottom boundaries, $\mathscr{B}_0^{\mathrm{T}}$ and $\mathscr{B}_0^{\mathrm{B}}$ respectively, are given by (5.14) which proved to equal zero. Due to their periodicity, the sum of the integrals over the opposite edges on the left and the right side $\mathscr{B}_0^{\mathrm{L}}$ and $\mathscr{B}_0^{\mathrm{R}}$ respectively, vanishes as described. The sum of the particular parts of (5.14) and (5.15),

$$\frac{1}{w_0} \int\limits_{\partial \mathscr{B}_0^{\mathrm{T}} \cup \partial \mathscr{B}_0^{\mathrm{B}}} \boldsymbol{t}_0 \cdot [\delta \boldsymbol{\varphi} - \langle \delta \boldsymbol{F} \rangle \cdot \boldsymbol{X}] \mathrm{d}A + \frac{1}{w_0} \int\limits_{\partial \mathscr{B}_0^{\mathrm{L}} \cup \partial \mathscr{B}_0^{\mathrm{R}}} [\boldsymbol{t}_0^{\mathrm{L}} + \boldsymbol{t}_0^{\mathrm{R}}] \cdot [\delta \boldsymbol{\varphi} - \langle \delta \boldsymbol{F} \rangle \cdot \boldsymbol{X}] \mathrm{d}A = 0 \,, \tag{5.16}$$

is then zero as well, and thus the proposed hybrid boundary conditions are admissible.

5.4 Computational homogenization

The proposed homogenization framework is transferred to a computational homogenization scheme. As in Chapter 4, this framework relies on a nested solution scheme involving both the macro and the micro boundary value problem, which are both solved by means of the finite-element method. Situated between the bulk elements on the macro scale, cohesive interface elements represent the material layer. The constitutive behaviour of the bulk is assumed a priori, for which a constitutive routine is provided. Contrary, the constitutive behaviour or rather the traction–separation relation (5.4) of the interface element is obtained from the underlying microstructure.

5.4.1 Nested multiscale solution scheme

The nested multiscale solution procedure is illustrated in Figure 5.6. The macro specimen is discretized with cohesive interface elements and bulk finite elements

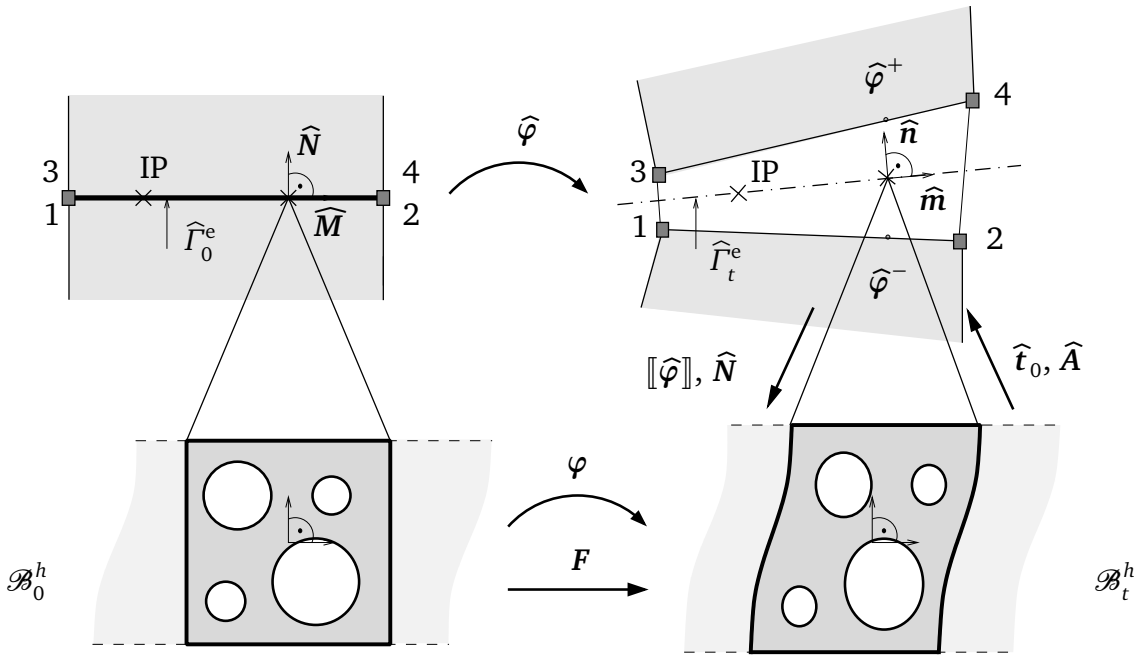

Figure 5.6: Computational homogenization between the interface integration point (IP) of the interface element on $\widehat{\Gamma}_0^{\mathrm{e}}$ at the macro scale and the underlying representative volume element $\mathscr{B}_0^h$ with boundary $\partial\mathscr{B}_0^h$.

on $\widehat{\Gamma}_0^h$ and $\widehat{\mathscr{B}}_0^h$. The RVE is discretized with a finite element mesh on $\mathscr{B}_0^h$. In order to handle the in-plane periodicity being part of the hybrid boundary conditions presented in Section 5.3.2, this RVE mesh is subject to the restriction that the left and the right boundary, $\partial\mathscr{B}_0^{h\mathrm{L}}$ and $\partial\mathscr{B}_0^{h\mathrm{R}}$, respectively, have equal arrangement.

An iterative solution is employed at both the macro and the micro level, e. g. using a Newton–Raphson algorithm. At each integration point of each interface element on Γ_0^h the macro separation $[\![\widehat{\boldsymbol{\varphi}}]\!]$ is evaluated iteratively, being zero initially. Its increments deliver the boundary conditions to the RVE finite element mesh, see (5.9). During each macro iteration step, the nonlinear micro system is solved subject to these incremental boundary conditions. When equilibrium is obtained at the RVE level, both the homogenized macroscopic tangent operator $\widehat{\boldsymbol{A}}$ and the macroscopic traction vector $\widehat{\boldsymbol{t}}_0$, (5.4), at each integration point along the interface are computed by means of this solution. Precisely, the stiffness matrix and the residual vector of the RVE boundary are extracted to this end. With the constitutive macro quantities at hand, the macro system is solved iteratively until a global solution for the current load step is obtained.

A Gauss quadrature is used for the numerical integration within the interface elements. Other numerical integration schemes, as e. g. studied by Schellekens and de Borst (1993a), go beyond the scope of the current contribution.

If in the computation, the interface coordinate system is not directly aligned with

the global coordinate system, the tangential and the normal components of the separation vector are transferred to the RVE.

5.4.2 Numerical solution of the RVE boundary value problem at the micro level

Following the procedure described in Section 4.2.5, the stiffness matrix (4.22) and the residual vector of the RVE problem are assembled from the individual finite-element contributions.

To account for the in-plane periodicity (5.10), being present for the proposed hybrid boundary conditions, we utilize the approach of Kouznetsova et al. (2002) discussed in Remark 4.2.1. Therefore the entire system of equation is transformed into a system of independent degrees of freedom exclusively. For the hybrid boundary conditions, these independent degrees of freedom comprise the degrees of freedom of all boundary nodes at the top and bottom (including all corner nodes), on the left, as well as all interior nodes. Complementary, the right boundary nodes (excluding all corner nodes) supply the set of dependent degrees of freedom.

In this reduced system, the displacement-boundary conditions (5.9) stemming from the interface deformation, are imposed on the top and bottom nodes. The vector of unknowns is updated, before the independent and the dependent degrees of freedom are gathered into a vector containing all nodal deformations. This way the nonlinear micro system of equations is iteratively solved until equilibrium is reached in the RVE.

5.4.3 Homogenized macro quantities

The sought-for macroscopic quantities, i. e. the traction vector $(5.3)_2$ and the tangent operator (5.4) at each interface integration point, are retrieved from a computational homogenization based on the solved micro system. Therefore the system in terms of the independent degrees of freedom is further condensed so that it renders the stiffness matrix K_{IL} and the nodal reaction force vector f_I in terms of the prescribed degrees of freedoms, which belong to nodes I, L, only.

Macro traction vector. At each integration point of the macro interface elements, we obtain the homogenized macro traction vector (5.6) with the average of the Piola stress $(4.6)_2$, as

$$\widehat{\boldsymbol{t}}_0 = \frac{1}{V_0} \sum_{I}^{n_{\text{pre}}} \left[\mathsf{f}_I \otimes \boldsymbol{X}_I \right] \cdot \widehat{\boldsymbol{N}}, \qquad I \in \partial \mathscr{B}^{h\text{B}} \cup \partial \mathscr{B}^{h\text{T}} \tag{5.17}$$

through a summation over all n_{pre} prescribed nodes on $\partial \mathscr{B}_0^{h\mathrm{T}} \cup \partial \mathscr{B}_0^{h\mathrm{B}}$ for the present choice of hybrid boundary conditions.

Macro tangent operator. To obtain the tangent, we consider the increment of a macroscopic load step. In equation (5.17), the increment of the nodal reaction force at the prescribed nodes I and L is replaced by

$$\Delta \mathsf{f}_I = \mathsf{K}_{IL} \cdot \Delta \boldsymbol{\varphi}_L \,. \tag{5.18}$$

After the following steps using the prescribed deformation boundary conditions (5.9) at nodes L,

$$\begin{aligned} \widehat{\boldsymbol{t}}_0 &= \frac{1}{V_0} \sum_I^{n_{\text{pre}}} \sum_K^{n_{\text{pre}}} \left[\mathsf{K}_{IL} \cdot \left[\Delta \boldsymbol{\varphi}_L \otimes \boldsymbol{X}_I \right] \right] \cdot \widehat{\boldsymbol{N}} \\ &= \frac{1}{V_0} \sum_I^{n_{\text{pre}}} \sum_K^{n_{\text{pre}}} \left[\mathsf{K}_{IL} \cdot \left[\frac{1}{h_0} \left[\Delta \boldsymbol{I} + [\![\Delta \widehat{\boldsymbol{\varphi}}]\!] \otimes \widehat{\boldsymbol{N}} \right] \cdot \boldsymbol{X}_L \right] \otimes \boldsymbol{X}_I \right] \cdot \widehat{\boldsymbol{N}} \\ &= \left[\frac{1}{w_0^2 h_0} \sum_I^{n_{\text{pre}}} \sum_K^{n_{\text{pre}}} \left[\widehat{\boldsymbol{N}} \otimes \widehat{\boldsymbol{N}} \right] : \left[\left[\boldsymbol{X}_L \otimes \boldsymbol{X}_I \right] \otimes \mathsf{K}_{IL} \right] \right] \cdot [\![\Delta \widehat{\boldsymbol{\varphi}}]\!] \,, \end{aligned} \tag{5.19}$$

we can identify the term in the outer brackets as the sought-for tangent operator as

$$\widehat{\boldsymbol{A}} = \frac{1}{w_0 h_0^2} \left[\widehat{\boldsymbol{N}} \otimes \widehat{\boldsymbol{N}} \right] : \left[\sum_I^{n_{\text{pre}}} \sum_L^{n_{\text{pre}}} [\boldsymbol{X}_L \otimes \boldsymbol{X}_I] \otimes \mathsf{K}_{IL} \right] , \qquad I, L \in \partial \mathscr{B}^{h\mathrm{B}} \cup \partial \mathscr{B}^{h\mathrm{T}} . \tag{5.20}$$

With these quantities at hand, the computational multiscale framework for the material layer is achieved.

5.5 Numerical examples

To illustrate the proposed computational homogenization procedure, numerical examples are presented. Underlying to a material layer, microstructures with either voids or inclusions are simulated. First, we study the proper choice of the RVE at the example of a periodic microstructure within a material layer, Section 5.5.1 with a single interface element. More complex macro boundary value problems are studied in Sections 5.5.2 and 5.5.3.

At the macro level, the cohesive interface is embedded into a bulk finite-element mesh with linear, respectively bilinear approximations. The underlying microstructure modelled by RVEs is discretized with biquadratic bulk elements.

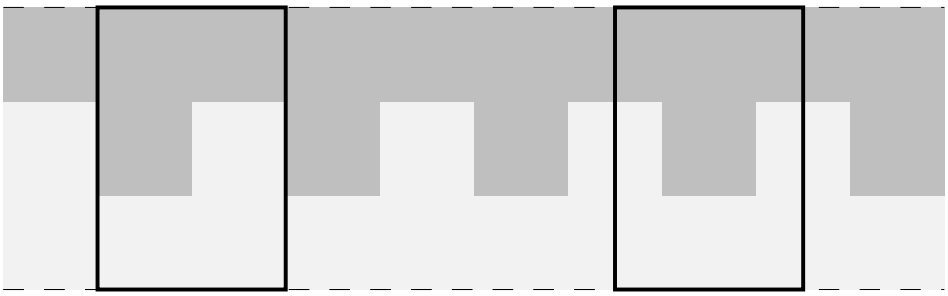

Figure 5.7: Periodic microstructure: choice of nonsymmetric RVE vs. symmetric RVE

5.5.1 Choice of the RVE

A material layer with a periodic microstructure is considered, as depicted in Figure 5.7. Thereby in the darker grey region, the Young's modulus is chosen 5 times stiffer as in the lighter one. For this periodic microstructure, the proper choice of the RVE is investigated. To this end, out of the various possible options, one nonsymmetric and one symmetric RVE are chosen.

With the aid of the simplest possible macro problem, a single interface element, we study the homogenized macro response to fully prescribed mixed-mode loading, $\widehat{u}_{\widehat{M}} = 5\,\widehat{u}_{\widehat{N}}$. This deformation is applied step-wise until a final shearing of $\widehat{u}_{\widehat{M}} = 0.4h_0$ is reached. The response is evaluated for both cases, the nonsymmetric and the symmetric RVEs. Figure 5.8 shows the spatial meshes of these after the first load step. With the naked eye, these two spatial RVEs can be distinguished, because in the stiffer regions hardly any stretch is recognized.

The stress in the RVE is considered next. Figure 5.9 shows the individual components of the Cauchy type stress in the RVE. In the first row the stress in the nonsymmetric and in the second row that of the symmetric RVE are plotted. Repetitive features in the stress distribution can be recognized. The fact that the stress patterns are not fully congruent close to the lateral boundaries of the respective RVE can be attributed to the stress smoothing algorithm, which does not involve the periodicity yet.

Although the stress distributions are not appear entirely identical, the macro response is. This is shown with the resulting traction–separation laws from the computational homogenization (5.17). It is compared for both RVE choices in Figure 5.10. The response in normal direction obeys a nonlinear relation, whereas the traction–separation curve for the shear is approximately linear. Both the tangential and the normal traction–separation curves of the two RVEs prove to coincide. Consequently, despite the slightly deviating stress, this choice of the RVE in the infinite layer has no impact on the macro response.

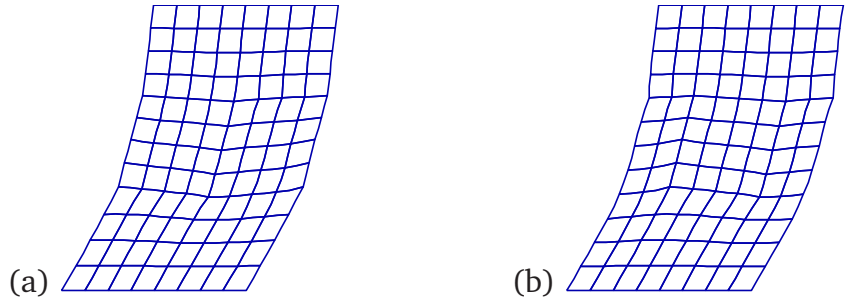

Figure 5.8: Spatial meshes of (a) nonsymmetric RVE vs. (b) symmetric RVE at $\widehat{u}_{\widehat{M}} = 5\,\widehat{u}_{\widehat{N}} = 0.04h_0$.

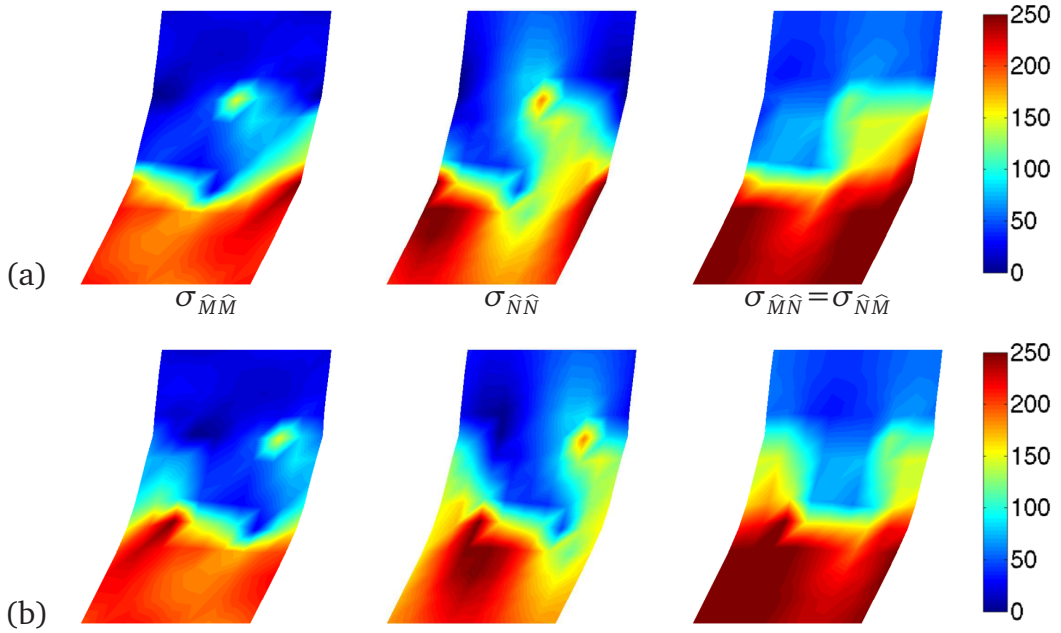

Figure 5.9: Cauchy stress components for (a) nonsymmetric and (b) symmetric RVE.

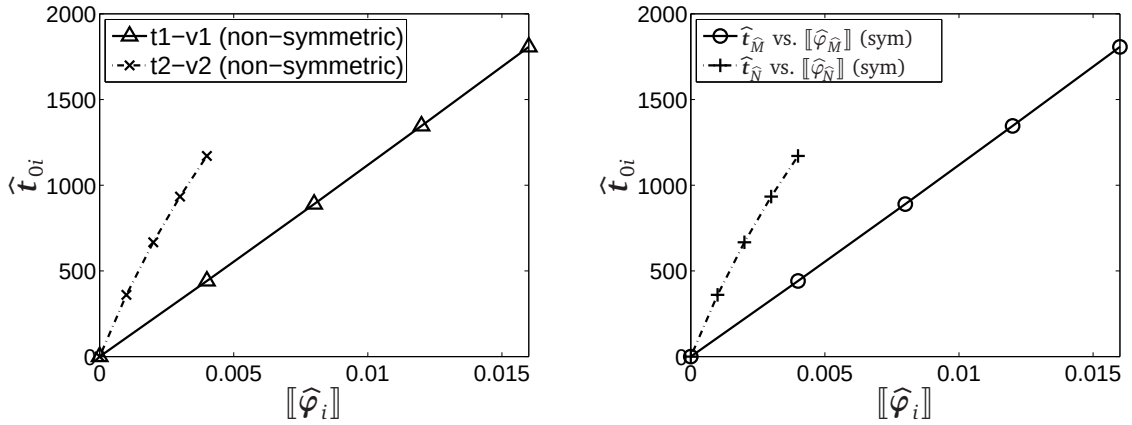

Figure 5.10: Traction–separation curve with nonsymmetric and symmetric RVE.

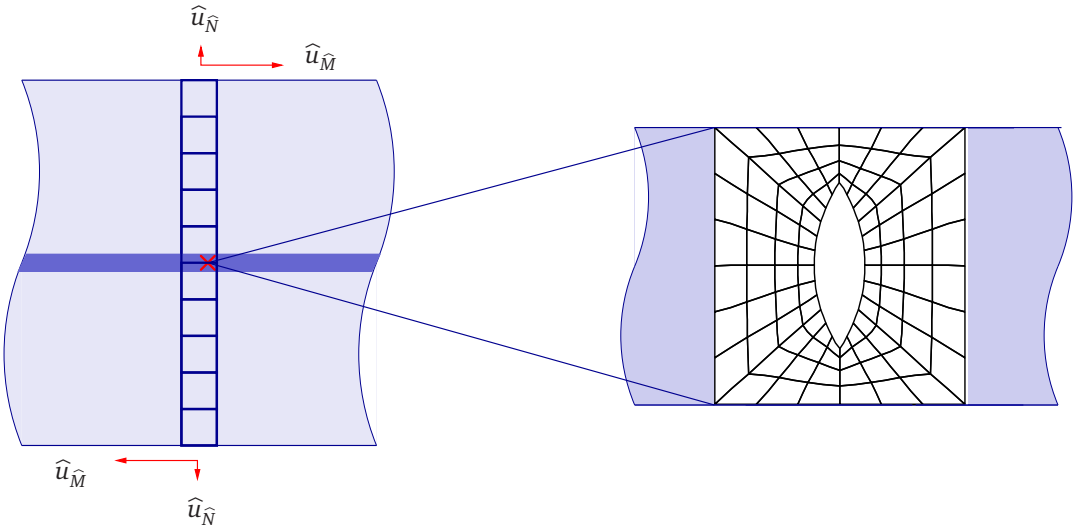

Figure 5.11: Infinite periodic shear layer including material layer: multiscale boundary value problem.

5.5.2 Material layer within an infinite shear layer under shear-dominated mixed-mode loading

To simulate a straight material layer of large in-plane extension, a single column of elements, comprising one interface element, is modelled periodically at the macro level, as depicted in Figure 5.11. For opposite nodes at the left and right side, periodic deformations are enforced. This way, the column represents a small portion of a layer with ideally infinite in-plane extension. The deformation of the problem is prescribed at the top and the bottom ($\widehat{\boldsymbol{u}}^{\mathrm{ext,T}} = -\widehat{\boldsymbol{u}}^{\mathrm{ext,B}}$), with a shear-dominated mixed mode, with the horizontal or rather tangential displacement being ten times the tensile or rather normal displacement. This deformation is applied step-wise, until a final tangential deformation of $\widehat{u}_{\widehat{M}}^{\mathrm{ext,T}} = 0.2\widehat{w}_0$ is reached.

Different micro meshes are examined: First, microstructures with a void of different shape and size are simulated and compared to the response of a homogeneous microstructure. After that, the shear layer is investigated with RVEs containing inclusions of higher stiffness and different distributions. At the macro level, bilinear shape functions are used.

Microstructures with voids

The problem is first studied for microstructures with voids. A homogeneous specimen is compared with two quadratic specimens with each containing a centred circular hole of 5% and 25% void ratio, respectively, and another quadratic specimen with a centred lentil-shaped void. These microstructures are discretized with bilinear finite elements. The material parameters are chosen to be $\widehat{E} = 100E$, $\widehat{\nu} = \nu = 0.3$. For a macro displacement load of $\widehat{\boldsymbol{u}}^{\mathrm{ext,T}} = -\widehat{\boldsymbol{u}}^{\mathrm{ext,B}} = 0.02\widehat{w}_0\,\widehat{\boldsymbol{M}} + 0.002\widehat{w}_0\,\widehat{\boldsymbol{N}}$, in Fig-

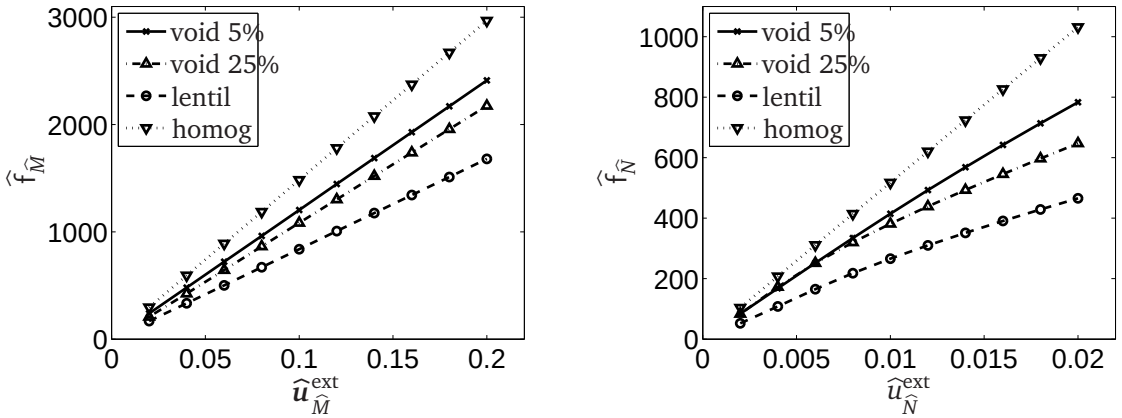

Figure 5.12: Shear layer with interface, underlying RVE with voids: load–displacement curves at top node.

ure 5.13(b)–(d) the respective spatial macro meshes are plotted, while the corresponding spatial micro meshes are shown in Figure 5.14.

Based on the different size and shape of the voids, the stiffness of the specimen differs. This is qualitatively reflected in the deformed meshes. The weaker the RVE reacts, the stronger is the deformation localized in the material layer. The differently stiff response is quantitatively analysed in Figure 5.12. The plotted force–displacement curves in tangential and normal direction are evaluated for the top nodes of the macro specimen. The specimen with the lentil-shaped void yields the least stiff response, while for decreasing size of the void, the stiffness increases. As a benchmark, the response of the homogeneous specimen is also evaluated. As expected, it yields by far the stiffest response. Moreover, the curve for the reaction normal to the interface plane is nearly linear.

The RVE Cauchy stress is plotted in Figure 5.14 as well. Trivially, for the homogeneous specimen, a homogeneous distributions of all stress components are obtained. In the other cases the stress is significantly higher around the void, whereas the distributions of the stress depend on the particular shape.

Microstructures with inclusions

Next, within the material layer situated within the periodic macro shear layer, microstructures equipped with inclusions are examined. These inclusions possess a greater stiffness than the surrounding matrix material in the material layer. The different material meshes are schematised in Figure 5.15, whereby in the darker elements, Young's modulus is chosen five times that of the light-grey elements, $E_2 = 5E_1 = \widehat{E}/200$, while Poisson's ratio is chosen equally as $\widehat{\nu} = \nu_1 = \nu_2 = 0.3$.

The spatial meshes of the RVEs are shown in Figure 5.16. Again it can be observed that the stiffer elements barely deform but rather experience a significant rotation.

As for the microstructures with voids in Section 5.5.2, the force–displacement curves at the top of the macro specimen are compared here in Figure 5.17. Depending on the size and distribution of the inclusions, the resulting macroscopic force–displacement differ from each other. As expected, the specimen with the largest inclusion ratio, Figure 5.15(b), exhibits the stiffest behaviour in both directions.

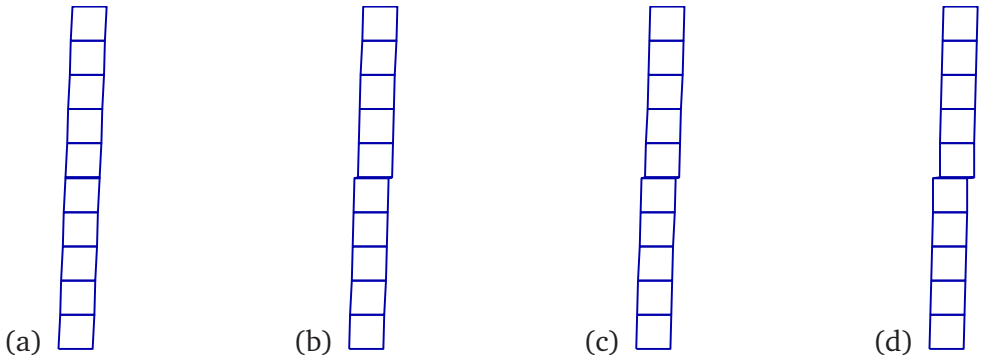

Figure 5.13: Shear layer with interface: spatial macro mesh at $\widehat{u}_{\widehat{M}} = 0.2\widehat{w}_0$ for different microstructures: (a) benchmark homogeneous microstructure, (b) 5% void, (c) 25% void, (d) lentil-shaped void.

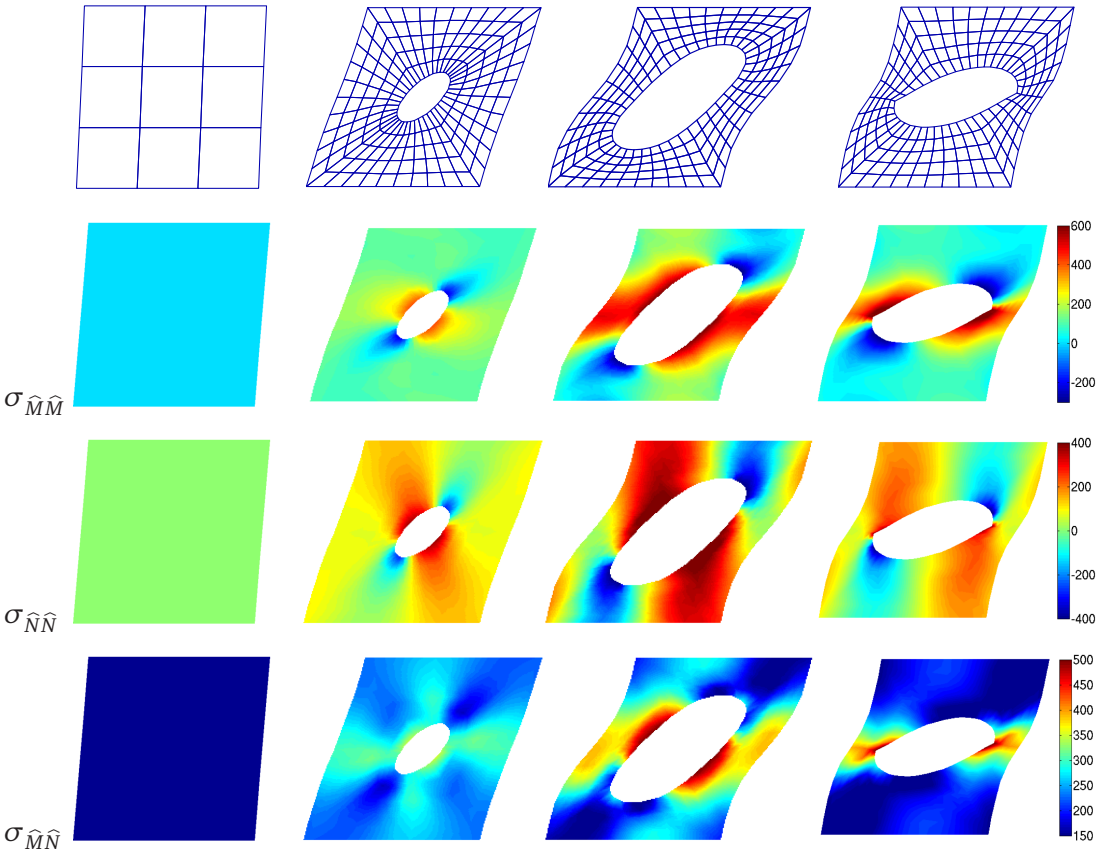

Figure 5.14: Shear layer with interface: spatial RVEs and Cauchy-stress $\boldsymbol{\sigma}$

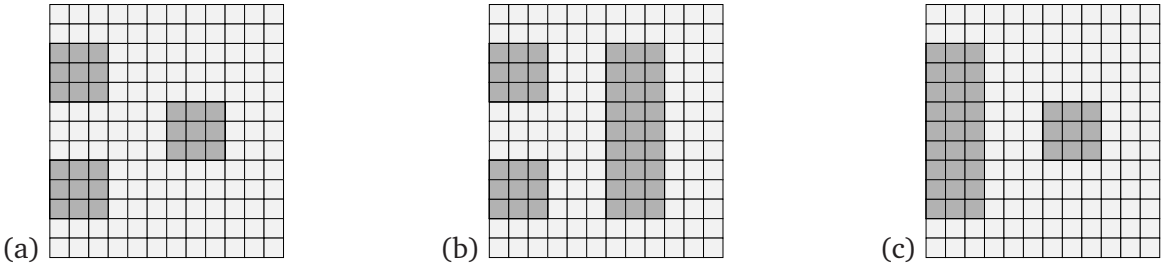

Figure 5.15: RVEs for microstructure with inclusions.

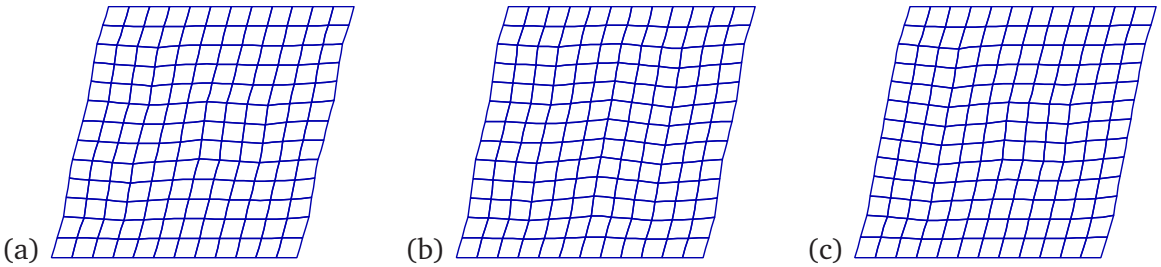

Figure 5.16: Spatial RVE meshes of microstructure with inclusions.

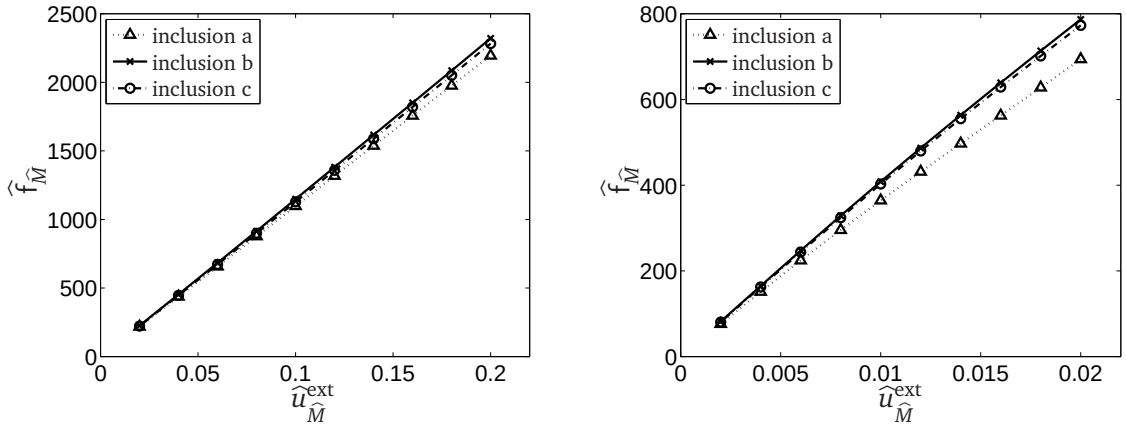

Figure 5.17: Microstructure with inclusions: macro force–displacement curves.

5.5.3 Macrostructure with material layer next to a hole

In a last example, at the macro level a specimen with an initially circular centred hole is considered, at the lateral sides of which a material layer is located. The response of this material layer is evaluated based on its underlying microstructure. In the discretized macro specimen shown in Figure 5.18(a), three interface elements are located at each lateral side of the hole. At their integration points, the microstructure is represented by an RVE with a centred lentil-shaped void. This RVE is similar to the one of Section 5.5.2, Figure 5.14. However, fewer elements with biquadratic shape functions are chosen here instead. In one case, the lentil-shaped void is oriented tangentially, while in the other case, the lentil-shaped hole is oriented vertically or rather in normal direction to the interface, see Figure 5.18(b)–(c).

The spatial RVEs at the integration points of the interface element are shown in Figure 5.19. Thereby $\widehat{\Xi} = 2\widehat{X}_{\widehat{M}}/\widehat{w}_0$ denotes the relative initial location compared to half the width of the macro specimen. Next to the spatial macro mesh, in Figure 5.20 the corresponding homogenized tractions $\widehat{t}_{\widehat{N}}$ and the separations $[\![\widehat{\varphi}_{\widehat{N}}]\!]$ at these macro Gauss points are plotted vs. their position $\widehat{\Xi}$. As expected, the closer to the macroscopic hole, the stronger both the traction and the deformation increase. Furthermore, the orientation of the lentil-shaped void plays a significant role. The horizontally oriented void attracts more separation and and less traction, while the slope of the traction–separation curve is less steep. Consequently, this specimen involves the weaker response than that with the vertically oriented void. This is also reflected in the two resulting traction–separation curves shown at the macro integration point closest to the hole, $\widehat{t}_{\widehat{N}}$ vs. $[\![\widehat{\varphi}_{\widehat{N}}]\!]$.

It can be observed that by their orientation and arrangement, heterogeneities in the microstructure can yield anisotropic effects in the global response.

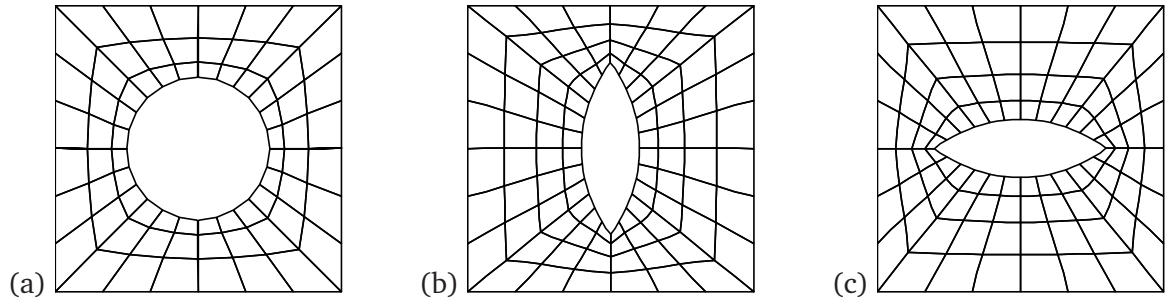

Figure 5.18: (a) Material discretized macrostructure, material discretized RVE with (b) vertically oriented and (c) horizontally oriented lentil-shaped void.

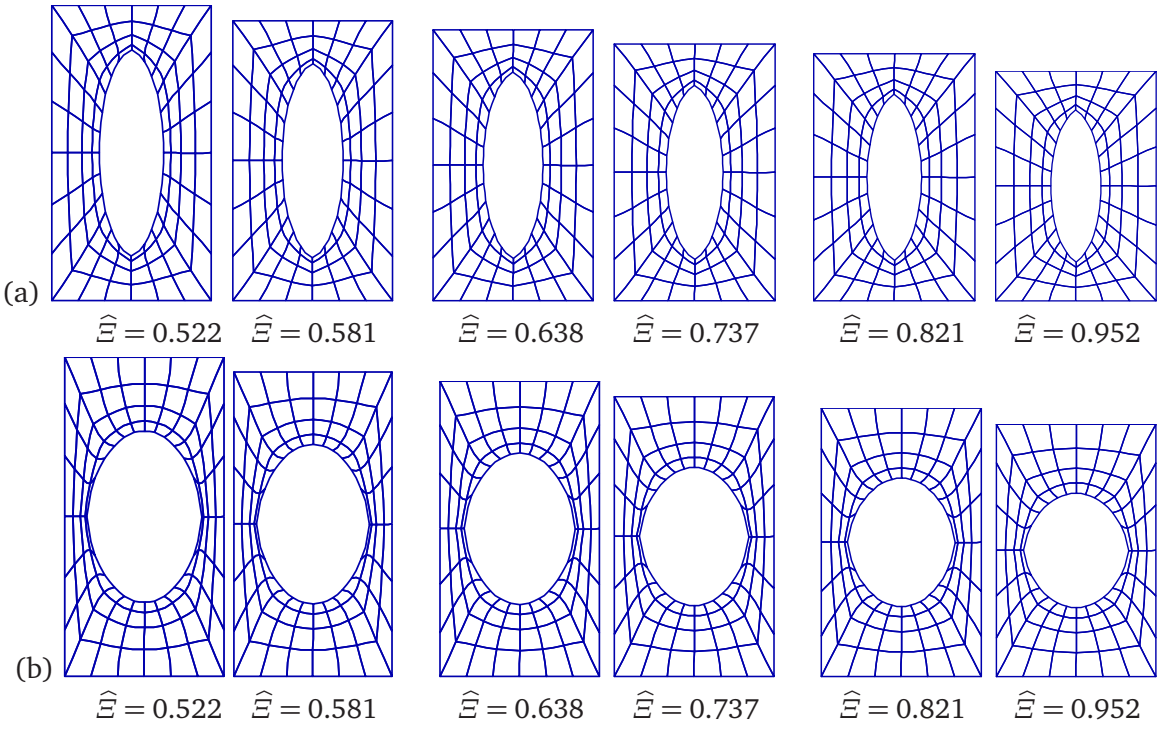

Figure 5.19: Spatial RVE meshes along the interface of specimen with (a) vertically and (b) horizontally oriented lentil-shaped void.

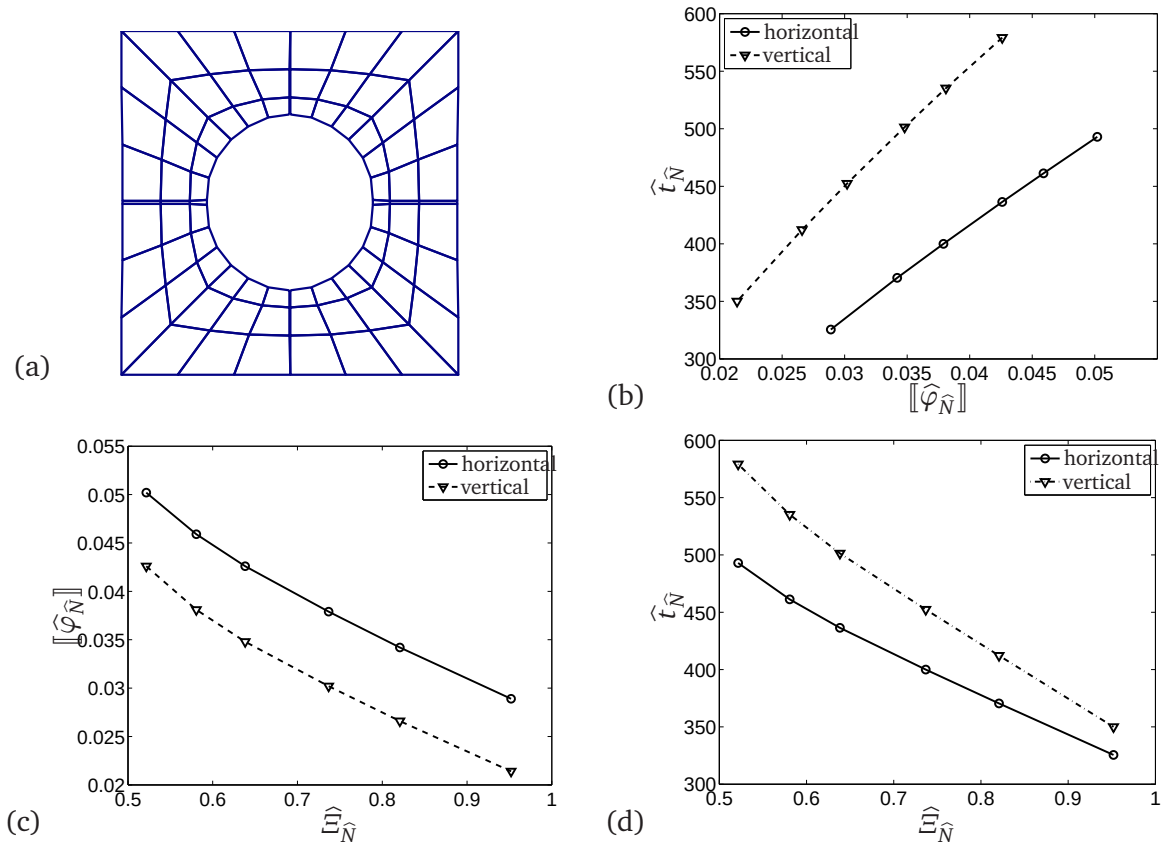

Figure 5.20: (a) Spatial macro mesh; (b) traction–separation curve and (c)–(d) traction and separation as a function of the position along the interface.

6 Computational Homogenization of Material Layers with Micromorphic Mesostructure

The modelling of a thin material layer is particularly challenging, when it consists of a material which possesses a distinct microstructure that is relatively large compared to the thickness of the layer. In such cases size effects arise, which classical continuum approaches fail to account for. As in Chapter 5, we employ the concept of homogenization to obtain the macroscopic response in the material layer. Once more the material layer at the macro level is resolved as a cohesive interface embedded into a continuum. Nevertheless we here employ a micromorphic continuum within the RVE to represent both the meso- and the microstructure as proposed in Hirschberger et al. (2008b) and illustrated in Figure 6.1. As pointed out in Chapter 3, this micromorphic continuum is characterized by so-called microcontinua that are endowed to each continuum point. The deformation of these kinematically independent microcontinua is considered separately. In the constitutive assumption an internal-length parameter is contained that accounts for the size dependence, and furthermore, a coupling between meso and micro deformation is provided.

In the homogenization that links both scales, the averages of the characteristic quantities over the micromorphic representative volume element are related to the corresponding macro quantities in the interface under fulfilment of equivalence conditions. Thereby the finite height of the mesostructure is directly given by the width of the material layer. The boundary conditions on the micromorphic representative volume element are chosen to fulfil the Hill conditions, while they reflect the particular deformation modes occurring within the interface, as seen in Chapter 5.

As in Chapter 5, the interface homogenization approach is implemented into a finite-element-based computational homogenization. Likewise within the numerical multiscale framework, cohesive interface elements represent the material layer at the macro level. In order to account for its underlying microstructured mesostructure, a micromorphic finite element boundary value problem is solved within the representative volume element utilizing the numerical framework of Section 3.4. Since the micromorphic finite elements within the RVE incorporate both the standard and the additional micro degrees of freedom, a coupled system of equation is to be solved in the RVE. The macroscopic traction vector and the tangent opera-

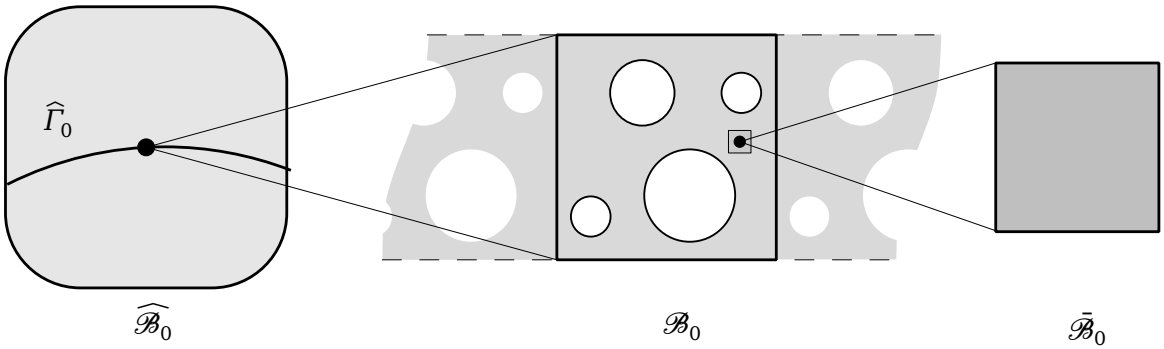

Figure 6.1: Multiscale framework for material layer with micromorphic mesostructure.

tor are obtained on the RVE and passed to the macro level from the computational homogenization procedure.

Like the computational homogenisation of Section 4.3, the present approach is reverse to the second-order homogenization proposed by Kouznetsova et al. (2002, 2004), which regards second gradients of deformation (compare Section 2.3) at the macro level whereas the RVE is modelled with classical continuum. Related approaches can be found in the literature, e. g. with a micropolar continuum at the macro level (Larsson and Zhang, 2007) or in the homogenization of thin sheet structures (Geers et al., 2007). In both cases, which belong to the category of second-order homogenization of plane structures, the generalized continuum is involved at the macro level, which accounts for distinct gradient effects along the plane.

Outline. The remainder of this chapter is organised as follows. We briefly recall the continuum mechanics framework for the macro level, Section 6.1, and in the subsequent Section 6.2 review the micromorphic framework for the representative volume element. Based upon these macro and micro/meso scale descriptions, the homogenization framework to consistently link these scales is presented in Section 6.3,. The corresponding computational homogenization is outlined in Section 6.4, followed by benchmark numerical examples in Section 6.5 that display the effect of the micromorphic mesostructure on the macroscopic response.

6.1 Material layer as an interface at the macro level

The thin material layer at the macro level is modelled as a cohesive interface in the same manner as in the previous Chapter 5. Recall that this cohesive interface illustrated in Figure 5.2 is governed by its opening $[\![\widehat{\varphi}]\!]$, and transmits cohesive tractions: For the full set of equations of the macro framework for both the bulk and the interface is is gathered in Table 6.1.

Table 6.1: Governing equations at the macro and the meso/micro level

macro boundary value problem			
	kinematics		
bulk deformation	$\widehat{\boldsymbol{x}} = \widehat{\boldsymbol{\varphi}}(\widehat{\boldsymbol{X}}, t)$	$\widehat{\boldsymbol{F}} = \nabla_{\widehat{\boldsymbol{X}}}\widehat{\boldsymbol{\varphi}}$	$\forall\ \widehat{\boldsymbol{X}}$ in $\widehat{\mathscr{B}_0}\backslash\widehat{\Gamma}_0$
interface separation	$[\![\widehat{\boldsymbol{\varphi}}]\!] = \widehat{\boldsymbol{\varphi}}^{+} - \widehat{\boldsymbol{\varphi}}^{-}$		$\forall\ \widehat{\boldsymbol{X}}$ in $\widehat{\Gamma}_0$
	equilibrium		
weak formulation	$\int_{\widehat{\mathscr{B}_0}\backslash\widehat{\Gamma}_0} \widehat{\boldsymbol{P}} : \delta\widehat{\boldsymbol{F}}\,\mathrm{d}V + \int_{\widehat{\Gamma}_0} \widehat{\boldsymbol{t}}_0 \cdot [\![\delta\widehat{\boldsymbol{\varphi}}]\!]\,\mathrm{d}A = \int_{\partial\widehat{\mathscr{B}_0}} \widehat{\boldsymbol{t}}_0 \cdot \delta\widehat{\boldsymbol{\varphi}}\,\mathrm{d}A + \int_{\widehat{\mathscr{B}_0}} \widehat{\boldsymbol{b}}_0 \cdot \delta\widehat{\boldsymbol{\varphi}}\,\mathrm{d}V$		
bulk equilibrium	$\mathrm{Div}\,\widehat{\boldsymbol{P}} + \widehat{\boldsymbol{b}}_0 = \boldsymbol{0}$		in $\widehat{\mathscr{B}_0}\backslash\widehat{\Gamma}_0$
boundary conditions	$\widehat{\boldsymbol{P}} \cdot \widehat{\boldsymbol{N}} =: \widehat{\boldsymbol{t}}_0^{\mathrm{pre}}$ on $\partial\widehat{\mathscr{B}_0}^{\widehat{P}}$,	$\widehat{\boldsymbol{\varphi}} =: \widehat{\boldsymbol{\varphi}}^{\mathrm{pre}}$	on $\partial\widehat{\mathscr{B}_0}^{\widehat{\varphi}}$
interface equilibrium	$[\![\widehat{\boldsymbol{P}}]\!] \cdot \widehat{\boldsymbol{N}} = \boldsymbol{0}$,	$\{\widehat{\boldsymbol{P}}\} \cdot \widehat{\boldsymbol{N}} = \widehat{\boldsymbol{t}}_0$	on $\widehat{\Gamma}_0$
	constitutive formulation		
bulk	e. g. a priori stated		
interface	not stated, but obtained from micro level		
meso boundary value problem			
	kinematics		
meso map, gradient	$\boldsymbol{x} = \boldsymbol{\varphi}(\boldsymbol{X})$	$\boldsymbol{F} = \nabla_{\boldsymbol{X}}\boldsymbol{\varphi}$	
micro map, gradient	$\bar{\boldsymbol{x}} = \bar{\boldsymbol{F}}(\boldsymbol{X}) \cdot \boldsymbol{X}$	$\bar{\boldsymbol{G}} = \nabla_{\boldsymbol{X}}\bar{\boldsymbol{F}}$	
	balance of momentum		
weak formulation	$\int_{\mathscr{B}_0} \boldsymbol{P} : \delta\boldsymbol{F} + \bar{\boldsymbol{P}} : \bar{\boldsymbol{F}} + \bar{\boldsymbol{Q}} \mathbin{:\cdot} \bar{\boldsymbol{G}}\,\mathrm{d}V = \int_{\partial\mathscr{B}_0} \boldsymbol{t}_0 \cdot \delta\boldsymbol{\varphi}\,\mathrm{d}A + \int_{\partial\mathscr{B}_0} \bar{\boldsymbol{t}}_0 : \delta\bar{\boldsymbol{F}}\,\mathrm{d}A$		
meso equilibrium	$\mathrm{Div}\,\boldsymbol{P} = \boldsymbol{0}$		in $\mathscr{B}_0$
micro equilibrium	$\mathrm{Div}\,\bar{\boldsymbol{Q}} - \bar{\boldsymbol{P}} = \boldsymbol{0}$		in $\mathscr{B}_0$
	boundary conditions		
traction, double traction	$\boldsymbol{P} \cdot \boldsymbol{N} =: \boldsymbol{t}_0^{\mathrm{pre}}$ on $\partial\mathscr{B}_0^{P}$,	$\bar{\boldsymbol{Q}} \cdot \boldsymbol{N} =: \bar{\boldsymbol{t}}_0^{\mathrm{pre}}$	on $\partial\mathscr{B}_0^{\bar{Q}}$
meso, micro deformation	$\boldsymbol{\varphi} =: \boldsymbol{\varphi}^{\mathrm{pre}}$ on $\partial\mathscr{B}_0^{\varphi}$,	$\bar{\boldsymbol{F}} =: \bar{\boldsymbol{F}}^{\mathrm{pre}}$	on $\partial\mathscr{B}_0^{\bar{F}}$
	constitutive formulation		
	a priori stated		

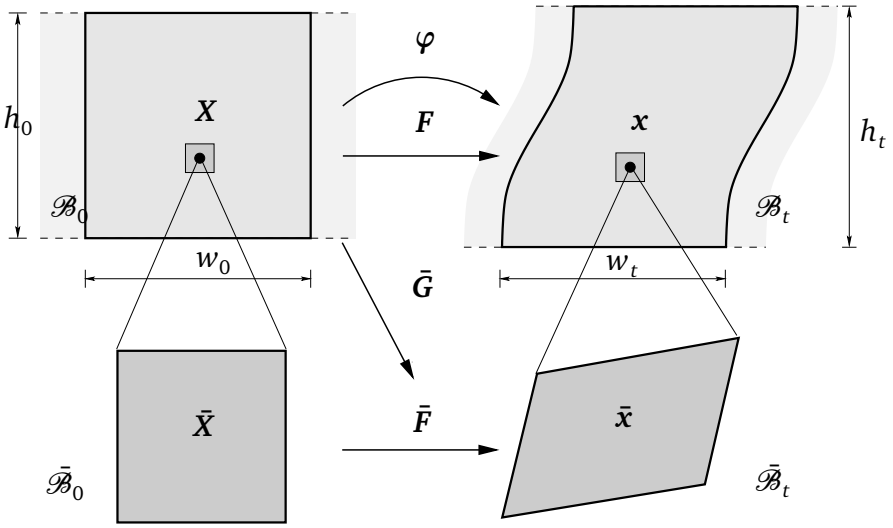

Figure 6.2: Micromorphic RVE, deformation mappings.

The key goal of this chapter is to find the cohesive traction–separation relation $\widehat{\boldsymbol{t}}_0(\llbracket\widehat{\boldsymbol{\varphi}}\rrbracket)$ based on a homogenization of the underlying micromorphic mesostructure. In view of the computational homogenization, we are particularly interested its incremental formulation

$$\delta\widehat{\boldsymbol{t}}_0 = \widehat{\boldsymbol{A}}\cdot\llbracket\delta\widehat{\boldsymbol{\varphi}}\rrbracket\,, \qquad\qquad \widehat{\boldsymbol{A}} := \mathrm{D}_{\llbracket\widehat{\boldsymbol{\varphi}}\rrbracket}\widehat{\boldsymbol{t}}_0\,. \tag{6.1}$$

The representation of the micromorphic mesostructure is treated in the following section.

6.2 Micromorphic representative volume element at the meso level

The geometric features of the RVE follow those introduced in Section 5.2. It is essential to keep in mind that the height h_0 of the RVE delivers the initial thickness of the material layer itself. To resolve its intrinsic substructure a micromorphic continuum model rather than a standard continuum is used within the RVE. The continuum and constitutive framework as presented in Chapter 3 are adopted to this end. In view of the homogenization, it is crucial to convey non-homogeneous Neumann boundary conditions introduced Section 4.3.1. The micromorphic deformation within the RVE is described within the framework of finite-deformation kinematics. As illustrated in Figure 6.2, to each meso-continuum point $\mathscr{P}$ within the RVE, a so-called microcontinuum $\bar{\mathscr{B}}$ is attached, which deforms homogeneously and kinematically independently from the continuum. The governing quantities and equations introduced in Section 3.2.1 are recalled in Table 6.1. The omission of body forces is

again essential at the RVE level. As in Section 4.3.1, the micromorphic hyperelastic formulation for the stored-energy density (3.49)–(3.50) is adopted as proposed by Hirschberger et al. (2007b).

The boundary value problem at the RVE level needs to be solved according to boundary conditions imposed by the interface at the macro level. The particular relations between the RVE and the interface will be addressed in the following section.

6.3 Meso–macro transition

Between the interface at the macro level and the micromorphic RVE at the meso/micro level, a scale transition is achieved via a homogenization. The governing quantities in the interface, i. e. the traction, the deformation jump and the virtual work, are related to the averages of the corresponding quantities within the RVE. The macro deformation or traction are applied as boundary conditions on the RVE, which must fulfil the Hill condition. We present different consistent options for these boundary conditions, before we introduce a hybrid boundary condition that accounts particularly well for the geometry and deformation modes imposed by the material layer.

6.3.1 Homogenization

Since the cohesive interface at the macro level is embedded into a classical continuum and within the RVE we consider a micromorphic continuum, we relate the micromorphic meso quantities to the corresponding measures in the interface, which are found in Table 6.1. Thereby the height h_0 of the material layer, being equally part of both the macro and the meso geometry, is especially taken into account.

Deformation. The average of the meso-deformation gradient over the RVE, $\langle \boldsymbol{F} \rangle$, is related to the macroscopic deformation measure in the interface as

$$\boldsymbol{I} + \frac{1}{h_0} [\![\widehat{\boldsymbol{\varphi}}]\!] \otimes \widehat{\boldsymbol{N}} \equiv \langle \boldsymbol{F} \rangle \tag{6.2}$$

with the average deformation gradient $(4.6)_1$.

Traction. In order to relate the macroscopic traction vector across the interface, we employ the Cauchy theorem to relate the average RVE meso-stress $\langle \boldsymbol{P} \rangle$ to the traction across the interface as

$$\widehat{\boldsymbol{t}}_0 = \{\widehat{\boldsymbol{P}}\} \cdot \widehat{\boldsymbol{N}}\,, \qquad \text{with} \qquad \{\widehat{\boldsymbol{P}}\} \equiv \langle \boldsymbol{P} \rangle \tag{6.3}$$

with the average stress given in $(4.6)_2$. Herein $\boldsymbol{t}_0$ denotes the spatial meso traction vector at the micromorphic meso boundary.

Virtual work. For the response of a macro continuum point $\widehat{\mathscr{P}}$ in the cohesive interface $\widehat{\Gamma}$ and the average response in its corresponding RVE to be equivalent, the macroscopic virtual work performed in the interface and the average of the virtual work performed in the RVE must be identical:

$$\widehat{\boldsymbol{t}}_0 \cdot [\![\delta\widehat{\boldsymbol{\varphi}}]\!] \equiv h_0 \langle \boldsymbol{P} : \delta\boldsymbol{F} + \bar{\boldsymbol{P}} : \delta\bar{\boldsymbol{F}} + \bar{\boldsymbol{Q}} :\cdot \delta\bar{\boldsymbol{G}} \rangle \,. \tag{6.4}$$

The RVE virtual work comprises contributions of all micromorphic stress measures. Inserting the kinematics (6.2) and the traction (6.3), we obtain a second aspect of the Hill condition. The macro virtual work in the interface then equals the product of average meso stress (6.3) and average virtual meso-deformation gradient (6.2),

$$\langle \boldsymbol{P} \rangle : \langle \delta\boldsymbol{F} \rangle \equiv \langle \boldsymbol{P} : \delta\boldsymbol{F} + \bar{\boldsymbol{P}} : \delta\bar{\boldsymbol{F}} + \bar{\boldsymbol{Q}} :\cdot \delta\bar{\boldsymbol{G}} \rangle \,. \tag{6.5}$$

The scale transition is not complete before appropriate boundary conditions have been defined, which follow next.

6.3.2 Boundary conditions on the micromorphic representative volume element

The boundary conditions to be imposed on the RVE ensure a correct scale transition if they meet the Hill condition. The aspired boundary condition shall account for the two deformation modes occurring in the interface, i. e. relative shear and normal tension.

To show that the boundary conditions of Section 6.3.2 chosen for the micromorphic RVE underlying to the material layer meet the Hill condition (6.5), the relation (4.28) is used once more. The Hill condition as rewritten in (4.28) multiplied by h_0 serves as a bases to check the admissibility.

Deformation boundary conditions. We propose the following homogeneous Dirichlet boundary conditions for the meso- and the micro-deformation map:

$$\boldsymbol{\varphi}(\boldsymbol{X}) \equiv \left[\boldsymbol{I} + \frac{1}{h_0} [\![\widehat{\boldsymbol{\varphi}}]\!] \otimes \widehat{\boldsymbol{N}} \right] \cdot \boldsymbol{X} \qquad \forall \boldsymbol{X} \in \partial\mathscr{B}_0 \,, \tag{6.6}$$

$$\bar{\boldsymbol{F}}(\boldsymbol{X}) \equiv \boldsymbol{I} \qquad \forall \boldsymbol{X} \in \partial\mathscr{B}_0 \,. \tag{6.7}$$

For the given RVE geometry, the meso deformation at the top and bottom boundary simplifies to

$$\boldsymbol{\varphi}(\boldsymbol{X}) \equiv \begin{cases} \frac{1}{2}[\![\widehat{\boldsymbol{\varphi}}]\!] & \forall \boldsymbol{X} \in \partial \mathscr{B}_0^{\mathrm{T}} \\ -\frac{1}{2}[\![\widehat{\boldsymbol{\varphi}}]\!] & \forall \boldsymbol{X} \in \partial \mathscr{B}_0^{\mathrm{B}} \end{cases}, \tag{6.8}$$

as explained in (5.9), while the deformation at the left and right boundary is prescribed linearly as well. The admissibility of these boundary conditions a shown in Section 4.3.3 for the continuous macrostructure can directly be transferred to the case of the material layer. Equations (6.6)–(6.8) are verified here with (4.28):

$$\begin{aligned} & h_0\langle \boldsymbol{P} : \delta\boldsymbol{F} + \bar{\boldsymbol{P}} : \delta\bar{\boldsymbol{F}} + \bar{\boldsymbol{Q}} \vdots \cdot \delta\bar{\boldsymbol{G}} \rangle - h_0\langle \boldsymbol{P} : \langle \delta\boldsymbol{F} \rangle \rangle \\ =& \frac{1}{w_0} \int_{\partial \mathscr{B}_0} \delta\boldsymbol{\varphi} \cdot \boldsymbol{P} \cdot \boldsymbol{N} - \langle \delta\boldsymbol{F} \rangle : [\boldsymbol{P} \cdot \boldsymbol{N} \otimes \boldsymbol{X}] + \delta\bar{\boldsymbol{F}} : \bar{\boldsymbol{Q}} \cdot \boldsymbol{N} \, \mathrm{d}A \\ =& \frac{1}{w_0} \int_{\partial \mathscr{B}_0} [\delta\boldsymbol{\varphi} - \langle \delta\boldsymbol{F} \rangle \cdot \boldsymbol{X}] \cdot \boldsymbol{t}_0 + \delta\bar{\boldsymbol{F}} : \bar{\boldsymbol{t}}_0 \, \mathrm{d}A \doteq 0 \,. \end{aligned} \tag{6.9}$$

This term identically equals zero if the deformation boundary condition (6.6) is applied.

Hybrid boundary conditions. To account for the deformation modes and the geometry of the material layer, at the top and bottom boundaries of the RVE, which are conceptually aligned with the positive and negative edges of the interface, $\widehat{\Gamma}_0^+$ and $\widehat{\Gamma}_0^-$, respectively, we fully prescribe the meso-deformation boundary conditions by means of the separation $[\![\widehat{\boldsymbol{\varphi}}]\!]$ as examined for the uniform displacement boundary conditions (6.8). For the micro-deformation map, the boundary condition (6.7) must be fulfilled both at the top and at the bottom:

$$\bar{\boldsymbol{F}}(\boldsymbol{X}) = \boldsymbol{I} \qquad \forall \boldsymbol{X} \in \partial \mathscr{B}_0^{\mathrm{T}} \cup \partial \mathscr{B}_0^{\mathrm{B}} \,. \tag{6.10}$$

In the plane of the interface, periodic deformations and antiperiodic tractions are applied as presented in Equations (4.34)–(4.35) of Section 4.3.3. Thus the periodic deformation and antiperiodic traction boundary condition in plane specify to be formulated with respect to the left and right corner as

$$\boldsymbol{\varphi}^{\mathrm{R}} - \boldsymbol{\varphi}^{\mathrm{L}} = \boldsymbol{0} \quad \forall \boldsymbol{X} \in \partial \mathscr{B}_0^{\mathrm{L/R}}, \qquad \boldsymbol{t}_0^{\mathrm{R}} + \boldsymbol{t}_0^{\mathrm{L}} = \boldsymbol{0} \quad \forall \boldsymbol{X} \in \partial \mathscr{B}_0^{\mathrm{L/R}}, \tag{6.11}$$

$$\bar{\boldsymbol{F}}^{\mathrm{R}} - \bar{\boldsymbol{F}}^{\mathrm{L}} = \boldsymbol{0} \quad \forall \boldsymbol{X} \in \partial \mathscr{B}_0^{\mathrm{L/R}}, \qquad \bar{\boldsymbol{t}}_0^{\mathrm{R}} + \bar{\boldsymbol{t}}_0^{\mathrm{L}} = \boldsymbol{0} \quad \forall \boldsymbol{X} \in \partial \mathscr{B}_0^{\mathrm{L/R}}. \tag{6.12}$$

This strong contraint on the periodicity of the meso-deformation map $\boldsymbol{\varphi}^{\mathrm{L/R}}$ along the interface plane results from the kinematic assumption (6.2) for the interface

deformation modes, which does not allow for lateral extension.

This hybrid choice of boundary conditions can be shown to be admissible with respect to the Hill condition (6.5). The derivation for the top and bottom boundary is already given by Equation (6.6). The validity of the periodicity for the opposite left and right edges can directly be adopted from the fully periodic case (4.34)–(4.34) of Section 4.3.2, the admissibility of which was shown in Section 4.3.3. Analogously to (4.37)–(4.38), the integral, here only evaluated at the left and the right boundary,

$$\begin{aligned}&\frac{1}{w_0}\int_{\partial\mathscr{B}_0^{\mathrm{L}}}[\delta\boldsymbol{\varphi}-\langle\delta\boldsymbol{F}\rangle\cdot\boldsymbol{X}]\cdot\boldsymbol{t}_0+\delta\bar{\boldsymbol{F}}:\bar{\boldsymbol{t}}_0\,\mathrm{d}A\\+&\frac{1}{w_0}\int_{\partial\mathscr{B}_0^{\mathrm{R}}}[\delta\boldsymbol{\varphi}-\langle\delta\boldsymbol{F}\rangle\cdot\boldsymbol{X}]\cdot\boldsymbol{t}_0+\delta\bar{\boldsymbol{F}}:\bar{\boldsymbol{t}}_0\,\mathrm{d}A=0\end{aligned}\tag{6.13}$$

will vanish over opposite periodic boundaries if both the traction $\boldsymbol{t}_0$ and the double traction $\bar{\boldsymbol{t}}_0$ are antiperiodic. Combining this and (4.31) on the top and bottom boundary leads to

$$\begin{aligned}&\frac{1}{w_0}\int_{\partial\mathscr{B}_0^{\mathrm{T}}\cup\partial\mathscr{B}_0^{\mathrm{B}}}\boldsymbol{t}_0\cdot[\delta\boldsymbol{\varphi}-\langle\delta\boldsymbol{F}\rangle\cdot\boldsymbol{X}]+\delta\bar{\boldsymbol{t}}_0:\bar{\boldsymbol{F}}\,\mathrm{d}A\\+&\frac{1}{w_0}\int_{\partial\mathscr{B}_0^{\mathrm{L}}\cup\partial\mathscr{B}_0^{\mathrm{R}}}[\boldsymbol{t}_0^{\mathrm{L}}+\boldsymbol{t}_0^{\mathrm{R}}]\cdot[\delta\boldsymbol{\varphi}-\langle\delta\boldsymbol{F}\rangle\cdot\boldsymbol{X}]+[\bar{\boldsymbol{t}}_0^{\mathrm{L}}+\bar{\boldsymbol{t}}_0^{\mathrm{R}}]:\delta\bar{\boldsymbol{F}}\,\mathrm{d}A=0\,,\end{aligned}\tag{6.14}$$

which consequently is zero, too. Thus the proposed hybrid boundary conditions are admissible for the micromorphic RVE underlying to the material layer.

6.4 Computational homogenization

As in Section 5, boundary value problems are solved by means of a nested solution schemed involving a finite-element discretization at both the macro and the meso level, as illustrated in Figure 6.3 is performed. At the macro level, interface elements situated between continuum elements represent the material layer. While the constitutive behaviour of the bulk is postulated a priori, the traction–separation relation (6.1) of the interface element is obtained from the underlying micromorphic mesostructure. The computational interface homogenization approach presented in Chapter 5.4 is modified to account for the micromorphic mesostructure represented by the RVE.

Algorithmically the multiscale solution procedure is completely analogous to the scheme of Section 5.4.1. The complication lies in the more sophisticated system of

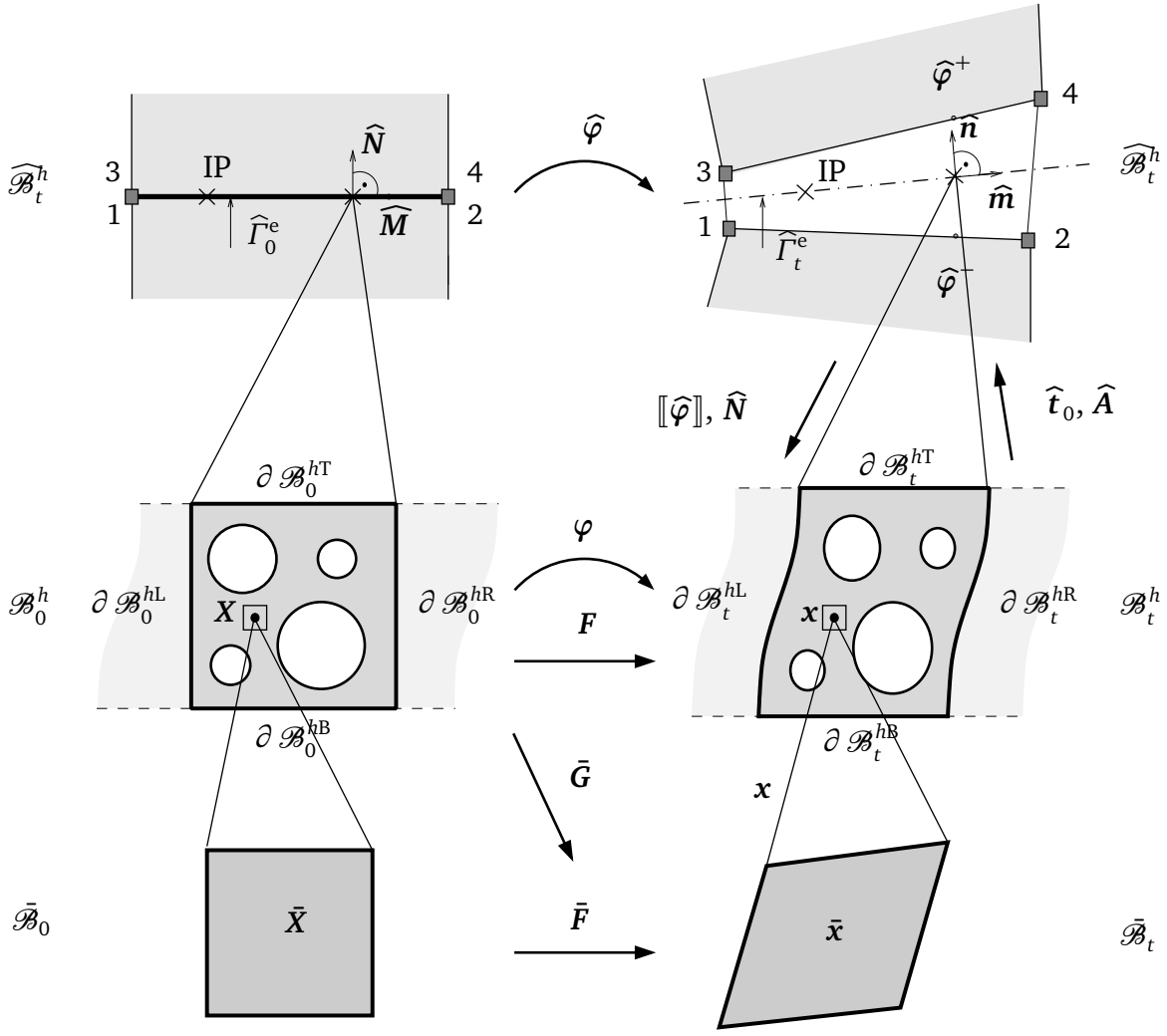

Figure 6.3: Computational homogenization between the interface integration point (IP) of the interface element on $\widehat{\Gamma}_0^e$ at the macro level and the underlying representative volume element $\mathscr{B}_0^h$ with boundary $\partial \mathscr{B}_0^h$ and microcontinua $\bar{\mathscr{B}}_0$ delivering additional degrees of freedom.

equations within the RVE. On the one hand, this requires the elaborate numerical scheme presented in 3.4 involving the coupled problem with elements of 'mixed' approximation order. On the other hand, the additional boundary conditions evolving from the micro deformation have to be taken into account.

6.4.1 Numerical solution of the RVE problem

For the solution of the micromorphic RVE boundary value problem, the numerical framework presented in Section 3.4 is adopted. The primary unknown variables at the finite-element nodes are the meso deformation map $\boldsymbol{\varphi}_L$ and the micro deformation map $\bar{\boldsymbol{F}}_M$ of (3.56). The micromorphic coupled system to be solved is given by (3.60).

We apply the hybrid boundary conditions of Section 6.3.2 on the RVE, which account both quantitatively and qualitatively for the interface deformation. The deformation (6.8) and (6.10) stemming from the interface is applied incrementally as a boundary condition to all top and bottom nodes of the RVE within the reduced system of equations. The coupled system of equations (3.64) within the RVE is solved iteratively. When equilibrium is found, we recompute the dependent degrees of freedom. Moreover, we obtain the spatial reaction forces at the nodes with prescribed deformation as $\mathbf{f}_I^{\text{pre}}$ and $\bar{\mathbf{f}}_I^{\text{pre}}$ from equation (3.64) with $\mathbf{f}_I^{\text{int}} = \mathbf{0}$ and $\bar{\mathbf{f}}_J^{\text{int}} = \mathbf{0}$, which is true at algorithmic equilibrium.

6.4.2 Homogenized interface quantities

We want to extract the macroscopic traction vector $\widehat{\boldsymbol{t}}_0$ and the tangent operator $\widehat{\boldsymbol{A}}$ at the integration point of the interface element.

Therefore the system of equations on the RVE is condensed such that only the stiffness matrix and the residual vector for the prescribed degrees of freedom remain. These prescribed degrees of freedoms are those of all the nodes at the top and the bottom of the RVE, $\partial\mathscr{B}^{h\mathrm{B}} \cup \partial\mathscr{B}^{h\mathrm{T}}$, for the present choice of hybrid boundary conditions.

Macroscopic traction vector. The macro traction vector $(6.1)_1$ is obtained based on the traction vector involving the average Piola stress (6.3). This is rewritten discretely in terms of the reaction forces $\mathbf{f}_I^{\text{pre}}$ as

$$\widehat{\boldsymbol{t}}_0 = \frac{1}{V_0} \sum_I^{n_{\text{pre}}} \mathbf{f}_I^{\text{pre}} \otimes \boldsymbol{X}_I \cdot \widehat{\boldsymbol{N}}\,, \qquad I \in \partial\mathscr{B}^{h\mathrm{B}} \cup \partial\mathscr{B}^{h\mathrm{T}}\,. \tag{6.15}$$

The summation runs over all n_{pre} RVE boundary nodes with prescribed deformation.

Macroscopic tangent operator. To derive the tangent operator $(6.1)_2$, we consider an increment of the traction vector (6.15), $\Delta\widehat{\boldsymbol{t}}_0$. With the spatial reaction force in the coupled system (3.64) and the prescribed deformation (6.8) and (6.10), the following steps are performed,

$$\begin{aligned}
\Delta\widehat{\boldsymbol{t}}_0 &= \frac{1}{V_0}\sum_{I}^{n_{\text{pre}}} \Delta\mathbf{f}_I^{\text{pre}} \otimes \boldsymbol{X}_I \cdot \widehat{\boldsymbol{N}} \\
&= \frac{1}{V_0}\sum_{I}^{n_{\text{pre}}}\sum_{L,M}^{n_{\text{pre}}} \left[[\mathsf{K}_{IL}^{\varphi\varphi} \cdot \Delta\boldsymbol{\varphi}_L + \mathsf{K}_{IM}^{\varphi\bar{F}} \cdot \Delta\bar{\boldsymbol{F}}_M] \otimes \boldsymbol{X}_I \right] \cdot \widehat{\boldsymbol{N}} \\
&= \frac{1}{V_0}\sum_{I}^{n_{\text{pre}}}\sum_{L,M}^{n_{\text{pre}}} \left[\left[\mathsf{K}_{IL}^{\varphi\varphi} \cdot \left[\Delta\boldsymbol{I} + \frac{1}{h_0}[\![\Delta\widehat{\boldsymbol{\varphi}}]\!] \otimes \widehat{\boldsymbol{N}} \right] \cdot \boldsymbol{X}_L + \mathsf{K}_{IM}^{\varphi\bar{F}} \cdot \boldsymbol{0} \right] \otimes \boldsymbol{X}_I \right] \cdot \widehat{\boldsymbol{N}} \qquad (6.16) \\
&= \left[\frac{1}{h_0 V_0} \left[\widehat{\boldsymbol{N}} \otimes \widehat{\boldsymbol{N}} \right] : \sum_{I}^{n_{\text{pre}}}\sum_{L}^{n_{\text{pre}}} \left[\boldsymbol{X}_L \otimes \boldsymbol{X}_I \right] : \mathsf{K}_{IL}^{\varphi\varphi} \right] \cdot [\![\Delta\widehat{\boldsymbol{\varphi}}]\!] .
\end{aligned}$$

Thereby the trivial identity $\Delta\boldsymbol{I} = \boldsymbol{0}$ as well as $\Delta\bar{\boldsymbol{F}}_M = \boldsymbol{0}$, which follows from (6.10), are used. The term in the bracket is identified as the macroscopic tangent operator, which reads

$$\widehat{\boldsymbol{A}} = \frac{1}{w_0 h_0^2}[\widehat{\boldsymbol{N}} \otimes \widehat{\boldsymbol{N}}] : \left[\sum_{I}^{n_{\text{pre}}}\sum_{L}^{n_{\text{pre}}} [\boldsymbol{X}_L \otimes \boldsymbol{X}_I] : \mathsf{K}_{IL}^{\varphi\varphi} \right] , \qquad I, L \in \partial\mathscr{B}^{h\text{B}} \cup \partial\mathscr{B}^{h\text{T}} . \qquad (6.17)$$

With these quantities at hand for the particular macro interfacial integration point, the constitutive part of macro boundary value problem is complete and the iterative macro solution can be proceeded.

6.5 Numerical examples

The framework of the computational homogenization with the interface element on the macro level and the micromorphic RVE on the meso and micro level is applied to numerical examples.

A finite element simulation is performed on both the macro- and the meso level, with the boundary value problem described for the macro scale and its constitutive response evaluated within the RVE. At the macro level, we use four-node plane-strain elements with bilinear interpolations for the bulk as well as linear interface elements with four nodes and two Gaussian integration points. For the micromorphic RVE we utilize Lagrangian plane-strain elements with biquadratic interpolation for both the meso placement $\boldsymbol{X}$ and the meso deformation map $\boldsymbol{\varphi}$, as well as bilinear interpolation for the micro-deformation map $\bar{\boldsymbol{F}}$. Throughout the section, the components of the respective displacement jumps and tractions will be expressed in terms of the orthonormal macro basis $\widehat{\boldsymbol{M}}$, $\widehat{\boldsymbol{N}}$ shown in Figure 6.3.

6.5.1 Interface under fully prescribed shear mode loading

As a benchmark problem, we first consider a single interface element, which is subject to shear mode loading, as depicted in Figure 6.4. The deformation of the surrounding bulk is fully controlled so that no degrees of freedom are activated there. The RVE is modelled as a quadratic specimen with a circular centred hole of 20 % void fraction, meshed with 96 micromorphic elements. Within the RVE of height h_0, the sample material parameters, i. e. Young's modulus $E = 1000$ and Poisson's ratio $\nu = 0.3$ are chosen for all computations. At first, the internal length is varied for a fixed scale-transition parameter, $p/E = 10$, see Section 6.5.1. Secondly, the scale-transition parameter is varied for a fixed internal length of $l = 0.2h_0$.

Influence of the micromorphic internal length – size dependence. The traction–separation curves at an integration point in the interface element are shown for different values of the micromorphic internal-length parameter related to the total height of the interface in Figure 6.6. The traction–separation curve in loading direction in Figure 6.6(a), $\widehat{t}_{\widehat{M}}$ vs. $[\![\widehat{\varphi}_{\widehat{M}}]\!]$, obeys an approximately linear relation. Moreover a strong size dependence is observed: Larger internal-length parameters yield a notably stiffer response. The traction–separation curve, $\widehat{t}_{\widehat{N}}$ vs. $[\![\widehat{\varphi}_{\widehat{M}}]\!]$, perpendicular to the loading direction shown in Figure 6.6(b) reveals a coupled response. The tangential tractions are much smaller than the normal components, nevertheless a nonlinear relation is observed. The dependence of the internal length is reverse compared to the first curve: smaller internal length yield the stiffer normal response for the shear loading.

The corresponding spatial configurations with the micromorphic meso stress are

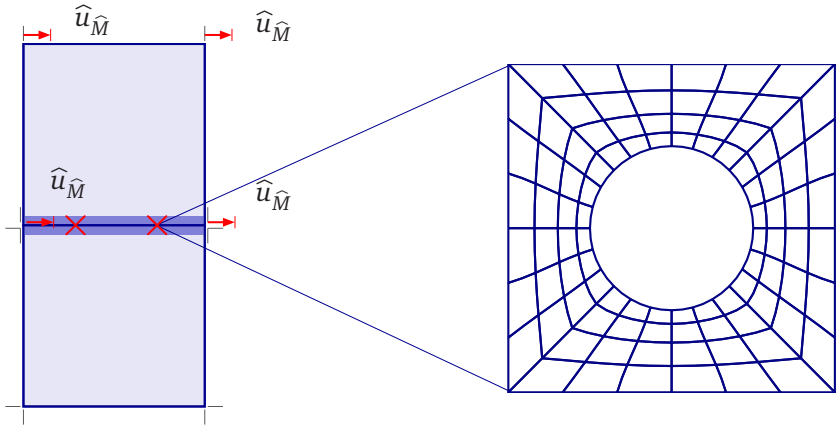

Figure 6.4: Benchmark problem for multiscale framework: Single interface element subjected to shear.

displayed in Figure 6.2. We observe that for increasing internal length, the deformation of the specimen around the hole becomes less pronounced. Moreover, for non-zero internal length we observe the typical nonsymmetric meso stress, when looking at the shear components. Especially, the shear component $\sigma_{\widehat{M}\widehat{N}}$ is significantly higher for the largest internal length. Also the normal stress in tangential direction $\sigma_{\widehat{M}\widehat{M}}$ is remarkably larger, while the influence on the other two components is rather weak.

Influence of the micromorphic scale-transition parameter. Next, we study the influence of the scale-transition parameter p, which controls the kinematic correlation between the meso and the micro scale. For a variation of the parameter p in exponential steps to the basis ten, the spatial meshes of the macro and the mesostructure are presented in Figure 6.7. The resulting traction–separation curves, $\widehat{t}_{\widehat{M}}$ vs. $[\![\widehat{\varphi}_{\widehat{M}}]\!]$ and $\widehat{t}_{\widehat{N}}$ vs. $[\![\widehat{\varphi}_{\widehat{M}}]\!]$, are shown in Figure 6.8. First of all, we notice that the response is coupled in the sense that an exclusively shearing deformation also yields normal tractions. As observed before, the shear component $\widehat{t}_{\widehat{M}}$ vs. $[\![\widehat{\varphi}_{\widehat{M}}]\!]$ obeys an approximately linear relation, while the tension response to the shear deformation $\widehat{t}_{\widehat{N}}$ vs. $[\![\widehat{\varphi}_{\widehat{M}}]\!]$ is strongly nonlinear, however significantly smaller. Furthermore, we observe that smaller scale transition parameters yield a stiffer response in the shear traction $\widehat{t}_{\widehat{M}}$ vs. $[\![\widehat{\varphi}_{\widehat{M}}]\!]$ and a weaker response in the normal traction, $\widehat{t}_{\widehat{N}}$ vs. $[\![\widehat{\varphi}_{\widehat{M}}]\!]$.

The meso stress components are plotted in Figure 6.3. For larger scale-transition parameters, all stress components become more pronounced in the direct vicinity of the hole.

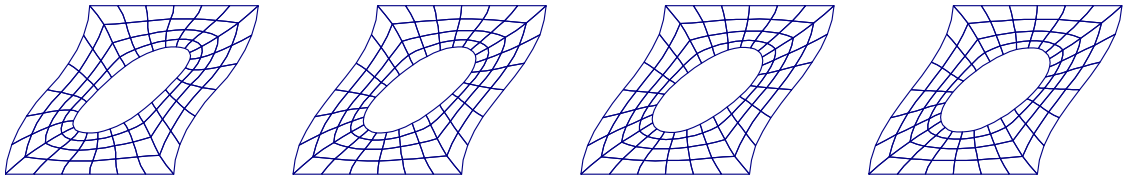

Figure 6.5: Spatial RVE meshes at different internal-length parameters.

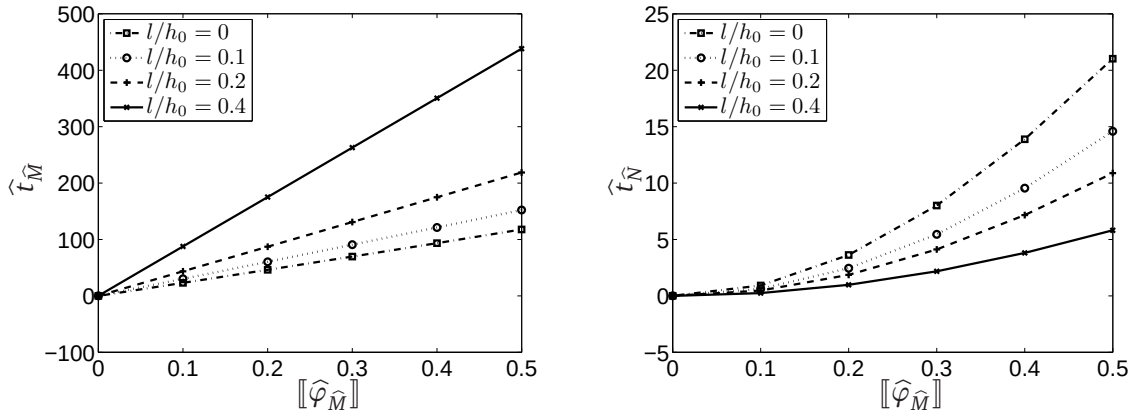

Figure 6.6: Traction–separation curves for different internal-length parameters.

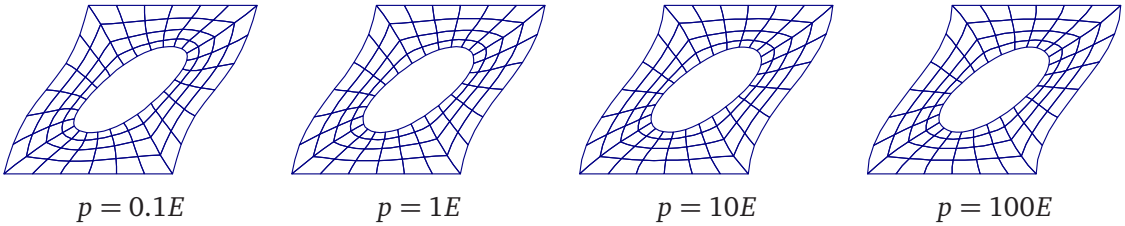

Figure 6.7: Spatial RVE meshes at different scale-transition parameters.

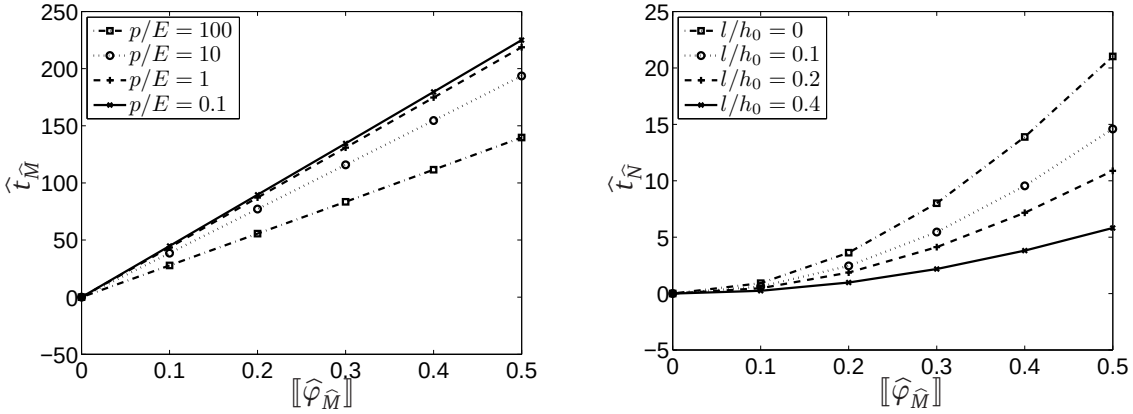

Figure 6.8: Macro traction–separation curves for different scale-transition parameters.

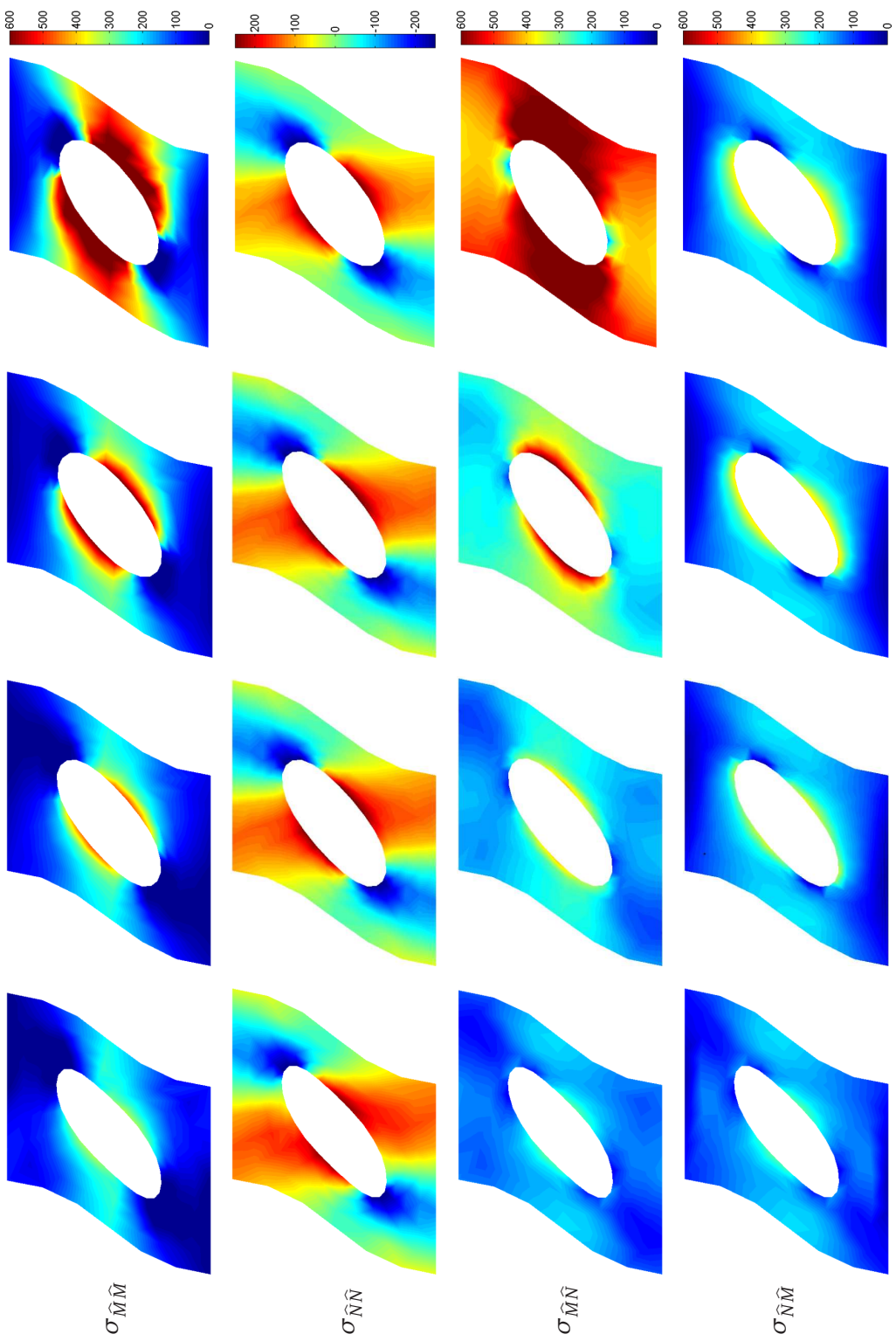

Table 6.2: Cauchy-type meso shear stress at different internal-length parameters.

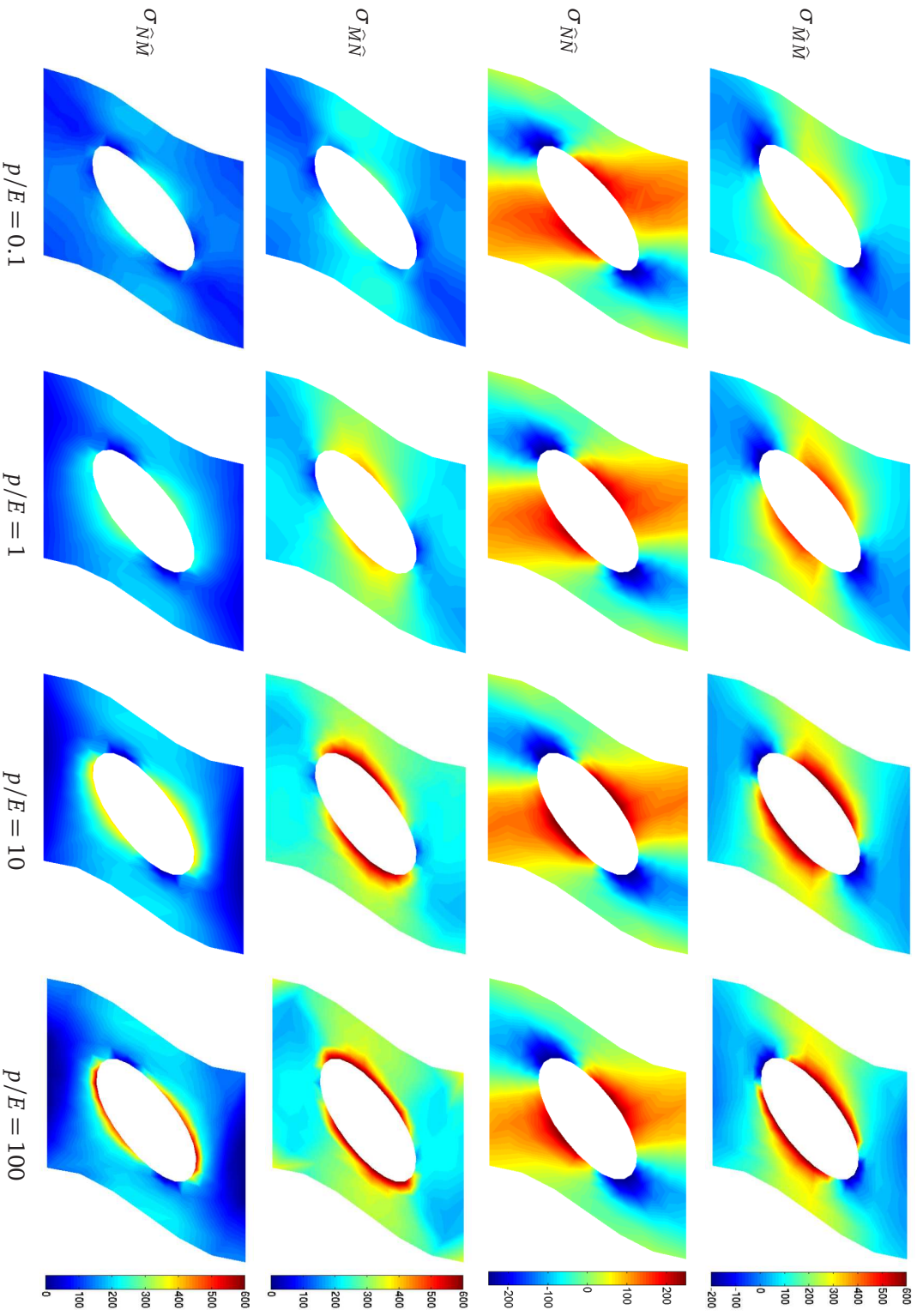

Table 6.3: Cauchy-type stress for different scale-transition parameters

6.5.2 Interface under fully prescribed tensile-mode loading

The second benchmark problem for the interface homogenization is simulated with the same macro and meso geometry as above, however here the interface deformation is applied in the tensile mode. Also the material parameters are adopted from the previous section.

While the material multiscale boundary value problem is illustrated in Figure 6.9, the corresponding spatial meshes of the RVE are displayed in Figures 6.10 and 6.13.

In the following, we once more investigate the influence of both additional micromorphic material parameters on the response, i. e. the internal-length parameter l and the scale-transition parameter p. From Figures 6.11 and 6.14, we directly observe that the tangential traction component, $\widehat{t}_{\widehat{M}}$, is zero for any of the considered combination of material parameters. This fact is attributed to the kinematic restriction imposed by the interface that does not allow for a lateral contraction and restricts the top and the bottom nodes to maintain the same distance tangential to the interface.

Influence of the micromorphic internal length – size dependence. For the present tensile-mode loading, the traction–separation curves in loading direction, $\widehat{t}_{\widehat{N}}$ vs. $[\![\widehat{\varphi}_{\widehat{N}}]\!]$, are compared for different internal length parameters in Figure 6.11. This response obeys a nonlinear behaviour, whereby the curves display a stiffer response for larger internal-length parameters l. The deformed meso meshes in Figure 6.10 reflect the same observation: For a larger internal length, the opening of the void is less pronounced which underlines the stiffer continuum response. The particular components of the meso stress of Cauchy type are shown in Figure 6.12. Again for a larger internal length, the non-symmetry of the Cauchy type meso stress proves to be stronger. However, different from the shear loading, where the distribution of the shear meso stress underwent a significant influence, the qualitative influence is comparatively small for the tension loading at hand.

Influence of the micromorphic scale-transition parameter. The influence of the micromorphic scale-transition parameter p on the macroscopic traction–separation response is plotted in Figure 6.14. Thereby the parameter is varied in exponential steps to the basis ten. We observe that the specimen with the higher scale-transition parameter p exhibits a stiffer behaviour. This is reflected by the deformed meshes in Figure 6.13 particularly in the direct vicinity of the hole. In the corresponding Cauchy-type meso stress component, shown in Figure 6.15, for larger p, again the stress is significantly larger at the edge of the hole. This matches well the observations of Hirschberger et al. (2007b), that for larger scale-transition parameters p, the region in which the meso deformation map and the deformation gradient deviate from each other are strongly localized to the heterogeneity.

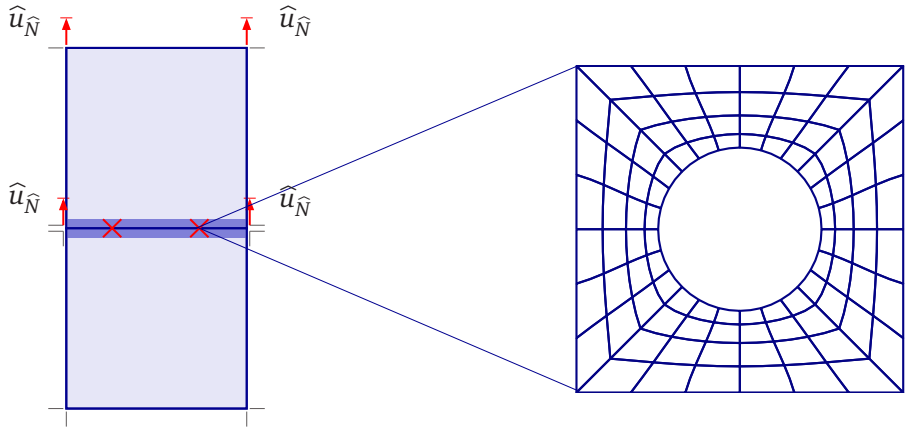

Figure 6.9: Benchmark problem for multiscale framework: Single interface element subjected to tension.

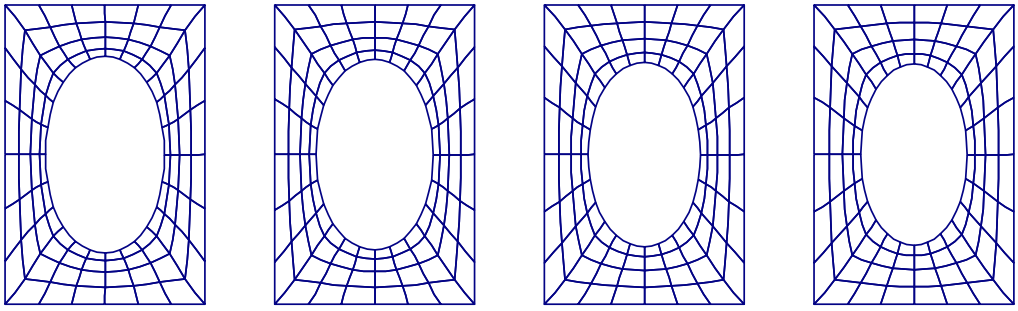

Figure 6.10: Spatial RVE meshes at different internal-length parameters.

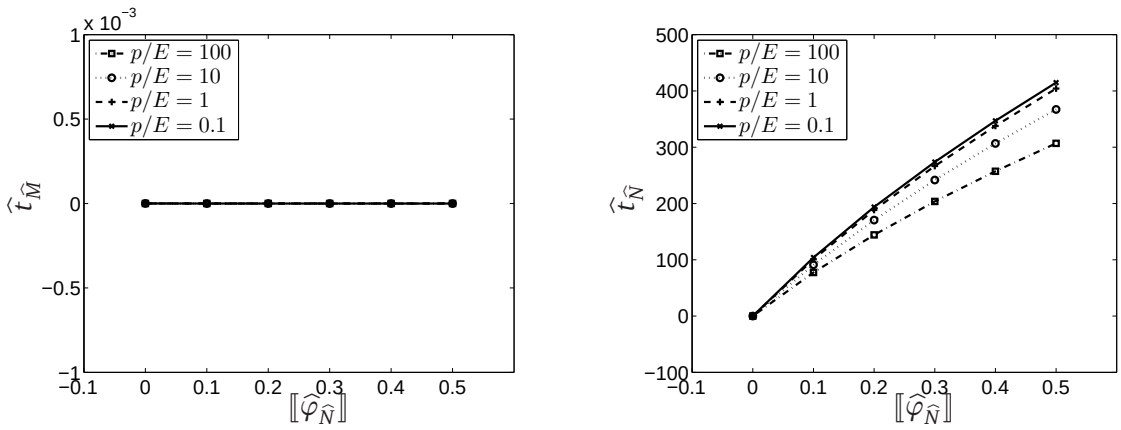

Figure 6.11: Traction–separation curves for different internal length parameters.

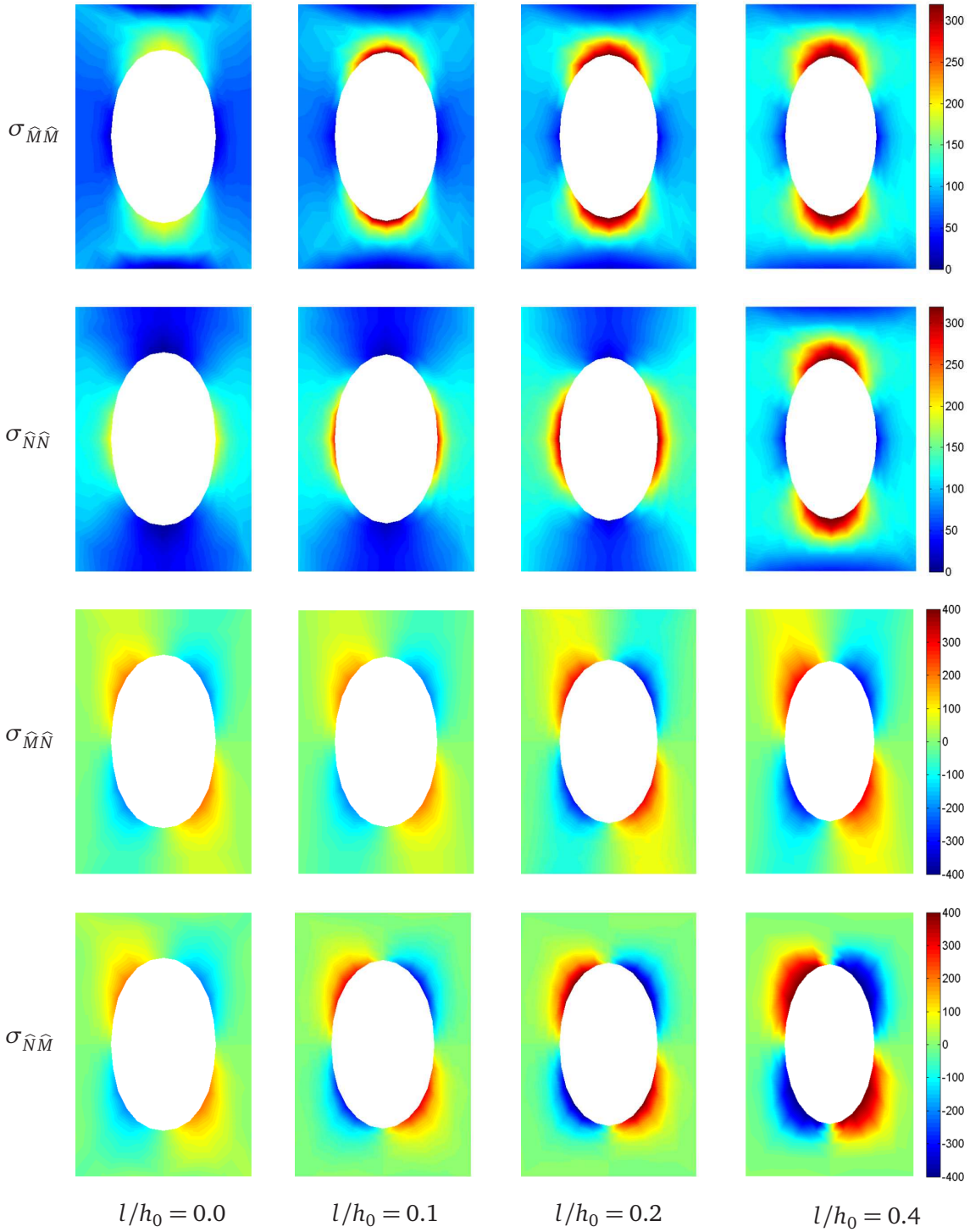

Figure 6.12: Cauchy-type meso shear stress at different internal-length parameters.

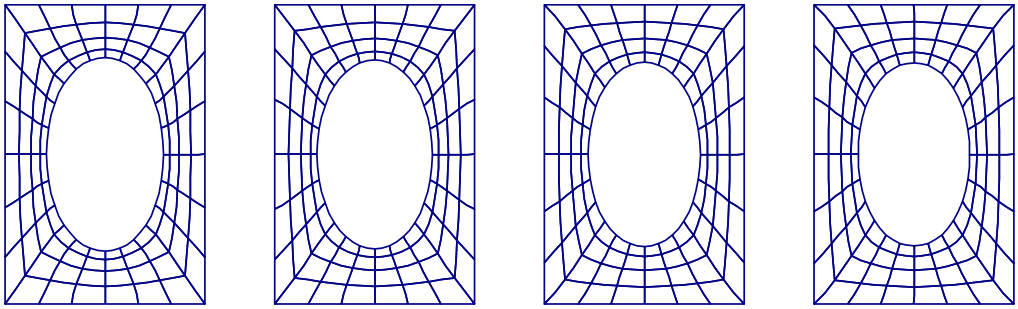

Figure 6.13: Spatial RVE meshes at different scale-transition parameters.

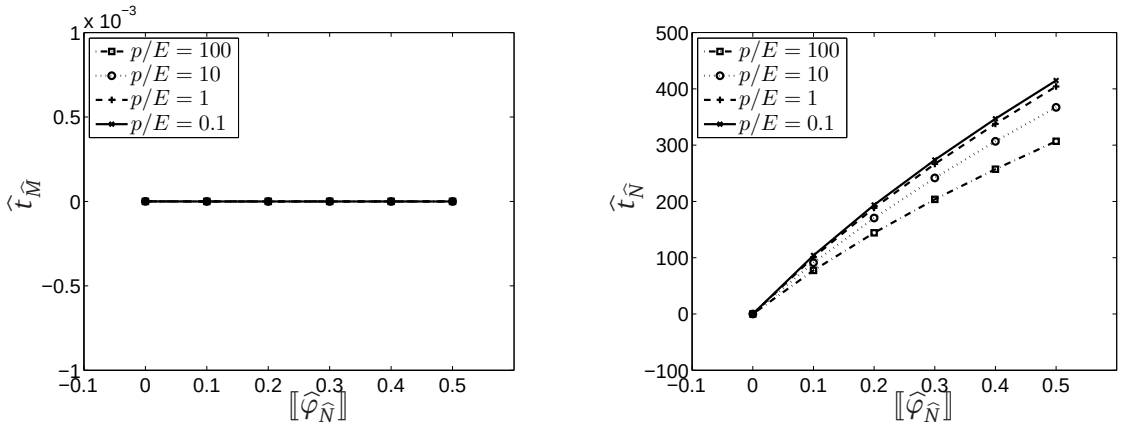

Figure 6.14: Macro traction–separation curves for different scale-transition parameters.

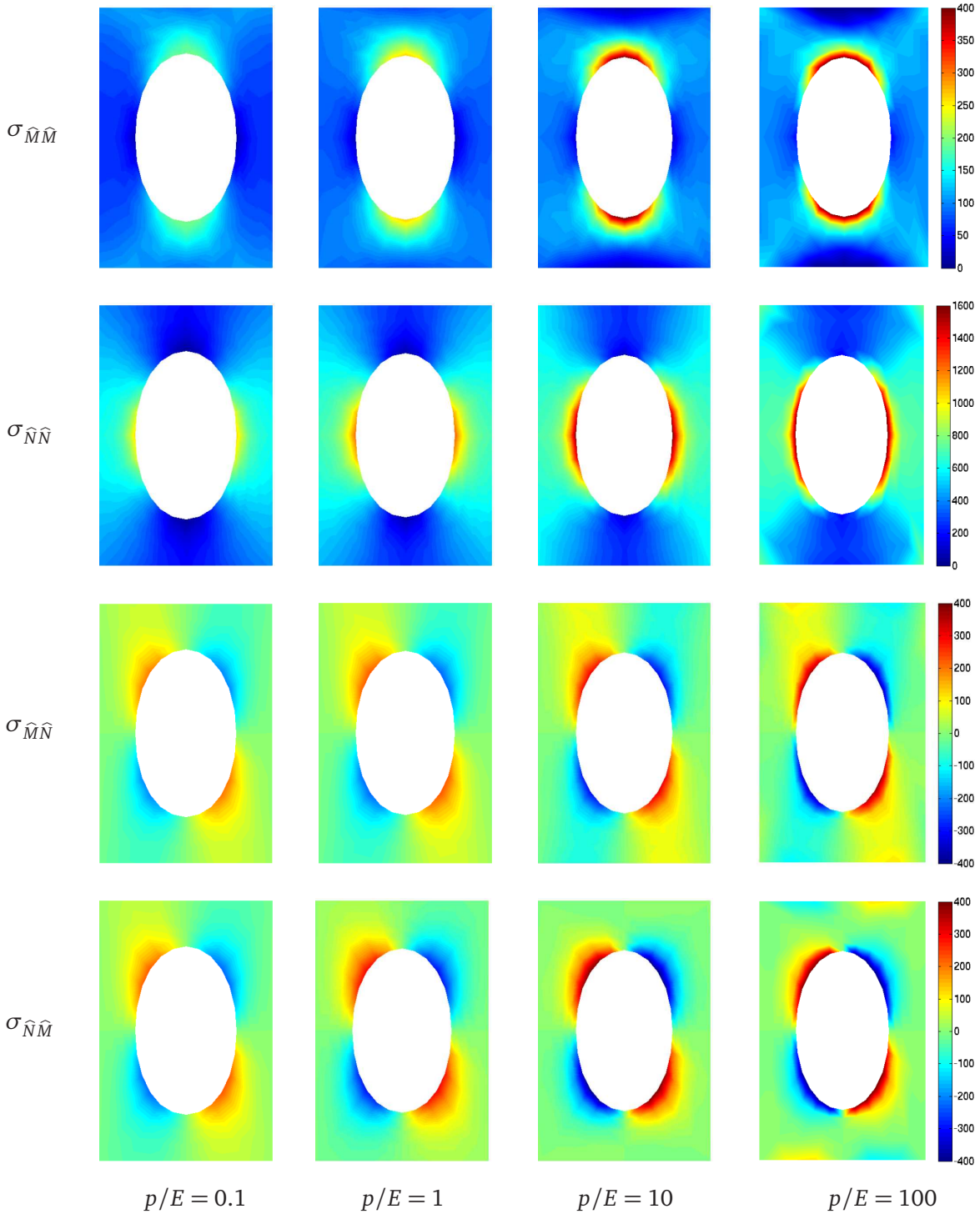

Figure 6.15: Cauchy-type meso shear stress at different scale-transition parameters.

6.5.3 Material layer within an infinite shear layer under shear-dominated mixed-mode loading

After the benchmark-type examples shown so far, which only considered the micromorphic RVE and the resulting homogenized traction–separation relations, now also the macro response is also taken account.

Therefore at the macro level the material layer within the periodic shear layer as seen in Section 5.5.2, Figure 5.11, is endowed with micromorphic representative volume elements. Micromorphic microstructures with the same geometry of those Section 5.5.3, i. e. a quadratic RVE with a lentil-shaped void of horizontal and vertical orientation, respectively, are compared with another specimen with a circular centered hole. Furthermore a homogeneous shear layer is considered as a benchmark RVE.

The deformation-driven load, $\widehat{u}_{\widehat{M}} = 5\widehat{u}_{\widehat{N}}$, is applied step-wise, at the top and in opposite direction at the bottom until the maximum lateral top displacement of $\widehat{u}_{\widehat{M}} = 0.2h_0$ is reached. A fixed set of material parameters is used. Particularly Young's modulus in the RVE is chosen significantly weaker than that of the macro bulk, $\widehat{E}/2000 = E = p$; lateral contraction is allowed by setting Poisson's ratio to $\widehat{\nu} = \nu = 0.3$. The internal length is chosen to be $l = 0.1h_0$, while the height of the material layer relative to the height of the macro shear layer is $w_0/\widehat{H}_0 = 0.05$.

While Figure 6.16 shows the considered column of elements for the periodic shear layer for the different RVEs at the after the last load step, the RVE meshes after the first step are plotted in Figure 6.17. While at the macro level, the bulk elements are deformed homogeneously as under simple shear, the spatial RVE of Figure 6.17(d), representing an infinite homogeneous shear layer, obeys an S-shape. This appears due to the boundary conditions for the micro-deformation map at the top and bottom boundaries of the RVE.

Figure 6.18 shows the load displacement curves at the top of the macro column for the different microstructures. The response to the shear dominated mixed mode loading caused by the vertically orientated lentil void is the stiffest, while the other two differ for the considered component, i. e. normal or tangential. Contrary to the classical RVE in Section 5.5.2, the homogeneous RVE does here not deliver the stiffest response. This can be attributed to the fact that, due to the nearly homogeneous deformation, the additional micro degrees of freedom and thus especially the gradient of the micro deformation map are barely excited and the respective contributions in the potential-energy density (3.49) do not come into play as strongly as for the heterogeneous specimens.

With this example it is succesfully shown that macroscopic boundary value problems involving a material interface can be solved numerically by applying a computational homogenization to obtain the response of the latter. An investigation of the influence of different material parameters on the response of a homogeneous RVE remains for future considerations.

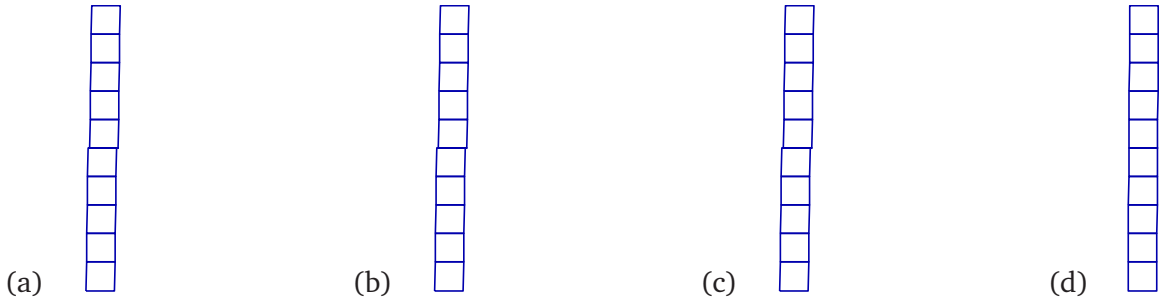

Figure 6.16: Shear layer: spatial macro meshes at $\widehat{u}_{\widehat{M}} = 0.2h_0$, for RVE with (a) hole, (b) vertical lentil-shaped void, (c) horizontal lentil-shaped void, (d) homogenenous shear layer.

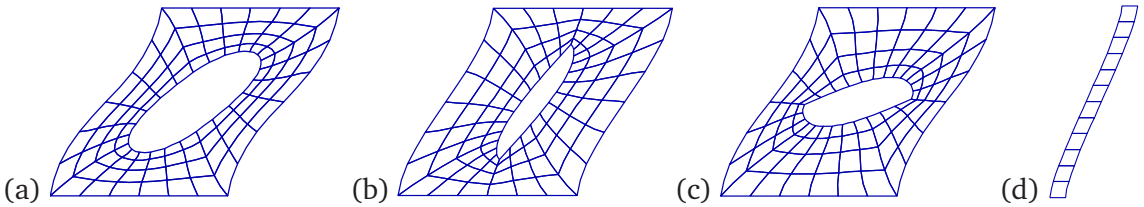

Figure 6.17: Shear layer: spatial RVEs with (a) hole, (b) vertical lentil-shaped void, (c) horizontal lentil-shaped void, (d) homogeneous shear layer at $\widehat{u}_{\widehat{M}} = 0.02h_0$.

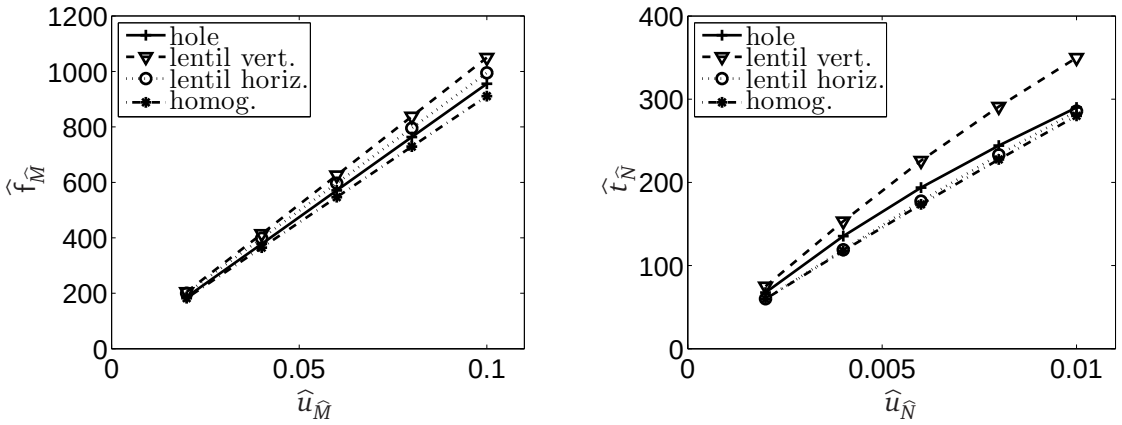

Figure 6.18: Shear layer: force–displacement curve at top of the macro shear layer.

6.5.4 Material layer within a specimen with a hole

The last example consists of a quadratic specimen with a circular centred hole at the macro level, comparable to the meso specimen in Sections 6.5.1 and 6.5.2, meshed with 72 bulk elements. Additionally at both lateral sides of the hole, a horizontal layer of three interface elements is arranged. The specimen is subject to constant uniaxial tension in vertical direction. At each interface integration point, the underlying micromorphic RVE of Sections 6.5.1 and 6.5.2 is evaluated. Once more, the internal-length parameter in the RVE is varied for an otherwise fixed set of material parameters ($\widehat{E} = 100E = 1 \times 10^5$, $\widehat{\nu} = \nu = 0.3$, $p/E = 1000 = 10\widehat{E}$, $\widehat{h}_0 = 20h_0$).

In Figure 6.19, next to the spatial macrostructure, the deformed RVEs at the six interfacial integration points along the material layer are shown for the maximum displacement applied, $\widehat{u}_{\widehat{N}}/\widehat{h}_0 = 0.025$. The particular deformed heights h_t of the RVEs qualitatively coincide well with the expected peak of both normal stress and normal strain close to the heterogeneity, the hole. This is also reflected by the normal components of the macro separation, $[\![\widehat{\varphi}_{\widehat{N}}]\!]$, and the macro traction, $\widehat{t}_{\widehat{N}}$, which are plotted versus the horizontal coordinate of the relative placement, $\widehat{\Xi}$, in Figure 6.20. This relative horizontal position $\widehat{\Xi} = 2\widehat{X}/\widehat{w}_0$ is given relative to the half width of the macro specimen.

While the normal separation $[\![\widehat{\varphi}_{\widehat{N}}]\!]$ is larger for smaller internal length, the normal traction $\widehat{t}_{\widehat{N}}$ increases with internal length. This observation matches well with the stiffer behaviour for larger internal length that the traction–separation curves in Figure 6.21 display. The macroscopic response is illustrated in the same figure: the prescribed displacement in vertical direction, $u_{\widehat{N}}$, at the top of the macro specimen is plotted versus the total reaction force at this edge. Here an influence of the underlying RVE is observed: once more the specimen with the RVE of the highest internal lengths obeys the stiffest macro response.

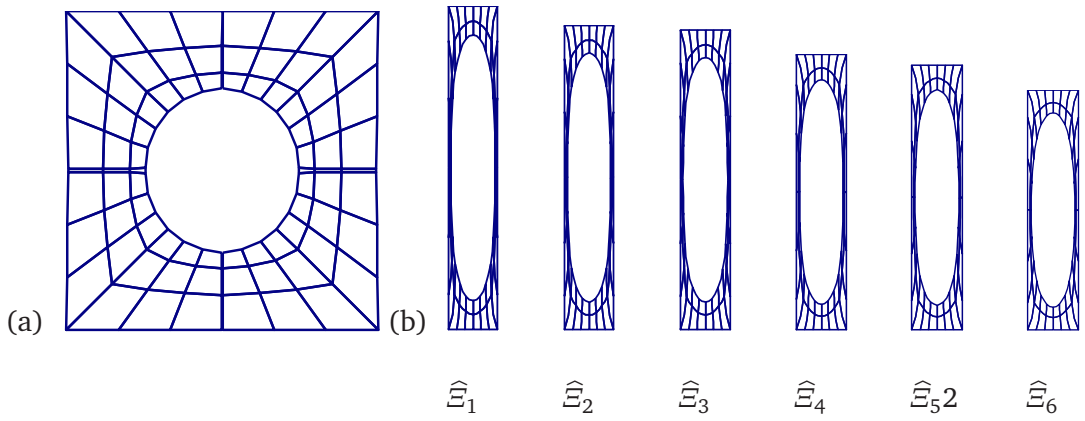

Figure 6.19: (a) Spatial macro mesh, (b) spatial meso meshes at the macro interface integration points located at $\widehat{\Xi}_i = 0.522, 0.581, 0.638, 0.737, 0.821, 0.952$.

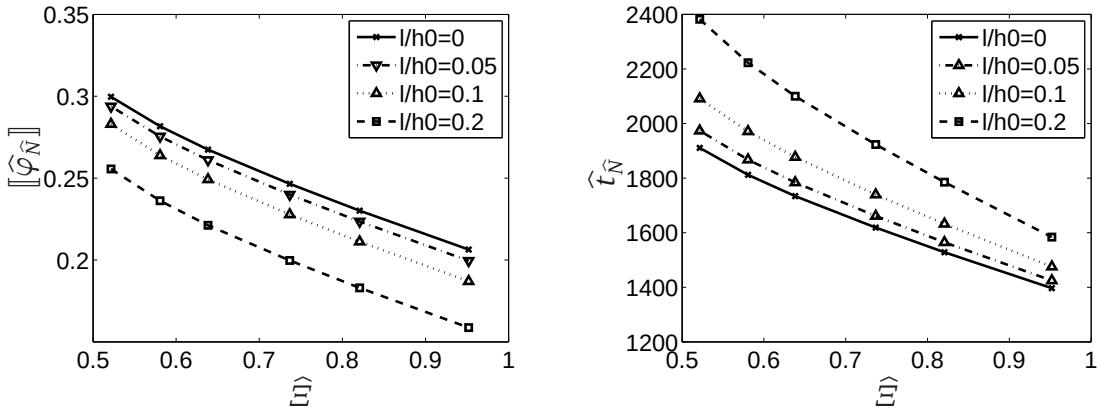

Figure 6.20: Separation vs. placement, homogenized traction vs. placement along the interface

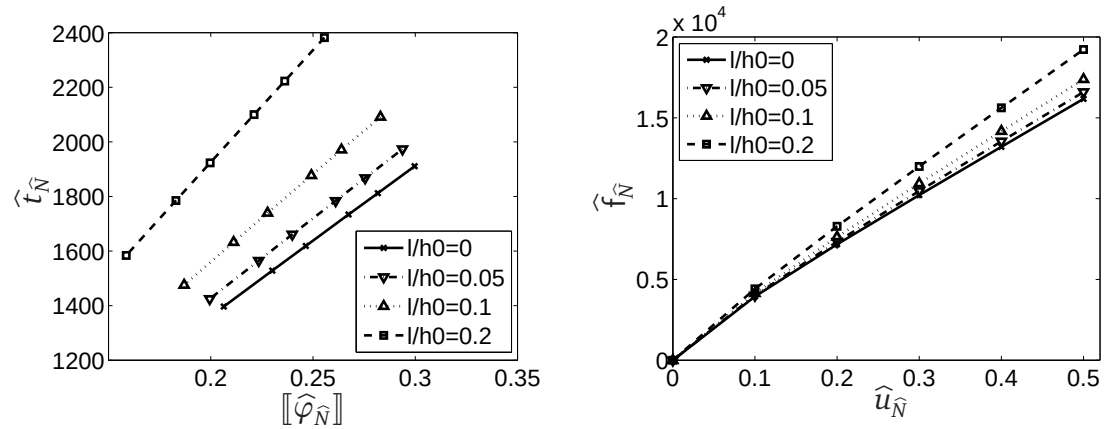

Figure 6.21: Traction–separation curve near the hole, load–displacement curve at macro top nodes for different internal-length parameters,

7 Concepts of Generalized Plasticity

Formulations of generalized inelasticity have attracted a growing portion of the mechanics research community within the last decades. This can be attributed to two main features. On the one hand, these theories well account for inelastic deformations of very small structures (on a micro scale) and thus reflect the reported size effects (Aifantis, 1984, Fleck et al., 1994, Stölken and Evans, 1998). On the other hand, the formulations of generalized plasticity have proven particularly useful when it comes to the numerical simulation of softening behaviour. Here due to the non-local effect which goes along with the considered internal length, an ill-posedness, as it arises in classical softening inelasticity, is circumvented and the occurring localized inelastic deformations are regularized. The proposed generalized plasticity theories comprise formulations of gradient plasticity, nonlocal plasticity, and micromorphic and the micropolar plasticity included in the latter.

Although a variety of different generalized plasticity formulations have been contributed, their respective features cannot be recognized clearly in each case. We aim at a clear classification with respect to the key features and seek connections to existing theories. To this end, similar to the work of Hirschberger and Steinmann (2007), here in particular different formulations of both gradient plasticity and micromorphic plasticity are presented, which prove thermodynamically consistent by fulfilling the second law of thermodynamics. Thereby we vary key features in a structured manner and investigate the impact on the formulation, with respect to the complexity of the balance of momentum, the boundary conditions, degrees of freedoms, the dissipation inequality, the yield condition and the flow rule as well as issues arising in a numerical implementation. We restrict ourselves to the isothermal case.

Outline. This chapter is structured as follows: After a brief review of a classical perfect elastoplastic formulation in Section 7.1, we address two major parts: The first part, Section 7.2, concerns formulations of gradient plasticity, whereas in the latter, Section 7.3, we present the analogous formulations of micromorphic plasticity. At the end of each section, we briefly summarise each class and review the variants with respect to their particular advantages and disadvantages. Throughout this chapter, we restrict ourselves to quasi-static problems within a geometrically

linear framework. We omit body forces for the sake of brevity without loss of generality.

7.1 Classical plasticity

The constitutive framework of the generalized plasticity formulations are based on that of classical plasticity, which was pioneered by Coleman (1964), Green and Naghdi (1965), Coleman and Gurtin (1967). In order to account for the irreversible character of the material response, particularly the second law of thermodynamics has to be fulfilled. Its reformulation as the Clausius-Duhem or dissipation inequality is directly applicable to the elasto-plastic framework.

The essential framework of small-strain classical plasticity, which bases on the framework of classical elasticity introduced in Section 2.2.2, is recalled here in order to introduce the concept and clarify notation for the subsequent sections on gradient and micromorphic plasticity.

7.1.1 Fundamental formulation of perfect elastoplasticity of a classical continuum at small strain

In order to account for both the reversible and the irreversible deformation respectively, the strain tensor (2.15) is additively decomposed into its elastic and its plastic part as

$$\boldsymbol{\varepsilon} := \boldsymbol{\varepsilon}_{\mathrm{e}} + \boldsymbol{\varepsilon}_{\mathrm{p}}^{\mathrm{int}} . \tag{7.1}$$

The free-energy density $\mathscr{W}$ depends on the elastic part of the strain only. However, we may rewrite it as a function of the displacement and the plastic strain, which is, in a standard manner, considered as an internal variable:

$$\mathscr{W} = \tilde{\mathscr{W}}(\boldsymbol{\varepsilon}(\boldsymbol{u}) - \boldsymbol{\varepsilon}_{\mathrm{p}}^{\mathrm{int}}) = \check{\mathscr{W}}(\boldsymbol{u}; \boldsymbol{\varepsilon}_{\mathrm{p}}^{\mathrm{int}}) . \tag{7.2}$$

The non-negative dissipation $\mathscr{D}$ obeys the following format:

$$\mathscr{D} = \boldsymbol{\sigma} : \dot{\boldsymbol{\varepsilon}} - \dot{\mathscr{W}} = \boldsymbol{\sigma}_{\mathrm{p}}^{\mathrm{int}} : \dot{\boldsymbol{\varepsilon}}_{\mathrm{p}}^{\mathrm{int}} \geq 0 , \tag{7.3}$$

with the stress (2.20) and the following definition of the plastic stress:

$$\boldsymbol{\sigma}_{\mathrm{p}}^{\mathrm{int}} := -\partial_{\boldsymbol{\varepsilon}_{\mathrm{p}}^{\mathrm{int}}} \mathscr{W} . \tag{7.4}$$

For elastoplasticity without hardening, which we here consider for the sake of simplicity, the yield condition in the form

$$\mathscr{F} = \tilde{\Phi}(\boldsymbol{\sigma}_{\mathrm{p}}^{\mathrm{int}}) \leq 0 \tag{7.5}$$

ensures that the stress does not exceed an admissible range. The function $\mathscr{F}$ is referred to as the yield function. Moreover, an associated flow rule relates the plastic stress and the plastic strain rate as

$$\dot{\boldsymbol{\varepsilon}}_{\mathrm{p}}^{\mathrm{int}} = \gamma \partial_{\boldsymbol{\sigma}_{\mathrm{p}}^{\mathrm{int}}} \mathscr{F} \,. \tag{7.6}$$

Herein γ takes the role of a Lagrange multiplier. The Karush–Kuhn–Tucker or rather loading/unloading conditions together with the consistency condition read

$$\gamma \geq 0 \,, \qquad \mathscr{F} \leq 0 \,, \qquad \gamma \mathscr{F} = 0 \,, \qquad \gamma \dot{\mathscr{F}} = 0 \,. \tag{7.7}$$

7.2 Gradient plasticity formulations

In formulations coined as gradient plasticity a gradient effect can be incorporated in different ways. The theory can either be establish based on a gradient continuum theory as described in Section 2.3, or by involving an additional gradient on quantities other than the primary strain variable in a constitutive sense. The model proposed by Fleck and Hutchinson (1993) is based on the couple stress theory (Toupin, 1962, Mindlin and Tiersten, 1962, Koiter, 1964) as a special kind of gradient continuum theory, while their succeeding article (Fleck and Hutchinson, 1997) is based on the gradient continuum itself. The latter model was also more recently discussed by Garikipati (2003).

Most formulations however belong to the latter group and are thus based on a classical continuum as reviewed in Section 2.2. Particularly, the contributions by Zbib and Aifantis (1992), Fleck and Hutchinson (2001), Menzel and Steinmann (2000), Forest and Sievert (2003) and Peerlings (2007) include the gradient of the plastic strain within the constitutive framework. Instead, gradients of internal hardening variables are involved in various contributions (Aifantis, 1984, Vardoulakis and Aifantis, 1991, Mühlhaus and Aifantis, 1991, Borst and Mühlhaus, 1992, Aifantis, 1992, Borst and Pamin, 1996, Valanis, 1996, Liebe and Steinmann, 2001, Liebe et al., 2003b, Liebe, 2003, Voyiadjis and Al-Rub, 2005, Al-Rub and Voyiadjis, 2006, Zhu et al., 1995). The gradient elastoplasticity of Zervos et al. (2001) both relies on a higher-gradient continuum and moreover involves gradients on internal variables. Gurtin (2003) assumes the plastic strain and its gradient as additional primary variables for which an additional balance holds, along the lines of the contributions of himself and co-workers (Gurtin and Podio-Guidugli, 1992, Gurtin, 2000a, Cermelli and Gurtin, 2002, Anand et al., 2005). Several contributions deal with gradi-

ent plasticity in the context of crystal plasticity, e. g. Gurtin (2000a, 2002), Menzel and Steinmann (2000), Regueiro et al. (2002), Evers et al. (2004), Creighton et al. (2004), Bayley et al. (2006), a framework that deals with very small scale phenomena to begin with.

Comparisons of different pairings of formulations are given e. g. in Borst et al. (1999), Peerlings et al. (2001), Niordson (2002), Gudmundson (2004), Jirasek (2005), Papenfuss and Forest (2006), Engelen et al. (2006).

7.2.1 Classification approach

Based on the classical plasticity framework, recapitulated in Section 7.1, several formulations of gradient plasticity are introduced. Hereby the particular properties of these different types of gradient plasticity are varied with respect to

1. the approach to the plastic variables (*internal* vs. *external*),
2. the gradient operating on either the *total* or the *plastic* strain,
3. the compatibility of the plastic strain and the plastic strain gradient (*compatible* vs. *incompatible*).

Just as small-strain classical plasticity, small-strain gradient plasticity generally relies on the additive decomposition of the strain tensor into an elastic and a plastic contribution. Whereas usually, the plastic contribution is captured by an *internal variable* (which is adopted in Sections 7.2.2 and 7.2.3), we aim to represent the plastic strain by an independent external field in the *external variable approach* (Sections 7.2.4 and 7.2.5), as pursued e. g. by Fried (1996). The resulting varieties of gradient plasticity are illustrated in Figure 7.1 and briefly explained here: The *gradient plasticity based on the total strain* formulations, GP–IT (Section 7.2.2) and GP–ET (Section 7.2.4), respectively, are built into a full gradient continuum, which has been reviewed in Section 2.3. Contrary to that, the classical continuum reviewed in Section 2.2 underlies the formulations we call *gradient plasticity based on the plastic strain*, GP–IP and GP–EP respectively, see Sections 7.2.3 and 7.2.5. For each of these four types of gradient plasticity, a further distinction is made with respect to the *compatibility* of the plastic strain and its gradient. Within the formulations involving the gradient on plastic strain GP–⋆P⋆, no distinction is made between gradient plasticity formulations in which the gradient operates on the plastic strains and such in which it operates on internal variables.

In the following, all eight variations are examined with respect to the thermomechanical framework of kinematics, free-energy density, stresses, balance of momentum and the corresponding boundary conditions as well as dissipation, flow rule and yield condition. In addition to these general considerations, we illustrate each individual variation of gradient plasticity with a model constitutive assumption for

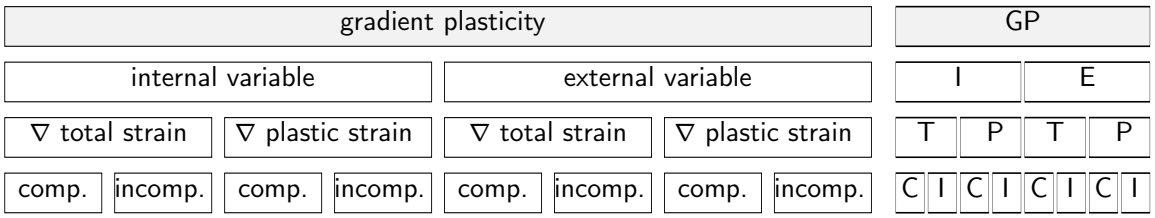

Figure 7.1: Classification scheme for gradient plasticity formulations (left: full titles; right: abbreviations used throughout the chapter).

the free-energy density. Furthermore we tabularly contrapose the formulations in Tables 7.1 and 7.2.

Remark 7.2.1 *Whenever internal variables are involved, the Karush–Kuhn–Tucker conditions* (7.7) *must be fulfilled without further mentioning.*

7.2.2 Gradient plasticity based on total strain: internal variable approach (GP–IT)

For a gradient plasticity that is based on the total strain involving internal variables (GP–IT), we employ the kinematics of the second gradient continuum (2.30), recalled here,

$$\boldsymbol{\varepsilon}(\boldsymbol{u}) := \nabla^{\mathrm{sym}}\boldsymbol{u}\,, \qquad\qquad \boldsymbol{\eta}(\boldsymbol{u}) := \nabla\nabla^{\mathrm{sym}}\boldsymbol{u} = \nabla\boldsymbol{\varepsilon}\,, \tag{7.8}$$

and incorporate plasticity. Particularly, the strain is additively decomposed as in Equation (7.1) of classical plasticity as

$$\boldsymbol{\varepsilon} := \boldsymbol{\varepsilon}_{\mathrm{e}} + \boldsymbol{\varepsilon}_{\mathrm{p}}^{\mathrm{int}}\,. \tag{7.9}$$

In the sequel we will present two formulations that differ by the type of the strain-gradient decomposition.

Compatible formulation (GP–ITC) In the first formulation, we additively decompose the strain gradient $(2.30)_2$ into its elastic and its plastic contributions:

$$\boldsymbol{\eta} = \nabla\boldsymbol{\varepsilon}_{\mathrm{e}} + \nabla\boldsymbol{\varepsilon}_{\mathrm{p}}^{\mathrm{int}}\,. \tag{7.10}$$

We call this decomposition *compatible*, since the elastic and plastic parts of the strain gradient represent the gradients of the elastic and plastic strain of (7.1), respectively. The free-energy density will depend on the elastic kinematic quantities, which them-

selves only depend on the displacement and the plastic strain:

$$\mathscr{W} = \check{\mathscr{W}}(\boldsymbol{\varepsilon}(\boldsymbol{u}) - \boldsymbol{\varepsilon}_{\mathrm{p}}^{\mathrm{int}},\, \boldsymbol{\eta}(\boldsymbol{u}) - \nabla\boldsymbol{\varepsilon}_{\mathrm{p}}^{\mathrm{int}}) = \tilde{\mathscr{W}}(\boldsymbol{u};\, \boldsymbol{\varepsilon}_{\mathrm{p}}^{\mathrm{int}})\,. \tag{7.11}$$

Additionally to the total stress (2.38) of gradient elasticity, we define the plastic stress and double stress as:

$$\boldsymbol{\sigma}_{\mathrm{p}}^{\mathrm{int}} := -\partial_{\boldsymbol{\varepsilon}_{\mathrm{p}}^{\mathrm{int}}}\mathscr{W}\,, \qquad\qquad \boldsymbol{\tau}_{\mathrm{p}}^{\mathrm{int}} := -\partial_{\nabla\boldsymbol{\varepsilon}_{\mathrm{p}}^{\mathrm{int}}}\mathscr{W}\,. \tag{7.12}$$

The compatibility of the third-order plastic strain gradient and the second order plastic strain requires to consider a nonlocality residual, compare Remark 7.2.2, which can be circumvented by the consideration of global dissipation:

$$\int_{\mathscr{B}_{\mathrm{p}}} \mathscr{D}\mathrm{d}V = \int_{\mathscr{B}_{\mathrm{p}}} \boldsymbol{\sigma}_{\mathrm{p}}^{\mathrm{int}\star} : \dot{\boldsymbol{\varepsilon}}_{\mathrm{p}}^{\mathrm{int}}\mathrm{d}V + \int_{\partial\mathscr{B}_{\mathrm{p}}} \dot{\boldsymbol{\varepsilon}}_{\mathrm{p}}^{\mathrm{int}} : \boldsymbol{\tau}_{\mathrm{p}}^{\mathrm{int}} \cdot \boldsymbol{n}\mathrm{d}A \geq 0\,, \tag{7.13}$$

whereby the effective plastic stress is defined with Remark 2.3.3 as

$$\boldsymbol{\sigma}_{\mathrm{p}}^{\mathrm{int}\star} := \boldsymbol{\sigma}_{\mathrm{p}}^{\mathrm{int}} - \operatorname{div}\boldsymbol{\tau}_{\mathrm{p}}^{\mathrm{int}}\,. \tag{7.14}$$

Conditions on the plastic boundary need to be set, e. g. as

$$\boldsymbol{t}^{\tau_{\mathrm{p}}^{\mathrm{int}}} = \boldsymbol{\tau}_{\mathrm{p}}^{\mathrm{int}} \cdot \boldsymbol{n} \doteq \boldsymbol{0} \quad \text{on } \partial\mathscr{B}_{\mathrm{p}}^{\tau} \qquad \text{or} \qquad \dot{\boldsymbol{\varepsilon}}_{\mathrm{p}}^{\mathrm{int}} = \boldsymbol{0} \quad \text{on } \partial\mathscr{B}_{\mathrm{p}}^{\varepsilon} \tag{7.15}$$

see e. g. Polizzotto (2007), Peerlings (2007). The yield condition and the flow rule now read

$$\mathscr{F} = \check{\mathscr{F}}(\boldsymbol{\sigma}_{\mathrm{p}}^{\mathrm{int}\star}) \leq 0 \qquad\qquad \dot{\boldsymbol{\varepsilon}}_{\mathrm{p}}^{\mathrm{int}} = \gamma\partial_{\boldsymbol{\sigma}_{\mathrm{p}}^{\mathrm{int}\star}}\mathscr{F}\,. \tag{7.16}$$

Remark 7.2.2 (Nonlocality Residual) *Edelen and Laws (1971) showed that for nonlocal continua, the rate, at which energy is supplied to a particle by the rest of the body, is zero in an integrated sense over the whole body, but locally nonzero. This concept has been extended to plastic boundaries by Polizzotto and Borino (1998), Polizzotto (2007) and references cited therein. The local dissipation inequality,*

$$\mathscr{D} = \boldsymbol{\sigma} : \dot{\boldsymbol{\varepsilon}} + \boldsymbol{\tau} \mathbin{:\cdot} \dot{\boldsymbol{\eta}} - \dot{\mathscr{W}} + \mathscr{R} \geq 0\,,$$

holds true for the whole body, while $\mathscr{R} \neq 0$ inside $\mathscr{B}_{\mathrm{p}}$. Hereby, no energy exchange occurs between the particles in the plastic region $\mathscr{B}_{\mathrm{p}}$ and those outside $\mathscr{B}_{\mathrm{p}}$. This is

captured by the insulation condition

$$\int_{\mathscr{B}_\mathrm{p}} \mathscr{R}\,\mathrm{d}V = 0\,,$$

which implies to consider the dissipation globally.

Remark 7.2.3 (Constitutive assumption) *Based on the assumption of Table 2.1 for gradient elasticity, we propose the following formulation, which is quadratic in terms of elastic strains and elastic strain gradients*

$$\mathscr{W} = \tfrac{1}{2}\,\boldsymbol{\varepsilon}_\mathrm{e} : \mathsf{E} : \boldsymbol{\varepsilon}_\mathrm{e} + \tfrac{1}{2}\,\mu l^2 \|\nabla\boldsymbol{\varepsilon}_\mathrm{e}\|^2\,.$$

With the definitions (2.38) we derive the particular stress and double stress as

$$\boldsymbol{\sigma} = \mathsf{E} : \boldsymbol{\varepsilon}_\mathrm{e} = \boldsymbol{\sigma}_\mathrm{p}^\mathrm{int}\,, \qquad\qquad \boldsymbol{\tau} = \mu l^2 \nabla\boldsymbol{\varepsilon}_\mathrm{e} = \boldsymbol{\tau}_\mathrm{p}^\mathrm{int}$$

which can with (7.12) also be identified as the internal plastic stresses. With the effective stress (2.35), which here obeys the format $\boldsymbol{\sigma}_\mathrm{p}^{\mathrm{int}\star} = \mathsf{E} : \boldsymbol{\varepsilon}_\mathrm{e} - \mu l^2 \Delta\boldsymbol{\varepsilon}_\mathrm{e}$*, we obtain the following dependence of the yield function:*

$$\mathscr{F} = \tilde{\mathscr{F}}(\mathsf{E} : \boldsymbol{\varepsilon}_\mathrm{e} - \mu l^2 \Delta\boldsymbol{\varepsilon}_\mathrm{e}) \leq 0\,.$$

Consequently, this constitutive formulation inserts gradient effects into the equilibrium condition and the yield condition.

Incompatible formulation (GP–ITI). Unlike in the compatible case, a decomposition of the strain gradient $(2.30)_2$ into

$$\boldsymbol{\eta} = \boldsymbol{\eta}_\mathrm{e} + \boldsymbol{\eta}_\mathrm{p}^\mathrm{int} \tag{7.17}$$

allows for an elastic and a plastic part of the strain gradient to generally be incompatible to (7.1) in the sense that $\boldsymbol{\eta}_\mathrm{e} \neq \nabla\boldsymbol{\varepsilon}_\mathrm{e}$ and $\boldsymbol{\eta}_\mathrm{p}^\mathrm{int} \neq \nabla\boldsymbol{\varepsilon}_\mathrm{p}^\mathrm{int}$. With this at hand, the free-energy density has the following dependencies:

$$\mathscr{W} = \check{\mathscr{W}}(\boldsymbol{\varepsilon}(\boldsymbol{u}) - \boldsymbol{\varepsilon}_\mathrm{p}^\mathrm{int},\, \boldsymbol{\eta}(\boldsymbol{u}) - \boldsymbol{\eta}_\mathrm{p}^\mathrm{int}) = \tilde{\mathscr{W}}(\boldsymbol{u}; \boldsymbol{\varepsilon}_\mathrm{p}^\mathrm{int}, \boldsymbol{\eta}_\mathrm{p}^\mathrm{int})\,. \tag{7.18}$$

Besides the total stress of equation (2.38), we define the according plastic stress measures as

$$\boldsymbol{\sigma}_\mathrm{p}^\mathrm{int} := -\partial_{\boldsymbol{\varepsilon}_\mathrm{p}^\mathrm{int}} \mathscr{W} \qquad\qquad \boldsymbol{\tau}_\mathrm{p}^\mathrm{int} := -\partial_{\boldsymbol{\eta}_\mathrm{p}^\mathrm{int}} \mathscr{W}\,. \tag{7.19}$$

With these at hand, the non-negative dissipation simplifies to

$$\mathscr{D} = \boldsymbol{\sigma}_{\mathrm{p}}^{\mathrm{int}} : \dot{\boldsymbol{\varepsilon}}_{\mathrm{p}}^{\mathrm{int}} + \boldsymbol{\tau}_{\mathrm{p}}^{\mathrm{int}} \vdots \dot{\boldsymbol{\eta}}_{\mathrm{p}}^{\mathrm{int}} \geq 0\,. \tag{7.20}$$

The yield condition depends on the two plastic stresses (7.19),

$$\mathscr{F} = \tilde{\mathscr{F}}(\boldsymbol{\sigma}_{\mathrm{p}}^{\mathrm{int}}, \boldsymbol{\tau}_{\mathrm{p}}^{\mathrm{int}}) \leq 0\,, \tag{7.21}$$

and consequently two flow rules are formulated separately:

$$\dot{\boldsymbol{\varepsilon}}_{\mathrm{p}}^{\mathrm{int}} = \gamma \partial_{\boldsymbol{\sigma}_{\mathrm{p}}^{\mathrm{int}}} \mathscr{F}\,, \qquad\qquad \dot{\boldsymbol{\eta}}_{\mathrm{p}}^{\mathrm{int}} = \gamma \partial_{\boldsymbol{\tau}_{\mathrm{p}}^{\mathrm{int}}} \mathscr{F} \tag{7.22}$$

with the same multiplier γ.

Remark 7.2.4 (Constitutive assumption) *As in the compatible case, from a constitutive assumption*

$$\mathscr{W} = \tfrac{1}{2}\,\boldsymbol{\varepsilon}_{\mathrm{e}} : \mathsf{E} : \boldsymbol{\varepsilon}_{\mathrm{e}} + \tfrac{1}{2}\,\mu l^2 \|\boldsymbol{\eta}_{\mathrm{e}}\|^2$$

we can identify the stress and double stress and identically the plastic stress and double stress as

$$\boldsymbol{\sigma} = \mathsf{E} : \boldsymbol{\varepsilon}_{\mathrm{e}} = \boldsymbol{\sigma}_{\mathrm{p}}^{\mathrm{int}}, \qquad\qquad \boldsymbol{\tau} = \mu l^2 \boldsymbol{\eta}_{\mathrm{e}} = \boldsymbol{\tau}_{\mathrm{p}}^{\mathrm{int}}$$

from the relation (2.38) and (7.19). Thus the yield function reads:

$$\mathscr{F} = \tilde{\mathscr{F}}(\mathsf{E} : \boldsymbol{\varepsilon}_{\mathrm{e}}, \mu l^2 \boldsymbol{\eta}_{\mathrm{e}}) \leq 0\,.$$

Consequently, the gradient effects are solely captured by the equilibrium conditions rather than by the yield function.

7.2.3 Gradient plasticity based on plastic strain: internal variable approach: (GP–IP)

The gradient plasticity based on the plastic strain, relies on the plasticity formulation of the classical continuum of Section 7.1. Analogously, the strain is decomposed as

$$\boldsymbol{\varepsilon} := \boldsymbol{\varepsilon}_{\mathrm{e}} + \boldsymbol{\varepsilon}_{\mathrm{p}}^{\mathrm{int}}\,. \tag{7.23}$$

Additionally, gradients of the plastic strain are considered. Again, both a compatible and the incompatible formulation are presented.

Compatible formulation (GP–IPC). We call the formulation compatible when we consider the gradient of the plastic strain, $\nabla \boldsymbol{\varepsilon}_{\mathrm{p}}^{\mathrm{int}}$, itself. This quantity represents

a higher-grade plastic internal variable. With this, the free-energy density of the classical plasticity (7.2) is enhanced towards

$$\mathscr{W} = \check{\mathscr{W}}(\boldsymbol{\varepsilon}(\boldsymbol{u}) - \boldsymbol{\varepsilon}_{\mathrm{p}}^{\mathrm{int}}, \nabla\boldsymbol{\varepsilon}_{\mathrm{p}}^{\mathrm{int}}) = \tilde{\mathscr{W}}(\boldsymbol{u}; \boldsymbol{\varepsilon}_{\mathrm{p}}^{\mathrm{int}}). \tag{7.24}$$

We define the corresponding total stress (2.20), as well as the second-order plastic stress and the third-order plastic double stress tensor as in Equation (7.12). Again the compatible plastic strain measures necessitate the evaluation of the global dissipation inequality,

$$\int_{\mathscr{B}_{\mathrm{p}}} \mathscr{D}\,\mathrm{d}V = \int_{\mathscr{B}_{\mathrm{p}}} \boldsymbol{\sigma}_{\mathrm{p}}^{\mathrm{int}\star} : \dot{\boldsymbol{\varepsilon}}_{\mathrm{p}}^{\mathrm{int}}\,\mathrm{d}V + \int_{\partial\mathscr{B}_{\mathrm{p}}} \dot{\boldsymbol{\varepsilon}}_{\mathrm{p}}^{\mathrm{int}} : \boldsymbol{\tau}_{\mathrm{p}}^{\mathrm{int}} \cdot \boldsymbol{n}\,\mathrm{d}A \geq 0\,, \tag{7.25}$$

with the same effective plastic stress (compare Remark 2.3.3) and the plastic boundary condition (7.15) as in the compatible version of Section 7.2.2. The effective plastic stress enters the yield condition

$$\mathscr{F} = \check{\mathscr{F}}(\boldsymbol{\sigma}_{\mathrm{p}}^{\mathrm{int}\star}) \leq 0\,, \tag{7.26}$$

and the single flow rule read:

$$\dot{\boldsymbol{\varepsilon}}_{\mathrm{p}}^{\mathrm{int}} = \gamma\,\partial_{\boldsymbol{\sigma}_{\mathrm{p}}^{\mathrm{int}\star}}\mathscr{F}\,. \tag{7.27}$$

Remark 7.2.5 (Constitutive assumption) *With a simple constitutive assumption for the free-energy density,*

$$\mathscr{W} = \tfrac{1}{2}\,\boldsymbol{\varepsilon}_{\mathrm{e}} : \mathsf{E} : \boldsymbol{\varepsilon}_{\mathrm{e}} + \tfrac{1}{2}\,\mu l^2 \|\nabla\boldsymbol{\varepsilon}_{\mathrm{p}}^{\mathrm{int}}\|^2\,,$$

we obtain the following stresses:

$$\boldsymbol{\sigma} = \mathsf{E} : \boldsymbol{\varepsilon}_{\mathrm{e}} = \boldsymbol{\sigma}_{\mathrm{p}}^{\mathrm{int}}\,, \qquad\qquad \boldsymbol{\tau}_{\mathrm{p}}^{\mathrm{int}} = -\mu l^2 \nabla\boldsymbol{\varepsilon}_{\mathrm{p}}^{\mathrm{int}}\,,$$

based on the definitions (2.20) and (7.12). Thus the effective plastic stress results in $\boldsymbol{\sigma}_{\mathrm{p}}^{\mathrm{int}\star} = \mathsf{E} : \boldsymbol{\varepsilon}_{\mathrm{e}} + \mu l^2 \Delta\boldsymbol{\varepsilon}_{\mathrm{p}}^{\mathrm{int}}$*, which enters the yield condition as follows:*

$$\mathscr{F} = \check{\mathscr{F}}(\mathsf{E} : \boldsymbol{\varepsilon}_{\mathrm{e}} + \mu l^2 \Delta\boldsymbol{\varepsilon}_{\mathrm{p}}^{\mathrm{int}}) \leq 0\,.$$

Summarising, the formulation inserts a gradient effect only into the yield condition.

Incompatible formulation (GP–IPI). Here, we consider a third-order plastic strain 'gradient' $\boldsymbol{\eta}_{\mathrm{p}}^{\mathrm{int}}$ which is not the gradient of the plastic strain $\boldsymbol{\varepsilon}_{\mathrm{p}}^{\mathrm{int}}$, but rather an additional independent internal tensor-valued variable of third order. With this

choice, the free-energy density is set up as follows

$$\mathscr{W} = \check{\mathscr{W}}(\boldsymbol{\varepsilon}(\boldsymbol{u}) - \boldsymbol{\varepsilon}_{\mathrm{p}}^{\mathrm{int}},\, \boldsymbol{\eta}_{\mathrm{p}}^{\mathrm{int}}) = \tilde{\mathscr{W}}(\boldsymbol{u};\, \boldsymbol{\varepsilon}_{\mathrm{p}}^{\mathrm{int}}, \boldsymbol{\eta}_{\mathrm{p}}^{\mathrm{int}}) \tag{7.28}$$

The total stress is given by Equation (2.20), while the plastic stresses are defined by Equation (7.19). Due to the independent plastic strain 'gradient', a local dissipation condition ,

$$\mathscr{D} = \boldsymbol{\sigma}_{\mathrm{p}}^{\mathrm{int}} : \dot{\boldsymbol{\varepsilon}}_{\mathrm{p}}^{\mathrm{int}} + \boldsymbol{\tau}_{\mathrm{p}}^{\mathrm{int}} \vdots \dot{\boldsymbol{\eta}}_{\mathrm{p}}^{\mathrm{int}} \geq 0\,, \tag{7.29}$$

together with the yield condition

$$\mathscr{F} = \check{\mathscr{F}}(\boldsymbol{\sigma}_{\mathrm{p}}^{\mathrm{int}}, \boldsymbol{\tau}_{\mathrm{p}}^{\mathrm{int}}) \leq 0\,, \tag{7.30}$$

and the flow rules

$$\dot{\boldsymbol{\varepsilon}}_{\mathrm{p}}^{\mathrm{int}} = \gamma \partial_{\boldsymbol{\sigma}_{\mathrm{p}}^{\mathrm{int}}} \mathscr{F}\,, \qquad\qquad \dot{\boldsymbol{\eta}}_{\mathrm{p}}^{\mathrm{int}} = \gamma \partial_{\boldsymbol{\tau}_{\mathrm{p}}^{\mathrm{int}}} \mathscr{F}\,, \tag{7.31}$$

accounts for the plastic behaviour. In conclusion, this formulation boils down to a standard elasto-plasticity framework with an extended set of internal variables.

Remark 7.2.6 (Constitutive assumption) *We propose the formulation*

$$\mathscr{W} = \tfrac{1}{2}\,\boldsymbol{\varepsilon}_{\mathrm{e}} : \mathsf{E} : \boldsymbol{\varepsilon}_{\mathrm{e}} + \tfrac{1}{2}\,\mu l^2 \|\boldsymbol{\eta}_{\mathrm{p}}^{\mathrm{int}}\|^2$$

for the free-energy density (7.28), which renders the stresses (2.20) and (7.19) as:

$$\boldsymbol{\sigma} = \mathsf{E} : \boldsymbol{\varepsilon}_{\mathrm{e}} = \boldsymbol{\sigma}_{\mathrm{p}}^{\mathrm{int}}\,, \qquad\qquad \boldsymbol{\tau}_{\mathrm{p}}^{\mathrm{int}} = -\mu l^2 \boldsymbol{\eta}_{\mathrm{p}}^{\mathrm{int}}$$

There are no special gradient effects resulting from this formulation. Rather we retrieve standard plasticity with an additional internal variable of third order.

7.2.4 Gradient plasticity based on total strain: external variable approach (GP–ET)

As the GP–IT of Section 7.2.2, the external-variable approach to total-strain-gradient plasticity (GP–ET) bases upon the gradient continuum described in Section 2.3.2. However, instead of internal plastic variables as in GP–IT, in the current external variable approach, we employ external variables in the decomposition of both the strain (2.30), i. e.

$$\boldsymbol{\varepsilon} := \boldsymbol{\varepsilon}_{\mathrm{e}} + \boldsymbol{\varepsilon}_{\mathrm{p}}^{\mathrm{ext}}\,, \tag{7.32}$$

and the strain gradient $\boldsymbol{\eta}$. Both a compatible and an incompatible formulation are introduced, which differ by the respective decomposition of the strain gradient.

Compatible formulation (GP–ETC). In the first formulation, we additively decompose the gradient of total strain into the gradients of the elastic and the 'plastic' contribution, respectively:

$$\boldsymbol{\eta} := \nabla\boldsymbol{\varepsilon}_\mathrm{e} + \nabla\boldsymbol{\varepsilon}_\mathrm{p}^\mathrm{ext}\,. \tag{7.33}$$

Naturally, $\boldsymbol{\varepsilon}_\mathrm{p}^\mathrm{ext}$ is a second-order tensor, and thus its gradient $\nabla\boldsymbol{\varepsilon}_\mathrm{p}^\mathrm{ext}$ is of third order. Again, the free-energy density is postulated to depend on the elastic parts of the strain and its gradient:

$$\mathscr{W} = \check{\mathscr{W}}(\boldsymbol{\varepsilon}(\boldsymbol{u}) - \boldsymbol{\varepsilon}_\mathrm{p}^\mathrm{ext},\, \boldsymbol{\eta}(\boldsymbol{u}) - \nabla\boldsymbol{\varepsilon}_\mathrm{p}^\mathrm{ext}) = \tilde{\mathscr{W}}(\boldsymbol{u}, \boldsymbol{\varepsilon}_\mathrm{p}^\mathrm{ext})\,. \tag{7.34}$$

From the gradient continuum, the total stress definition (2.38) is adopted, and the equilibrium (2.32) and the regular boundary condition (2.33) hold here as well. Additionally we define two measures of 'plastic' stress and 'plastic' double stress as

$$\boldsymbol{\sigma}_\mathrm{p}^\mathrm{ext} = -\partial_{\boldsymbol{\varepsilon}_\mathrm{p}^\mathrm{ext}}\mathscr{W}\,, \qquad\qquad \boldsymbol{\tau}_\mathrm{p}^\mathrm{ext} = -\partial_{\nabla\boldsymbol{\varepsilon}_\mathrm{p}^\mathrm{ext}}\mathscr{W}\,, \tag{7.35}$$

which unify to the effective 'plastic' stress $\boldsymbol{\sigma}_\mathrm{p}^{\mathrm{ext}\star} := \boldsymbol{\sigma}_\mathrm{p}^\mathrm{ext} - \operatorname{div}\boldsymbol{\tau}_\mathrm{p}^\mathrm{ext}$ according to Remark 2.3.3. Due to the external or rather additional primary variables, from a consideration of the weak form, we additionally obtain a second balance relation,

$$\boldsymbol{\sigma}_\mathrm{p}^{\mathrm{ext}\star} = \boldsymbol{0} \qquad \text{in } \mathscr{B}\,, \tag{7.36}$$

with the corresponding boundary condition

$$\boldsymbol{t}^{\tau_\mathrm{p}^\mathrm{ext}} = \boldsymbol{\tau}_\mathrm{p}^\mathrm{ext}\cdot\boldsymbol{n} \qquad \text{on } \partial\mathscr{B}^{\tau_\mathrm{p}^\mathrm{ext}}\,. \tag{7.37}$$

Remark 7.2.7 (Constitutive assumption) *With the model constitutive assumption*

$$\mathscr{W} = \tfrac{1}{2}\,\boldsymbol{\varepsilon}_\mathrm{e} : \mathsf{E} : \boldsymbol{\varepsilon}_\mathrm{e} + \tfrac{1}{2}\,\mu l^2 \|\nabla\boldsymbol{\varepsilon}_\mathrm{e}\|^2\,,$$

we derive the stress and double stress using Equations (2.38) and (7.35) as:

$$\boldsymbol{\sigma} = \mathsf{E} : \boldsymbol{\varepsilon}_\mathrm{e} = \boldsymbol{\sigma}_\mathrm{p}^\mathrm{ext}\,, \qquad\qquad \boldsymbol{\tau} = \mu l^2 \nabla\boldsymbol{\varepsilon}_\mathrm{e} = \boldsymbol{\tau}_\mathrm{p}^\mathrm{ext}\,.$$

Thus it directly follows $\boldsymbol{\sigma}_\mathrm{p}^{\mathrm{ext}\star} = \boldsymbol{\sigma}^\star$, which with the extra balance (7.36) yields the undesired results that $\boldsymbol{\sigma} - \operatorname{div}\boldsymbol{\tau} = \boldsymbol{0}$.

Incompatible formulation (GP–ETI). In the incompatible formulation of GP–ET, we complement the strain decomposition of equation (7.32) by the decomposition of the strain gradient according to

$$\boldsymbol{\eta} = \boldsymbol{\eta}_{\mathrm{e}} + \boldsymbol{\eta}_{\mathrm{p}}^{\mathrm{ext}}, \tag{7.38}$$

whereby $\boldsymbol{\eta}_{\mathrm{p}}^{\mathrm{ext}}$ is a tensor of third order, which enters as another external variable and generally will be 'incompatible' in the sense that $\boldsymbol{\eta}_{\mathrm{p}}^{\mathrm{ext}} \neq \nabla \boldsymbol{\varepsilon}_{\mathrm{p}}^{\mathrm{ext}}$. With this kinematics, the free-energy density is a function of the following quantities:

$$\mathscr{W} = \check{\mathscr{W}}(\boldsymbol{\varepsilon}(\boldsymbol{u}) - \boldsymbol{\varepsilon}_{\mathrm{p}}^{\mathrm{ext}}, \boldsymbol{\eta}(\boldsymbol{u}) - \boldsymbol{\eta}_{\mathrm{p}}^{\mathrm{ext}}) = \tilde{\mathscr{W}}(\boldsymbol{u}, \boldsymbol{\varepsilon}_{\mathrm{p}}^{\mathrm{ext}}, \boldsymbol{\eta}_{\mathrm{p}}^{\mathrm{ext}}). \tag{7.39}$$

The consideration of the dissipation (Remark 7.2.8) allows us to introduce two additional stresses

$$\boldsymbol{\sigma}_{\mathrm{p}}^{\mathrm{ext}} = -\partial_{\boldsymbol{\varepsilon}_{\mathrm{p}}^{\mathrm{ext}}} \mathscr{W}, \qquad \boldsymbol{\tau}_{\mathrm{p}}^{\mathrm{ext}} = -\partial_{\boldsymbol{\eta}_{\mathrm{p}}^{\mathrm{ext}}} \mathscr{W}, \tag{7.40}$$

due to the independent external variables $\boldsymbol{\varepsilon}_{\mathrm{p}}^{\mathrm{ext}}$ and $\boldsymbol{\eta}_{\mathrm{p}}^{\mathrm{ext}}$, which supplement the total stresses (2.38). However, a consideration of the weak formulation results in a trivial balance of momentum

$$\boldsymbol{\sigma}_{\mathrm{p}}^{\mathrm{ext}} = \boldsymbol{0}, \qquad \boldsymbol{\tau}_{\mathrm{p}}^{\mathrm{ext}} = \boldsymbol{0}, \qquad \text{in } \mathscr{B} \tag{7.41}$$

for the additional quantities, which supplements the known balance equation (2.32) and the boundary condition (2.33). With the definitions (7.40), the dependence of the free-energy density (7.39) on the additional external kinematic quantities $\boldsymbol{\varepsilon}_{\mathrm{p}}^{\mathrm{ext}}$ and $\boldsymbol{\eta}_{\mathrm{p}}^{\mathrm{ext}}$ must vanish, i. e. $\tilde{\mathscr{W}}(\boldsymbol{u})$. As a conclusion *gradient elasticity is retrieved*, which is further documented by Remark 7.2.8.

Remark 7.2.8 *The dissipation with external 'plastic' variables is evaluated as*

$$\mathscr{D} = \boldsymbol{\sigma} : \dot{\boldsymbol{\varepsilon}} + \boldsymbol{\tau} \vdots \dot{\boldsymbol{\eta}} - \boldsymbol{\sigma}_{\mathrm{p}}^{\mathrm{ext}} : \dot{\boldsymbol{\varepsilon}}_{\mathrm{p}}^{\mathrm{ext}} - \boldsymbol{\tau}_{\mathrm{p}}^{\mathrm{ext}} \vdots \boldsymbol{\eta}_{\mathrm{p}}^{\mathrm{ext}} - \dot{\mathscr{W}} \geq 0, \tag{7.42}$$

which turns out to equal zero.

Remark 7.2.9 (Constitutive assumption) *For the naive constitutive assumption for the free-energy density,*

$$\mathscr{W} = \tfrac{1}{2}\, \boldsymbol{\varepsilon}_{\mathrm{e}} : \mathsf{E} : \boldsymbol{\varepsilon}_{\mathrm{e}} + \tfrac{1}{2}\, \mu l^2 \|\boldsymbol{\eta}_{\mathrm{e}}\|^2,$$

the stresses given by (2.38) and (7.40) are derived as follows:

$$\boldsymbol{\sigma} = \mathsf{E} : \boldsymbol{\varepsilon}_{\mathrm{e}} = \boldsymbol{\sigma}_{\mathrm{p}}^{\mathrm{ext}}, \qquad \boldsymbol{\tau} = \mu l^2 \boldsymbol{\eta}_{\mathrm{e}} = \boldsymbol{\tau}_{\mathrm{p}}^{\mathrm{ext}}.$$

Nevertheless, due to the additional balance relation (7.41), it follows that all stresses equally vanish, i. e. $\boldsymbol{\sigma} \doteq \mathbf{0}$ *and* $\boldsymbol{\tau} \doteq \mathbf{0}$*, which can be considered non-physical.*

7.2.5 Gradient plasticity based on plastic strain: external variable approach (GP–EP)

The external-variable approach to plastic-strain-gradient plasticity is based on the classical elastoplastic formulation of Section 7.1. As in the previous section, we use an external field to account for the 'plastic' strain. Thus we again employ the additive decomposition $\boldsymbol{\varepsilon} = \boldsymbol{\varepsilon}_{\mathrm{e}} + \boldsymbol{\varepsilon}_{\mathrm{p}}^{\mathrm{ext}}$ already known from Equation (7.32) and distinguish between two formulations based on the character of the third-order 'plastic' tensor.

Compatible formulation (GP–EPC). In the compatible formulation, we consider the external variable and its gradient, $\nabla\boldsymbol{\varepsilon}_{\mathrm{p}}^{\mathrm{ext}}$. With these quantities at hand, the free-energy density exhibits the following dependencies:

$$\mathscr{W} = \check{\mathscr{W}}(\boldsymbol{\varepsilon}(\boldsymbol{u}) - \boldsymbol{\varepsilon}_{\mathrm{p}}^{\mathrm{ext}}, \nabla\boldsymbol{\varepsilon}_{\mathrm{p}}^{\mathrm{ext}}) = \tilde{\mathscr{W}}(\boldsymbol{u}, \boldsymbol{\varepsilon}_{\mathrm{p}}^{\mathrm{ext}}). \tag{7.43}$$

Besides the stress $\boldsymbol{\sigma}$, see (2.20), we introduce both a second-order tensor $\boldsymbol{\sigma}_{\mathrm{p}}^{\mathrm{ext}}$ and a third-order tensor $\boldsymbol{\tau}_{\mathrm{p}}^{\mathrm{ext}}$ as in Equation (7.35), which represent the energetically conjugate variables to the external 'plastic' variable $\boldsymbol{\varepsilon}_{\mathrm{p}}^{\mathrm{ext}}$ and to its gradient, $\nabla\boldsymbol{\varepsilon}_{\mathrm{p}}^{\mathrm{ext}}$, respectively. With the effective 'plastic' stress $\boldsymbol{\sigma}_{\mathrm{p}}^{\mathrm{ext}\star} := \boldsymbol{\sigma}_{\mathrm{p}}^{\mathrm{ext}} - \operatorname{div}\boldsymbol{\tau}_{\mathrm{p}}^{\mathrm{ext}}$ in the sense of Remark 2.3.3, the classical balance of momentum (2.17) is supplemented by the additional balance:

$$\boldsymbol{\sigma}_{\mathrm{p}}^{\mathrm{ext}\star} = \mathbf{0}, \qquad \text{in } \mathscr{B} \tag{7.44}$$

and its corresponding 'plastic' Neumann boundary condition

$$\boldsymbol{t}^{\tau_{\mathrm{p}}^{\mathrm{ext}}} = \boldsymbol{\tau}_{\mathrm{p}}^{\mathrm{ext}} \cdot \boldsymbol{n} \qquad \text{on } \partial\mathscr{B}^{\tau_{\mathrm{p}}^{\mathrm{ext}}}. \tag{7.45}$$

Remark 7.2.10 (Constitutive assumption) *For the simplistic assumption*

$$\mathscr{W} = \tfrac{1}{2}\,\boldsymbol{\varepsilon}_{\mathrm{e}} : \mathsf{E} : \boldsymbol{\varepsilon}_{\mathrm{e}} + \tfrac{1}{2}\,\mu l^2 \|\nabla\boldsymbol{\varepsilon}_{\mathrm{p}}^{\mathrm{ext}}\|^2$$

for the free-energy density, the stress and the 'plastic' stresses render the formats:

$$\boldsymbol{\sigma} = \mathsf{E} : \boldsymbol{\varepsilon}_{\mathrm{e}} = \boldsymbol{\sigma}_{\mathrm{p}}^{\mathrm{ext}}, \qquad\qquad \boldsymbol{\tau}_{\mathrm{p}}^{\mathrm{ext}} = -\mu l^2 \nabla\boldsymbol{\varepsilon}_{\mathrm{p}}^{\mathrm{ext}}.$$

With these, the effective 'plastic' stress reads: $\boldsymbol{\sigma}_{\mathrm{p}}^{\mathrm{ext}\star} = \mathsf{E} : \boldsymbol{\varepsilon}_{\mathrm{e}} + \mu l^2 \Delta\boldsymbol{\varepsilon}_{\mathrm{p}}^{\mathrm{ext}}$*. By consideration of the additional balance (7.44) we obtain*

$$\operatorname{div}\boldsymbol{\sigma} = \operatorname{div}(\operatorname{div}\boldsymbol{\tau}_{\mathrm{p}}^{\mathrm{ext}}) = -\mu l^2 \operatorname{div}\Delta\boldsymbol{\varepsilon}_{\mathrm{p}}^{\mathrm{ext}} = \mathbf{0}.$$

Incompatible formulation (GP–EPI). In the incompatible formulation, the additive decomposition (7.32) of the strain is supplemented by an independent external variable $\boldsymbol{\eta}_{\mathrm{p}}^{\mathrm{ext}}$ being a third-order tensor. Thus the free-energy density reads:

$$\mathscr{W} = \check{\mathscr{W}}(\boldsymbol{\varepsilon}(\boldsymbol{u}) - \boldsymbol{\varepsilon}_{\mathrm{p}}^{\mathrm{ext}}, \boldsymbol{\eta}_{\mathrm{p}}^{\mathrm{ext}}) = \tilde{\mathscr{W}}(\boldsymbol{u}, \boldsymbol{\varepsilon}_{\mathrm{p}}^{\mathrm{ext}}, \boldsymbol{\eta}_{\mathrm{p}}^{\mathrm{ext}}) . \tag{7.46}$$

Again we define the 'plastic stresses' as in Equation (7.35) to supplement the total stress (2.20). The consideration of the Dirichlet principle yields the balance of momentum (2.17) plus the trivial solutions

$$\boldsymbol{\sigma}_{\mathrm{p}}^{\mathrm{ext}} = \mathbf{0} \qquad\qquad \boldsymbol{\tau}_{\mathrm{p}}^{\mathrm{ext}} = \mathbf{0} \qquad \text{in } \mathscr{B} \tag{7.47}$$

for the additional stress measures. Consequently, the dependence of the free-energy density (7.46) on the external 'plastic' variables $\boldsymbol{\varepsilon}_{\mathrm{p}}^{\mathrm{ext}}$ and $\boldsymbol{\eta}_{\mathrm{p}}^{\mathrm{ext}}$ vanishes as already seen for GP–ETI (Section 7.2.4).

Due to the underlying classical continuum, *classical elasticity* is retrieved with this formulation.

Remark 7.2.11 (Constitutive assumption) *The straightforward constitutive assumption*

$$\mathscr{W} = \tfrac{1}{2}\,\boldsymbol{\varepsilon}_{\mathrm{e}} : \mathsf{E} : \boldsymbol{\varepsilon}_{\mathrm{e}} + \tfrac{1}{2}\,\mu l^2 \|\boldsymbol{\eta}_{\mathrm{p}}^{\mathrm{ext}}\|^2$$

is adopted for the free-energy density. With this formulation, both stress and 'plastic' stress are evaluated as follows:

$$\boldsymbol{\sigma} = \mathsf{E} : \boldsymbol{\varepsilon}_{\mathrm{e}} = \boldsymbol{\sigma}_{\mathrm{p}}^{\mathrm{ext}} , \qquad\qquad \boldsymbol{\tau}_{\mathrm{p}}^{\mathrm{ext}} = -\mu l^2 \boldsymbol{\eta}_{\mathrm{p}}^{\mathrm{ext}} .$$

With these at hand and with the trivial additional balance (7.47), the trivial solutions $\boldsymbol{\varepsilon}_{\mathrm{e}} \doteq \mathbf{0}$ *and* $\boldsymbol{\eta}_{\mathrm{p}}^{\mathrm{ext}} \doteq \mathbf{0}$ *for the elastic strain and the third-order external 'plastic' kinematic variable are obtained.*

7.2.6 Conclusion on gradient-plasticity formulations

The afore-introduced eight formulations of gradient plasticity are summarized here. The governing equations are summarized in Tables 7.1 and 7.2, according to the classification scheme of Figure 7.1. We observe repetitive properties, which can be attributed to the input assumptions. For the sake of clarity we briefly review the individual theories and investigate their particular benefits.

GP–ITC *(Compatible formulation of gradient plasticity based on total strain: internal variable approach of Section 7.2.2)* involves the full framework of a second

Table 7.1: Internal-variable approach to gradient plasticity: hierarchy of key properties.

	GP–I			
kinematics	$\boldsymbol{\varepsilon} = \nabla^{\mathrm{sym}} \boldsymbol{u}$			
decomposition	$\boldsymbol{\varepsilon} = \boldsymbol{\varepsilon}_{\mathrm{e}} + \boldsymbol{\varepsilon}_{\mathrm{p}}^{\mathrm{int}}$			
energy	$\check{\mathscr{W}}(\boldsymbol{\varepsilon} - \boldsymbol{\varepsilon}_{\mathrm{p}}^{\mathrm{int}}, \dots)$			
total stress	$\boldsymbol{\sigma} = \partial_{\boldsymbol{\varepsilon}} \mathscr{W}$			
plastic stress	$\boldsymbol{\sigma}_{\mathrm{p}}^{\mathrm{int}} := -\partial_{\boldsymbol{\varepsilon}_{\mathrm{p}}^{\mathrm{int}}} \mathscr{W}$			
	GP–IT		**GP–IP**	
strain gradient	$\boldsymbol{\eta} = \nabla \boldsymbol{\varepsilon}$		—	
double stress	$\boldsymbol{\tau} = \partial_{\boldsymbol{\eta}} \mathscr{W}$		—	
balance of momentum	$\operatorname{div} \boldsymbol{\sigma}^{\star} = \boldsymbol{0}$ in $\mathscr{B}$		$\operatorname{div} \boldsymbol{\sigma} = \boldsymbol{0}$ in $\mathscr{B}$	
traction boundary	$\boldsymbol{t}^{\sigma} = \boldsymbol{\sigma}^{\star} \cdot \boldsymbol{n} + K\boldsymbol{\tau} : [\boldsymbol{n} \otimes \boldsymbol{n}] + \nabla[\boldsymbol{\tau} \cdot \boldsymbol{n}] : \boldsymbol{T}$ on $\partial \mathscr{B}^{\sigma}$		$\boldsymbol{t}^{\sigma} = \boldsymbol{\sigma} \cdot \boldsymbol{n}$ on $\partial \mathscr{B}^{\sigma}$	
double-traction boundary	$\boldsymbol{t}^{\tau} = \boldsymbol{\tau} : [\boldsymbol{n} \otimes \boldsymbol{n}]$ on $\partial \mathscr{B}^{\tau}$		—	
	GP–ITC	**GP–ITI**	**GP–IPC**	**GP–IPI**
strain-gradient (decomposition)	$\boldsymbol{\eta} = \nabla \boldsymbol{\varepsilon}_{\mathrm{e}} + \nabla \boldsymbol{\varepsilon}_{\mathrm{p}}^{\mathrm{int}}$	$\boldsymbol{\eta} = \boldsymbol{\eta}_{\mathrm{e}} + \nabla \boldsymbol{\eta}_{\mathrm{p}}^{\mathrm{int}}$	$\nabla \boldsymbol{\varepsilon}_{\mathrm{p}}^{\mathrm{int}}$	$\nabla \boldsymbol{\eta}_{\mathrm{p}}^{\mathrm{int}}$
energy	$\check{\mathscr{W}}(\dots, \boldsymbol{\eta} - \nabla \boldsymbol{\varepsilon}_{\mathrm{p}}^{\mathrm{int}})$	$\check{\mathscr{W}}(\dots, \boldsymbol{\eta} - \boldsymbol{\eta}_{\mathrm{p}}^{\mathrm{int}})$	$\check{\mathscr{W}}(\dots, \nabla \boldsymbol{\varepsilon}_{\mathrm{p}}^{\mathrm{int}})$	$\check{\mathscr{W}}(\dots, \boldsymbol{\eta}_{\mathrm{p}}^{\mathrm{int}})$
plastic double stress	$\boldsymbol{\tau}_{\mathrm{p}}^{\mathrm{int}} := -\partial_{\nabla \boldsymbol{\varepsilon}_{\mathrm{p}}^{\mathrm{int}}} \mathscr{W}$	$\boldsymbol{\tau}_{\mathrm{p}}^{\mathrm{int}} := -\partial_{\boldsymbol{\eta}_{\mathrm{p}}^{\mathrm{int}}} \mathscr{W}$	$\boldsymbol{\tau}_{\mathrm{p}}^{\mathrm{int}} := -\partial_{\nabla \boldsymbol{\varepsilon}_{\mathrm{p}}^{\mathrm{int}}} \mathscr{W}$	$\boldsymbol{\tau}_{\mathrm{p}}^{\mathrm{int}} := -\partial_{\boldsymbol{\eta}_{\mathrm{p}}^{\mathrm{int}}} \mathscr{W}$
effective plastic stress	$\boldsymbol{\sigma}_{\mathrm{p}}^{\mathrm{int}\star} = \boldsymbol{\sigma}_{\mathrm{p}}^{\mathrm{int}} - \operatorname{div} \boldsymbol{\tau}_{\mathrm{p}}^{\mathrm{int}}$	—	$\boldsymbol{\sigma}_{\mathrm{p}}^{\mathrm{int}\star} = \boldsymbol{\sigma}_{\mathrm{p}}^{\mathrm{int}} - \operatorname{div} \boldsymbol{\tau}_{\mathrm{p}}^{\mathrm{int}}$	—
yield function	$\check{\mathscr{F}}(\boldsymbol{\sigma}_{\mathrm{p}}^{\mathrm{int}\star})$	$\check{\mathscr{F}}(\boldsymbol{\sigma}_{\mathrm{p}}^{\mathrm{int}}, \boldsymbol{\tau}_{\mathrm{p}}^{\mathrm{int}})$	$\check{\mathscr{F}}(\boldsymbol{\sigma}_{\mathrm{p}}^{\mathrm{int}\star})$	$\check{\mathscr{F}}(\boldsymbol{\sigma}_{\mathrm{p}}^{\mathrm{int}}, \boldsymbol{\tau}_{\mathrm{p}}^{\mathrm{int}})$
flow rules	$\dot{\boldsymbol{\varepsilon}}_{\mathrm{p}}^{\mathrm{int}} = \gamma \partial_{\boldsymbol{\sigma}_{\mathrm{p}}^{\mathrm{int}\star}} \mathscr{F}$	$\dot{\boldsymbol{\varepsilon}}_{\mathrm{p}}^{\mathrm{int}} = \gamma \partial_{\boldsymbol{\sigma}_{\mathrm{p}}^{\mathrm{int}}} \mathscr{F}$ $\dot{\boldsymbol{\eta}}_{\mathrm{p}}^{\mathrm{int}} = \gamma \partial_{\boldsymbol{\tau}_{\mathrm{p}}^{\mathrm{int}}} \mathscr{F}$	$\dot{\boldsymbol{\varepsilon}}_{\mathrm{p}}^{\mathrm{int}} = \gamma \partial_{\boldsymbol{\sigma}_{\mathrm{p}}^{\mathrm{int}\star}} \mathscr{F}$	$\dot{\boldsymbol{\varepsilon}}_{\mathrm{p}}^{\mathrm{int}} = \gamma \partial_{\boldsymbol{\sigma}_{\mathrm{p}}^{\mathrm{int}}} \mathscr{F}$ $\dot{\boldsymbol{\eta}}_{\mathrm{p}}^{\mathrm{int}} = \gamma \partial_{\boldsymbol{\tau}_{\mathrm{p}}^{\mathrm{int}}} \mathscr{F}$

Table 7.2: Internal variable approaches to gradient plasticity: hierarchy of key properties.

	GP–E			
kinematics	$\boldsymbol{\varepsilon} = \nabla^{\mathrm{sym}} \boldsymbol{u}$			
decomposition	$\boldsymbol{\varepsilon} = \boldsymbol{\varepsilon}_{\mathrm{e}} + \boldsymbol{\varepsilon}_{\mathrm{p}}^{\mathrm{ext}}$			
energy	$\check{\mathscr{W}}(\boldsymbol{\varepsilon} - \boldsymbol{\varepsilon}_{\mathrm{p}}^{\mathrm{ext}}, \dots)$			
total stress	$\boldsymbol{\sigma} = \partial_{\boldsymbol{\varepsilon}} \mathscr{W}$			
plastic stress	$\boldsymbol{\sigma}_{\mathrm{p}}^{\mathrm{ext}} := -\partial_{\boldsymbol{\varepsilon}_{\mathrm{p}}^{\mathrm{ext}}} \mathscr{W}$			
	GP–ET		GP–EP	
strain gradient	$\boldsymbol{\eta} = \nabla \boldsymbol{\varepsilon}$		—	
double stress	$\boldsymbol{\tau} = \partial_{\boldsymbol{\eta}} \mathscr{W}$		—	
balance of momentum	$\operatorname{div} \boldsymbol{\sigma}^{\star} = \boldsymbol{0}$ in $\mathscr{B}$		$\operatorname{div} \boldsymbol{\sigma} = \boldsymbol{0}$ in $\mathscr{B}$	
traction boundary	$\boldsymbol{t}^{\sigma} = \boldsymbol{\sigma}^{\star} \cdot \boldsymbol{n} + K\boldsymbol{\tau} : [\boldsymbol{n} \otimes \boldsymbol{n}] + \nabla[\boldsymbol{\tau} \cdot \boldsymbol{n}] : \boldsymbol{T}$ on $\partial \mathscr{B}^{\sigma}$		$\boldsymbol{t}^{\sigma} = \boldsymbol{\sigma} \cdot \boldsymbol{n}$ on $\partial \mathscr{B}^{\sigma}$	
double-traction boundary	$\boldsymbol{t}^{\tau} = \boldsymbol{\tau} : [\boldsymbol{n} \otimes \boldsymbol{n}]$ on $\partial \mathscr{B}^{\tau}$		—	
	GP–ETC	**GP–ETI**	**GP–EPC**	**GP–EPI**
strain-gradient decomposition	$\boldsymbol{\eta} = \nabla \boldsymbol{\varepsilon}_{\mathrm{e}} + \nabla \boldsymbol{\varepsilon}_{\mathrm{p}}^{\mathrm{ext}}$	$\boldsymbol{\eta} = \boldsymbol{\eta}_{\mathrm{e}} + \nabla \boldsymbol{\eta}_{\mathrm{p}}^{\mathrm{ext}}$	$\nabla \boldsymbol{\varepsilon}_{\mathrm{p}}^{\mathrm{ext}}$	$\nabla \boldsymbol{\eta}_{\mathrm{p}}^{\mathrm{ext}}$
energy	$\check{\mathscr{W}}(\dots, \boldsymbol{\eta} - \nabla \boldsymbol{\varepsilon}_{\mathrm{p}}^{\mathrm{ext}})$	$\check{\mathscr{W}}(\dots, \boldsymbol{\eta} - \boldsymbol{\eta}_{\mathrm{p}}^{\mathrm{ext}})$	$\check{\mathscr{W}}(\dots, \nabla \boldsymbol{\varepsilon}_{\mathrm{p}}^{\mathrm{ext}})$	$\check{\mathscr{W}}(\dots, \boldsymbol{\eta}_{\mathrm{p}}^{\mathrm{ext}})$
plastic double stress	$\boldsymbol{\tau}_{\mathrm{p}}^{\mathrm{ext}} := -\partial_{\nabla \boldsymbol{\varepsilon}_{\mathrm{p}}^{\mathrm{ext}}} \mathscr{W}$	$\boldsymbol{\tau}_{\mathrm{p}}^{\mathrm{ext}} := -\partial_{\boldsymbol{\eta}_{\mathrm{p}}^{\mathrm{ext}}} \mathscr{W}$	$\boldsymbol{\tau}_{\mathrm{p}}^{\mathrm{ext}} := -\partial_{\nabla \boldsymbol{\varepsilon}_{\mathrm{p}}^{\mathrm{ext}}} \mathscr{W}$	$\boldsymbol{\tau}_{\mathrm{p}}^{\mathrm{ext}} := -\partial_{\boldsymbol{\eta}_{\mathrm{p}}^{\mathrm{ext}}} \mathscr{W}$
effective plastic stress	$\boldsymbol{\sigma}_{\mathrm{p}}^{\mathrm{ext}\star} = \boldsymbol{\sigma}_{\mathrm{p}}^{\mathrm{ext}} - \operatorname{div} \boldsymbol{\tau}_{\mathrm{p}}^{\mathrm{ext}}$	—	$\boldsymbol{\sigma}_{\mathrm{p}}^{\mathrm{ext}\star} = \boldsymbol{\sigma}_{\mathrm{p}}^{\mathrm{ext}} - \operatorname{div} \boldsymbol{\tau}_{\mathrm{p}}^{\mathrm{ext}}$	—
'plastic' balance	$\boldsymbol{\sigma}_{\mathrm{p}}^{\mathrm{ext}\star} = \boldsymbol{0}$ in $\mathscr{B}$ $\boldsymbol{t}^{\tau_{\mathrm{p}}^{\mathrm{ext}}} = \boldsymbol{\tau}_{\mathrm{p}}^{\mathrm{ext}} \cdot \boldsymbol{n}$ on $\partial \mathscr{B}^{\tau_{\mathrm{p}}^{\mathrm{ext}}}$	$\boldsymbol{\sigma}_{\mathrm{p}}^{\mathrm{ext}} = \boldsymbol{0}$, $\boldsymbol{\tau}_{\mathrm{p}}^{\mathrm{ext}} = \boldsymbol{0}$ in $\mathscr{B}$	$\boldsymbol{\sigma}_{\mathrm{p}}^{\mathrm{ext}\star} = \boldsymbol{0}$ in $\mathscr{B}$ $\boldsymbol{t}^{\tau_{\mathrm{p}}^{\mathrm{ext}}} = \boldsymbol{\tau}_{\mathrm{p}}^{\mathrm{ext}} \cdot \boldsymbol{n}$ on $\partial \mathscr{B}^{\tau_{\mathrm{p}}^{\mathrm{ext}}}$	$\boldsymbol{\sigma}_{\mathrm{p}}^{\mathrm{ext}} = \boldsymbol{0}$, $\boldsymbol{\tau}_{\mathrm{p}}^{\mathrm{ext}} = \boldsymbol{0}$ in $\mathscr{B}$

gradient of displacement theory. It therefore requires high standards with respect to continuity, higher-order boundary conditions, and consequently its numerical implementation. Furthermore, difficulties arise due to the compatible gradient of plastic strain: This renders the problem of the occurrence of both a nonlocality residual and plastic boundary conditions. However, it is difficult to keep track of this plastic boundary.

GP–ITI *(Incompatible formulation of gradient plasticity based on total strain: internal variable approach of Section 7.2.2)* incorporates the full framework of a second gradient of displacement theory. Thus it requires high standards with respect to continuity, higher-order boundary conditions, and the numerical implementation into a finite element formulation. However we do not encounter the difficulty of plastic boundary conditions. The gradient plasticity of Fleck and Hutchinson (1993), which is based on the couple stress theory (Toupin, 1962, Mindlin and Tiersten, 1962, Koiter, 1964), is a special case of this formulation.

GP–IPC *(Compatible formulation of gradient plasticity based on plastic strain: internal variable approach of Section 7.2.3)* as a gradient-enhanced classical plasticity is the approach that most publications in gradient plasticity have pursued (e. g. Aifantis (1984), Menzel and Steinmann (2000), Fleck and Hutchinson (2001)). It has the advantage of a simple underlying continuum, however we encounter the difficulties of the plastic boundary conditions.

GP–IPI *(Incompatible formulation of gradient plasticity based on plastic strain: internal variable approach of Section 7.2.3)* is a standard plasticity formulation which is endowed with an additional internal variable of third order.

GP–ETC *(Incompatible formulation of gradient plasticity based on total strain: external variable approach of Section 7.2.4)* also involves the full framework of a gradient continuum, which is supplemented by an external variable and its gradient. This approach clearly falls into the framework of elastic multifield theories (Capriz, 1989) whereby the displacement field is dominated by a second gradient theory.

GP–ETI *(Compatible formulation of gradient plasticity based on total strain: external variable approach of Section 7.2.4)* is based on the full framework of gradient continuum, which is supplemented by one external tensorial variable of second and another of third order. Clearly, plasticity is not covered at all, and from the trivial additional balance relations at first glance, we retrieve gradient elasticity.

GP–EPC *(Compatible formulation of gradient plasticity based on plastic strain: external variable approach Section 7.2.5)* is a classical continuum theory, in which the 'plastic' strain and its gradient are represented by an external variable. Again, a multifield theory is retrieved, while the displacement field obeys a classical elasticity formulation.

GP–EPI *(Incompatible formulation of gradient plasticity based on plastic strain: external variable approach Section 7.2.5)* Within a classical continuum, both the 'plastic' strain and another tensor of third order are introduced as external variables, nevertheless this results in a trivial solution for the external contributions.

Discussion. As a conclusion, with some formulations we retrieved established versions of what is coined as strain gradient plasticity. In particular the GP–ITI is the full gradient plasticity which in a further specified variant can be found in Fleck and Hutchinson (1993), furthermore the GP– IPC describes the gradient of plastic strain theories that have for instance been presented by Aifantis (1984), Menzel and Steinmann (2000), Fleck and Hutchinson (2001). Other formulations boil down to existing theories of classical plasticity. While with the internal-variable approach, in fact plasticity formulations are acquired, the gradient formulations involving external variables, GP–E, do not cover plasticity, at most they fall into the category of elastic multifield theories (Capriz, 1985, 1989)

Particularly we found out that all formulations of gradient plasticity constructed with external plastic variables proved to be not beneficial since no dissipation is connected with the external variables.

In view of their numerical implementation within a finite-element framework, it is advantageous to realize that within the gradient-plasticity formulations only those that incorporate the gradient effect through the plastic strain, require the desirable C^0 continuity for the displacement. Contrary, the formulations based on the total strain experience the more arduous requirement of C^1-continuous functions for the displacement.

7.3 Micromorphic plasticity formulations

Within the micromorphic continuum theory and its above- mentioned subclasses, compare Section 2.4, some plasticity formulations have been developed. However, most of these concern the micropolar continuum, which is characterized by additional rotational degrees of freedom only. In this context, for instance the contributions of Besdo (1974), Borst (1991), Diepolder et al. (1991), Steinmann and Willam (1991), Steinmann (1994), Dietsche et al. (1993), Ehlers and Volk (1997, 1998) as well as those of Grammenoudis and Tsakmakis (2001, 2005a,b, 2007),

Grammenoudis et al. (2007) are mentioned. The microstrain model is a special case of micromorphic plasticity by Forest and Sievert (2006), Forest (2007), who furthermore outline its relation to gradient plasticity.

7.3.1 Classification approach

Based on the elastic framework of the micromorphic continuum, as recapitulated in Section 2.4, we introduce several formulations of micromorphic plasticity. Hereby, in analogy to the gradient plasticity of Section 7.2, we vary the properties of the different formulations of micromorphic plasticity with respect to

1. the approach to plastic micro variables (*internal* vs. *external*),

2. the incorporation of the gradient of either the *total micro strain* or the *plastic micro strain*,

3. the *compatibility* of the plastic micro strain and the plastic micro-strain gradient.

These variations of micromorphic plasticity again result in eight different types, which inherit the structure of the analogous formulations of gradient plasticity, as illustrated in Figure 7.2. Within the micromorphic plasticity, additional to formulations with internal plastic variables only (Sections 7.3.2 and 7.3.3), we again aim to incorporate external 'plastic' variables (Sections 7.3.4 and 7.3.5). However, contrary to the gradient plasticity formulations, these enter at the micro scale, while the macro level always remains with standard plasticity using internal variables to represent the plastic strain. The formulations of micromorphic plasticity based on the total micro strain (Sections 7.3.2 and 7.3.4) employ the full micromorphic continuum theory introduced in Section 2.4. Contrary to that, formulations of micromorphic plasticity based on the gradient of plastic micro strain (Sections 7.3.3 and 7.3.5) are based on the classical plasticity reviewed in Section 7.1 and enhanced only by plastic micro variables. Again for each of the four formulations of micromorphic plasticity, a further distinction is made between formulations with compatible second- and third-order micro strain, i. e. the micro-strain gradient, and incompatible variant with a separate third order tensor. The above-mentioned eight formulations of micromorphic plasticity are presented in the sequel, and their key equations are collocated in Tables 7.3 and 7.4 to give a clear overview.

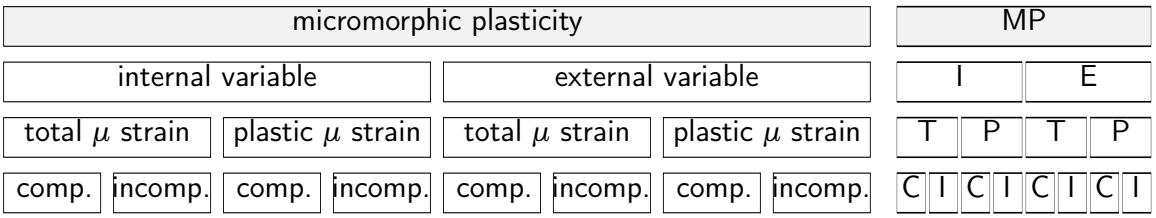

Figure 7.2: Classification scheme for formulations of micromorphic plasticity, $\mu \equiv$ 'micro', (left: full titles; right: abbreviations used throughout the chapter).

7.3.2 Micromorphic plasticity based on total micro strain: internal-micro-variable approach (MP–IT)

The micromorphic plasticity based on total micro strain is constituted upon the full micromorphic continuum presented in the Section 2.4:

$$\boldsymbol{\varepsilon}(\boldsymbol{u}) = \nabla \boldsymbol{u}\,, \qquad\qquad \bar{\boldsymbol{\eta}} := \nabla \bar{\boldsymbol{\varepsilon}}\,. \tag{7.48}$$

In particular the formulations rely on the additive decomposition of both the macro and the micro strain:

$$\boldsymbol{\varepsilon} = \boldsymbol{\varepsilon}_{\mathrm{e}} + \boldsymbol{\varepsilon}_{\mathrm{p}}^{\mathrm{int}}\,, \qquad\qquad \bar{\boldsymbol{\varepsilon}} = \bar{\boldsymbol{\varepsilon}}_{\mathrm{e}} + \bar{\boldsymbol{\varepsilon}}_{\mathrm{p}}^{\mathrm{int}}\,. \tag{7.49}$$

However, the decomposition of the gradient of micro stain, $\bar{\boldsymbol{\eta}}$, is first approached in a 'compatible' and then in an 'incompatible' manner. The consequences of either approaches will presented in the sequel.

Compatible formulation (MP–ITC). In the so-called compatible formulation, the gradient of the micro strain is decomposed in such way that the respective elastic and plastic parts are the gradients of the elastic and plastic parts of the micro strain itself:

$$\bar{\boldsymbol{\eta}} = \nabla \bar{\boldsymbol{\varepsilon}}_{\mathrm{e}} + \nabla \bar{\boldsymbol{\varepsilon}}_{\mathrm{p}}^{\mathrm{int}}\,. \tag{7.50}$$

The free-energy density is formulated as a function of the elastic kinematic variables, which with the compatibility reduces according to

$$\mathscr{W} = \check{\mathscr{W}}(\boldsymbol{\varepsilon}(\boldsymbol{u}) - \boldsymbol{\varepsilon}_{\mathrm{p}}^{\mathrm{int}}, \bar{\boldsymbol{\varepsilon}} - \bar{\boldsymbol{\varepsilon}}_{\mathrm{p}}^{\mathrm{int}}, \bar{\boldsymbol{\eta}}(\bar{\boldsymbol{\varepsilon}}) - \nabla \bar{\boldsymbol{\varepsilon}}_{\mathrm{p}}^{\mathrm{int}}) = \tilde{\mathscr{W}}(\boldsymbol{u}, \bar{\boldsymbol{\varepsilon}}; \bar{\boldsymbol{\varepsilon}}_{\mathrm{p}}^{\mathrm{int}})\,. \tag{7.51}$$

Additional to the total micromorphic stresses (2.45) defined formerly,

$$\boldsymbol{\sigma} := \partial_{\boldsymbol{\varepsilon}} \mathscr{W}\,, \qquad\qquad \bar{\boldsymbol{\sigma}} := \partial_{\bar{\boldsymbol{\varepsilon}}} \mathscr{W}\,, \qquad\qquad \bar{\boldsymbol{\tau}} := \partial_{\bar{\boldsymbol{\eta}}} \mathscr{W}\,, \tag{7.52}$$

we introduced the following micromorphic plastic stress measures:

$$\boldsymbol{\sigma}_{\mathrm{p}}^{\mathrm{int}} := -\partial_{\boldsymbol{\varepsilon}_{\mathrm{p}}^{\mathrm{int}}} \mathscr{W}\,, \qquad \bar{\boldsymbol{\sigma}}_{\mathrm{p}}^{\mathrm{int}} := -\partial_{\bar{\boldsymbol{\varepsilon}}_{\mathrm{p}}^{\mathrm{int}}} \mathscr{W}\,, \qquad \bar{\boldsymbol{\tau}}_{\mathrm{p}}^{\mathrm{int}} := -\partial_{\nabla\bar{\boldsymbol{\varepsilon}}_{\mathrm{p}}^{\mathrm{int}}} \mathscr{W}\,. \tag{7.53}$$

They are denoted as the plastic macro, micro and double stress, respectively. Due to the compatibility of the plastic micro strain and its gradient, a nonlocality residual occurs, which entails to consider the dissipation globally:

$$\int_{\mathscr{B}_{\mathrm{p}}} \mathscr{D}\mathrm{d}V = \int_{\mathscr{B}_{\mathrm{p}}} \boldsymbol{\sigma}_{\mathrm{p}}^{\mathrm{int}} : \dot{\boldsymbol{\varepsilon}}_{\mathrm{p}}^{\mathrm{int}} + \bar{\boldsymbol{\sigma}}_{\mathrm{p}}^{\mathrm{int}\star} : \dot{\bar{\varepsilon}}_{\mathrm{p}}\mathrm{d}V + \int_{\partial\mathscr{B}_{\mathrm{p}}} \dot{\bar{\varepsilon}}_{\mathrm{p}}^{\mathrm{int}} : \bar{\boldsymbol{\tau}}_{\mathrm{p}}^{\mathrm{int}} \cdot \boldsymbol{n}\mathrm{d}A \geq 0\,. \tag{7.54}$$

Herein, the effective plastic micro stress is defined as $\bar{\boldsymbol{\sigma}}_{\mathrm{p}}^{\mathrm{int}\star} := \bar{\boldsymbol{\sigma}}_{\mathrm{p}}^{\mathrm{int}} - \operatorname{div}\bar{\boldsymbol{\tau}}_{\mathrm{p}}^{\mathrm{int}}$ according to Remark 2.3.3. The corresponding yield condition then depends on both the plastic macro and effective plastic micro stress,

$$\mathscr{F} = \breve{\mathscr{F}}(\boldsymbol{\sigma}, \bar{\boldsymbol{\sigma}}^{\star}) \leq 0\,, \tag{7.55}$$

while two separate flow rules,

$$\dot{\boldsymbol{\varepsilon}}_{\mathrm{p}}^{\mathrm{int}} = \gamma\partial_{\boldsymbol{\sigma}_{\mathrm{p}}^{\mathrm{int}\star}}\mathscr{F}\,, \qquad \dot{\bar{\varepsilon}}_{\mathrm{p}}^{\mathrm{int}} = \gamma\partial_{\bar{\boldsymbol{\sigma}}^{\mathrm{int}\star}}\mathscr{F}\,, \tag{7.56}$$

control the plastic process at the macro and the micro level, respectively. A plastic boundary condition on the boundary of the plastic region, chosen e. g. as

$$\bar{\boldsymbol{t}}^{\bar{\tau}_{\mathrm{p}}^{\mathrm{int}}} = \bar{\boldsymbol{\tau}}_{\mathrm{p}}^{\mathrm{int}} \cdot \boldsymbol{n} = \boldsymbol{0} \qquad \text{on } \partial\mathscr{B}_{\mathrm{p}}\,, \tag{7.57}$$

evolves from the global dissipation. However it remains unclear how to determine the placement of the plastic boundary.

Remark 7.3.1 (Constitutive assumption) *Based on Table 2.1, we propose the ansatz*

$$\mathscr{W} = \tfrac{1}{2}\,\boldsymbol{\varepsilon}_{\mathrm{e}} : \mathsf{E} : \boldsymbol{\varepsilon}_{\mathrm{e}} + \tfrac{1}{2}\,\mu l^2 \nabla\bar{\boldsymbol{\varepsilon}}_{\mathrm{e}} \vdots \nabla\bar{\boldsymbol{\varepsilon}}_{\mathrm{e}} + \tfrac{1}{2}\,p\|\boldsymbol{\varepsilon}_{\mathrm{e}} - \bar{\boldsymbol{\varepsilon}}_{\mathrm{e}}\|^2$$

for the free-energy density (7.51). With this at hand, the definitions of the total stresses (2.45) and plastic stresses (7.53) yield the particular formats:

$$\boldsymbol{\sigma} = \mathsf{E} : \boldsymbol{\varepsilon}_{\mathrm{e}} + p[\boldsymbol{\varepsilon}_{\mathrm{e}} - \bar{\boldsymbol{\varepsilon}}_{\mathrm{e}}] = \boldsymbol{\sigma}_{\mathrm{p}}^{\mathrm{int}}\,, \qquad \bar{\boldsymbol{\sigma}} = p[\bar{\boldsymbol{\varepsilon}}_{\mathrm{e}} - \boldsymbol{\varepsilon}_{\mathrm{e}}] = \bar{\boldsymbol{\sigma}}_{\mathrm{p}}^{\mathrm{int}}\,, \qquad \bar{\boldsymbol{\tau}} = \mu l^2 \nabla\bar{\boldsymbol{\varepsilon}}_{\mathrm{e}} = \bar{\boldsymbol{\tau}}_{\mathrm{p}}^{\mathrm{int}}\,.$$

The yield condition (7.55) then reads

$$\mathscr{F} = \breve{\mathscr{F}}(\mathsf{E} : \boldsymbol{\varepsilon}_{\mathrm{e}} + p[\boldsymbol{\varepsilon}_{\mathrm{e}} - \bar{\boldsymbol{\varepsilon}}_{\mathrm{e}}], p[\bar{\boldsymbol{\varepsilon}}_{\mathrm{e}} - \boldsymbol{\varepsilon}_{\mathrm{e}}] - \mu l^2 \Delta\bar{\boldsymbol{\varepsilon}}_{\mathrm{e}}) \leq 0\,.$$

Gradient effects are captured by the balance of micromomentum and—due to the

compatibility—also enter the yield function.

Incompatible formulation (MP–ITI). Different from the compatible case, in the incompatible formulation, we decompose the gradient of the micro strain $(2.39)_2$ into its elastic and its plastic parts:

$$\bar{\boldsymbol{\eta}} = \bar{\boldsymbol{\eta}}_{\mathrm{e}} + \bar{\boldsymbol{\eta}}_{\mathrm{p}}^{\mathrm{int}} . \tag{7.58}$$

This decomposition allows for the elastic and a plastic part to be generally incompatible to $(7.49)_2$ in the sense that $\bar{\boldsymbol{\eta}}_{\mathrm{e}} \neq \nabla(\bar{\boldsymbol{\varepsilon}}_{\mathrm{e}})$ and $\bar{\boldsymbol{\eta}}_{\mathrm{p}}^{\mathrm{int}} \neq \nabla(\bar{\boldsymbol{\varepsilon}}_{\mathrm{p}}^{\mathrm{int}})$. Consequently the free-energy density depends on six independent variables:

$$\mathscr{W} = \check{\mathscr{W}}(\boldsymbol{\varepsilon}(\boldsymbol{u}) - \boldsymbol{\varepsilon}_{\mathrm{p}}^{\mathrm{int}}, \bar{\boldsymbol{\varepsilon}} - \bar{\boldsymbol{\varepsilon}}_{\mathrm{p}}^{\mathrm{int}}, \bar{\boldsymbol{\eta}}(\bar{\boldsymbol{\varepsilon}}) - \bar{\boldsymbol{\eta}}_{\mathrm{p}}^{\mathrm{int}}) = \check{\mathscr{W}}(\boldsymbol{u}, \bar{\boldsymbol{\varepsilon}}; \boldsymbol{\varepsilon}_{\mathrm{p}}^{\mathrm{int}}, \bar{\boldsymbol{\varepsilon}}_{\mathrm{p}}^{\mathrm{int}}, \bar{\boldsymbol{\eta}}_{\mathrm{p}}^{\mathrm{int}}) . \tag{7.59}$$

We adopt the definitions of the plastic macro and micro stress from the compatible case $(7.53)_{1,2}$, while we define the plastic double stress differently:

$$\bar{\boldsymbol{\tau}}_{\mathrm{p}}^{\mathrm{int}} := -\partial_{\bar{\boldsymbol{\eta}}_{\mathrm{p}}^{\mathrm{int}}} \mathscr{W} . \tag{7.60}$$

Due to the incompatibility, the dissipation can be formulated locally:

$$\mathscr{D} = \boldsymbol{\sigma}_{\mathrm{p}}^{\mathrm{int}} : \dot{\boldsymbol{\varepsilon}}_{\mathrm{p}}^{\mathrm{int}} + \bar{\boldsymbol{\sigma}}_{\mathrm{p}}^{\mathrm{int}} : \dot{\bar{\boldsymbol{\varepsilon}}}_{\mathrm{p}}^{\mathrm{int}} + \bar{\boldsymbol{\tau}}_{\mathrm{p}}^{\mathrm{int}} \vdots \dot{\bar{\boldsymbol{\eta}}}_{\mathrm{p}}^{\mathrm{int}} \geq 0 . \tag{7.61}$$

The yield condition,

$$\mathscr{F} = \check{\mathscr{F}}(\boldsymbol{\sigma}_{\mathrm{p}}^{\mathrm{int}}, \bar{\boldsymbol{\sigma}}_{\mathrm{p}}^{\mathrm{int}}, \bar{\boldsymbol{\tau}}_{\mathrm{p}}^{\mathrm{int}}) \leq 0 , \tag{7.62}$$

depends on all three plastic stress, while three flow rules,

$$\dot{\boldsymbol{\varepsilon}}_{\mathrm{p}}^{\mathrm{int}} = \gamma \partial_{\boldsymbol{\sigma}_{\mathrm{p}}^{\mathrm{int}}} \mathscr{F} , \qquad \dot{\bar{\boldsymbol{\varepsilon}}}_{\mathrm{p}}^{\mathrm{int}} = \gamma \partial_{\bar{\boldsymbol{\sigma}}_{\mathrm{p}}^{\mathrm{int}}} \mathscr{F} , \qquad \dot{\bar{\boldsymbol{\eta}}}_{\mathrm{p}}^{\mathrm{int}} = \gamma \partial_{\bar{\boldsymbol{\tau}}_{\mathrm{p}}^{\mathrm{int}}} \mathscr{F} , \tag{7.63}$$

act separately with the plastic multiplier γ.

Remark 7.3.2 (Constitutive assumption) *For the free-energy density (7.59) we propose the straightforward assumption*

$$\mathscr{W} = \tfrac{1}{2} \boldsymbol{\varepsilon}_{\mathrm{e}} : \mathsf{E} : \boldsymbol{\varepsilon}_{\mathrm{e}} + \tfrac{1}{2} \mu l^2 \bar{\boldsymbol{\eta}}_{\mathrm{e}} \vdots \bar{\boldsymbol{\eta}}_{\mathrm{e}} + \tfrac{1}{2} p \| \boldsymbol{\varepsilon}_{\mathrm{e}} - \bar{\boldsymbol{\varepsilon}}_{\mathrm{e}} \|^2 .$$

which is equivalent to that of Table 2.1. With this at hand, the total stresses (2.45) and the plastic stresses (7.60) render:

$$\boldsymbol{\sigma} = \mathsf{E} : \boldsymbol{\varepsilon}_{\mathrm{e}} + p[\boldsymbol{\varepsilon}_{\mathrm{e}} - \bar{\boldsymbol{\varepsilon}}_{\mathrm{e}}] = \boldsymbol{\sigma}_{\mathrm{p}}^{\mathrm{int}} , \qquad \bar{\boldsymbol{\sigma}} = p[\bar{\boldsymbol{\varepsilon}}_{\mathrm{e}} - \boldsymbol{\varepsilon}_{\mathrm{e}}] = \bar{\boldsymbol{\sigma}}_{\mathrm{p}}^{\mathrm{int}} , \qquad \bar{\boldsymbol{\tau}} = \mu l^2 \bar{\boldsymbol{\eta}}_{\mathrm{e}} = \bar{\boldsymbol{\tau}}_{\mathrm{p}}^{\mathrm{int}} .$$

The yield condition (7.62) thus obeys the following dependency

$$\mathscr{F} = \tilde{\mathscr{F}}(\mathsf{E} : \boldsymbol{\varepsilon}_{\mathrm{e}} + p[\boldsymbol{\varepsilon}_{\mathrm{e}} - \bar{\boldsymbol{\varepsilon}}_{\mathrm{e}}], p[\bar{\boldsymbol{\varepsilon}}_{\mathrm{e}} - \boldsymbol{\varepsilon}_{\mathrm{e}}], \mu l^2 \bar{\boldsymbol{\eta}}_{\mathrm{e}}) \leq 0\,.$$

There are no gradient effects on in the yield function, rather these are only captured by the balance of micromomentum (2.42)$_2$.

7.3.3 Micromorphic plasticity based on plastic micro strain: internal micro variable approach (MP–IP)

A micromorphic plasticity that is based on the gradient of the plastic micro strain is introduced here. Its foundation lies in the classical plasticity of Section 7.1, which is enhanced by a plastic micro variable and its gradient. The macro strain given by (2.15) is subject to the additive decomposition (7.1) recalled here:

$$\boldsymbol{\varepsilon} = \boldsymbol{\varepsilon}_{\mathrm{e}} + \boldsymbol{\varepsilon}_{\mathrm{p}}^{\mathrm{int}}\,. \tag{7.64}$$

The additionally considered plastic micro strain is denoted by $\bar{\boldsymbol{\varepsilon}}_{\mathrm{p}}^{\mathrm{int}}$. We present two formulations which differ by either a compatible or an incompatible introduction of the micro-strain gradient.

Compatible formulation (MP–IPC). In the compatible formulation we involve the (compatible) gradient $\nabla\bar{\boldsymbol{\varepsilon}}_{\mathrm{p}}^{\mathrm{int}}$ of the micro strain. With the kinematic quantities at hand, the free-energy density reads:

$$\mathscr{W} = \check{\mathscr{W}}(\boldsymbol{\varepsilon}(\boldsymbol{u}) - \boldsymbol{\varepsilon}_{\mathrm{p}}^{\mathrm{int}}, \bar{\boldsymbol{\varepsilon}}_{\mathrm{p}}^{\mathrm{int}}, \nabla\bar{\boldsymbol{\varepsilon}}_{\mathrm{p}}^{\mathrm{int}}) = \tilde{\mathscr{W}}(\boldsymbol{u}, \boldsymbol{\varepsilon}_{\mathrm{p}}^{\mathrm{int}}, \bar{\boldsymbol{\varepsilon}}_{\mathrm{p}}^{\mathrm{int}})\,. \tag{7.65}$$

Although the underlying classical continuum provides only one (macro) stress measure, (2.20), we define the plastic macro, micro and double stress measures as in Equation (7.53) of MP–ITC, presented in Section 7.3.2. Consequently, we adopt the dissipation (7.54), the yield condition (7.55) and the flow rule (7.56), which involve the effective plastic micro stress. Due to the compatibility, we face the necessity to choose boundary conditions on the plastic boundary as well.

Remark 7.3.3 (Constitutive assumption) *We propose the following formulation for the free-energy density (7.65):*

$$\mathscr{W} = \tfrac{1}{2}\,\boldsymbol{\varepsilon}_{\mathrm{e}} : \mathsf{E} : \boldsymbol{\varepsilon}_{\mathrm{e}} + \tfrac{1}{2}\,\mu l^2 \nabla\bar{\boldsymbol{\varepsilon}}_{\mathrm{p}}^{\mathrm{int}} \mathbin{:\cdot} \nabla\bar{\boldsymbol{\varepsilon}}_{\mathrm{p}}^{\mathrm{int}} + \tfrac{1}{2}\,p\|\boldsymbol{\varepsilon}_{\mathrm{p}}^{\mathrm{int}} - \bar{\boldsymbol{\varepsilon}}_{\mathrm{p}}^{\mathrm{int}}\|^2\,.$$

With this at hand we obtain the particular stress measures $\boldsymbol{\sigma} = \mathsf{E} : \boldsymbol{\varepsilon}_{\mathrm{e}}$ *as well as*

$$\boldsymbol{\sigma}_{\mathrm{p}}^{\mathrm{int}} = \mathsf{E} : \boldsymbol{\varepsilon}_{\mathrm{e}} - p[\boldsymbol{\varepsilon}_{\mathrm{p}}^{\mathrm{int}} - \bar{\boldsymbol{\varepsilon}}_{\mathrm{p}}^{\mathrm{int}}] \qquad \bar{\boldsymbol{\sigma}}_{\mathrm{p}}^{\mathrm{int}} = p[\bar{\boldsymbol{\varepsilon}}_{\mathrm{p}}^{\mathrm{int}} - \boldsymbol{\varepsilon}_{\mathrm{p}}^{\mathrm{int}}]\,, \qquad \bar{\boldsymbol{\tau}}_{\mathrm{p}}^{\mathrm{int}} = \mu l^2 \nabla\bar{\boldsymbol{\varepsilon}}_{\mathrm{p}}^{\mathrm{int}}\,,$$

by applying the definitions of the total stress (2.20) and plastic stresses (7.53), whereby we observe that $\boldsymbol{\sigma}_{\mathrm{p}}^{\mathrm{int}} = \boldsymbol{\sigma} - \bar{\boldsymbol{\sigma}}_{\mathrm{p}}^{\mathrm{int}}$. *The yield condition (7.55) then in particular reads:*

$$\mathscr{F} = \tilde{\mathscr{F}}(\mathsf{E} : \boldsymbol{\varepsilon}_{\mathrm{e}} - p[\boldsymbol{\varepsilon}_{\mathrm{p}}^{\mathrm{int}} - \bar{\boldsymbol{\varepsilon}}_{\mathrm{p}}^{\mathrm{int}}], p[\bar{\boldsymbol{\varepsilon}}_{\mathrm{p}}^{\mathrm{int}} - \boldsymbol{\varepsilon}_{\mathrm{p}}^{\mathrm{int}}] - \mu l^2 \Delta \bar{\boldsymbol{\varepsilon}}_{\mathrm{p}}^{\mathrm{int}}) .$$

Due to the compatibility of the micro strain and the micro-strain gradient, we only face gradient effects on the constitutive level, namely in the yield function.

Incompatible formulation (MP–IPI). In the incompatible formulation of the same type of micromorphic plasticity, we choose an independent tensor of third order $\bar{\boldsymbol{\eta}}_{\mathrm{p}}^{\mathrm{int}}$ to advocate the gradient of plastic micro strain. Thus now the free-energy density reads:

$$\mathscr{W} = \check{\mathscr{W}}(\boldsymbol{\varepsilon}(\boldsymbol{u}) - \boldsymbol{\varepsilon}_{\mathrm{p}}^{\mathrm{int}}, \bar{\boldsymbol{\varepsilon}}_{\mathrm{p}}^{\mathrm{int}}, \bar{\boldsymbol{\eta}}_{\mathrm{p}}^{\mathrm{int}}) = \tilde{\mathscr{W}}(\boldsymbol{u}; \boldsymbol{\varepsilon}_{\mathrm{p}}^{\mathrm{int}}, \bar{\boldsymbol{\varepsilon}}_{\mathrm{p}}^{\mathrm{int}}, \bar{\boldsymbol{\eta}}_{\mathrm{p}}^{\mathrm{int}}) . \tag{7.66}$$

Out of the set of stresses of the compatible formulation, we redefine the plastic double stress according to (7.60). The dissipation, the yield condition, and the flow rule take the same form as in Equations (7.61) through (7.63) in the incompatible formulation of micromorphic plasticity based on total micro strain of Section 7.3.2. Thus we do not encounter the difficulty to define any plastic boundary conditions.

Remark 7.3.4 (Constitutive assumption) *We propose the formulation (7.66):*

$$\mathscr{W} = \tfrac{1}{2}\, \boldsymbol{\varepsilon}_{\mathrm{e}} : \mathsf{E} : \boldsymbol{\varepsilon}_{\mathrm{e}} + \tfrac{1}{2}\, \mu l^2 \bar{\boldsymbol{\eta}}_{\mathrm{p}}^{\mathrm{int}} \vdots \bar{\boldsymbol{\eta}}_{\mathrm{p}}^{\mathrm{int}} + \tfrac{1}{2}\, p \| \boldsymbol{\varepsilon}_{\mathrm{p}}^{\mathrm{int}} - \bar{\boldsymbol{\varepsilon}}_{\mathrm{p}}^{\mathrm{int}} \|^2$$

for the free-energy density. With this at hand, the stress measures obey $\boldsymbol{\sigma} = \mathsf{E} : \boldsymbol{\varepsilon}_{\mathrm{e}}$ *and*

$$\boldsymbol{\sigma}_{\mathrm{p}}^{\mathrm{int}} = \mathsf{E} : \boldsymbol{\varepsilon}_{\mathrm{e}} - p[\boldsymbol{\varepsilon}_{\mathrm{p}}^{\mathrm{int}} - \bar{\boldsymbol{\varepsilon}}_{\mathrm{p}}^{\mathrm{int}}] , \qquad \bar{\boldsymbol{\sigma}}_{\mathrm{p}}^{\mathrm{int}} = p[\boldsymbol{\varepsilon}_{\mathrm{p}}^{\mathrm{int}} - \bar{\boldsymbol{\varepsilon}}_{\mathrm{p}}^{\mathrm{int}}] , \qquad \bar{\boldsymbol{\tau}}_{\mathrm{p}}^{\mathrm{int}} = \mu l^2 \bar{\boldsymbol{\eta}}_{\mathrm{p}}^{\mathrm{int}} ,$$

by evaluating the definitions of the total stress (2.20) and the plastic stresses $(7.53)_1$ *and (7.60). The yield condition takes the format*

$$\mathscr{F} = \tilde{\mathscr{F}}(\mathsf{E} : \boldsymbol{\varepsilon}_{\mathrm{e}} - p[\boldsymbol{\varepsilon}_{\mathrm{p}}^{\mathrm{int}} - \bar{\boldsymbol{\varepsilon}}_{\mathrm{p}}^{\mathrm{int}}], p[\boldsymbol{\varepsilon}_{\mathrm{p}}^{\mathrm{int}} - \bar{\boldsymbol{\varepsilon}}_{\mathrm{p}}^{\mathrm{int}}], \mu l^2 \bar{\boldsymbol{\eta}}_{\mathrm{p}}^{\mathrm{int}}) .$$

With these arguments to the yield function, we experience no gradient effects at all.

7.3.4 Micromorphic plasticity based on total micro strain: external micro variable approach (MP–ET)

We alternate the micromorphic plasticity MP–IT of Section 7.3.2 with respect the decomposition of the micro strain and its gradient. While the decomposition of the macro strain into an elastic and an internal plastic variable is achieved as before, see Equation $(7.49)_1$, we employ an external variable $\bar{\boldsymbol{\varepsilon}}_{\mathrm{p}}^{\mathrm{ext}}$ to account for the micro

plasticity and write the decomposition of the micro strain as:

$$\bar{\boldsymbol{\varepsilon}} = \bar{\boldsymbol{\varepsilon}}_{\mathrm{e}} + \bar{\boldsymbol{\varepsilon}}_{\mathrm{p}}^{\mathrm{ext}} . \tag{7.67}$$

The two variants, we will present in the sequel, differ with respect to the decomposition of the micro-strain gradient $\bar{\boldsymbol{\eta}}$ introduced in Equation $(2.39)_2$.

Compatible formulation (MP–ETC). In the compatible formulation, the gradient of the micro strain is decomposed into the gradient of the elastic and the gradient of the plastic part of the micro strain (7.67), respectively:

$$\bar{\boldsymbol{\eta}} = \nabla \bar{\boldsymbol{\varepsilon}}_{\mathrm{e}} + \nabla \bar{\boldsymbol{\varepsilon}}_{\mathrm{p}}^{\mathrm{ext}} . \tag{7.68}$$

With this choice, the free-energy density reads:

$$\mathscr{W} = \check{\mathscr{W}}(\boldsymbol{\varepsilon}(\boldsymbol{u}) - \boldsymbol{\varepsilon}_{\mathrm{p}}^{\mathrm{int}}, \bar{\boldsymbol{\varepsilon}} - \bar{\boldsymbol{\varepsilon}}_{\mathrm{p}}^{\mathrm{ext}}, \bar{\boldsymbol{\eta}}(\bar{\boldsymbol{\varepsilon}}) - \nabla \bar{\boldsymbol{\varepsilon}}_{\mathrm{p}}^{\mathrm{ext}}) = \tilde{\mathscr{W}}(\boldsymbol{u}, \bar{\boldsymbol{\varepsilon}}, \bar{\boldsymbol{\varepsilon}}_{\mathrm{p}}^{\mathrm{ext}}; \boldsymbol{\varepsilon}_{\mathrm{p}}^{\mathrm{int}}) . \tag{7.69}$$

Additional to the total stress measures (2.45) and the plastic macro stress $(7.53)_1$, we define the 'plastic' micro stress and the 'plastic' double stress,

$$\bar{\boldsymbol{\sigma}}_{\mathrm{p}}^{\mathrm{ext}} := -\partial_{\bar{\boldsymbol{\varepsilon}}_{\mathrm{p}}^{\mathrm{ext}}} \mathscr{W} , \qquad \bar{\boldsymbol{\tau}}_{\mathrm{p}}^{\mathrm{ext}} := -\partial_{\nabla \bar{\boldsymbol{\varepsilon}}_{\mathrm{p}}^{\mathrm{ext}}} \mathscr{W} , \tag{7.70}$$

as the energetically conjugate variables to the external 'plastic' micro strain measure $\bar{\boldsymbol{\varepsilon}}_{\mathrm{p}}^{\mathrm{ext}}$ and its gradient. According to this framework, the dissipation, the yield condition and the flow rule take the form (7.3) through (7.6) of the classical plasticity of Section 7.1. From an evaluation of the Dirichlet principle or rather the weak formulation, we obtain the balance of momentum of the full micromorphic theory (2.41) supplemented by the additional balance relation

$$\bar{\boldsymbol{\sigma}}_{\mathrm{p}}^{\mathrm{ext}\star} = \boldsymbol{0} \quad \text{in } \mathscr{B} , \tag{7.71}$$

in terms of the effective plastic stress $\bar{\boldsymbol{\sigma}}_{\mathrm{p}}^{\mathrm{ext}\star} := \operatorname{div} \bar{\boldsymbol{\tau}}_{\mathrm{p}}^{\mathrm{ext}} - \bar{\boldsymbol{\sigma}}_{\mathrm{p}}^{\mathrm{ext}}$. The corresponding Neumann boundary condition arises as

$$\bar{\boldsymbol{\tau}}_{\mathrm{p}}^{\mathrm{ext}} \cdot \boldsymbol{n} := \bar{\boldsymbol{t}}^{\bar{\sigma}_{\mathrm{p}}^{\mathrm{ext}}} \quad \text{on } \partial \mathscr{B} . \tag{7.72}$$

As a conclusion, we retrieve micromorphic micro elasticity incorporating classical elastoplasticity on the macro scale.

Remark 7.3.5 (Energy Density) *We propose the same formulation of the free-energy density (7.69) as in Remark 7.3.1. The total stresses (2.45) and additional stresses (7.70) then become*

$$\boldsymbol{\sigma} = \mathsf{E} : \boldsymbol{\varepsilon}_{\mathrm{e}} + p[\boldsymbol{\varepsilon}_{\mathrm{e}} - \bar{\boldsymbol{\varepsilon}}_{\mathrm{e}}] = \boldsymbol{\sigma}_{\mathrm{p}}^{\mathrm{int}} , \qquad \bar{\boldsymbol{\sigma}} = p[\bar{\boldsymbol{\varepsilon}}_{\mathrm{e}} - \boldsymbol{\varepsilon}_{\mathrm{e}}] = \bar{\boldsymbol{\sigma}}_{\mathrm{p}}^{\mathrm{ext}} , \qquad \bar{\boldsymbol{\tau}} = \mu l^2 \nabla \bar{\boldsymbol{\varepsilon}}_{\mathrm{e}} = \bar{\boldsymbol{\tau}}_{\mathrm{p}}^{\mathrm{ext}}$$

from which follows $\bar{\boldsymbol{\sigma}}_{\mathrm{p}}^{\mathrm{ext}\star} = \bar{\boldsymbol{\sigma}} - \mu l^2 \Delta \bar{\boldsymbol{\varepsilon}}_{\mathrm{e}}^{\mathrm{ext}}$. *The yield function depends only on* $\boldsymbol{\sigma}_{\mathrm{p}}^{\mathrm{int}}$ *as*

$$\mathscr{F} = \tilde{\mathscr{F}}(\mathbf{E} : \boldsymbol{\varepsilon}_{\mathrm{e}} + p[\boldsymbol{\varepsilon}_{\mathrm{e}} - \bar{\boldsymbol{\varepsilon}}_{\mathrm{e}}]) .$$

Hereby the external variables and its corresponding additional balance relation (7.71) enter the yield condition indirectly through the elastic micro strain $\bar{\boldsymbol{\varepsilon}}_{\mathrm{e}}$.

Incompatible formulation (MP–ETI). In order to achieve an incompatible formulation of this type of micromorphic plasticity, we choose an independent external tensor variable of third order $\bar{\boldsymbol{\eta}}_{\mathrm{p}}^{\mathrm{ext}}$ to represent the plastic part of the gradient of micro strain:

$$\bar{\boldsymbol{\eta}} = \bar{\boldsymbol{\eta}}_{\mathrm{e}} + \bar{\boldsymbol{\eta}}_{\mathrm{p}}^{\mathrm{ext}} . \tag{7.73}$$

With this, the free-energy density reads

$$\text{`}\mathscr{W} = \text{`}\check{\mathscr{W}}(\boldsymbol{\varepsilon}(\boldsymbol{u}) - \boldsymbol{\varepsilon}_{\mathrm{p}}^{\mathrm{int}}, \bar{\boldsymbol{\varepsilon}} - \bar{\boldsymbol{\varepsilon}}_{\mathrm{p}}^{\mathrm{ext}}, \bar{\boldsymbol{\eta}}(\bar{\boldsymbol{\varepsilon}}) - \bar{\boldsymbol{\eta}}_{\mathrm{p}}^{\mathrm{ext}}) = \text{`}\tilde{\mathscr{W}}(\boldsymbol{u}, \bar{\boldsymbol{\varepsilon}}, \bar{\boldsymbol{\varepsilon}}_{\mathrm{p}}^{\mathrm{ext}}, \bar{\boldsymbol{\eta}}_{\mathrm{p}}^{\mathrm{ext}}; \boldsymbol{\varepsilon}_{\mathrm{p}}^{\mathrm{int}}) . \tag{7.74}$$

We adopt the stress measures of the compatible variant including the total stress measures (2.45) and the plastic macro stress $(7.53)_1$ and the 'plastic' micro stress $(7.70)_1$. However we define the 'plastic' double stress,

$$\bar{\boldsymbol{\tau}}_{\mathrm{p}}^{\mathrm{ext}} := -\partial_{\bar{\boldsymbol{\eta}}_{\mathrm{p}}^{\mathrm{ext}}} \text{`}\mathscr{W} , \tag{7.75}$$

through its energetically conjugate counterpart $\bar{\boldsymbol{\eta}}_{\mathrm{p}}^{\mathrm{ext}}$. Again, the macro quantities inherit the plastic framework of classical elastoplasticity of Section 7.1, which includes the non-negative dissipation, yield condition and flow rule (7.3) through (7.6). We consider the Dirichlet principle and obtain the micromorphic balance of momentum and boundary conditions, (2.41) and (2.43) respectively, on the one hand, and the following trivial balance equations for the additional stresses

$$\bar{\boldsymbol{\sigma}}_{\mathrm{p}}^{\mathrm{ext}} = \mathbf{0} , \qquad \bar{\boldsymbol{\tau}}_{\mathrm{p}}^{\mathrm{ext}} = \mathbf{0} \qquad \text{in } \mathscr{B} , \tag{7.76}$$

on the other hand. With the stress definitions $(7.70)_1$ and (7.75), the dependency of the free-energy density (7.74) on the external variables vanishes analogously to GP–ETI of Section 7.2.4: i. e. $\text{`}\tilde{\mathscr{W}}(\boldsymbol{u}, \bar{\boldsymbol{\varepsilon}}; \boldsymbol{\varepsilon}_{\mathrm{p}}^{\mathrm{int}})$. As a conclusion, with this formulation we retrieve micromorphic elasticity incorporating classical elastoplasticity on the macro scale.

Remark 7.3.6 (Constitutive assumption) *We naively propose the same formulation for the free-energy density (7.69) as in Remark 7.3.2 again. The total stresses*

(2.45) and the additional stresses (7.70) then read

$$\boldsymbol{\sigma} = \mathsf{E} : \boldsymbol{\varepsilon}_{\mathrm{e}} + p[\boldsymbol{\varepsilon}_{\mathrm{e}} - \bar{\boldsymbol{\varepsilon}}_{\mathrm{e}}] = \boldsymbol{\sigma}_{\mathrm{p}}^{\mathrm{ext}}, \qquad \bar{\boldsymbol{\sigma}} = p[\bar{\boldsymbol{\varepsilon}}_{\mathrm{e}} - \boldsymbol{\varepsilon}_{\mathrm{e}}] = \bar{\boldsymbol{\sigma}}_{\mathrm{p}}^{\mathrm{ext}}, \qquad \bar{\boldsymbol{\tau}} = \mu l^2 \bar{\boldsymbol{\eta}}_{\mathrm{e}} = \bar{\boldsymbol{\tau}}_{\mathrm{p}}^{\mathrm{ext}},$$

whereby with (7.76) the micro stress and the micro double stress vanish: $\bar{\boldsymbol{\sigma}} = \mathbf{0}$, $\bar{\boldsymbol{\tau}} = \mathbf{0}$, *respectively. With this constitutive assumption, the the yield function (7.5) depends on the macro stress only:*

$$\mathscr{F} = \tilde{\mathscr{F}}(\mathsf{E} : \boldsymbol{\varepsilon}_{\mathrm{e}}) \leq 0\,.$$

Thus all micro contributions vanish, and the present MP–ETI formulation is further reduced to classical plasticity.

7.3.5 Micromorphic plasticity based on plastic micro strain: external micro variable approach (MP–EP)

Along the lines of the MP–IP presented in Section 7.3.3, we introduce a micromorphic plasticity using external variables to represent the plastic micro strain. This procedure is also based on the classical elastoplasticity of Section 7.1 with its corresponding kinematics and (macro) plasticity framework, and enhanced by an external plastic micro strain $\bar{\boldsymbol{\varepsilon}}_{\mathrm{p}}^{\mathrm{ext}}$ and a further plastic micro strain 'gradient'. In the sequel we again illuminate two formulations that differ by the manner the third order 'plastic' micro strain is introduced.

Compatible formulation (MP–EPC). First the compatible formulation in which the gradient of the external 'plastic' micro strain, $\nabla\bar{\boldsymbol{\varepsilon}}_{\mathrm{p}}^{\mathrm{ext}}$, is considered. Within this framework, the free-energy density reads

$$\text{ʬ} = \text{ʬ}(\boldsymbol{\varepsilon}(\boldsymbol{u}) - \boldsymbol{\varepsilon}_{\mathrm{p}}^{\mathrm{int}}, \bar{\boldsymbol{\varepsilon}}_{\mathrm{p}}^{\mathrm{ext}}, \nabla\bar{\boldsymbol{\varepsilon}}_{\mathrm{p}}^{\mathrm{ext}}) = \tilde{\text{ʬ}}(\boldsymbol{u}, \bar{\boldsymbol{\varepsilon}}_{\mathrm{p}}^{\mathrm{ext}}; \boldsymbol{\varepsilon}_{\mathrm{p}}^{\mathrm{int}})\,. \tag{7.77}$$

The total (macro) stress of the classical continuum (2.20) goes along with the 'plastic' micro stress and the 'plastic' double stress,

$$\bar{\boldsymbol{\sigma}}_{\mathrm{p}}^{\mathrm{ext}} = -\partial_{\bar{\boldsymbol{\varepsilon}}_{\mathrm{p}}^{\mathrm{ext}}} \text{ʬ}\,, \qquad\qquad \bar{\boldsymbol{\tau}}_{\mathrm{p}}^{\mathrm{ext}} = -\partial_{\nabla\bar{\boldsymbol{\varepsilon}}_{\mathrm{p}}^{\mathrm{ext}}} \text{ʬ}\,, \tag{7.78}$$

respectively, arising from the external plastic strain variable and its gradient. The plastic macro stress defined in (7.4) constitutes the sole internal plastic stress, for which the dissipation, the yield condition, and the flow rule again take the format as in the classical plasticity, (7.3) through (7.6). However, the external variables again involve the additional balance equation (7.71), which goes along with the boundary condition (7.72) as for MP–ETC in Section 7.3.4. In conclusion, with this formulation we retrieve classical elastoplasticity on the macro-scale with micromor-

phic micro-elasticity. Due to the additional micro field equation, which influences the yield function, we expect this formulation prove especially useful in the context of regularization.

Remark 7.3.7 (Constitutive assumption) *For the free-energy density of (7.77) we suggest the straightforward formulation:*

$$\mathscr{W} = \tfrac{1}{2}\,\boldsymbol{\varepsilon}_{\mathrm{e}} : \mathsf{E} : \boldsymbol{\varepsilon}_{\mathrm{e}} + \tfrac{1}{2}\,\mu l^2 \|\nabla \bar{\boldsymbol{\varepsilon}}_{\mathrm{p}}^{\mathrm{ext}}\|^2 + \tfrac{1}{2}\,p \|\boldsymbol{\varepsilon}_{\mathrm{p}}^{\mathrm{int}} - \bar{\boldsymbol{\varepsilon}}_{\mathrm{p}}^{\mathrm{ext}}\|^2 .$$

This renders the stress measures: $\boldsymbol{\sigma} = \mathsf{E} : \boldsymbol{\varepsilon}_{\mathrm{e}}$*, as well as*

$$\boldsymbol{\sigma}_{\mathrm{p}}^{\mathrm{int}} = \mathsf{E} : \boldsymbol{\varepsilon}_{\mathrm{e}} - p[\boldsymbol{\varepsilon}_{\mathrm{p}}^{\mathrm{int}} - \bar{\boldsymbol{\varepsilon}}_{\mathrm{p}}^{\mathrm{ext}}], \qquad \bar{\boldsymbol{\sigma}}_{\mathrm{p}}^{\mathrm{ext}} = p[\boldsymbol{\varepsilon}_{\mathrm{p}}^{\mathrm{int}} - \bar{\boldsymbol{\varepsilon}}_{\mathrm{p}}^{\mathrm{ext}}], \qquad \bar{\boldsymbol{\tau}}_{\mathrm{p}}^{\mathrm{ext}} = -\mu l^2 \nabla \bar{\boldsymbol{\varepsilon}}_{\mathrm{p}}^{\mathrm{ext}} .$$

We observe that $\boldsymbol{\sigma}_{\mathrm{p}}^{\mathrm{int}} = \boldsymbol{\sigma} - \bar{\boldsymbol{\sigma}}_{\mathrm{p}}^{\mathrm{ext}}$*, which, with the extra balance (7.71), yields the yield function as:*

$$\mathscr{F} = \tilde{\mathscr{F}}(\mathsf{E} : \boldsymbol{\varepsilon}_{\mathrm{e}} + \mu l^2 \Delta \bar{\boldsymbol{\varepsilon}}_{\mathrm{p}}^{\mathrm{ext}}) \leq 0 .$$

With this, both the macro stress and the external plastic strain gradient influence the plastic yielding.

Incompatible formulation (MP–EPI). In the second formulation of this type of micromorphic plasticity the third-order external 'plastic' micro variable $\bar{\boldsymbol{\eta}}_{\mathrm{p}}^{\mathrm{ext}}$ is chosen independently, such that it will generally not equal the gradient of $\bar{\boldsymbol{\varepsilon}}_{\mathrm{p}}^{\mathrm{ext}}$. With this assumption, the free-energy density renders the following dependencies

$$\mathscr{W} = \check{\mathscr{W}}(\boldsymbol{\varepsilon}(\boldsymbol{u}) - \boldsymbol{\varepsilon}_{\mathrm{p}}^{\mathrm{int}}, \bar{\boldsymbol{\varepsilon}}_{\mathrm{p}}^{\mathrm{ext}}, \bar{\boldsymbol{\eta}}_{\mathrm{p}}^{\mathrm{ext}}) = \tilde{\mathscr{W}}(\boldsymbol{u}, \bar{\boldsymbol{\varepsilon}}_{\mathrm{p}}^{\mathrm{ext}}, \bar{\boldsymbol{\eta}}_{\mathrm{p}}^{\mathrm{ext}}; \boldsymbol{\varepsilon}_{\mathrm{p}}^{\mathrm{int}}) \tag{7.79}$$

All stresses are inherited from the compatible version of the present formulation, except for the 'plastic' double stress, which is defined by (7.75). The framework of dissipation, yield condition, and flow rule are again adopted from classical plasticity of Section 7.1, (7.3) through (7.6). By an examination of the weak formulation, besides the canonical balance of momentum (2.17), we once more obtain trivial balance equations for the 'plastic' stress and double stress (7.76). Since this implies that the contributions of the external variables $\bar{\boldsymbol{\varepsilon}}_{\mathrm{p}}^{\mathrm{ext}}$ and $\bar{\boldsymbol{\eta}}_{\mathrm{p}}^{\mathrm{ext}}$ in the free-energy density function (7.79) vanish, i. e. $\tilde{\mathscr{W}}(\boldsymbol{u}; \boldsymbol{\varepsilon}_{\mathrm{p}}^{\mathrm{int}})$, we retrieve classical elastoplasticity.

Remark 7.3.8 (Constitutive assumption) *The simplistic model formulation for the free energy*

$$\mathscr{W} = \tfrac{1}{2}\,\boldsymbol{\varepsilon}_{\mathrm{e}} : \mathsf{E} : \boldsymbol{\varepsilon}_{\mathrm{e}} + \tfrac{1}{2}\,\mu l^2 \|\bar{\boldsymbol{\eta}}_{\mathrm{p}}^{\mathrm{ext}}\|^2 + \tfrac{1}{2}\,p \|\boldsymbol{\varepsilon}_{\mathrm{p}}^{\mathrm{int}} - \bar{\boldsymbol{\varepsilon}}_{\mathrm{p}}^{\mathrm{ext}}\|^2$$

renders the particular stress measures to become $\boldsymbol{\sigma} = \mathsf{E} : \boldsymbol{\varepsilon}_{\mathrm{e}}$*,*

$$\boldsymbol{\sigma}_{\mathrm{p}}^{\mathrm{int}} = \mathsf{E} : \boldsymbol{\varepsilon}_{\mathrm{e}} - p[\boldsymbol{\varepsilon}_{\mathrm{p}}^{\mathrm{int}} - \bar{\boldsymbol{\varepsilon}}_{\mathrm{p}}^{\mathrm{ext}}], \qquad \bar{\boldsymbol{\sigma}}_{\mathrm{p}}^{\mathrm{ext}} = p[\boldsymbol{\varepsilon}_{\mathrm{p}}^{\mathrm{int}} - \bar{\boldsymbol{\varepsilon}}_{\mathrm{p}}^{\mathrm{ext}}], \qquad \bar{\boldsymbol{\tau}}_{\mathrm{p}}^{\mathrm{ext}} = -\mu l^2 \bar{\boldsymbol{\eta}}_{\mathrm{p}}^{\mathrm{ext}}.$$

From the trivial balance (7.76) follows that

$$\boldsymbol{\varepsilon}_{\mathrm{p}}^{\mathrm{int}} = \bar{\boldsymbol{\varepsilon}}_{\mathrm{p}}^{\mathrm{ext}}, \qquad\qquad \bar{\boldsymbol{\eta}}_{\mathrm{p}}^{\mathrm{ext}} = \mathbf{0}.$$

Thus only the stress $\boldsymbol{\sigma}_{\mathrm{p}}^{\mathrm{int}} = \boldsymbol{\sigma}$ *remains, which is completely in line with the classical plasticity framework.*

7.3.6 Conclusion on micromorphic plasticity formulations

The governing equations of the above formulation of micromorphic plasticity are summarized in the sequel. Additionally an hierarchic overview is given in Tables 7.3 and 7.4. We have varied the three key features indicated formerly. From the individual constellation of key properties of the micromorphic plasticity formulations, certain characteristics are obtained, which we briefly review as follows:

MP–ITC *(Compatible micromorphic plasticity based on total micro strain: internal-micro-variable approach of Section 7.3.2)* is formulated for the full micromorphic continuum. Thus the formulation represents a complete micromorphic continuum plasticity. However, the large number of degrees of freedom makes it computationally rather expensive. Furthermore the compatibility in the plastic strain gradients causes the cumbersome necessity to determine the plastic boundary.

MP–ITI *(Incompatible micromorphic plasticity based on total micro strain: internal-micro-variable approach of Section 7.3.2)* is a full micromorphic theory with plastic micro strain and a plastic double strain, which are independent of each other and are captured by separate flow rules. With respect to the number of unknowns, this framework is computationally as expensive as the former, however it lacks any difficulty of plastic boundaries.

MP–IPC *(Compatible micromorphic plasticity based on plastic micro strain: internal-micro-variable approach of Section 7.3.3)* is based on the classical plasticity, which is enhanced by the gradient on the plastic strain. Although, concerning the number of primary variables, this formulation is computationally less expensive, the problem to track the plastic boundary is present.

MP–IPI *(Incompatible micromorphic plasticity based on plastic micro strain: internal-micro-variable approach of Section 7.3.3)* represents a plasticity formulation

Table 7.3: Internal-variable approaches to micromorphic plasticity: hierarchy of key properties.

	MP–I			
macro kinematics	$\boldsymbol{\varepsilon} = \nabla \boldsymbol{u}$			
decomposition	$\boldsymbol{\varepsilon} = \boldsymbol{\varepsilon}_{\mathrm{e}} + \boldsymbol{\varepsilon}_{\mathrm{p}}^{\mathrm{int}}$			
energy	$\widetilde{\mathscr{W}}(\boldsymbol{\varepsilon} - \boldsymbol{\varepsilon}_{\mathrm{p}}^{\mathrm{int}}, \ldots, \ldots)$			
total macro stress	$\boldsymbol{\sigma} = \partial_{\boldsymbol{\varepsilon}} \mathscr{W}$			
balance of macro momentum	$\operatorname{div} \boldsymbol{\sigma} = \boldsymbol{0}$ in $\mathscr{B}$			
macro traction at boundary	$\boldsymbol{t} = \boldsymbol{\sigma} \cdot \boldsymbol{n}$ on $\partial \mathscr{B}^{\sigma}$			
yield function	$\widetilde{\mathscr{F}}(\boldsymbol{\sigma}_{\mathrm{p}}^{\mathrm{int}}, \ldots)$			
flow rule	$\dot{\boldsymbol{\varepsilon}}_{\mathrm{p}}^{\mathrm{int}} = \gamma \partial_{\boldsymbol{\sigma}_{\mathrm{p}}^{\mathrm{int}}} \mathscr{F}$			
	MP–IT		MP–IP	
micro decomposition	$\bar{\boldsymbol{\varepsilon}} = \bar{\boldsymbol{\varepsilon}}_{\mathrm{e}} + \bar{\boldsymbol{\varepsilon}}_{\mathrm{p}}^{\mathrm{int}}$		$\bar{\boldsymbol{\varepsilon}}_{\mathrm{p}}^{\mathrm{int}}$	
micro-strain gradient	$\bar{\boldsymbol{\eta}} = \nabla \bar{\boldsymbol{\varepsilon}}$		—	
energy	$\bar{\boldsymbol{\sigma}} = \partial_{\bar{\boldsymbol{\varepsilon}}} \mathscr{W}$, $\bar{\boldsymbol{\tau}} = \partial_{\bar{\boldsymbol{\eta}}} \mathscr{W}$		—	
balance of micro momentum	$\bar{\boldsymbol{\sigma}}^{\star} = \boldsymbol{0}$ in $\mathscr{B}$		—	
micro traction at boundary	$\bar{\boldsymbol{t}}^{\bar{\tau}} = \bar{\boldsymbol{\tau}} \cdot \boldsymbol{n}$ on $\partial \mathscr{B}^{\bar{\tau}}$		—	
energy	$\widetilde{\mathscr{W}}(\ldots, \bar{\boldsymbol{\varepsilon}} - \bar{\boldsymbol{\varepsilon}}_{\mathrm{p}}^{\mathrm{int}}, \ldots)$		$\widetilde{\mathscr{W}}(\ldots, \bar{\boldsymbol{\varepsilon}}_{\mathrm{p}}^{\mathrm{int}}, \ldots)$	
	MP–ITC	MP–ITI	MP–IPC	MP–IPI
decomposition of micro-strain gradient	$\bar{\boldsymbol{\eta}} = \nabla \bar{\boldsymbol{\varepsilon}}_{\mathrm{e}} + \nabla \bar{\boldsymbol{\varepsilon}}_{\mathrm{p}}^{\mathrm{int}}$	$\bar{\boldsymbol{\eta}} = \bar{\boldsymbol{\eta}}_{\mathrm{e}} + \nabla \bar{\boldsymbol{\eta}}_{\mathrm{p}}^{\mathrm{int}}$	$\nabla \bar{\boldsymbol{\varepsilon}}_{\mathrm{p}}^{\mathrm{int}}$	$\nabla \bar{\boldsymbol{\eta}}_{\mathrm{p}}^{\mathrm{int}}$
energy	$\widetilde{\mathscr{W}}(\ldots, \ldots, \bar{\boldsymbol{\eta}} - \nabla \bar{\boldsymbol{\varepsilon}}_{\mathrm{p}}^{\mathrm{int}})$	$\widetilde{\mathscr{W}}(\ldots, \ldots, \bar{\boldsymbol{\eta}} - \bar{\boldsymbol{\eta}}_{\mathrm{p}}^{\mathrm{int}})$	$\widetilde{\mathscr{W}}(\ldots, \ldots, \nabla \bar{\boldsymbol{\varepsilon}}_{\mathrm{p}}^{\mathrm{int}})$	$\widetilde{\mathscr{W}}(\ldots, \ldots, \bar{\boldsymbol{\eta}}_{\mathrm{p}}^{\mathrm{int}})$
yield function	$\widetilde{\mathscr{F}}(\ldots, \bar{\boldsymbol{\sigma}}_{\mathrm{p}}^{\mathrm{int}\star})$	$\widetilde{\mathscr{F}}(\ldots, \bar{\boldsymbol{\sigma}}_{\mathrm{p}}^{\mathrm{int}}, \bar{\boldsymbol{\tau}}_{\mathrm{p}}^{\mathrm{int}})$	$\widetilde{\mathscr{F}}(\ldots, \bar{\boldsymbol{\sigma}}_{\mathrm{p}}^{\mathrm{int}\star})$	$\widetilde{\mathscr{F}}(\ldots, \bar{\boldsymbol{\sigma}}_{\mathrm{p}}^{\mathrm{int}}, \bar{\boldsymbol{\tau}}_{\mathrm{p}}^{\mathrm{int}})$
effective plastic micro stress	$\bar{\boldsymbol{\sigma}}_{\mathrm{p}}^{\mathrm{int}\star} := \bar{\boldsymbol{\sigma}}_{\mathrm{p}}^{\mathrm{int}} - \operatorname{div} \bar{\boldsymbol{\tau}}_{\mathrm{p}}^{\mathrm{int}}$	—	$\bar{\boldsymbol{\sigma}}_{\mathrm{p}}^{\mathrm{int}\star} := \bar{\boldsymbol{\sigma}}_{\mathrm{p}}^{\mathrm{int}} - \operatorname{div} \bar{\boldsymbol{\tau}}_{\mathrm{p}}^{\mathrm{int}}$	—
micro flow rule	$\dot{\bar{\boldsymbol{\varepsilon}}}_{\mathrm{p}}^{\mathrm{int}} = \gamma \partial_{\bar{\boldsymbol{\sigma}}_{\mathrm{p}}^{\mathrm{int}\star}} \mathscr{F}$	$\dot{\bar{\boldsymbol{\varepsilon}}}_{\mathrm{p}}^{\mathrm{int}} = \gamma \partial_{\bar{\boldsymbol{\sigma}}_{\mathrm{p}}^{\mathrm{int}}} \mathscr{F}$ $\dot{\bar{\boldsymbol{\eta}}}_{\mathrm{p}}^{\mathrm{int}} = \gamma \partial_{\bar{\boldsymbol{\tau}}_{\mathrm{p}}^{\mathrm{int}}} \mathscr{F}$	$\dot{\bar{\boldsymbol{\varepsilon}}}_{\mathrm{p}}^{\mathrm{int}} = \gamma \partial_{\bar{\boldsymbol{\sigma}}_{\mathrm{p}}^{\mathrm{int}\star}} \mathscr{F}$	$\dot{\bar{\boldsymbol{\varepsilon}}}_{\mathrm{p}}^{\mathrm{int}} = \gamma \partial_{\bar{\boldsymbol{\sigma}}_{\mathrm{p}}^{\mathrm{int}}} \mathscr{F}$ $\dot{\bar{\boldsymbol{\eta}}}_{\mathrm{p}}^{\mathrm{int}} = \gamma \partial_{\bar{\boldsymbol{\tau}}_{\mathrm{p}}^{\mathrm{int}}} \mathscr{F}$

Table 7.4: External-variable approaches to micromorphic plasticity: hierarchy of key properties.

	MP–E			
macro kinematics	$\boldsymbol{\varepsilon} = \nabla \boldsymbol{u}$			
macro-strain decomposition	$\boldsymbol{\varepsilon} = \boldsymbol{\varepsilon}_{\mathrm{e}} + \boldsymbol{\varepsilon}_{\mathrm{p}}^{\mathrm{int}}$			
energy	$\widetilde{\mathscr{W}}(\boldsymbol{\varepsilon} - \boldsymbol{\varepsilon}_{\mathrm{p}}^{\mathrm{int}}, \dots, \dots)$			
total macro stress	$\boldsymbol{\sigma} = \partial_{\boldsymbol{\varepsilon}} \mathscr{W}$			
balance of macro momentum	$\operatorname{div} \boldsymbol{\sigma} = \boldsymbol{0}$ in $\mathscr{B}$			
macro traction at boundary	$\boldsymbol{t} = \boldsymbol{\sigma} \cdot \boldsymbol{n}$ on $\partial \mathscr{B}^{\sigma}$			
yield function	$\widetilde{\mathscr{F}}(\boldsymbol{\sigma}_{\mathrm{p}}^{\mathrm{int}}, \dots)$			
flow rule	$\dot{\boldsymbol{\varepsilon}}_{\mathrm{p}}^{\mathrm{int}} = \gamma \partial_{\boldsymbol{\sigma}_{\mathrm{p}}^{\mathrm{int}}} \mathscr{F}$			
	MP–ET		MP–EP	
micro-strain decomposition	$\bar{\boldsymbol{\varepsilon}} = \bar{\boldsymbol{\varepsilon}}_{\mathrm{e}} + \bar{\boldsymbol{\varepsilon}}_{\mathrm{p}}^{\mathrm{ext}}$		$\bar{\boldsymbol{\varepsilon}}_{\mathrm{p}}^{\mathrm{ext}}$	
micro-strain gradient	$\bar{\boldsymbol{\eta}} = \nabla \bar{\boldsymbol{\varepsilon}}$		—	
total micro stress	$\bar{\boldsymbol{\sigma}} = \partial_{\bar{\boldsymbol{\varepsilon}}} \mathscr{W}$, $\bar{\boldsymbol{\tau}} = \partial_{\bar{\boldsymbol{\eta}}} \mathscr{W}$		—	
balance of micro momentum	$\bar{\boldsymbol{\sigma}}^{\star} = \boldsymbol{0}$ in $\mathscr{B}$		—	
micro traction at the boundary	$\bar{\boldsymbol{t}}^{\bar{\tau}} = \bar{\boldsymbol{\tau}} \cdot \boldsymbol{n}$ on $\partial \mathscr{B}^{\bar{\tau}}$		—	
energy	$\widetilde{\mathscr{W}}(\dots, \bar{\boldsymbol{\varepsilon}} - \bar{\boldsymbol{\varepsilon}}_{\mathrm{p}}^{\mathrm{ext}}, \dots)$		$\widetilde{\mathscr{W}}(\dots, \bar{\boldsymbol{\varepsilon}}_{\mathrm{p}}^{\mathrm{ext}}, \dots)$	
	MP–ETC	MP–ETI	MP–EPC	MP–EPI
micro-strain-gradient decomposition	$\bar{\boldsymbol{\eta}} = \nabla \bar{\boldsymbol{\varepsilon}}_{\mathrm{e}} + \nabla \bar{\boldsymbol{\varepsilon}}_{\mathrm{p}}^{\mathrm{ext}}$	$\bar{\boldsymbol{\eta}} = \bar{\boldsymbol{\eta}}_{\mathrm{e}} + \nabla \bar{\boldsymbol{\eta}}_{\mathrm{p}}^{\mathrm{ext}}$	$\nabla \bar{\boldsymbol{\varepsilon}}_{\mathrm{p}}^{\mathrm{ext}}$	$\nabla \bar{\boldsymbol{\eta}}_{\mathrm{p}}^{\mathrm{ext}}$
energy	$\widetilde{\mathscr{W}}(\dots, \dots, \bar{\boldsymbol{\eta}} - \nabla \bar{\boldsymbol{\varepsilon}}_{\mathrm{p}}^{\mathrm{ext}})$	$\widetilde{\mathscr{W}}(\dots, \dots, \bar{\boldsymbol{\eta}} - \bar{\boldsymbol{\eta}}_{\mathrm{p}}^{\mathrm{ext}})$	$\widetilde{\mathscr{W}}(\dots, \dots, \nabla \bar{\boldsymbol{\varepsilon}}_{\mathrm{p}}^{\mathrm{ext}})$	$\widetilde{\mathscr{W}}(\dots, \dots, \bar{\boldsymbol{\eta}}_{\mathrm{p}}^{\mathrm{ext}})$
'plastic' balance	$\boldsymbol{\sigma}_{\mathrm{p}}^{\mathrm{ext}\star} = 0$ in $\mathscr{B}$	$\boldsymbol{\sigma}_{\mathrm{p}}^{\mathrm{ext}} = 0$, $\boldsymbol{\tau}_{\mathrm{p}}^{\mathrm{ext}} = 0$ in $\mathscr{B}$	$\boldsymbol{\sigma}_{\mathrm{p}}^{\mathrm{ext}\star} = 0$ in $\mathscr{B}$	$\boldsymbol{\sigma}_{\mathrm{p}}^{\mathrm{ext}} = 0$, $\boldsymbol{\tau}_{\mathrm{p}}^{\mathrm{ext}} = 0$ in $\mathscr{B}$
'plastic' boundary condition	$t^{\tau_{\mathrm{p}}^{\mathrm{ext}}} = \boldsymbol{\tau}_{\mathrm{p}}^{\mathrm{ext}} \cdot \boldsymbol{n}$		$t^{\tau_{\mathrm{p}}^{\mathrm{ext}}} = \boldsymbol{\tau}_{\mathrm{p}}^{\mathrm{ext}} \cdot \boldsymbol{n}$	

within the classical continuum, which is endowed with an additional independent plastic tensorial micro variable of second and third order, respectively.

MP–ETC *(Compatible micromorphic plasticity based on total micro strain: external-micro-variable approach of Section 7.3.4)* is based on a full micromorphic continuum. While the plasticity framework is restricted to the macro level, we obtain balance of momentum for the macro and the micro quantities as well as an extra balance resulting from the external micro variable and its gradient.

MP–ETI *(Incompatible micromorphic plasticity based on total micro strain: external-micro-variable approach of Section 7.3.4)* incorporates the micromorphic continuum framework including balance of macro and micro momentum, while the plasticity framework is retained solely at the macro level.

MP–EPC *(Compatible micromorphic plasticity based on plastic micro strain: external-micro-variable approach of Section 7.3.5)* is a classical plasticity which is endowed with additional balance relations for the external variables on the micro scale.

MP–EPI *(Incompatible micromorphic plasticity based on plastic micro strain: external-micro-variable approach of Section 7.3.5)* is based on the classical continuum. Since the introduced external variables trivially vanish, only the balance of macro momentum remains. Thus we retrieve a classical plasticity formulation.

Discussion. In micromorphic plasticity, contrary to the gradient plasticity formulations, we obtain a set of equations for the macro quantities that is identical for all formulations, no matter which variant we pursue. For internal plastic micro variables (MP–I••) we obey a plasticity formulation, which takes into account the plastic macro stress as well as the plastic micro stress and the double stress. Contrary with the introduction of an external micro variable (MP–E••), the actual plasticity constitutive framework reduces to classical plasticity on the macro scale with additional balance relations acting on the micro scale. These approaches show decisive parallels to the contributions of Gurtin and Podio-Guidugli (1992), Gurtin (2000a, 2003), Cermelli and Gurtin (2002), Anand et al. (2005). The micromorphic-plasticity formulations based on total micro strain (MP–•T•) incorporate the full micromorphic continuum framework with its respective macro and micro balance of momentum and the corresponding boundary conditions. Contrary, the micromorphic plastic-strain formulation (MP– •P•), which are based on the classical continuum, require only a single balance of momentum with the well-known classical boundary condition. We further notic that all compatible formulations (MP–••C) involve a nonzero

nonlocality residual, which can only be resolved by considering the dissipation inequality globally and goes along with the necessity to keep track of the plastic boundary. All micromorphic formulations only require C_0 continuity for the displacement.

Within the discussed micromorphic plasticity formulations, we believe that the formulation we denoted as MP–EPC can prove significantly advantageous in the context of regularization. On the one hand, this formulation is based on the classical continuum, which keeps the computational costs low with respect to the number of degrees of freedom (and the continuity requirements), and on the other hand, such formulation allows to control the yield process by an external variable. Particularly it is smoothed out through the external balance equation that has to be satisfied.

8 Conclusion

The main objective of this thesis was to develop a numerical multiscale framework that allows to obtain the global response of a material layer with a microstructure displaying size effects. In this concluding chapter, the work is briefly summarized chapter by chapter in Section 8.1. Upon this summary, the main contribution of this thesis is emphasized in Section 8.2. The chapter closes with an outlook on research topics which evolve from the findings.

8.1 Summary

Chapter 2 *(Generalized continuum theories)* An overview on different continuum theories was given. In this context, first the respective key characteristics of the classical, the gradient, and the micromorphic continuum were illustrated by the aid of the nonlinear deformation mapping of a finite line element. For these particular theories, a continuum mechanics framework was both examined with respect to finite and infinitesimal deformations.

Chapter 3 *(Micromorphic continua)* A micromorphic continuum formulation was introduced, which is characterized by the additional consideration of a microstructure attached at each continuum point. In this theory extra kinematic quantities account for the deformation of these microcontinua. Both a macro and micro balance of momentum were derived based upon the enhanced finite-deformation kinematics considering variational principles. In this consideration of the micromorphic continuum the duality of the spatial- and the material-motion problem was especially emphasized. The relations of the kinematic quantities, the stress quantities and the balance relations in the two perspectives were pointed out. For a constitutive framework, we presented a hyperelastic constitutive ansatz that accounts for both the macro and the micro scale, and additionally couples both by a so-called scale-transition term. For the solution of the coupled micromorphic boundary value problems, we derived a finite-element approximation scheme. In this numerical context we particularly applied the material-force method based on the material-motion problem considered before. Besides the nodal material force of the macro scale, which conforms to that known from the classical continuum, an additional quantity for the micro scale was derived, which we denote as the nodal configurational double force. The chapter was completed with numerical examples. For

two different boundary value problems, the discretized spatial- motion problem was solved and moreover the presented quantities from the micromorphic material-force method were computed in a post-processing step. The theory together with the numerical formulation renders the typical features, such as nonsymmetric stress and size-effects.

Chapter 4 *(Computational homogenization of a continuous medium)* A brief introduction to the fundamental concept of the direct multiscale approach and the resulting computational homogenization approach was given. Thereby, first the scale transition between a classical continuum at the macro level and the same framework at the micro level was reviewed. Especially in view of Chapter 6, we augmented this multiscale approach to the homogenization of a continuum with an underlying mesostructure with intrinsic microstructure and modelled the RVE with a micromorphic continuum. All considerations were pursued within the general framework of finite deformations.

Chapter 5 *(Computational homogenization of a heterogeneous material layer)* In this chapter, we proposed a computational homogenization approach for a microscopically heterogeneous material layer. This approach allows to obtain the macroscopic response of this material layer based on its underlying microstructural constitution. Situated within a continuum, a cohesive interface represents the material layer. Based on the continuum-homogenization standards reviewed in Chapter 4, we related the vectorial quantities traction and separation at the macro level to the averaged tensorial stress and deformation gradient at the micro level. The height of the RVE was considered as the height of the material layer itself and entered the equivalence of the virtual work of both scales. To account for the two possible deformation modes in the interface, i. e. tension and shear, customized boundary conditions were presented, which are hybrid between prescribed deformation out of plane and periodic deformation in plane of the interface. The developed theoretical framework was successfully embedded into a computational homogenization procedure. As documented in numerical examples, the obtained macroscopic response depends on the particular geometry and material properties of the respective microstructure.

Chapter 6 *(Computational homogenization of material layers with micromorphic mesostructure)* The homogenization framework for material layers of Chapter 5, was successfully extended to material layers with an underlying micromorphic mesostructure. The macro quantities, which are governed by the deformation jump, were linked to their corresponding quantities on the RVE level by homogenization. Thereby the two different types of continua, i. e. a classical continuum at the macro

level and a micromorphic continuum at the meso/micro level, are consistently related to each other by means of a homogenization approach in the framework of finite deformations. In this context boundary conditions were developed that clearly account for the deformation induced by the interface, while they fulfil the Hill condition. As in the preceding chapter, we translated the theoretical concept into a computational homogenization. Particularly the dependence of the global response on the internal length in the micromorphic RVE was displayed in numerical examples.

Chapter 7 *(Classification of generalized plasticity)* A classification of formulations of both gradient plasticity and micromorphic plasticity was proposed. For both superordinate theories we varied (i) the type of plastic variable (as an external or internal variable), (ii) the type of higher-order strain acting on either the total or the plastic (micro) strain, and (iii) the compatibility of the plastic strain and the plastic higher-order strain. As a conclusion, with some formulations we retrieved established versions of what is coined as strain gradient plasticity. In particular the GP–ITI is the full gradient plasticity which in a further specified variant can be found in Fleck and Hutchinson (1993), furthermore the GP–IPC identifies the gradient of plastic strain theories that have for instance been presented by Aifantis (1984), Menzel and Steinmann (2000), Fleck and Hutchinson (2001). Other formulations boil down to existing theories of classical plasticity. Particularly we found out that all formulations of gradient plasticity constructed with external plastic variables proved to be not beneficial since no dissipation is connected with the external variables.

8.2 Main contribution

Since in this thesis, the micromorphic continuum (Eringen, 1999) was addressed in its entire duality of configurational and deformational mechanics, the material-force method was enabled to be applied. Based on the resulting material tractions and double tractions, both material forces and double forces were derived, which are expected to prove useful when focusing on defect mechanics for micromorphic or related generalized continua. With the constitutive assumption at finite deformations, we introduced a numerical finite-element framework. This enables the simulation of size-dependent elasticity without arduous continuity requirements as known from higher-gradient continua.

Based upon the existing homogeneous approaches for continuous media, a computational homogenization for material layers was presented. With this methodology, the traction-separation relations for such material layers can be extracted numerically for a known microstructural constitution. With the continuous representative volume element under the proposed hybrid boundary conditions, in particular mixed-mode loading is captured in a natural manner. Additionally to existing

approaches to mixed-mode response (e. g. Ortiz and Pandolfi (1999), van den Bosch et al. (2006)), the behaviour is here obtained directly based on the microstructure rather than by an a priori constitutive assumption for the material layer. Through the incorporation of the micromorphic continuum within the representative volume element, the procedure moreover accounts for size effects, which arise due to an underlying microstructure in the material layer, as can for instance be found in geomaterials, metals, polymers, etc. The proposed multiscale finite-element framework for the micromorphic hyperelastic continuum allows to compute multiscale boundary value problems of interest numerically.

Furthermore, a classification of concepts in thermodynamically consistent generalised plasticity was given. While some formulations resulting from the schematic variation of key features proved unphysical, meaningful approaches were especially pointed out and could partially be identified with existing formulations. The classification is considered as a platform for the development of further particularizations.

8.3 Outlook

Micromorphic continua and generalized plasticity In the modelling of hyperelastic micromorphic continua further constitutive models could be developed that accomplish the coupling between the macro and the micro deformation maps in a different manner.

The studied formulations of generalized plasticity call for a numerical implementation in order to further investigate their respective advantages and drawbacks. This could for instance document that or if the formulation we denoted as MP–EPC can prove advantageous in the context of regularization. Moreover it is desirable to advance the useful concepts of generalized, especially micromorphic, plasticity to finite strain.

Computational homogenization of material layers For the modelling of heterogeneous material layers, in addition to the hyperelastic constitutive format chosen here, the incorporation of irreversible or even softening behaviour within the microstructure remain a challenge for future research. Such choices are expected to render typical cohesive laws (Needleman, 1987, 1990a, Xu and Needleman, 1993, Ortiz and Pandolfi, 1999, van den Bosch et al., 2006). A distinct improvement with respect to these phenomenological approaches is particularly expected for mixed-mode loading that now can be treated more accurately under incorporation of the response of the underlying micro- or mesostructure.

The material layers with micromorphic mesostructure call for an incorporation of the envisioned irreversible micromorphic material models into the multiscale framework. By a consideration of the micromorphic mesostructure, a third scale has intrinsically been involved in the model. It can be seen as a challenge for future

research to link the present model representation of the attached microcontinua to actual physical microstructures, such as granular assemblies as e. g. treated by Meier et al. (2008a) and in the framework of homogenization (Ehlers et al., 2003, Miehe and Dettmar, 2004, Dettmar, 2006, Meier et al., 2008b). Such granular assemblies can be modelled by means of granular representative volume elements underlying to the micromorphic mesostructure. In a homogenization of these representative volume elements, e. g. intergranular friction is expected to result in nonsymmetric homogenized stresses. Therefore these models particularly motivate to be connected with a micromorphic or micropolar continuum at the meso level.

In the context of numerics, further improvements can be made with respect to interface element technology. The incorporation of contact algorithms should be involved to capture compression within the interface. Besides finite interface elements also more elaborate methods for the handling of the cohesive interface representing the material layer can be employed. Among the most prominent approaches are the extended finite element method (Moës et al., 1999, Sukumar et al., 2000, 2004) or the approaches based on Nitsche's method (Hansbo and Hansbo, 2003, Mergheim et al., 2005, 2007, Mergheim, 2006, Jäger et al., 2008, 2007). These enable a treatment of the layer which is independent of the finite element mesh geometry.

A Second-Gradient Continuum: Balance of Momentum and Boundary Conditions

For the large strain formulation of the second-gradient continuum of Section 2.3.1 the derivation of the local static balance of momentum and the corresponding Neuman boundary conditions is presented here. This fundamental derivation goes back to Mindlin (1965) for small strain, while it has been exploited towards large strain formulations for instance in Sunyk and Steinmann (2003), Kirchner and Steinmann (2005).

We directly obtain the weak formulation of the static balance of momentum from the Dirichlet principle (2.23):

$$\int_{\mathscr{B}_0} \boldsymbol{P} : \delta\boldsymbol{F} + \boldsymbol{Q} \vdots \delta\boldsymbol{G}\,\mathrm{d}V \doteq \int_{\mathscr{B}_0} \boldsymbol{b}_0 \cdot \delta\boldsymbol{\varphi}\,\mathrm{d}V + \int_{\partial\mathscr{B}_0} \boldsymbol{t}_0^P \cdot \delta\boldsymbol{\varphi} + \boldsymbol{t}_0^Q \cdot \delta\boldsymbol{G}\,\mathrm{d}A\,. \tag{A.1}$$

Therein the stress and double stress are given in (2.38). With the kinematics (2.30) the left-hand side is tranformed as follows:

$$\begin{aligned}
&\int_{\mathscr{B}_0} \boldsymbol{P} : \delta\boldsymbol{F} + \boldsymbol{Q} \vdots \boldsymbol{G}\,\mathrm{d}V \\
&= \int_{\mathscr{B}_0} \mathrm{Div}\,(\delta\boldsymbol{\varphi}\cdot\boldsymbol{P}) - \delta\boldsymbol{\varphi}\cdot\mathrm{Div}\,\boldsymbol{P}\,\mathrm{d}V \;+ \mathrm{Div}\,(\nabla_X\delta\boldsymbol{\varphi}\cdot\boldsymbol{Q}) \\
&- \int_{\mathscr{B}_0} \mathrm{Div}\,(\delta\boldsymbol{\varphi}\cdot\mathrm{Div}\,\boldsymbol{Q}) - \delta\boldsymbol{\varphi}\cdot\mathrm{Div}\,(\mathrm{Div}\,\boldsymbol{Q})\,\mathrm{d}V \\
&= \int_{\mathscr{B}_0} \delta\boldsymbol{\varphi}\cdot\mathrm{Div}\,(\mathrm{Div}\,\boldsymbol{Q} - \boldsymbol{P})\,\mathrm{d}V + \int_{\partial\mathscr{B}_0} \delta\boldsymbol{\varphi}\cdot[\boldsymbol{P} - \mathrm{Div}\,\boldsymbol{Q}]\,\mathrm{d}A + \int_{\partial\mathscr{B}_0} \delta\nabla_X\boldsymbol{\varphi} : [\boldsymbol{Q}\cdot\boldsymbol{N}]\,\mathrm{d}A\,.
\end{aligned} \tag{A.2}$$

Herein the last term deserves special consideration. We apply a split into a normal and a tangential contribution to the gradient operator

$$\nabla_X(\bullet) := \nabla_X(\bullet)^N \otimes \boldsymbol{N} + \nabla_X^T(\bullet) \tag{A.3}$$

wherein the normal gradient is defined as $\nabla_X^N(\bullet) := \nabla_X(\bullet)\cdot\boldsymbol{N}$ and the tangential as $\nabla_X^T(\bullet) := \nabla_X(\bullet)\cdot\boldsymbol{T} = \nabla_X(\bullet)\cdot[\boldsymbol{I}-\boldsymbol{N}\otimes\boldsymbol{N}]$. With this split, we can reformulate the last term in (A.2) as

$$\int_{\partial\mathscr{B}_0} \delta\nabla_X\boldsymbol{\varphi} : \boldsymbol{Q}\cdot\boldsymbol{N}\,\mathrm{d}A = \int_{\partial\mathscr{B}_0} \nabla_X^N(\delta\boldsymbol{\varphi})\cdot[\boldsymbol{Q} : [\boldsymbol{N}\otimes\boldsymbol{N}]]\mathrm{d}A + \int_{\partial\mathscr{B}_0} \nabla_X^T(\delta\boldsymbol{\varphi}) : [\boldsymbol{Q}\cdot\boldsymbol{N}]\mathrm{d}A. \tag{A.4}$$

The latter term is rewritten as

$$\int_{\partial\mathscr{B}_0} [\nabla_X(\delta\boldsymbol{\varphi})\cdot\boldsymbol{T}] : [\boldsymbol{Q}\cdot\boldsymbol{N}]\,\mathrm{d}A = \int_{\partial\mathscr{B}_0} \nabla_X(\delta\boldsymbol{\varphi}\cdot\boldsymbol{Q}\cdot\boldsymbol{N}) : \boldsymbol{T} - \delta\boldsymbol{\varphi}\cdot\nabla_X(\boldsymbol{Q}\cdot\boldsymbol{N}) : \boldsymbol{T}\,\mathrm{d}A \tag{A.5}$$

To simplify this expression, we apply the surface divergence theorem based on Stokes theorem for the closed surface, which reads for a vector $\boldsymbol{a}$

$$\int_{\partial\mathscr{B}_0} \nabla_X\boldsymbol{a} : \mathscr{T} + K\boldsymbol{a}\cdot\boldsymbol{N}\,\mathrm{d}A = 0 \tag{A.6}$$

Hereby $K := -\nabla_X\boldsymbol{N} : \boldsymbol{T} = -\nabla_X^T\boldsymbol{N} : \boldsymbol{I}$ defines the total curvature of the surface $\partial\mathscr{B}_0$. With the vectorial expression taken as $\boldsymbol{a} = \delta\boldsymbol{\varphi}\cdot\boldsymbol{Q}\cdot\boldsymbol{N}$, the term (A.5) is transformed to

$$\begin{aligned}\int_{\partial\mathscr{B}_0} \nabla_X^T(\delta\boldsymbol{\varphi}) : [\boldsymbol{Q}\cdot\boldsymbol{N}]\mathrm{d}A &= -\int_{\partial\mathscr{B}_0} K\,\delta\boldsymbol{\varphi}\cdot[\boldsymbol{Q}\cdot\boldsymbol{N}]\cdot\boldsymbol{N} + \delta\boldsymbol{\varphi}\cdot\nabla_X(\boldsymbol{Q}\cdot\boldsymbol{N}) : \boldsymbol{T}\,\mathrm{d}A \\ &= -\int_{\partial\mathscr{B}_0} \delta\boldsymbol{\varphi}\cdot\left[K\,\boldsymbol{Q}[\boldsymbol{N}\otimes\boldsymbol{N}] + \nabla_X^T(\boldsymbol{Q}\cdot\boldsymbol{N}) : \boldsymbol{I}\right]\mathrm{d}A \end{aligned} \tag{A.7}$$

In the latter term we recognize the operator $\mathscr{L}(\boldsymbol{Q}\cdot\boldsymbol{N}) := -K\,\boldsymbol{Q} : [\boldsymbol{N}\otimes\boldsymbol{N}] + \nabla_X^T[\boldsymbol{Q}\cdot\boldsymbol{N}] : \boldsymbol{I}$

of Remark 2.3.1. The balance is rewritten in total as

$$\int_{\mathscr{B}_0} \delta\boldsymbol{\varphi} \cdot \mathrm{Div}\,(\mathrm{Div}\,\boldsymbol{Q} - \boldsymbol{P})\mathrm{d}V + \int_{\partial\mathscr{B}_0} \delta\boldsymbol{\varphi} \cdot [\boldsymbol{P} - \mathrm{Div}\,\boldsymbol{Q}]\,\mathrm{d}A$$

$$- \int_{\partial\mathscr{B}_0} \delta\boldsymbol{\varphi} \cdot \left[K\,\boldsymbol{Q}[\boldsymbol{N}\otimes\boldsymbol{N}] + \nabla_X^T(\boldsymbol{Q}\cdot\boldsymbol{N}) : \boldsymbol{I}\right]\,\mathrm{d}A + \int_{\partial\mathscr{B}_0} \nabla_X^N(\delta\boldsymbol{\varphi}) \cdot [\boldsymbol{Q} : [\boldsymbol{N}\otimes\boldsymbol{N}]]\mathrm{d}A \quad \text{(A.8)}$$

$$= \int_{\mathscr{B}_0} \boldsymbol{b}_0 \cdot \delta\boldsymbol{\varphi}\,\mathrm{d}V + \int_{\partial\mathscr{B}_0} \boldsymbol{t}_0^P \cdot \delta\boldsymbol{\varphi} + \boldsymbol{t}_0^Q \cdot \delta\boldsymbol{G}\,\mathrm{d}A.$$

From is equation, the bulk contributions deliver the local static balance of momentum

$$\mathrm{Div}\,(\boldsymbol{P} - \mathrm{Div}\,\boldsymbol{Q}) = -\boldsymbol{b}_0 \qquad \text{in } \mathscr{B}_0\,, \tag{A.9}$$

while the Neumann boundary conditions are given by the surface contributions:

$$[\boldsymbol{P} - \mathrm{Div}\,\boldsymbol{Q}] \cdot \boldsymbol{N} + \mathscr{L}(\boldsymbol{Q}\cdot\boldsymbol{N}) := \boldsymbol{t}_0^P \qquad \text{on } \partial\mathscr{B}_0^P \tag{A.10}$$

$$\boldsymbol{Q} : [\boldsymbol{N}\otimes\boldsymbol{N}] := \boldsymbol{t}_0^Q \qquad \text{on } \partial\mathscr{B}_0^Q\,. \tag{A.11}$$

In an analogous manner, this derivation can be applied to the small strain case of Section 2.3.2 as well.

B An Alternative Constitutive Assumption for Micromorphic Hyperelasticity

Alternatively to the additive relation in $(3.50)_3$, the scale transition in the energy formulation (3.49) can as well be obtained by a multiplicative formulation

$$\mathscr{W}_0^{\text{scale}} = \tfrac{1}{2}\, p\, [\bar{\boldsymbol{f}} \cdot \boldsymbol{F} - \boldsymbol{I}] : [\bar{\boldsymbol{f}} \cdot \boldsymbol{F} - \boldsymbol{I}]\,. \tag{B.1}$$

Spatial-motion stresses With the alternative stored-energy density formulation (B.1), the Piola-type stresses (3.9) result in

$$\begin{aligned} \boldsymbol{P} &= \mathrm{D}_{\boldsymbol{F}} \mathscr{W}_0 = [\lambda \ln J - \mu]\boldsymbol{f}^{\mathrm{t}} + \mu \boldsymbol{F} + p\bar{\boldsymbol{f}}^{\mathrm{t}} \cdot [\bar{\boldsymbol{f}} \cdot \boldsymbol{F} - \boldsymbol{I}]\,, \\ \bar{\boldsymbol{P}} &= \mathrm{D}_{\bar{\boldsymbol{F}}} \mathscr{W}_0 = p\bar{\boldsymbol{f}}^{\mathrm{t}} \cdot [\boldsymbol{I} - \bar{\boldsymbol{f}} \cdot \boldsymbol{F}] \cdot \boldsymbol{F}^{\mathrm{t}} \cdot \bar{\boldsymbol{f}}^{\mathrm{t}}\,, \\ \bar{\boldsymbol{Q}} &= \mathrm{D}_{\bar{\boldsymbol{G}}} \mathscr{W}_0 = \mu l^2 \bar{\boldsymbol{G}}\,. \end{aligned} \tag{B.2}$$

With the relations (3.18) the Cauchy-type stresses are then obtained as

$$\begin{aligned} \boldsymbol{\sigma} &= j[[\lambda \ln J - \mu]\boldsymbol{f}^{\mathrm{t}} + \mu \boldsymbol{F} + p\bar{\boldsymbol{f}}^{\mathrm{t}} \cdot [\bar{\boldsymbol{f}} \cdot \boldsymbol{F} - \boldsymbol{I}]] \cdot \boldsymbol{F}^{\mathrm{t}}\,, \\ \bar{\boldsymbol{\sigma}} &= j[p\bar{\boldsymbol{f}}^{\mathrm{t}} \cdot [\boldsymbol{I} - \bar{\boldsymbol{f}} \cdot \boldsymbol{F}] \cdot \boldsymbol{F}^{\mathrm{t}} + \mu l^2 \bar{\boldsymbol{G}} \overset{2,3}{\vdots} \bar{\boldsymbol{G}}]\,, \\ \bar{\boldsymbol{\tau}} &= j\mu l^2 \bar{\boldsymbol{G}} : [\bar{\boldsymbol{F}}^{\mathrm{t}} \overline{\otimes} \boldsymbol{F}^{\mathrm{t}}]\,. \end{aligned} \tag{B.3}$$

for the present constitutive model. The same restrictions to the symmetry of the stress apply as for the additive scale transition $(3.50)_3$.

Material-motion stresses In the absence of body forces, the following expressions for the purely material stresses of Eshelby type are obtained with (B.1) and (3.46)

$$\begin{aligned} \boldsymbol{\Sigma} &= [\mathscr{W}_0 - \lambda \ln J + \mu]\boldsymbol{I} - \mu \boldsymbol{F}^{\mathrm{t}} \cdot \boldsymbol{F} + p\boldsymbol{F}^{\mathrm{t}} \cdot \bar{\boldsymbol{f}}^{\mathrm{t}} \cdot [\boldsymbol{I} - \bar{\boldsymbol{f}} \cdot \boldsymbol{F}] - \mu l^2 \bar{\boldsymbol{G}} \overset{1,2}{\vdots} \bar{\boldsymbol{G}}\,, \\ \bar{\boldsymbol{\Sigma}} &= p[\bar{\boldsymbol{f}} \cdot \boldsymbol{F} - \boldsymbol{I}] \cdot \boldsymbol{F}^{\mathrm{t}} \cdot \bar{\boldsymbol{f}}^{\mathrm{t}} - \mu l^2 \bar{\boldsymbol{G}} \overset{1,3}{\vdots} \bar{\boldsymbol{G}}\,, \\ \bar{\mathscr{T}} &= -\mu l^2 \bar{\boldsymbol{F}}^{\mathrm{t}} \cdot \bar{\boldsymbol{G}} \end{aligned} \tag{B.4}$$

In the same manner the Piola-type stresses (3.25) of the material-motion problem can be derived as

$$\begin{aligned}
\boldsymbol{p} &= j[[\mathscr{W}_0 - \lambda \ln J + \mu]\boldsymbol{I} - \mu \boldsymbol{F}^{\mathrm{t}} \cdot \boldsymbol{F} + p\boldsymbol{F}^{\mathrm{t}} \cdot \bar{\boldsymbol{f}}^{\mathrm{t}} \cdot [\bar{\boldsymbol{f}} \cdot \boldsymbol{F} - \boldsymbol{I}] - \mu l^2 \bar{\boldsymbol{G}} \overset{1,2}{\vdots} \bar{\boldsymbol{G}}] \cdot \boldsymbol{F}^{\mathrm{t}} \\
\bar{\boldsymbol{p}} &= jp[\bar{\boldsymbol{f}} \cdot \boldsymbol{F} - \boldsymbol{I}] \cdot \boldsymbol{F}^{\mathrm{t}} \\
\bar{\boldsymbol{q}} &= -j\mu l^2 \bar{\boldsymbol{F}}^{\mathrm{t}} \cdot \bar{\boldsymbol{G}} : [\bar{\boldsymbol{F}}^{\mathrm{t}} \overline{\otimes} \boldsymbol{F}^{\mathrm{t}}] .
\end{aligned} \tag{B.5}$$

using $\mathscr{U}_t \equiv \mathscr{W}_t$.

Tangent Operator For a numerical solution within the finite-element framework presented in Section 3.4, the particular components of the tangent stiffness operator derived from multiplicative scale transition and the corresponding Piola-type stresses (B.2) read:

$$\begin{aligned}
\mathrm{D}_{\boldsymbol{F}}\boldsymbol{P} &= \lambda \boldsymbol{f}^{\mathrm{t}} \otimes \boldsymbol{f}^{\mathrm{t}} + \left[\mu - \lambda \ln J\right] \boldsymbol{f}^{\mathrm{t}} \underline{\otimes} \boldsymbol{f} + \mu \boldsymbol{I} \overline{\otimes} \boldsymbol{I} + p[\bar{\boldsymbol{f}}^{\mathrm{t}} \cdot \bar{\boldsymbol{f}}] \overline{\otimes} \boldsymbol{I} \\
\mathrm{D}_{\bar{\boldsymbol{F}}}\boldsymbol{P} &= -p \left[\bar{\boldsymbol{f}}^{\mathrm{t}} \underline{\otimes} [[\bar{\boldsymbol{f}} \cdot \boldsymbol{F} - \boldsymbol{I}]^{\mathrm{t}} \cdot \bar{\boldsymbol{f}}] + [\bar{\boldsymbol{f}}^{\mathrm{t}} \cdot \bar{\boldsymbol{f}}] \overline{\otimes} [\boldsymbol{F}^{\mathrm{t}} \cdot \bar{\boldsymbol{f}}^{\mathrm{t}}]\right] \\
\mathrm{D}_{\boldsymbol{F}}\bar{\boldsymbol{P}} &= -p \left[[\bar{\boldsymbol{f}}^{\mathrm{t}} \cdot \bar{\boldsymbol{f}}] \overline{\otimes} [\bar{\boldsymbol{f}} \cdot \boldsymbol{F}] + [\bar{\boldsymbol{f}}^{\mathrm{t}} \cdot [\boldsymbol{I} - \bar{\boldsymbol{f}} \cdot \boldsymbol{F}]] \overline{\otimes} \bar{\boldsymbol{f}}\right] \\
\mathrm{D}_{\bar{\boldsymbol{F}}}\bar{\boldsymbol{P}} &= p\bar{\boldsymbol{f}}^{\mathrm{t}} \underline{\otimes} [\bar{\boldsymbol{f}} \cdot \boldsymbol{F} \cdot [\bar{\boldsymbol{f}} \cdot \boldsymbol{F} - \boldsymbol{I}]^{\mathrm{t}} \cdot \bar{\boldsymbol{f}}] + [\bar{\boldsymbol{f}}^{\mathrm{t}} \cdot \bar{\boldsymbol{f}}] \overline{\otimes} [\bar{\boldsymbol{f}} \cdot \boldsymbol{F} \cdot \boldsymbol{F}^{\mathrm{t}} \cdot \bar{\boldsymbol{f}}^{\mathrm{t}}] \\
&\quad + [\bar{\boldsymbol{f}}^{\mathrm{t}} \cdot [\bar{\boldsymbol{f}} \cdot \boldsymbol{F} - \boldsymbol{I}] \cdot \boldsymbol{F}^{\mathrm{t}} \cdot \bar{\boldsymbol{f}}^{\mathrm{t}}] \underline{\otimes} \bar{\boldsymbol{f}}\Big] , \\
\mathrm{D}_{\bar{\boldsymbol{G}}}\bar{\boldsymbol{Q}} &= +\mu l^2 \boldsymbol{I} \underline{\otimes} \left[\boldsymbol{I} \overline{\otimes} \boldsymbol{I}\right] , \\
\mathrm{D}_{\boldsymbol{F}}\bar{\boldsymbol{Q}} &= \boldsymbol{0}
\end{aligned} \tag{B.6}$$

Bibliography

E. C. Aifantis. On the microstructural origin of certain inelastic models. *J. Engng. Mater. Technol.*, 106:326–330, 1984.

E. C. Aifantis. On the role of gradients in the localization of deformation and fracture. *Int. J. Eng. Sci.*, 30:1279–1299, 1992.

R. K. Abu Al-Rub and G. Z. Voyiadjis. A physically based gradient plasticity theory. *Int. J. Plast.*, 22:654–684, 2006.

E. Amanatidou and A. Aravas. Mixed finite element formulations of strain-gradient elasticity problems. *Comput. Methods Appl. Mech. Engrg.*, 191:1723–1751, 2002.

L. Anand, M. E. Gurtin, S. P. Lele, and C. Gething. A one-dimensional theory of strain-gradient plasticity: Formulation, analysis, numerical results. *J. Mech. Phys. Solid.*, 53: 1789–1826, 2005.

H. Askes, E. Kuhl, and P. Steinmann. An ALE formulation based on spatial and material settings of continuum mechanics – Part 2: Classification and applications. *Comput. Methods Appl. Mech. Engrg.*, 193:4223–4235, 2004.

C. J. Bayley, W. A. M. Brekelmans, and M. G. D. Geers. A comparison of dislocation induced back stress formulations in strain gradient crystal plasticity. *Int. J. Solid Struct.*, 43:7268–7286, 2006.

C. Bayreuther. *Mehrskalenmodelle in der Festkörpermechanik und Kopplung von Mehrgittermethoden mit Homogenisierungsverfahren*. Phd thesis, Bericht: I–16, Institut für Mechanik (Bauwesen) Lehrstuhl I, Universität Stuttgart, 2005.

Z. P. Bazant. Size effect. *Int. J. Solid Struct.*, 37:69–80, 2000.

Z. P. Bazant, T. B. Belytschko, and T.-P. Chang. Instability, ductility and size effect in strain softening concrete. *J. Engineering Mech.*, 102:225–238, 1976.

G. Beer. An isoparametric joint/interface element for finite element analysis. *Int. J. Numer. Meth. Engng*, 21:585–600, 1985.

D. Besdo. Ein Beitrag zur nichtlinearen Theorie des Cosserat-Kontinuums. *Acta Mech.*, 20: 105–131, 1974.

R. de Borst. Simulation of strain localization: A reappraisal of the Cosserat continuum. *Engineering Computations*, 8:317–332, 1991.

R. de Borst and H.-B. Mühlhaus. Gradient-dependent plasticity: formulation and algorithmic aspects. *Int. J. Numer. Meth. Engng*, 35:521–539, 1992.

R. de Borst and J. Pamin. Some novel developments in finite element procedures for gradient-dependent plasticity. *Int. J. Numer. Meth. Engng*, 39:2477–2505, 1996.

R. de Borst, J. Pamin, and M. G. D. Geers. On coupled gradient-dependent plasticity and damage theories with a view to localization analysis. *Eur. J. Mech. Solid*, 18:939–962, 1999.

G. Capriz. Continua with latent microstructure. *Arch. Rat. Mech. Anal.*, 90:43–56, 1985.

G. Capriz. *Continua with Microstructure*. Springer, 1989.

P. Cermelli and M. E. Gurtin. Geometrically necessary dislocations in viscoplastic single crystals and bicrystals undergoing small deformations. *Int. J. Solid Struct.*, 39:6281–6309, 2002.

P. Chadwick. *Continuum Mechanics – Concise Theory and Problems*. Dover, 1976.

J.-S. Chen, C.-T. Wu, and T. Belytschko. Regularisation of material instabilities by meshfree approximations with intrinsic length scales. *Int. J. Numer. Meth. Engng*, 47:1303–1322, 2000.

B. D. Coleman. On thermodynamics of materials with memory. *Arch. Rat. Mech. Anal.*, 17: 1–46, 1964.

B. D. Coleman and M. E. Gurtin. Thermodynamics with internal state variables. *J. Chem. Phys.*, 47:597–613, 1967.

E. Cosserat and F. Cosserat. *Théorie des Corps Déformables*. Herman et fils, Paris, 1909.

F. Costanzo, G. L. Gray, and P. C. Andia. On the definitions of effective stress and deformation gradient for use in MD: Hill's macro-homogeneity and the virial theorem. *Int. J. Numer. Meth. Engng*, 43:533–555, 2005.

S. L. Creighton, R. A. Regueiro, K. Garikipati, P. A. Klein, E. B. Marin, and D. J. Bammann. A variational multiscale method to incorporate strain gradients in a phenomenological plasticity model. *Comput. Methods Appl. Mech. Engrg.*, 193:5453–5475, 2004.

G. A. D'Addetta, E. Ramm, S. Diebels, and W. Ehlers. A particle center based homogenization strategy for granular assemblies. *Engineering Computations*, 21:360–383, 2004.

R. Denzer. *Computational Configurational Mechanics*. PhD thesis, Technische Universität Kaiserslautern, 2006.

R. Denzer, F. J. Barth, and P. Steinmann. Studies in elastic fracture mechanics based on the material force method. *Int. J. Numer. Meth. Engng*, 58:1817–1835, 2003.

R. Denzer, M. Scherer, and P. Steinmann. An adaptive singular finite element in nonlinear fracture mechanics. *Int. J. Fract.*, DOI: 10.1007/s10704-007-9154-6, 2007.

J. P. Dettmar. *Static and dynamic homogenization analyses of discrete granular and atomistic structures of different time and length scales*. Phd thesis, Universität Stuttgart, Institut für Mechanik, Lehrstuhl I, Bericht I–17, 2006.

S. Diebels and H. Steeb. Stress and couple stress in foams. *Comput. Mater. Sci.*, 28:714–722, 2003.

E. Diegele, R. Elsäßer, and C. Tsakmakis. Linear micropolar elastic crack-tip fields under mixed mode loading conditions. *Int. J. Fract.*, 129:309–339, 2004.

W. Diepolder, V. Mannl, and H. Lippmann. The Cosserat continuum, a model for grain rotations in metals? *Int. J. Plast.*, 7:313–328, 1991.

A. Dietsche, P. Steinmann, and K. Willam. Micropolar elastoplasticity and its role in localization analysis. *Int. J. Plast.*, 9:813–831, 1993.

T. Ebinger, H. Steeb, and S. Diebels. Modeling macroscopic extended continua with the aid of numerical homogenization schemes. *Comput. Mater. Sci.*, 32:337–347, 2005.

D. Edelen and N. Laws. On the thermodynamics of systems with nonlocality. *Arch. Rat. Mech. Anal.*, 43:24–35, 1971.

W. Ehlers and W. Volk. On shear band localization phenomena of liquid-saturated granular elastoplastic porous solid materials accounting for fluid viscosity and micropolar solid rotations. *Mech. of Cohes.-Frict. Mater.*, 2:301–320, 1997.

W. Ehlers and W. Volk. On theoretical and numerical methods in the theory of porous media based on polar and non-polar elasto-plastic solid materials. *Int. J. Solid Struct.*, 35: 4597–4617, 1998.

W. Ehlers and S. Wenz. From particle ensembles to Cosserat continua: Definition of the macroscopic variables. In P. A. Vermeer, W. Ehlers, H. J. Herrmann, and E. Ramm, editors, *Modelling of Cohesive-Frictional Materials*, pages 149–159. Taylor & Francis, 2004.

W. Ehlers, E. Ramm, S. Diebels, and G. A. D'Addetta. From particle ensembles to Cosserat continua: homogenization of contact forces towards stresses and couple stresses. *Int. J. Solid Struct.*, 40:6681–6702, 2003.

R. A. B. Engelen, N. A. Fleck, R. H. J. Peerlings, and M. G. D. Geers. An evaluation of higher-order plasticity theories for prediction size effects and localisation. *Int. J. Solid Struct.*, 43:1857–1877, 2006.

M. Epstein and G. A. Maugin. The energy-momentum tensor and material uniformity in finite elasticity. *Acta Mech.*, 83:127–133, 1990.

A. C. Eringen. Mechanics of micromorphic materials. In H. Görtler, editor, *Proc. 11th Int. Congress of Appl. Mech.*, pages 131–138, New York, 1964. Springer-Verlag.

A. C. Eringen. Linear theory of micropolar elasticity. *J. Math. Mech.*, 15:909–923, 1966.

A. C. Eringen. Linear theory of micropolar viscoelasticity. *Int. J. Eng. Sci.*, 5:191–204, 1967.

A. C. Eringen. Mechanics of micromorphic continua. In E. Kröner, editor, *Mechanics of Generalized Continua*, Freudenstadt/Stuttgart, 1968. IUTAM Symposium, Springer.

A. C. Eringen. *Continuum Physics. IV: Polar and Nonlocal Field Theories*. Academic Press, 1976.

A. C. Eringen. *Microcontinuum Field Theories: I. Foundations and Solids*. Springer, New York, 1999.

J. D. Eshelby. Force on an elastic singularity. *Phil. Trans. Roy. Soc. Lond. A*, 244:87–112, 1951.

J. D. Eshelby. The elastic energy-momentum tensor. *J. Elasticity*, 5:321–335, 1975.

L. P. Evers, W. A. M. Brekelmans, and M. G. D. Geers. Scale dependent crystal plasticity framework with dislocation density and grain boundary effects. *Int. J. Solid Struct.*, 41: 5209–5230, 2004.

F. Feyel and J.-L. Chaboche. FE^2 multiscale approach for modelling the elastoviscoplastic behaviour of long fibre SiC/Ti composites materials. *Comput. Methods Appl. Mech. Engrg.*, 183:309–330, 2000.

N. A. Fleck and J. W. Hutchinson. A phenomenological theory for strain gradient effects in plasticity. *J. Mech. Phys. Solid.*, 41:1825–1857, 1993.

N. A. Fleck and J. W. Hutchinson. Strain gradient plasticity. *Adv. Appl. Mech.*, 33:295–362, 1997.

N. A. Fleck and J. W. Hutchinson. A reformulation of strain gradient plasticity. *J. Mech. Phys. Solid.*, 49:2245–2271, 2001.

N. A. Fleck, G. M. Muller, M. F. Ashby, and J. W. Hutchinson. Strain gradient plasticity: Theory and experiment. *Acta metall. Mater.*, 42:475–487, 1994.

S. Forest. Generalized continuum modelling of crystal plasticity. Lecture notes of the CISM Advanced Course "Generalised continua and dislocation theory. Theoretical concepts, computational methods and experimental verification", July 9–13, 2007.

S. Forest and J.-M. Cardona. Thermoelasticity of second-grade media. In G. A. Maugin, R. Drouot, and F. Sidoroff, editors, *Continuum Thermodynamics, The Art and Science of Modelling Material Behaviour, Paul Germain's Anniversary Volume*, pages 163–176. Kluwer, 2000.

S. Forest and R. Sievert. Elastoviscoplastic constitutive frameworks for generalized continua. *Acta Mech.*, 160:71–111, 2003.

S. Forest and R. Sievert. Nonlinear microstrain theories. *Int. J. Solid Struct.*, 43:7224–7245, 2006.

S. Forest, F. Barbe, and G. Cailletaud. Cosserat modelling of size effects in the mechanical behaviour of polycrystals and multi-phase materials. *Physica D*, 37:7150–7126, 2000.

E. Fried. Continua described by a microstructural field. *Z. Angew. Math. Phys.*, 47:168–175, 1996.

K. Garikipati. Variational multiscale methods to embed the macromechanical continuum formulation with fine-scale strain gradient theories. *Int. J. Numer. Meth. Engng*, 57:1283–1298, 2003.

M. G. D. Geers, V. G. Kouznetsova, and W. A. M. Brekelmans. Computational homogenization. Lecture notes of the CISM Advanced Course "Multiscale modeling and design of new materials", 2005.

M. G. D. Geers, E. W. C. Coenen, and V. G. Kouznetsova. Multi-scale computational homogenization of structured thin sheets. *Modelling Simul. Mater. Sci. Eng.*, 15:393–404, 2007.

P. Grammenoudis. *Mikropolare Plastizität*. PhD thesis, Technische Universität Darmstadt, 2003.

P. Grammenoudis and C. Tsakmakis. Hardening rules for finite deformation micropolar plasticity: Restrictions imposed by the second law of thermodynamics and the postulate of Il'Iushin. *Continuum Mech. Therm.*, 13:325–363, 2001.

P. Grammenoudis and C. Tsakmakis. Finite element implementation of large deformation micropolar plasticity exhibiting isotropic and kinematic hardening effects. *Int. J. Numer. Meth. Engng*, 62:1691–1720, 2005a.

P. Grammenoudis and C. Tsakmakis. Predictions of microtorsional experiments by micropolar plasticity. *Proc. R. Soc. A*, 461:189–205, 2005b.

P. Grammenoudis and C. Tsakmakis. Micropolar plasticity theories and their classical limits. Part I: Resulting model. *Acta Mech.*, 189:151–175, 2007.

P. Grammenoudis, C. Sator, and C. Tsakmakis. Micropolar plasticity theories and their classical limits. Part II: Comparison of responses predicted by the limiting and a standard classical model. *Acta Mech.*, 189:177–191, 2007.

A. E. Green and P. M. Naghdi. A general theory of an elastic-plastic continuum. *Arch. Rat. Mech. Anal.*, 18:251–281, 1965.

D. Gross, R. Müller, and S. Kolling. Configurational forces – morphology evolution and finite elements. *Mech. Res. Comm.*, 29:529–536, 2002.

D. Gross, S. Kolling, and R. Müller. Configurational forces and their application in solid mechanics. *Eur. J. Mech. Solid*, 22:669–692, 2003.

P. Gudmundson. A unified treatment of strain gradient plasticity. *J. Mech. Phys. Solid.*, 52: 1379–1406, 2004.

M. E. Gurtin. On the plasticity of single crystals: free energy, microforces, plastic-strain gradients. *J. Mech. Phys. Solid.*, 48:989–1036, 2000a.

M. E. Gurtin. *Configurational Forces as Basic Concepts of Continuum Physics*. Springer, 2000b.

M. E. Gurtin. A gradient theory of single-crystal viscoplasticity that accounts for geometrically necessary dislocations. *J. Mech. Phys. Solid.*, 50:5–32, 2002.

M. E. Gurtin. On a framework for small-deformation viscoplasticity: free energy, microforces, strain gradients. *Int. J. Plast.*, 19:47–90, 2003.

M. E. Gurtin and P. Podio-Guidugli. On the formulation of mechanical balance laws for structured continua. *Z. Angew. Math. Phys.*, 43:181–190, 1992.

M. E. Gurtin and P. Podio-Guidugli. Configurational forces and the basic laws for crack propagation. *J. Mech. Phys. Solid.*, 44:905–9270, 1996.

M. E. Gurtin and P. Podio-Guidugli. Configurational forces and a constitutive theory for crack propagation that allows for kinking and curving. *J. Mech. Phys. Solid.*, 46:1343–1378, 1998.

A. Hansbo and P. Hansbo. *A Finite Element Method for the Simulation of Strong and Weak Discontinuities in Elasticity*. Chalmers Finite Element Center, Chalmers University of Technology, Göteborg, 2003. ISSN 1404-4382.

R. Hill. Elastic properties of reinforced solids: Some theoretical principles. *J. Mech. Phys. Solid.*, 11:357–372, 1963.

R. Hill. On constitutive macro-variables for heterogeneous solids at finite strain. *Proc. Roy. Soc. Lond. A*, 326:131–147, 1972.

C. B. Hirschberger and P. Steinmann. Classification of concepts in thermodynamically consistent generalised plasticity. *J. Engineering Mech.*, submitted, 2007.

C. B. Hirschberger, E. Kuhl, and P. Steinmann. Computational modelling of micromorphic continua – theory, numerics, and visualisation challenges. In H. Hagen, A. Kerren, and P. Dannenmann, editors, *Visualization of large and unstructured data sets*, volume S-4 of *GI-Edition Lecture Notes in Informatics (LNI)*, pages 155–164, 2006.

C. B. Hirschberger, E. Kuhl, and P. Steinmann. Computational material forces in micromorphic continua. *Proc. Appl. Math. Mech.*, 6:379–380, 2007a.

C. B. Hirschberger, E. Kuhl, and P. Steinmann. On deformational and configurational mechanics of micromorphic hyperelasticity – theory and computation. *Comput. Methods Appl. Mech. Engrg.*, 196:4027–4044, 2007b.

C. B. Hirschberger, S. Ricker, P. Steinmann, and N. Sukumar. Deriving global material properties of a microscopically heterogeneous medium – computational homogenisation and opportunities in visualisation. In *Visualization of large and unstructured data sets – Volume 2*, GI-Edition Lecture Notes in Informatics (LNI), 2007c. accepted.

C. B. Hirschberger, S. Ricker, P. Steinmann, and N. Sukumar. On the computational homogenization of a heterogeneous material layer. *Eng. Fract. Mech.*, submitted, 2008a.

C. B. Hirschberger, N. Sukumar, and P. Steinmann. Computational homogenization of material layers with micromorphic mesostructure. *submitted for publication*, 2008b.

D. Hofer. *Simulation von Größeneffekten mit mikromorphen Theorien*. PhD thesis, Forschungszentrum Karlsruhe/Technische Universität Darmstadt, 2003.

G. A. Holzapfel. *Nonlinear Solid Mechanics: A Continuum Approach for Engineering*. John Wiley & Sons Ltd., 2000.

P. Jäger, P. Steinmann, and E. Kuhl. On local tracking algorithms for the simulation of three-dimensional discontinuities. *Comput. Mech.*, accepted, 2007.

P. Jäger, P. Steinmann, and E. Kuhl. Modeling three-dimensional crack propagation – A comparison of crack path tracking strategies. *Int. J. Numer. Meth. Engng*, published online, 2008. doi: 10.1002/nme.2353.

M. Jirasek. Modeling of localized inelastic deformation. Lecture notes of the short course at Czech Technical Univerisity, Prague, 2005.

N. Kirchner and P. Steinmann. A unifying treatise on variational principles for gradient and micro-morphic continua. *Phil. Mag.*, 85:3875–3895, 2005.

N. Kirchner and P. Steinmann. On the material setting of gradient hyperelasticity. *Math. Mech. Solid*, 12:559–580, 2007a.

N. Kirchner and P. Steinmann. Mechanics of extended continua: modeling and simulation of elastic microstretch materials. *Comput. Mech.*, 40:651–666, 2007b.

W. T. Koiter. Couple-stresses in the theory of elasticity I & II. *Proc. Roy. Netherlands Acad. Sci. (B)*, 67:17–29 (I), 30–44 (II), 1964.

V. G. Kouznetsova. *Computational Homogenization for the Multiscale Analysis of Multi-Phase Materials*. PhD thesis, Technische Universiteit Eindhoven, 2002.

V. G. Kouznetsova, W. A. M. Brekelmans, and F. P. T. Baaijens. An approach to micro-macro modeling of heterogeneous materials. *Comput. Mech.*, 27:37–48, 2001.

V. G. Kouznetsova, M. G. D. Geers, and W. A. M. Brekelmans. Multi-scale constitutive modelling of heterogeneous materials with a gradient-enhanced computational homogenization scheme. *Int. J. Numer. Meth. Engng*, 54:1235–1260, 2002.

V. G. Kouznetsova, M. G. D. Geers, and W. A. M. Brekelmans. Multi-scale second-order computational homogenization of multi-phase materials: a nested finite element solution strategy. *Comput. Methods Appl. Mech. Engrg.*, 193:5525–5550, 2004.

E. Kröner. Elastic moduli of perfectly disordered composites. *J. Mech. Phys. Solid.*, 15, 1967.

E. Kuhl. *Theory and Numerics of Open System Continuum Thermodynamics – Spatial and Material Settings –*. Habilitation thesis, Technische Universität Kaiserlautern, 2004.

E. Kuhl and P. Steinmann. Material forces in open system mechanics. *Comput. Methods Appl. Mech. Engrg.*, 193:2357–2381, 2004.

E. Kuhl and P. Steinmann. A hyperelastodynamic ALE formulation based on referential, spatial and material settings of continuum mechanics. *Acta Mech.*, 174:201–222, 2005.

E. Kuhl and P. Steinmann. Material forces in open system mechanics. *Comput. Methods Appl. Mech. Engrg.*, 193:2357–2381, 2006.

E. Kuhl, H. Askes, and P. Steinmann. An ALE formulation based on spatial and material settings of continuum mechanics – Part 1: Generic hyperelastic formulation. *Comput. Methods Appl. Mech. Engrg.*, 193:4207–4222, 2004a.

E. Kuhl, R. Denzer, F. J. Barth, and P. Steinmann. Application of the material force method to thermo-hyperelasticity. *Comput. Methods Appl. Mech. Engrg.*, 193:3303–3325, 2004b.

R. Larsson and Y. Zhang. Homogenization of microsystem interconnects based on micropolar theory and discontinuous kinematics. *J. Mech. Phys. Solid.*, 55:819–841, 2007.

R. Larsson, K. Runesson, and S. Sture. Finite element simulation of localized plastic deformation. *Arch. Appl. Mech.*, 61:305–317, 1991.

R. Larsson, K. Runesson, and N. S. Ottosen. Discontinuous displacement approximation for capturing plastic localization. *Int. J. Numer. Meth. Engng*, 36:2087–2105, 1993.

T. Liebe. *Theory and Numerics of Higher Gradient Inelastic Material Behaviour*. PhD Thesis, Technische Universität Kaiserslautern, 2003.

T. Liebe and P. Steinmann. Theory and numerics of a thermodynamically consistent framework for geometrically linear gradient plasticity. *Int. J. Numer. Meth. Engng*, 51:1437–1467, 2001.

T. Liebe, R. Denzer, and P. Steinmann. Application of the material force method to isotropic continuum damage. *Comput. Mech.*, 30:171–184, 2003a.

T. Liebe, A. Menzel, and P. Steinmann. Theory and numerics of geometrically non-linear gradient plasticity. *Int. J. Eng. Sci.*, 41:1603–1629, 2003b.

L. E. Malvern. *Introduction to the Mechanics of a Continuus Medium*. Prentice Hall, 1969.

J. E. Marsden and T. J. R. Hughes. *Mathematical Foundations of Elasticity*. Dover, 1983.

K. Matous, M. G. Kulkarni, and P. H. Geubelle. Multiscale cohesive failure modeling of heterogeneous adhesives. *J. Mech. Phys. Solid.*, 56:1511–1533, 2008.

G. A. Maugin. *Material Inhomogeneities in Elasticity*. Chapman & Hall/CRC, 1993.

G. A. Maugin. On the J-integral and energy-release rates in dynamical fracture. *Acta Mech.*, 105:33–47, 1994.

G. A. Maugin. Defects, dislocations and the general theory of material inhomogeneity. Lecture notes of the CISM Advanced Course "Generalised Continua and Dislocation Theory. theoretical concepts, computational methods and experimental verification", 2007.

G. A. Maugin and P. Steinmann. *Mechanics of Material Forces*. Springer, 2005.

G. A. Maugin and C. Trimarco. Pseudomomentum and material forces in nonlinear elasticity: variational formulations and application to brittle fracture. *Acta Mech.*, 94:1–28, 1992.

H. A. Meier, E. Kuhl, and P. Steinmann. A note on the generation of periodic granular microstructures based on grain size distributions. *Int. J. Numer. Anal. Meth. Geomech.*, 32 (5):509–522, 2008a.

H. A. Meier, P. Steinmann, and E. Kuhl. Towards multiscale computation of confined granular media – contact forces, stresses and tangent operators. *Technische Mechanik*, 28: 32–42, 2008b.

A. Menzel and P. Steinmann. On the continuum formulation of higher gradient plasticity for single and polycrystals. *J. Mech. Phys. Solid.*, 48:1777–1796, 2000. Erratum, 49:1179–1180, 2001.

A. Menzel and P. Steinmann. A note on material forces in finite inelasticity. *Arch. Appl. Mech.*, 74:800–807, 2005.

A. Menzel, R. Denzer, and P. Steinmann. On the comparison of two approaches to compute material forces for inelastic materials. application to single-slip crystal-plasticity. *Comput. Methods Appl. Mech. Engrg.*, 193:5411–5428, 2004.

J. Mergheim. *Computational Modeling of Strong and Weak Discontinuities*. PhD thesis, Technische Universität Kaiserslautern, 2006.

J. Mergheim, E. Kuhl, and P. Steinmann. A hybrid discontinuous Galerkin/interface method for the computational modelling of failure. *Commun. Numer. Meth. Engng*, 20:511–519, 2004.

J. Mergheim, E. Kuhl, and P. Steinmann. A finite element method for the computational modelling of cohesive cracks. *Int. J. Numer. Meth. Engng*, 63:276–289, 2005.

J. Mergheim, E. Kuhl, and P. Steinmann. Towards the algorithmic treatment of 3D strong discontinuities. *Commun. Numer. Meth. Engng*, 23:97–108, 2007.

J. C. Michel, H. Moulinec, and P. Suquet. Effective properties of composite materials with periodic microstructure: a computational approach. *Comput. Methods Appl. Mech. Engrg.*, 172:109–143, 1999.

C. Miehe. Computational micro-to-macro transitions discretized micro-structures of heterogeneous materials at finite strains based on the minimization of averaged incremental energy. *Comput. Methods Appl. Mech. Engrg.*, 192:559–591, 2003.

C. Miehe and J. Dettmar. A framework for micro-to-macro transitions in periodic particle aggregates of granular materials. *Comput. Methods Appl. Mech. Engrg.*, 193:225–256, 2004.

C. Miehe and A. Koch. Computational micro-to-macro transitions of discretized microstructures undergoing small strains. *Arch. Appl. Mech.*, 72:300–317, 2002.

C. Miehe and J. Schröder. Post-critical discontinuous localization analysis of small-strain softening elastoplastic solids. *Arch. Appl. Mech.*, 64:267–285, 1994.

C. Miehe, J. Schotte, and J. Schröder. Computational micro-macro transitions and overall moduli in the analysis of polycrystals at large strains. *Comput. Mater. Sci.*, 16:372–382, 1999a.

C. Miehe, J. Schröder, and J. Schotte. Computational homogenization analysis in finite plasticity. Simulation of texture development in polycrystalline materials. *Comput. Methods Appl. Mech. Engrg.*, 171:387–418, 1999b.

C. Miehe, J. Schotte, and M. Lambrecht. Homogenization of inelastic solid materials at finite strains based on incremental minimization principles. application to the texture analysis of polycrystals. *J. Mech. Phys. Solid.*, 50:2123–2167, 2002a.

C. Miehe, J. Schröder, and C. Bayreuther. On the homogenization analysis of composite materials based on discretized fluctuations on the micro-structure. *Comput. Mater. Sci.*, 155:1–16, 2002b.

C. Miehe, J. Schröder, and M. Becker. Computational homogenization analysis in finite elasticity: material and structural instabilities on the micro- and macro-scales of periodic composites and their interaction. *Comput. Methods Appl. Mech. Engrg.*, 191:4971–5005, 2002c.

R. D. Mindlin. Influence of couple-stress on stress concentrations. *Exp. Mech.*, 3:1–7, 1963.

R. D. Mindlin. Micro-structure in linear elasticity. *Arch. Rat. Mech. Anal.*, 16:51–78, 1964.

R. D. Mindlin. Second gradient of strain and surface-tension in linear elasticity. *Int. J. Solid Struct.*, 1:417–438, 1965.

R. D. Mindlin and N. N. Eshel. On first strain-gradient theories in linear elasticity. *Int. J. Solid Struct.*, 4:109–124, 1968.

R. D. Mindlin and H. F. Tiersten. Effects of couple-stress in linear elasticity. *Arch. Rat. Mech. Anal.*, 11:415–448, 1962.

N. Moës, J. Dolbow, and T. Belytschko. A finite element method for crack growth without remeshing. *International Journal for Numerical Methods in Engineering*, 46:131–150, 1999.

H. B. Mühlhaus and E. C. Aifantis. A variational principle for gradient plasticity. *Int. J. Solid Struct.*, 28:845–857, 1991.

R. Müller and G. A. Maugin. On material forces and finite element discretizations. *Comput. Mech.*, 29:52–60, 2002.

A. Needleman. A continuum model for void nucleation by inclusion debonding. *J. Appl. Mech.*, 54:525–531, 1987.

A. Needleman. An analysis of decohesion along an imperfect interface. *Int. J. Fract.*, 42: 21–40, 1990a.

A. Needleman. An analysis of tensile decohesion along an interface. *J. Mech. Phys. Solid.*, 38:289–324, 1990b.

A. Nemat-Nasser and M. Hori. *Micromechanics: Overall Properties of Heterogeneous Materials*. North-Holland Elsevier, 2nd revised edition, 1999.

O. Nguyen, E. A. Repetto, M. Ortiz, and R. A. Radovitzky. A cohesive model of fatigue crack growth. *Int. J. Fract.*, 110:351–369, 2001.

T. D. Nguyen, S. Govindjee, P. A. Klein, and H. Gao. A material force method for inelastic fracture mechanics. *J. Mech. Phys. Solid.*, 53:92–121, 2005.

C. F. Niordson. *Non-Local Modeling of Materials*. PhD thesis, Denmark Technical University, 2002.

R. W. Ogden. *Non-Linear Elastic Deformations*. Dover, 1997.

M. Ortiz and A. Pandolfi. Finite-deformation irreversible cohesive elements for three-dimensional crack-propagation analysis. *Int. J. Numer. Meth. Engng*, 44:1267–1282, 1999.

C. Papenfuss and S. Forest. Thermodynamical framework for higher grade material theories with internal variables or additional degrees of freedom. *Journal of Non-Equilibrium Thermodynamics*, 31:319–353, 2006.

R. H. J. Peerlings. On the role of moving elastic-plastic boundaries in strain-gradient plasticity. *Modelling Simul. Mater. Sci. Eng.*, 15:109–120, 2007.

R. H. J. Peerlings, M. G. D. Geers, R. de Borst, and W. A. M. Brekelmans. A critical comparison of nonlocal and gradient-enhanced softening continua. *Int. J. Solid Struct.*, 38: 7723–7746, 2001.

C. Polizzotto. Strain-gradient elastic-plastic material models and assessment of the higher order boundary conditions. *Eur. J. Mech. Solid*, 26:189–211, 2007.

C. Polizzotto and G. Borino. A thermodynamics-based formulation of gradient-dependent plasticity. *Eur. J. Mech. Solid*, 17:741–761, 1998.

R. A. Regueiro, D. J. Bammann, E. B. Marin, and K. Garikipati. A nonlocal phenomenological anisotropic finite deformation plasticity model accounting for dislocation defects. *ASME J. Eng. Mat. Technol.*, 124:380–387, 2002.

A. Reuss. Berechnung der Fließgrenze von Mischkristallen auf Grund der Plastizitätsbedingung für Einkristalle. *J. Appl. Math. Mech. Z. Angew. Math. Mech.*, 9:49–58, 1929.

J. R. Rice. A path-dependent integral and the approximate analysis of strain concentration by notches and cracks. *J. Appl. Mech.*, 35:379–388, 1968.

G. Sachs. Zur Ableitung einer Fließbedingung. *Z. Verein dt. Ing.*, 72, 1928.

C. Sansour and S. Skatulla. Generalised continua. Lecture notes of the CISM Advanced Course "Generalised continua and dislocation theory. Theoretical concepts, computational methods and experimental verification", 2007.

J. C. J. Schellekens and R. de Borst. On the numerical intergration of interface elements. *Int. J. Numer. Meth. Engng*, 36:43–66, 1993a.

J. C. J. Schellekens and R. de Borst. A non-linear finite element approach for the analysis of mode-I free edge delamination in composites. *Int. J. Solid Struct.*, 30:1239–1253, 1993b.

M. Scherer, R. Denzer, and P. Steinmann. Energy-based r-adaptivity: a solution strategy and applications to fracture mechanics. *Int. J. Fract.*, DOI: 10.1007/s10704-007-9143-9, 2007.

M. Scherer, R. Denzer, and P. Steinmann. On a solution strategy for energy-based mesh optimization in finite hyperelastostatics. *Comput. Methods Appl. Mech. Engrg.*, 197:609–622, 2008.

J. Y. Shu, W. E. King, and N. E. Fleck. Finite elements for materials with strain gradient effects. *Int. J. Numer. Meth. Engng*, 44:373–391, 1999.

R. J. M. Smit, W. A. M. Brekelmans, and H. E. H. Meijer. Prediction of the mechanical behaviour of nonlinear heterogeneous systems by multi-level finite element modeling. *Comput. Methods Appl. Mech. Engrg.*, 155:181–192, 1998.

H. Steeb and S. Diebels. Modeling thin films applying an extended continuum theory based on a scalar-valued order parameter – Part I: Isothermal case. *Int. J. Solid Struct.*, 41: 5071–5085, 2004.

P. Steinmann. A micropolar theory of finite deformation and finite rotation multiplicative elastoplasticity. *Int. J. Solid Struct.*, 31:1063–1084, 1994.

P. Steinmann. A model adaptive strategy to capture strong discontinuities at large inelastic strain. In S. Idelsohn, E. O nate, and E. Dvorking, editors, *Computational Mechanics. New Trends and Applications*, pages 1–12. CIMNE, Barcelona, 1998.

P. Steinmann. Application of material forces to hyperelastostatic fracture mechanics. I. Continuum mechanical setting. *Int. J. Solid Struct.*, 37:7371–7391, 2000.

P. Steinmann. On spatial and material settings of thermo-hyperelastodynamics. *J. Elasticity*, 66:109–157, 2002.

P. Steinmann. On boundary potential energies in deformational and configurational mechanics. *J. Mech. Phys. Solid.*, 2007. doi: doi:10.1016/j.jmps.2007.07.001.

P. Steinmann and P. Betsch. A localization capturing FE-interface based on regularized strong discontinuities at large inelastic strains. *Int. J. Solid Struct.*, 37:4061–4082, 2000.

P. Steinmann and E. Stein. A unifying treatise of variational principles for two types of micropolar continua. *Acta Mech.*, 121:215–232, 1997.

P. Steinmann and K. Willam. Localization within the framework of micro-polar elastoplasticity. In O. Brüller, V. Mannl, and J. Najar, editors, *Adv. Cont. Mech.*, pages 296–313. Springer, 1991.

P. Steinmann, D. Ackermann, and F. J. Barth. Application of material forces to hyperelastostatic fracture mechanics. II. Computational setting. *Int. J. Solid Struct.*, 38:5509–5526, 2001.

J. S. Stölken and A. G. Evans. A microbend test method for measuring the plasticity length scale. *Acta Mater.*, 46:5109–5115, 1998.

N. Sukumar, B. Moran, T. Black, and T. Belytschko. An element-free Galerkin method for three-dymensional fracture mechanics. *Comput. Mech.*, 20:170–175, 1997.

N. Sukumar, N. Moës, B. Moran, and T. Belytschko. Extended finite element method for three-dimensional crack modelling. *International Journal for Numerical Methods in Engineering*, 48:1549–1570, 2000.

N. Sukumar, B. Moran, A. Yu Semenov, and V. V. Belikov. Natural neighbour Galerkin methods. *Int. J. Numer. Meth. Engng*, 50:1–27, 2001.

N. Sukumar, Z. Y. Huang, J.-H. Prevost, and Z. Suo. Partition of unity enrichment for bimaterial interfaces cracks. *International Journal for Numerical Methods in Engineering*, 59: 1075–1102, 2004.

R. Sunyk and P. Steinmann. On higher gradients in continuum-atomistic modelling. *Int. J. Solid Struct.*, 40:6877–6896, 2003.

G. I. Taylor. Plastic strain in metals. *J. Institute of Metals*, 62:307–324, 1938.

R. A. Toupin. Elastic materials with couple-stress. *Arch. Rat. Mech. Anal.*, 11:385–414, 1962.

R. A. Toupin. Theory of elasticity with couple-stress. *Arch. Rat. Mech. Anal.*, 17:85–112, 1964.

V. Tvergaard and J. W. Hutchinson. The relation between crack growth resistance and fracture process parameters in elastic-plastic solids. *J. Mech. Phys. Solid.*, 40:1377–1397, 1992.

J. Utzinger, A. Menzel, P. Steinmann, and A. Benallal. Aspects of bifurcation in an isotropic elastic continuum with orthotropic inelastic interface. *Eur. J. Mech. Solid*, page doi:10.1016/j.euromechsol.2007.11.001, 2007.

J. Utzinger, M. Bos, M. Floeck, A. Menzel, E. Kuhl, R. Renz, K. Friedrich, A.K. Schlarb, and P. Steinmann. Computational modelling of thermal impact welded PEEK/steel single lap tensile specimens. *Comput. Mater. Sci.*, 41(3):287–296, 2008.

K. C. Valanis. A gradient theory of internal variables. *Acta Mech.*, 116:1–14, 1996.

M. J. van den Bosch, P. J. G. Schreurs, and M. G. D. Geers. An improved description of the exponential Xu and Needleman cohesive zone law for mixed-mode decohesion. *Eng. Fract. Mech.*, 73:1220–1234, 2006.

M. J. van den Bosch, P. J. G. Schreurs, and M. G. D. Geers. On the development of a 3d cohesive zone element in the presence of large deformations. *Comput. Mech.*, DOI 10.1007/s00466-007-0184-8, 2008.

I. Vardoulakis and E. C. Aifantis. A gradient flow theory of plasticity for granular materials. *Acta Mech.*, 87:197–217, 1991.

W. Voigt. Über die Beziehung zwischen den beiden Elastizitätskonstanten isotroper Körper. *Wied. Ann. Physik*, 38:573–587, 1889.

G. Z. Voyiadjis and R. K. Abu Al-Rub. Gradient plasticity theory with a variable length scale parameter. *Int. J. Solid Struct.*, 42:3998–4029, 2005.

P. Wriggers, S. Löhnert, and M. Hain. Multiscale modeling and design of new materials. Lecture notes of the CISM Advanced Course on ”Multiscale modeling and design of new materials”, 2005.

X.-P. Xu and A. Needleman. Void nucleation by inclusion debonding in a crystal matrix. *Modelling Simul. Mater. Sci. Eng.*, 1:111–132, 1993.

H. M. Zbib and E. C. Aifantis. On the gradient-dependent theory of plasticity and shear banding. *Acta Mech.*, 92:209–225, 1992.

A. Zervos, P. Papanastasiou, and I. Vardoulakis. A finite element displacement formulation for gradient elastoplasticity. *Int. J. Numer. Meth. Engng*, 50:1369–1388, 2001.

H. T. Zhu, H. M. Zbib, and E. C. Aifantis. On the role of strain gradients in adiabatic shear banding. *Acta Mech.*, 111:111–124, 1995.

Lebenslauf

Name:	Claudia Britta Hirschberger
Nationalität:	Deutsch
Geburtsdatum:	2. Januar 1976
Geburtsort:	Diez
Familienstand:	ledig

1982 – 1986	Karl-von-Ibell-Grundschule, Diez
1986 – 1988	Orientierungsstufe, Gymnasium / Realschule Diez
1988 – 1995	Gymnasium Diez, Allgemeine Hochschulreife
1995 – 1997	abgeschlossene Berufsausbildung zur Bauzeichnerin, Architekturbüro Horst Reichwein, Elz
10/1997 – 11/2003	Studium des Bauingenieurwesens und der Mechanik, Technische Universität Darmstadt
08/2000 – 05/2001	Integriertes Auslandsstudium, University of California, Berkeley, USA
11/2003	Diplom Bauingenieurwesen, Technische Universität Darmstadt
12/2003 – 01/2004	Wissenschaftliche Mitarbeiterin am Institut für Werkstoffe und Mechanik im Bauwesen, Technische Universität Darmstadt
02/2004 – 03/2005	Wissenschaftliche Mitarbeiterin am Institut für Mechanik (Bauwesen), Lehrstuhl II, Universität Stuttgart
seit 04/2005	Promotionstudentin als Stipendiatin im Internationalen DFG-Graduiertenkolleg 1131, Lehrstuhl für Technische Mechanik, Technische Universität Kaiserslautern

UKL/LTM-Schriftenreihe

bereits veröffentlicht wurden:

1 Menzel, A.: Modelling and Computation of Geometrically Nonlinear Anisotropic Inelasticity.
2002, ISBN 3-925178-86-4

2 Betsch, P.: Computational Methods for Flexible Multibody Dynamics.
2002, ISBN 3-925178-92-9

3 Liebe, T.: Theory and numerics of higher gradient inelastic material behavior.
2003, ISBN 3-936890-09-9

4 Groß, M.: Conserving Time Integrators for Nonlinear Elastodynamics.
2004, ISBN 3-936890-37-4

5 Kuhl, E.: Theory and Numerics of Open System Continuum Thermodynamics – Spatial and Material Settings –.
2004, ISBN 3-936890-42-0

6 Sunyk, R.: On Aspects of Mixed Continuum-Atomistic Material Modelling.
2004, ISBN 3-936890-51-X

7 Arockiarajan, A.: Computational Modeling of Domain Switching Effects in Piezoceramic Materials – A Micro-Macro Mechanical Approach.
2005, ISBN 3-936890-92-7

8 Mergheim, J.: Computational Modeling of Strong and Weak Discontinuties.
2006, ISBN 3-939432-02-4; 978-3-939432-02-4-9

9 Delibas, B.: Rate dependent nonlinear properties of perovskite tetragonal piezoelectric materials using a micromechanical model.
2006, ISBN 3-939432-05-9; 978-3-939432-05-0

10 Leyendecker, S.: Mechanical integrators for constrained dynamical systems in flexible multibody dynamics.
2006, ISBN 3-939432-09-1; 978-3-939432-09-8

11 Denzer, R.: Computational Configurational Mechanics.
2006, ISBN 3-939432-12-1; 978-3-939432-12-8

12 Krol, O.: Thermo-Mechanical Modelling of Solids and Interfaces – Theory, Numerics and Applications. 2007, ISBN 978-3-939432-45-6

13 Kleuter, B.: Generalized Parameter Identification for Finite Viscoelasticity. 2007, ISBN 978-3-939432-53-1

14 Menzel, A.: Frontiers in Inelastic Continuum Mechanics. 2007, ISBN 978-3-939432-55-5

15 Himpel, G.: Computational Modeling of Biomechanical Phenomena – Remodeling, Growth and Reorientierung. 2008, ISBN 978-3-939432-62-3

16 Bargmann, S.: Theory and numerics of non-classical thermo-hyperelasticity. 2008, ISBN 978-3-939432-77-7

17 Hirschberger, C. B.: A Treatise on Micromorphic Continua. Theory, Homogenization, Computation. 2008, ISBN 978-3-939432-80-7